

Some pages of this thesis may have been removed for copyright restrictions.

If you have discovered material in Aston Research Explorer which is unlawful e.g. breaches copyright, (either yours or that of a third party) or any other law, including but not limited to those relating to patent, trademark, confidentiality, data protection, obscenity, defamation, libel, then please read our [Takedown policy](#) and contact the service immediately (openaccess@aston.ac.uk)

Smart Design of Solid Base Catalysts with
Different Pore Architecture, Properties and
Functional Groups for the
Transesterification of Triglycerides and the
Selective Oxidation Cascade of Benzyl
Alcohol with Benzyl Amine.

Thomas Adam Bryant

Doctor of Philosophy

ASTON UNIVERSITY

February 2020

© Thomas Adam Bryant, 2020 asserts his moral right to be identified as the
author of this thesis

This copy of the thesis has been supplied on condition that anyone who
consults it is understood to recognise that its copyright belongs to its author and
that no quotation from the thesis and no information derived from it may be
published without appropriate permission or acknowledgement.

Aston University

Smart Design of Solid Base Catalysts with Different Pore Architecture, Properties and Functional Groups for the Transesterification of Triglycerides and the Selective Oxidation Cascade of Benzyl Alcohol with Benzyl Amine.

Thomas Adam Bryant

Doctor of Philosophy

February 2020

Internal diffusion limitations within a heterogeneous catalytic material can prove problematic for industrially relevant chemical reactions, especially when using large reagent molecules. This work explores the use of a smart pore system design through a dual templated silica support for biodiesel synthesis and oxidation reactions.

One-pot MgO/SBA-15 was synthesised, with selective functionalisation within the mesopores to allow for excellent dispersion. These materials were further improved by adding a macroporous network, resulting in a hierarchical pore system. When screened for the transesterification of triglycerides, the hierarchical materials outperformed the diffusion-limited mesoporous materials. In addition, the incorporation of a macroporous template improved the materials pore integrity and structure.

Through manipulation of the pH during synthesis, MgO/SBA-15 was further functionalised with gold to be screened in selective oxidation reactions. Again, hierarchical materials were superior to mesoporous materials. In addition, chemometrics was used to assess key variables related to performance and selectivity. The heat-treatment temperature proved to be crucial for the activity, with 400 °C being optimum to increase activity and prolong catalyst life-time. Additionally, the addition of potassium carbonate mitigated substantially the deactivation of the catalyst produced by the reaction products.

Subsequently, gold supported on MgO, CaO and SiO₂ materials were synthesised and screened for the selective oxidation of benzyl alcohol, with the aim to compare their performance against Au/MgO/SBA-15 synthesised materials. Initial activity was found to relate to the gold loading of each material. However, deactivation was correlated to the basic nature of the support, as predicted. The most basic supports Au/CaO and Au/MgO deactivated slower and were unaffected by the addition of potassium carbonate. Finally, all materials were screened for the oxidative coupling of alcohols and amines. Au/CaO and Au/MgO hindered the oxidative coupling. Upon addition of potassium carbonate, the Au/MgO/SBA-15 hierarchical material proved to be the superior material tested.

Heterogeneous, Catalysis, Transesterification, Selox, Gold

Acknowledgements

I would like to thank my supervisors Dr Marta Granollers-Mesa and Dr Georgios Kyriakou for giving me this opportunity, as well as their help and guidance. The research group had a turbulent period over the course of my studies, and I would recognise George for steadying me through the rougher patches. Marta has shown me to take a step back and approach problems from a smarter way, and I will always value that. Without her help, I doubt I could have brought this all together. I can say with confidence and too much experience she is the best supervisor I've had.

Furthermore, I am grateful to my colleagues at Aston University; Dr Mark Isaacs, Dr Chris Parlett, Dr Amin Osatiashtiani and Dr Jinesh Manayil for their advice and invaluable expertise. I would also like to acknowledge the people who put me on this path; Michael Shanks, Dr Shaun K. Johnston and Dr M. Grazia Francesconi.

Also the Brummie friends I have made along the way, who I bounced ideas off and kept me sane. I would especially like to thank Dr Lee Durndell, Dr Martin Taylor, Dr Kin Wai Cheah and Dr James Hunns, Dr Joe Socci and soon-to-be Drs Costanza Cucuzzella, Jorge Ordovas and Filipe Rego.

I've lived with some great people, but I'd like to particularly thank my Beneluxian besties; Lonieke for our lazy breakfasts and Sara for everything.

Finally, I'd like to thank my family and friends for supporting me and keeping me motivated and sane. Dotty, I couldn't have done it without you. You picked me up when I was at my lowest and were with me at my highest. Thank you.

Publications

- 1 Stabilization of Pd_{3-x}In_{1+x} Polymorphs with Pd-like Crystal Structure and their Superior Performance as Catalysts for Semi-Hydrogenation of Alkynes.
Shaun K. Johnston, Thomas A. Bryant, Jonathan Strong, Laura Lazzarini, Alex O. Ibadon, Maria Grazia Francesconi
ChemCatChem 2019, 11, 2909.
- 2 Transesterification of Triglycerides over MgO Functionalised Ordered Mesoporous and Hierarchically Porous Silica Catalysts.
Thomas A. Bryant, Lois Dampney, Mark A. Isaacs, Christopher M. A. Parlett, Marta Granollers-Mesa, Georgios Kyriakou, Karen Wilson, Adam F. Lee
[in preparation]
- 3 Au@MgO/SBA-15 based Selective Oxidation and Coupling of Benzyl Alcohol and Benzylamine; Chemometric Reaction Optimisation and Heat Treatment Study.
Thomas A. Bryant, Martin J. Taylor, Georgios Kyriakou, Marta Granollers-Mesa
[in preparation]
- 4 Au Functionalised Alkaline Earth Metal Oxide Basic Supports and their Catalytic Activity to Selective Oxidation and Coupling of Benzyl Alcohol and Benzylamine.
Thomas A. Bryant, Martin J. Taylor, Georgios Kyriakou, Marta Granollers-Mesa
[in preparation]

Presentations

- 1 Triglyceride Transesterification over MgO doped Hierarchical Porous SiO₂
Thomas A. Bryant, Mark A. Isaacs, Christopher M.A. Parlett, Karen Wilson,
Georgios Kyriakou and Adam F. Lee. 08/09/2017
SCI Materials Science Early Career Forum
- 2 Using Magnesium Silicates for Biodiesel Production
Thomas A. Bryant. 09/11/2017
Innovate UK
- 3 Transesterification over MgO Functionalised Hierarchical Porous SiO₂
Thomas A. Bryant, Mark A. Isaacs, Christopher M.A. Parlett, Karen Wilson,
Georgios Kyriakou and Adam F. Lee. 19/04/2018
Aston University, Engineering and Applied Science PGR Conference

List of Contents

Acknowledgements	3
Publications	4
Presentations.....	5
List of Contents.....	6
List of Abbreviations	10
List of Figures	13
List of Tables	24
List of Equations	24
Chapter 1.....	25
1.1 Background.....	26
1.1.1 Sustainable Chemistry through Catalytic Systems.....	26
1.1.1.1 Homogeneous Catalysis.....	27
1.1.1.2 Heterogeneous Catalysis.....	29
1.1.1.3 Electronic and Geometric Effects	31
1.1.2 Support Materials	35
1.1.2.1 Surfactant Soft Templates	35
1.1.2.2 Templated Ordered Mesoporous Silica	36
1.1.3 Biodiesel and its Catalytic Synthesis.....	39
1.1.3.1 Biodiesel and Transesterification.....	39
1.1.3.2 Heterogeneous Base Catalysed Transesterification.....	42
1.1.3.3 Alkaline Earth Metal Oxides.....	43
1.1.4 Nanoparticulate Gold and its Catalytic Applications.....	45
1.1.4.1 Nanoparticulate Gold Species	45
1.1.4.2 Gold Catalysed Chemical Reactions	47
1.1.4.3 Selective Oxidation of Alcohols	49
1.1.4.4 Synthesis of Schiff Bases via Oxidative Coupling	51
1.2 Thesis Aims and Objectives.....	55
1.3 References.....	56
Chapter 2.....	67
2.1 Chemical Table	68
2.2 Material Synthesis.....	69
2.2.1 Typical preparation of MgO supported on Ordered Mesoporous SBA-15 using cooperative self-assembly (CSA).....	69

2.2.2 Typical preparation of MgO supported on Ordered Mesoporous SBA-15 using true liquid crystal templating (TLCT)	69
2.2.3 Preparation of Polystyrene Nanosphere Hard Template:.....	69
2.2.4 Typical Preparation of Ordered Hierarchical MgO/SBA-15 using true liquid crystal template (TLCT):.....	70
2.2.5 Gold functionalisation of MgO/SBA-15 using double impregnation method (DIM)	70
2.2.6 Gold functionalisation of MgO/SBA-15 using deposition precipitation (DP) method	70
2.2.7 Gold functionalisation of MgO/SBA-15 using liquid phase deposition precipitation (LPRD) method	71
2.2.8 Gold functionalisation of bulk materials using double impregnation method (DIM)	71
2.3 Material Characterisation	72
2.3.1 X-Ray Diffraction (XRD)	72
2.3.2 Inductively Coupled Plasma–Optical Emission Spectroscopy (ICP-OES) ...	74
2.3.3 Nitrogen Porosimetry.....	75
2.3.4 Scanning Electron Microscope – Energy Dispersive X-ray Analysis.....	79
2.3.5 Scanning Transmission Electron Microscopy (STEM)	80
2.3.6 X-Ray Photoelectric Spectroscopy (XPS)	81
2.3.7 CO ₂ Chemisorption-Mass Spectrometry and CO ₂ TPD	82
2.3.8 Gas Chromatography – Flame Ionisation Detector	83
2.4 Catalytic Testing	85
2.4.1 Transesterification of tributyrin at 60 °C:	85
2.4.2 Transesterification of tributyrin, tricaprylin and trilaurin at 90 °C:	85
2.4.3 Selective oxidation of benzyl alcohol.....	86
2.4.4 Selective oxidative coupling of benzyl alcohol and benzylamine	87
2.4.5 Equations used for Screening	87
2.5 References.....	88
Chapter 3.....	90
3.1 Introduction	91
3.2 Results and Discussion.....	92
3.2.1 MgO functionalised CSA SBA-15.....	92
3.2.1.1. X-ray Diffractometry	92
3.2.1.2. Inductively coupled plasma with optical emission spectroscopy	93
3.2.2 MgO functionalised TLCT SBA-15	95
3.2.2.1. Inductively coupled plasma with optical emission spectroscopy	95

3.2.2.2. X-ray Diffractometry	96
3.2.2.3. Nitrogen Porosimetry	99
3.2.2.4. Microscopy (SEM and TEM).....	102
3.2.2.5. X-ray Photoelectron Spectroscopy	104
3.2.2.6. Active Site Probing	108
3.2.2.7. Characterisation summary.....	110
3.2.3 Catalytic Screening Experiments	111
3.2.3.1 Tributyrin (C ₄) Screening at 60 °C	112
3.2.3.2 Tributyrin Kinetic Study.....	113
3.2.3.3 Tributyrin (C ₄), Tricaprylin (C ₈) and Trilaurin (C ₁₂) Screening at 90 °C	115
3.2.3.4 Methanol:Tributyrin Ratio Study	116
3.2.3.5 Recycling Study at 60 °C	117
3.2.3.6 Catalytic Screening Summary	119
3.3 Conclusions and Recommendations for Further Work	120
3.4 References.....	122
Chapter 4.....	127
4.1 Introduction	128
4.2 Results and Discussion.....	129
4.2.1 Preliminary Synthesis Study.....	130
4.2.1.1 Preliminary Study Characterisation	130
4.2.1.2 Preliminary Study Screening	135
4.2.1.3 Preliminary Study Summary	138
4.2.2 Chemometrics Study	140
4.2.2.1 Chemometrics Experimental design	140
4.2.2.2 Chemometrics Results and Discussion	142
4.2.2.3 Chemometrics Summary	143
4.2.3 Heat-Treatment Study	144
4.2.3.1 Heat-Treatment Study Characterisation	144
4.2.3.2 Heat-Treatment Study Screening	156
4.2.3.3 Heat-Treatment Study Summary	161
4.2.4 Deactivation and Green Conditions Study	163
4.2.4.1 Deactivation Investigation.....	163
4.2.4.2 Green Conditions.....	168
4.2.4.3 Deactivation and Green Conditions Summary.....	172
4.3 Conclusions and Recommendations for Further Work	173
4.4 References.....	175
Chapter 5.....	179

5.1 Introduction	180
5.2 Results and Discussion.....	181
5.2.1 Au/Bulk Materials Characterisation	181
5.2.1.1 Wide and Diffractometry	182
5.2.1.2. Nitrogen Porosimetry	186
5.2.1.3. X-ray Photoelectron Spectroscopy	187
5.2.1.4. Scanning Transmission Electron Microscopy	193
5.2.1.5. Bulk Supported Gold Characterisation Summary	195
5.2.2 Selective Oxidation Screening	196
5.2.2.1. Selective Oxidation of Benzyl Alcohol	196
5.2.2.2 Comparison of bulk supported materials with Au@MgO/SBA-15 Materials	200
5.2.2.3. Selective Oxidation Summary.....	201
5.2.3 Oxidative Cross-Coupling Reaction	202
5.2.3.1 Oxidative Cross-Coupling of Benzyl Alcohol and Benzyl Amine	203
5.2.3.2 Effect of Basicity on Imine Synthesis.....	207
5.2.3.3 Oxidative Coupling Rate Profiles	210
5.2.3.4 Oxidative Coupling Summary	211
5.3 Conclusions and Recommendations for Further Work	212
5.4 References.....	214
Appendix.....	217
Appendix 1 for Chapter 1	218
Appendix 2 for Chapter 3.....	219
Appendix 3 for Chapter 4	225
Appendix 3a: Chemometrics and DoE Appendix	225
Appendix 3b: Heat Treatment Study Appendix	229
Appendix 3c: Magnesium Loading Study	236
Appendix 3d: Gold Loading Study.....	251
Appendix 3e: Deactivation Study	265
Appendix 4 for Chapter 5.....	266
Appendix 4a: Characterisation	266
Appendix 4b: Oxidative Coupling	269
Appendix References.....	273

List of Abbreviations and Nomenclature

Au/CaO	Gold functionalised calcium oxide
Au/hier	Mesoporous MgO/SBA-15 functionalised with gold
Au/meso	Hierarchical MgO/SBA-15 functionalised with gold
Au/MgO	Gold functionalised magnesium oxide
Au/SiO ₂	Gold functionalised silicon dioxide
Au@MgO/SBA-15	Gold functionalised onto magnesium oxide supported on SBA-15 (porosity not specified)
BE	Binding energy
BET	Brunauer, Emmet and Teller Adsorption theory
BJH	Barrett, Joyner and Halenda Pore Size Distribution method
C ₄	Alkyl chain length of 4 (-C ₄ H ₉)
C ₈	Alkyl chain length of 8 (-C ₈ H ₁₇)
C ₁₂	Alkyl chain length of 12 (-C ₁₂ H ₂₅)
CMC	Critical micelle concentration
CSA	Cooperative self-assembly
CTEM	Conventional transmission electron microscopy
DIM	Double Impregnation method
DIM H	Hierarchical MgO/SBA-15 functionalised with gold using double impregnation method
DIM H C	Hierarchical MgO/SBA-15 functionalised with gold using DIM, calcined (550 °C, 2 h, 10 °C min ⁻¹)
DIM M	Mesoporous MgO/SBA-15 functionalised with gold using double impregnation method
DIM M C	Mesoporous MgO/SBA-15 functionalised with gold using DIM, calcined (550 °C, 2 h, 10 °C min ⁻¹)
DP H	Hierarchical MgO/SBA-15 functionalised with gold using deposition precipitation method
DP H C	Hierarchical MgO/SBA-15 functionalised with gold using DP, calcined (550 °C, 2 h, 10 °C min ⁻¹)
DP M	Mesoporous MgO/SBA-15 functionalised with gold using deposition precipitation method
DP M C	Mesoporous MgO/SBA-15 functionalised with gold using DP, calcined (550 °C, 2 h, 10 °C min ⁻¹)
dV(d)	Log. of the differential intrusion
E _a	Activation energy
EDX	Energy dispersive X-ray spectroscopy
FAME	Fatty acid methyl ester
FFA	Free fatty acid
FID	Flame ionisation detector/detection
FWHM	Full width half maxima
GC	Gas chromatography
HXXX (XXX = 100-800)	Gold functionalised hierarchical MgO/SBA-15, heat treated to XXX °C for 2 hours, at 10 °C min ⁻¹

ICP-OES	Inductively coupled plasma optical emission spectroscopy
IUPAC	International Union of Pure and Applied Chemistry
LAXRD	Low-angle X-ray diffractometry
LPDR	Liquid phase reductive deposition
LPDR H	Hierarchical MgO/SBA-15 functionalised with gold using liquid phase reductive deposition
LPDR H C	Hierarchical MgO/SBA-15 functionalised with gold using LPRD, calcined (550 °C, 2 h, 10 °C min ⁻¹)
LPDR M	Mesoporous MgO/SBA-15 functionalised with gold using liquid phase reductive deposition
LPDR M C	Mesoporous MgO/SBA-15 functionalised with gold using LPRD, calcined (550 °C, 2 h, 10 °C min ⁻¹)
MeOH	Methanol
MS	Mass spectrometry
MXXX (XXX = 100-800)	Gold functionalised mesoporous MgO/SBA-15, heat treated to XXX degrees for 2 hours, at 10 °C min ⁻¹
PVC	Polyvinyl chloride
SBA-15	Santa Barbara Amorphous (15)
Selox	Selective oxidation
SEM	Scanning electron microscopy
SMSI	Strong metal-support interactions
STEM	Scanning electron microscopy
TAG	Triacylglyceride
TEM	Transmission electron microscopy
TEOS	Tetraethyl orthosilicate
TLCT	True liquid crystal templating
TLK	Terrace, Ledge, Kink model
TMOS	Tetramethyl orthosilicate
TOF	Turnover frequency
TPD	Temperature programmed desorption
WAXRD	Wide-angle X-ray diffraction
XPS	X-ray photoelectron spectroscopy
XRD	X-ray diffraction

[A]	Product concentration at time t
[A] ₀	Initial product concentration
[A] _{total}	Maximum theoretical concentration of product
[N]	Concentration of one of the products at time t
[S]	Substrate concentration at time t
[S] ₀	Initial substrate concentration
C	BET constant
d	Interplanar distance
d _{pore}	Pore diameter
K	Shape factor
n	Multiplication integer (order of reflection)
P	Equilibrium pressure
P ₀	Saturation pressure
t	Time during a reaction between start and end

t_0	Time at which the reaction began
V	Adsorbed gas quantity
V_m	Monolayer adsorbed gas quantity
θ	Diffraction/Bragg angle
λ	X-ray wavelength
τ	Mean crystallite size

List of Figures

Chapter 1

Figure 1.1. Energy diagram for a catalysed and uncatalysed reaction.....	26
Figure 1.2. The reaction mechanism for the homogeneous Zeigler-Natta catalysed synthesis of polymers	28
Figure 1.3. The reaction mechanism for the hydrogenation of nitrogen using the Haber-Bosch process	29
Figure 1.4. Reaction steps for heterogeneous catalytic reactions	30
Figure 1.5. Different adsorption mechanisms for heterogeneous catalysis.	31
Figure 1.6. Physisorption and chemisorption interaction energy profiles as a function of distance from the surface	32
Figure 1.7. Gold nanoparticles synthesised using DIM methodology supported on nano-CaO. SA and volume approximated using a spherical particle assumption and using the lattice parameter of gold.	33
Figure 1.8. TLK model representing sites on a heterogeneous catalytic surface	34
Figure 1.9. Different sizes and types of porosity.....	35
Figure 1.10. Diagram of surfactant lyotropic aggregates.....	36
Figure 1.11. Phase diagram of Pluronic P-123.....	37
Figure 1.12. Reaction schematics for the transesterification of triglycerides using (A1) basic and (A2) acidic catalysis, (B) hydrolysis of FAME with water and (C) saponification of FAME to form soap.....	40
Figure 1.13. Diagram of (top) base instigated method formation, (middle) mechanism for the transesterification of triglycerides, and (bottom) reaction scheme for sequential reactions	42
Figure 1.14. Diagram highlight the change in valance band with nanoparticles size ..	47
Figure 1.15. Coupling pathways to form benzyl benzoate for the selective oxidation of benzyl alcohol.....	49
Figure 1.16. The mechanism for the oxidation of benzyl alcohol using heterogeneous gold catalysis with subsequent site regeneration	50
Figure 1.17. Reaction scheme for the conventional synthesis of an imine from an amine and carbonyl-containing compound via condensation reaction.....	52
Figure 1.18. Reaction scheme for the synthesis of an imine from a secondary amine (top), and primary amine (bottom) via oxidative dehydration reaction.....	53
Figure 1.19. Reaction scheme for the synthesis of an imine from alcohol and amine via oxidative cross-coupling reaction.	54

Chapter 2

Figure 2.1. Illustration of Bragg's law.....	73
Figure 2.2. Low-angle X-rays diffracting off long-range ordered mesoporous silica....	74
Figure 2.3. Typical ICP-OES schematic showing the process of the sample solution reaching the plasma torch and passing through the optical spectrometer	75
Figure 2.4. The six adsorption/desorption isotherms exhibited by porous materials as defined by IUPAC	76
Figure 2.5. Nitrogen adsorption and desorption in a mesoporous material	77
Figure 2.6. Nitrogen Porosimetry isotherm for SBA-15 type materials, showing (a) type IV isotherms with H1 and H2 hysteresis curves	78
Figure 2.7. BET equation and plot.....	79
Figure 2.8. (a) SEM diagram and (b) electron shell interactions during SEM-EDX analysis.....	80
Figure 2.9. Basic schematic for a scanning transmission electron microscope.....	81
Figure 2.10. Diagram of electron shells during the initial excitation and expulsion of the photoelectron, and the subsequent relaxation and ejection of the Auger electron.....	82
Figure 2.11. Illustration highlighting (a) CO ₂ pulse titrations to calculate site density and (b) site strength derived by CO ₂ TPD-MS.....	83
Figure 2.12. ACE pressure flasks used for transesterification of tributyrin, tricaprilyn and trilaurin above the solvent boiling point.	85
Figure 2.13. Radleys 12 bed carousel reactor used for the selective oxidation of benzyl alcohol, and other reactions at atmospheric pressure.....	86

Chapter 3

Figure 3.1. X-ray Diffraction Patterns of MgO functionalised SBA-15 synthesised using a one-pot cooperative self-assembly method, employing low and wide-angle scans. .	93
Figure 3.2. ICP-OES analysis of MgO impregnated on SBA-15 using a one-pot cooperative self-assembly method.	93
Figure 3.3. Actual versus nominal loading determined by ICP-OES.	95
Figure 3.4. Wide-angle XRD patterns of mesoporous and hierarchical SBA-15. Reflections present at approximately 42° and 63° are characteristic of periclase magnesium oxide	96
Figure 3.5. Diagram explaining the proposed migration of MgO nanoparticles to the surface and lack of migration in meso and hierarchical MgO/SBA-15 respectively	97
Figure 3.6. Low-angle X-ray diffraction patterns of (a) mesoporous and (b) hierarchical SBA-15. Inset shows the 11 and 20 low-angle reflections characteristic of SBA-15....	98

Figure 3.7. Nitrogen porosimetry isotherms of (a) mesoporous and (b) hierarchical materials.....	99
Figure 3.8. BET surface area for (a) mesoporous and (b) hierarchical MgO/SBA-15 materials, with mesoporous and microporous contributions determined using N ₂ porosimetry.....	100
Figure 3.9. Pore size distributions for (a) mesoporous and (b) hierarchical MgO/SBA-15 materials determined using N ₂ porosimetry.....	101
Figure 3.10. Scanning electron micrographs of (a) polystyrene nanospheres and (b) hierarchical MgO/SBA-15, with inset particle and pore size distribution histograms respectively.....	102
Figure 3.11. TEM images of magnesium oxide deposited on (a) 2.1 wt.% mesoporous SBA-15, (b) 10.9 wt.% mesoporous SBA-15, (c) 1.6 wt.% hierarchical SBA-15 and (d) 10.9 wt.% hierarchical SBA-15 materials.	103
Figure 3.12. Mg 2p XPS of (a) mesoporous and (b) hierarchical MgO/SBA-15 normalised to show the appearance of new phases.	104
Figure 3.13. Si 2p XPS of (a) mesoporous and (b) hierarchical MgO/SBA-15.....	105
Figure 3.14. O 1s XPS of (a) mesoporous and (b) hierarchical MgO/SBA-15.....	106
Figure 3.15. Surface versus bulk MgO loading determined by XPS and ICP-OES respectfully	107
Figure 3.16. Tributyrin conversion versus magnesium loading, a) initial rate of tributyrin consumption normalised to the mass of catalyst, (b) total tributyrin conversion after 24 hours for both materials, (c) initial rate of tributyrin consumption normalised to the mass of magnesium, (d) initial rate of tributyrin consumption normalised to surface area..	112
Figure 3.17. Arrhenius plot (a) of the lowest and highest loaded SBA-15 type materials and subsequent (b) activation energy of each catalyst.	114
Figure 3.18. Screening data for the transesterification of triglycerides of different sizes, (a) initial rate of triglyceride consumption normalised to catalyst mass and (b) total conversion after 24 hours.....	115
Figure 3.19. (a) Initial rate of triglyceride consumption and (b) final conversion after 24 hours as a function of methanol to tributyrin ratio for mesoporous and hierarchical 4.4 wt% MgO/SBA-15.....	116
Figure 3.20. Methyl butyrate initial productivity as a function of sequential reaction cycles for mesoporous 4.4 wt% MgO/SBA-15, recovered and regenerated using washing or calcination.....	118

Chapter 4

Figure 4.1. ICP-OES atomic weight percentages of (a) magnesium and (b) gold for DP, DIM and LPRD methods.....	130
Figure 4.2. Wide-angle X-ray diffraction patterns for mesoporous and hierarchical materials impregnated using the three techniques. Low-angle X-ray diffraction patterns for mesoporous and hierarchical materials with inset of 11 and 20 reflections.	132
Figure 4.3. Nitrogen porosimetry isotherm for (a) DIM and (c) LPRD materials, with calculated pore size distributions for (b) DIM and (d) LPRD.	134
Figure 4.4. Reaction data for the screening of three preliminary synthesis materials using the selective oxidation of benzyl alcohol. Initial rate of selective product (a) normalised to catalyst mass and (b) final conversion of the substrate after 24 hours. The molar balance was determined of (c) pre- and (d) post-heat treated materials, and the relative standard deviations are displayed.....	136
Figure 4.5. Influence of factors on the responses monitored for the selective oxidation of benzyl alcohol.....	142
Figure 4.6. Magnesium and gold loadings determined using inductively coupled plasma optical emission spectroscopy (ICP-OES) for (a) mesoporous and (b) hierarchical materials.....	144
Figure 4.7. Low-angle X-ray diffractometry patterns for (a) mesoporous and (b) hierarchical materials, and wide-angle X-ray diffractometry patterns for (c) mesoporous and (d) hierarchical materials.	146
Figure 4.8. Nitrogen Porosimetry isotherms for (a) mesoporous and (b) hierarchical materials, with subsequent (c) pore size distributions and (d) surface area.....	147
Figure 4.9. Mg 2p distribution of features for (a) mesoporous and (b) hierarchical materials.....	148
Figure 4.10. O 1s distribution of features for (a) mesoporous and (b) hierarchical materials.....	149
Figure 4.11. Si 2p distribution of features for (a) mesoporous and (b) hierarchical materials.....	150
Figure 4.12. Au 4f XPS of (a) mesoporous and (b) hierarchical materials, (c) the ratio of metallic to cationic gold and (d) Au ⁰ _{7/2} Binding energy.	151
Figure 4.13. Transmission electron microscopy micrographs of (a,b) mesoporous and (c,d) hierarchical Au@MgO/SBA-15 materials, heat-treated at 400 °C.....	153
Figure 4.14. Average gold (a) particle size, gold particle size (b) distributions, (c) site density and (d) gold dispersion derived from transmission electron microscopy micrographs (●) and WAXRD Scherrer equation (▲).	155

Figure 4.15. The final conversion of benzyl alcohol after (a) 24 hours and (b) initial rate of productivity of the selective product benzaldehyde using the optimised conditions determined using chemometrics.....	156
Figure 4.16. Activation energy versus heat treatment temperature and particle size determined using TEM and WAXRD for mesoporous and hierarchical materials.....	158
Figure 4.17. Benzaldehyde productivity versus benzyl alcohol conversion plots between (a) mesoporous and (c) hierarchical materials and relative activity versus time plots between (b) mesoporous and (d) hierarchical materials.	159
Figure 4.18. Mesoporous and hierarchical initial productivity of benzaldehyde, displaying regions under the influence of basicity and particle size.	161
Figure 4.19. ICP-OES analysis of Au@MgO/hierarchical SBA-15 catalytic material taken at periodic intervals during selective oxidation of benzyl alcohol test, to check for functionality leaching.	163
Figure 4.20. Wide-angle X-ray diffraction (a) patterns and the associated (b) particle sizes (calculated using the Scherrer equation) of Au@MgO/hierarchical SBA-15 catalytic material taken at periodic intervals during selective oxidation of benzyl alcohol test, to check for gold particle size propagation.	164
Figure 4.21. Normalised rate loss as a function of time for Au@MgO/SBA-15 materials during selective oxidation of benzyl alcohol test.....	165
Figure 4.22. Benzyl alcohol conversion as a function of time for mesoporous and hierarchical materials screening for the selective oxidation of benzyl alcohol using an (a) oxygen-rich headspace and (b) under O ₂ flow.	166
Figure 4.23. Substrate conversion as a function of time for mesoporous and hierarchical in the presence of varying concentration of sodium and potassium carbonate.....	167
Figure 4.24. Change in rate and substrate conversion through the addition of base.	168
Figure 4.25. (a) Final conversion and rate and (b) final product yield and selectivity to the unwanted product of mesoporous (blue) and hierarchical (red) Au@MgO/SBA-15 materials screened in the absence of solvent.	169
Figure 4.26. Substrate conversion profile as a function of time for mesoporous and hierarchical materials screened with an (a) oxygen headspace and (b) in air.....	170
Figure 4.27. Mesoporous and hierarchical materials heated to different temperatures screened for the selox of benzyl alcohol at a reaction temperature of 60 °C.	170
Figure 4.28. (a) Final substrate conversion and initial productivity of fresh and spent materials and (b) fresh and older material.....	171

Chapter 5

Figure 5.1. ICP-OES of the gold content of Au functionalised bulk supports as a function of heat treatment temperature.	181
Figure 5.2. Wide-angle X-ray diffraction patterns of Au/SiO ₂ materials heat-treated at different temperatures, displaying the full pattern and the Au [111] reflection.....	182
Figure 5.3. Wide-angle X-ray diffraction patterns of Au/MgO materials heat-treated at different temperatures, displaying the full pattern (top), the Au and MgO [111] reflection (bottom left), as well as the Au [220] reflection (bottom right).	183
Figure 5.4. Wide-angle X-ray diffraction patterns of Au/CaO materials heat treated at different temperatures, displaying the full pattern (top), the Au and CaO [111] reflection (bottom left), as well as the Ca(OH) ₂ reflections (bottom right).	185
Figure 5.5. Surface area for gold functionalised bulk supports as a function of heat treatment temperature, with parent support surface area represented by lines.	186
Figure 5.6. X-ray photoelectron spectra of (a) Si 2p and (b) Au 4f for Au/SiO ₂ materials heat treated at different temperatures.	187
Figure 5.7. X-ray photoelectron spectrum of (a) O1s and (b) relative component concentrations for Au/SiO ₂ materials heat-treated at different temperatures.	188
Figure 5.8. X-ray photoelectron spectra of (a) Mg 2p and (b) Au 4f for Au/MgO materials heat-treated at different temperatures.	189
Figure 5.9. X-ray photoelectron spectrum of (a) O1s and (b) relative component concentrations for Au/MgO materials heat-treated at different temperatures.....	190
Figure 5.10. X-ray photoelectron spectra of (a) Ca 2p and (b) Au 4f for Au/CaO materials heat-treated at different temperatures.	191
Figure 5.11. X-ray photoelectron spectrum of (a) O1s and (b) relative component concentrations for Au/CaO materials heat-treated at different temperatures.	192
Figure 5.12. Gold (a) charge ratio and (b) binding energy as a function of temperature for bulk supported gold materials.	192
Figure 5.13. (a) Particle size distributions of Au/CaO, Au/MgO (500) and Au/SiO ₂ (500) materials and (b) Au particle size determined using both TEM and XRD.	194
Figure 5.14. Substrate conversion profiles for the selective oxidation of benzyl alcohol using bulk supported gold materials.	196
Figure 5.15. Substrate conversion profiles for the selective oxidation of benzyl alcohol using bulk supported gold materials in the presence of potassium carbonate.....	197
Figure 5.16. Initial benzaldehyde productivity of gold functionalised bulk supports, comparing rates with and without a potassium carbonate additive, featuring error calculated from experimental repeats.....	198

Figure 5.17. Benzyl alcohol conversion after 24 hours of gold functionalised bulk supports, comparing rates with and without a potassium carbonate additive, featuring error calculated from experimental repeats.	199
Figure 5.18. Normalised rate profile for gold functionalised bulk supports heat-treated to 500 °C, examining the influence of the presence of potassium carbonate.	200
Figure 5.19. Initial productivity of (a) benzaldehyde, and (b) final conversion of benzyl alcohol for SBA-15 type and bulk supported materials treated at 400 °C, with and without base additive.	200
Figure 5.20. Reaction steps for the oxidative cross-coupling of benzyl alcohol and benzylamine to produce the imine, N-Benzylidenebenzylamine.	202
Figure 5.21. Oxidative cross-coupling reaction profiles for selected catalysts in the absence (left) and presence (right) of potassium carbonate.	204
Figure 5.22. Gold nanoparticle size distribution and density for selected mesoporous, hierarchical and fumed silica supported gold.	205
Figure 5.23. Mechanism showing the protonation of the hemiaminal intermediate... ..	207
Figure 5.24. Conversion plots as a function of time for (●) benzyl alcohol and (◆) benzylamine for imine synthesis in the absence (left) and presence (right) of potassium carbonate.	209
Figure 5.25. Imine productivity as a function of benzylamine conversion to highlight the deactivation of both SBA-15 and bulk supported catalysts in (a) absence and (b) presence of potassium carbonate.	210

Appendix

Appendix Figure 2.1. Silica lattice contraction as a function of magnesium loading for mesoporous and hierarchical MgO/SBA-15 materials.	219
Appendix Figure 2.2. Interpore distances of mesoporous and hierarchical materials, calculated using low-angle X-ray diffraction reflections.	219
Appendix Figure 2.3. Transmission electron micrographs of 10.9 wt% mesoporous MgO/SBA-15, displaying (a) surface nanoparticle and (b) lattice structure.	220
Appendix Figure 2.4. Wide-angle X-ray diffraction pattern of MgO sample used as an XPS and catalyst benchmark.	221
Appendix Figure 2.5. (a) Base site density and (b) magnesium dispersion as a function of magnesium loading, for both mesoporous (blue) and hierarchical (red) materials.	221
Appendix Figure 2.6. Temperature programmed desorption of CO ₂ from (a) mesoporous and (b) hierarchical materials as a function of CO ₂ mass spectrometry signal over temperature.	222
Appendix Figure 2.7. Model of tributyrin calculated using Chemdraw.	222

Appendix Figure 2.8. Tributyrin conversion profile using a 10 wt% nominally loaded MgO/SBA-15 synthesised using a one-pot cooperative self-assembly method.....	223
Appendix Figure 2.9. Tributyrin conversion initial rate normalised to magnesium content of each material. Benchmark transesterification reaction using bulk MgO (calcined Mg precursor using same conditions), talc (hydrated magnesium silicate), mesoporous, and hierarchical magnesium oxide functionalised SBA-15.....	223
Appendix Figure 2.10. Tributyrin turnover frequency normalised using the bases site density, error calculated from the sum of catalytic screening and base site density percentage error.....	224
Appendix Figure 2.11. (a) Triglyceride conversion turn over frequency and (b) rate enhancement brought on from using a macropore network as a function of chain length for mesoporous and hierarchical 4.4 wt% MgO/SBA-15.....	224
Appendix Figure 3a.1. Cube schematic for the influence of reaction temperature, porosity and heat treatment on benzyl alcohol conversion.....	227
Appendix Figure 3a.2. Cube schematic for the influence of reaction temperature, porosity and heat treatment on benzaldehyde productivity.....	227
Appendix Figure 3a.3. Cube schematic for the influence of reaction temperature, porosity and substrate concentration on benzyl benzoate selectivity.....	228
Appendix Figure 3b.1. Interpore distance and gold particle size determined using LAXRD and WAXRD Scherrer equation respectively for (a) mesoporous and (b) hierarchical materials.....	229
Appendix Figure 3b.2. Mg 2p X-ray photoelectron spectra of (a) mesoporous and (b) hierarchical materials respectively.....	229
Appendix Figure 3b.3. O 1s X-ray photoelectron spectra of (a) mesoporous and (b) hierarchical materials respectively.....	230
Appendix Figure 3b.4. Si 2p X-ray photoelectron spectra of (a) mesoporous and (b) hierarchical materials respectively.....	231
Appendix Figure 3b.5. Colour change in mesoporous Au@MgO/SBA-15 materials heated from 100-800 °C.....	231
Appendix Figure 3b.6. Transmission electron microscopy micrographs of mesoporous (left) and hierarchical (right) Au@MgO/SBA-15 materials, heat-treated at 100, 200 and 300 °C.....	232
Appendix Figure 3b.7. Turn over frequencies taken from the initial productivity of benzaldehyde and normalised to the approximated site densities, taken from particle sizes counted from TEM and calculated using the Scherrer equation from WAXRD.	233

Appendix Figure 3b.8. The (a,b) final conversion of the substrate and (c,d) initial rate of productivity of the selective product benzaldehyde for (a,c) mesoporous and (b,d) hierarchical heat-treated materials for the selective oxidation of benzyl alcohol.	234
Appendix Figure 3b.9. Comparison between the materials produced in this study and other materials in the literature, as a function of activation energy.	235
Appendix Figure 3c.1. ICP-OES Au and Mg loading data for mesoporous and hierarchical Au@MgO/SBA-15 materials.	236
Appendix Figure 3c.2. (a) The low-angle and (b) wide-angle X-ray diffraction patterns for mesoporous and hierarchical Au@MgO/SBA-15 materials.	237
Appendix Figure 3c.3. Nitrogen Porosimetry isotherms for (a) mesoporous and (b) hierarchical Au@MgO/SBA-15 materials, with subsequent (c) pore size distributions and (d) surface areas.	238
Appendix Figure 3c.4. Relative component concentrations for (a) mesoporous and (b) hierarchical Au@0-6%MgO/SBA-15 in the Si 2p region.	239
Appendix Figure 3c.5. Relative component concentrations for (a) mesoporous and (b) hierarchical Au@0-6%MgO/SBA-15 in the O 1s region.	240
Appendix Figure 3c.6. Relative Mg 2p component concentrations for (a) mesoporous and (b) hierarchical Au@0-6%MgO/SBA-15 in the Mg 2p region.	240
Appendix Figure 3c.7. X-ray photoelectron Au 4f spectra of (a) Au@0-6%MgO/SBA-15 materials and the Au ⁰ (b) binding energy and (c) relative Au ⁰ concentration relative to magnesium loading.	241
Appendix Figure 3c.8. Transmission electron micrographs of (a,b) mesoporous and (c,d) hierarchical Au@MgO/SBA-15.	242
Appendix Figure 3c.9. Transmission electron microscopy micrographs of (a,b) mesoporous and (c,d) hierarchical Au@0.25MgO/SBA-15 materials.	243
Appendix Figure 3c.10. Transmission electron microscopy micrographs of (a,b) mesoporous and (c,d) hierarchical Au@0.5MgO/SBA-15 materials.	244
Appendix Figure 3c.11. Transmission electron microscopy micrographs of (a,b) mesoporous and (c,d) hierarchical Au@0.75MgO/SBA-15 materials.	245
Appendix Figure 3c.12. Data sets determined from TEM calculations of particle size, with; average particle size (top middle), particle size distributions for mesoporous and hierarchical (top right), gold dispersion (bottom left) and gold site density (bottom right) all as a function of magnesium loading.	246
Appendix Figure 3c.13. Screening data for the selective oxidation of benzyl alcohol, using mesoporous and hierarchical gold functionalised SBA-15 materials containing varying loadings of magnesium oxide. (a) Final substrate conversion after 24 hours (bottom left) and (b) selectivity to the aldehyde product.	247

Appendix Figure 3c.14. Raw (a) aldehyde productivity for mesoporous and hierarchical materials with varied Mg loading. Rate normalised to (b) gold loading (top right), (c) surface area and (d) approximated site density to give the turn over frequency (TOF). The outlying sample (M3.8) is outlined in red, due to the failed synthesis.	248
Appendix Figure 3c.15. The productivity of benzaldehyde product as a function of benzyl alcohol conversion for (a) mesoporous and (b) hierarchical.	249
Appendix Figure 3c.16. Normalised rate profiles for (a) mesoporous and (b) hierarchical as a function of time. Data points outlined in red are given as outliers.	250
Appendix Figure 3d.1. ICP-OES gold loadings for mesoporous and hierarchical Au@MgO/SBA-15 materials.	251
Appendix Figure 3d.2. The (a) low-angle and (b) wide-angle X-ray diffraction patterns of mesoporous and hierarchical Au@MgO/SBA-15 materials, with varied gold loadings notated by their weight percent.	252
Appendix Figure 3d.3. Nitrogen porosimetry (a) isotherms and (b) pore size distributions for Au@MgO/SBA-15 materials with varied gold loadings.	253
Appendix Figure 3d.4. O 1s relative component concentration as a function of Au Loading for (a) mesoporous and (b) hierarchical materials with varied gold loadings.	254
Appendix Figure 3d.5. Mg 2p relative component concentration as a function of Au Loading for (a) mesoporous and (b) hierarchical materials with varied gold loadings.	255
Appendix Figure 3d.6. Si 2p relative component concentration as a function of Au Loading for (a) mesoporous and (b) hierarchical materials with varied gold loadings.	256
Appendix Figure 3d.7. Au 4f XPS and Au ⁰ binding energy and (c) Au ⁰ :Au ⁺ ratio for mesoporous and hierarchical materials with varied gold loadings.	257
Appendix Figure 3d.8. TEM micrographs for (a,b) mesoporous and (c,d) hierarchical Au@MgO/SBA-15 materials with 0.13% nominal gold loadings.	258
Appendix Figure 3d.9. TEM micrographs for (a,b) mesoporous and (c,d) hierarchical Au@MgO/SBA-15 materials with 0.25% nominal gold loadings.	259
Appendix Figure 3d.10. TEM micrographs for (a,b) mesoporous and (c,d) hierarchical Au@MgO/SBA-15 materials with 0.5% nominal gold loadings.	260
Appendix Figure 3d.11. Average particle size, site density and particle size distributions for mesoporous and hierarchical materials with varied gold loadings.	261
Appendix Figure 3d.12. Screening data for the selective oxidation of benzyl alcohol, using mesoporous and hierarchical gold functionalised SBA-15 materials containing varying loadings of gold oxide. Selective product productivity and selectivity, final substrate conversion after 24 hours and Au mass normalised benzaldehyde rate.	262
Appendix Figure 3d.13. Gold content normalised rate versus substrate conversion for mesoporous and hierarchical Au@MgO/SBA-15 materials with varied gold content.	263

Appendix Figure 3d.14. Gold content normalised Au-rate versus time for mesoporous and hierarchical Au@MgO/SBA-15 materials with varied gold content.....	264
Appendix Figure 3e.1. Reaction profiles for (a) mesoporous and (b) hierarchical when 1 mmol of the substrate is added partway through the reaction.....	265
Appendix Figure 4a.1. (a) Nitrogen porosimetry isotherms and (b) pore size distributions for Au/SiO ₂ heat-treated to different temperatures.....	266
Appendix Figure 4a.2. (a) Nitrogen porosimetry isotherms and (b) pore size distributions for Au/MgO heat-treated to different temperatures.	266
Appendix Figure 4a.3. (a) Nitrogen porosimetry isotherms and (b) pore size distributions for Au/CaO heat-treated to different temperatures.....	267
Appendix Figure 4a.4. Extrapolation of particle size using gold metallic to gold cationic species ratio calculated using XPS.	267
Appendix Figure 4a.5. TEM micrographs of Au/SiO ₂ heat-treated at 500 °C.....	268
Appendix Figure 4a.6. TEM micrographs of Au/MgO heat-treated to 500 °C.	268
Appendix Figure 4a.7. TEM micrographs of Au/CaO heat-treated to 500 °C.....	269
Appendix Figure 4b.1. Imine concentration as a function of time for (a) mesoporous and (b) hierarchical catalysts without the added base.....	269
Appendix Figure 4b.2. The preliminary reaction between benzaldehyde and benzylamine.	270
Appendix Figure 4b.3. Benzaldehyde (left) and N-benzylidenebenzylamine (right) yield as a function of time for selected catalyst in the absence (NB – no base) and presence (BA – base added) of potassium carbonate.	271
Appendix Figure 4b.4. Preliminary homocoupling reaction of benzylamine.....	272

List of Tables

Table 2.1. List of Chemicals for synthesis, characterisation and screening of catalysts	68
Table 2.2. Gas chromatography methods for the transesterification of triglycerides, selective oxidation of aromatic primary alcohols and oxidative coupling of alcohols and amines.	84
Table 5.1. Data of initial rates, and conversion, yield and selectivity after 24 hours for the oxidative cross-coupling of benzyl alcohol and benzylamine for the different catalyst support tested.....	210
Appendix Table 2.1 The surface area determined using BET and t-plot microporosity analysis from micro and mesopores with pore sizes calculated with DFT (slit pore, NLDFT equilibrium mode) calculations respectively.....	220
Appendix Table 3a.1. Chemometric data showing how the 5 factors interacted with the 3 responses; conversion, activity, and selectivity. Data in green implies a significant interaction and data in amber signifying an interaction below error	226
Appendix Table 3b.1. Literature review of kinetic studies undertaken on materials used for the selective oxidation of benzyl alcohol.	235
Appendix Table 3d.1. Surface area and microporous area determined by BET and T-plot functions for nitrogen porosimetry data for mesoporous and hierarchical Au@MgO/SBA-15 materials with varied gold loading.	253

List of Equations

Equation 2.1. Braggs law	72
Equation 2.2. Scherrer equation.....	73
Equation 2.3. Conversion of Substrate.....	87
Equation 2.4. Initial rate of reaction.....	87
Equation 2.5. Selectivity to a product.....	87
Equation 2.6. The yield of a product.....	87

Chapter 1

Introduction

1.1 Background

1.1.1 Sustainable Chemistry through Catalytic Systems

The global economy is sustained by the consumption of finite fossil fuel resources, which is both unsustainable and damaging to the environment. Resource consumption is occurring through energy production or manufacturing, however, since the 1990's there has been a shift to a more sustainable approach.¹ To mitigate the huge energy consumption by the chemical production sector, IUPAC has defined twelve principles of green chemistry which determine where industrial chemistry should advance.² These principles range from preventative measures such as safe and renewable reagents to more efficient processes trying to reduce solvent use and boost atom economy. One of the key principles, which is the focus of the following body of work, is the use of catalysis to reduce energy costs, increase yields and improve efficiencies in chemical processes.

Catalysis is the process of a chemical species lowering the activation barrier to a chemical transformation by providing an alternate pathway,³ illustrated in **Figure 1.1**. This is achieved without perturbing the equilibrium and is returned to the initial state at the end of the catalytic cycle.

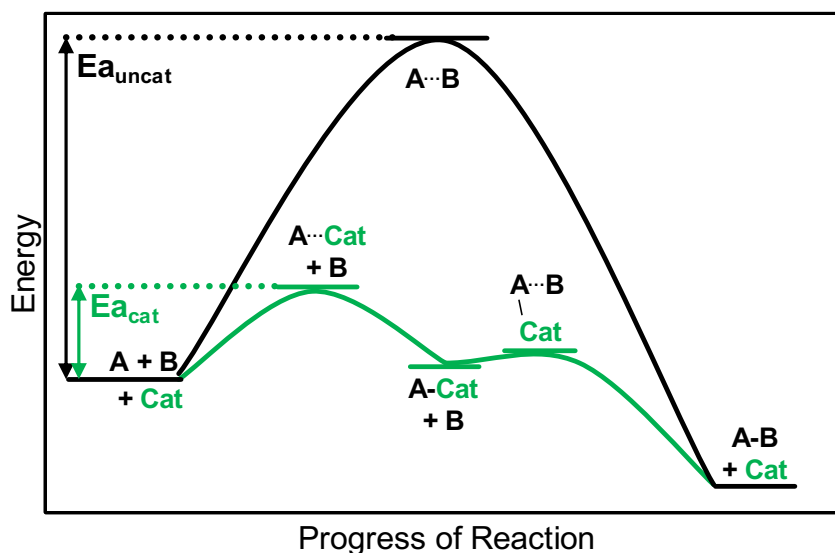


Figure 1.1. Energy diagram for a catalysed and uncatalysed reaction. $E_{a_{\text{uncat}}}$ = activation energy for an uncatalysed reaction, $E_{a_{\text{cat}}}$ = activation energy for a catalysed reaction.³

Catalytic species can be classified by functional groups, intended use or by the process of activation. Some would argue the most important class of catalytic species are enzymes, which perform complex chemical transformations at relatively low temperatures in highly specific biological environments. These species operate using a

complex 'lock and key' mechanisms, allowing for both chemo- and enantiomeric selectivity.⁴ Another group of catalysts which are of great interest are photocatalysts. These accelerate reactions which require the adsorption of light by one or more participants, allowing for reduced energy conditions.⁵ One of the more common uses is the degradation of organic pollutants.⁶ In industrial use however, catalytic species are typically separated into two classes according to their physical state compared to their specific substrates: homogeneous and heterogeneous.

1.1.1.1 Homogeneous Catalysis

Homogeneous catalysis refers to species in the same physical state as the reactants, with all reaction participants being in a liquid or gaseous phase. As both the homogeneous catalyst and reactant are in the same phase, there is a greater degree of interaction between the two species, giving a greater effective concentration which in turn allows for milder conditions without dramatically reducing the reaction rate.⁴ There is also added ease when designing these species, as characterisation of the specific molecule is easier than solid materials. Homogeneous catalysts are incredibly easy to modify for specific processes, as the majority function through coordination chemistry. A metal centre is surrounded by different chemical species known as ligands, which impart electronic, chemical and steric effects to the metal active site allowing for selectivity to different products.

A common example of a homogeneously catalysed reaction would be the synthesis of polymers using Zeigler-Natta catalysts, the mechanism of which is displayed in **Figure 1.2**.⁷ These catalytic species have contributed to the large scale industrial utilisation of petroleum-based chemicals to form plastics.⁸

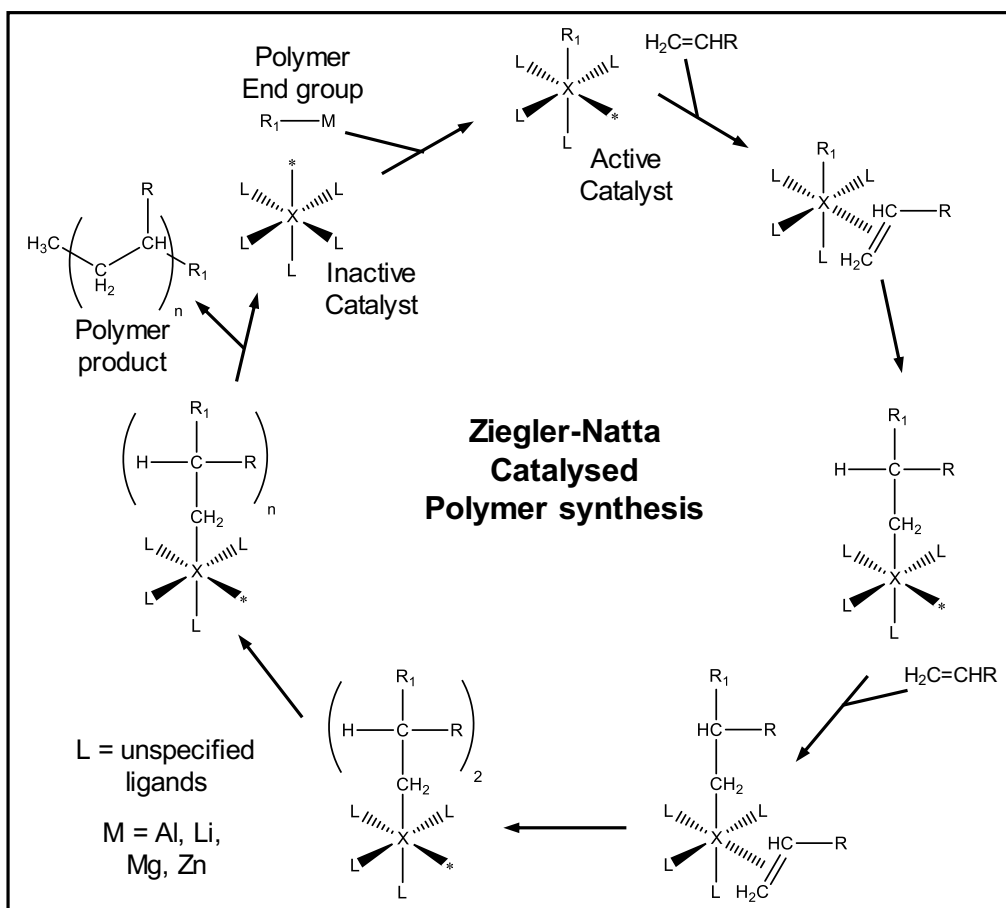


Figure 1.2. The reaction mechanism for the homogeneous Ziegler-Natta catalysed synthesis of polymers. Redrawn from reference.⁷

One of the main disadvantages using homogeneous catalysts is the difficulty with separating from the product.⁹ The principles of green chemistry encourage the recover and reuse of the catalytic species, therefore the homogeneous catalyst must be separated, in turn this increases the difficulty, economic and environmental cost. It is generally accepted that higher temperatures can be employed to increase the rate of reaction, a relationship defined by the Arrhenius equation.¹⁰ This has the capacity to be problematic for homogeneous species, as higher temperatures run the risk of evaporation of solvent or volatile substrate.⁹ Low-temperature conditions can mitigate this, however, this is not applicable to a lot of chemical transformations. While advantageous in some respects, homogeneous catalysis has many drawbacks when scaled up to an industrial setting. Heterogeneous catalysts have found great success in these applications, with approximately 85% of all catalysed processes occurring through heterogeneous routes.

1.1.1.2 Heterogeneous Catalysis

Heterogeneous catalysts differ from homogeneous catalysts as they are in a different physical state to their substrates. A heterogeneous catalyst typically consists of a catalytically active species that can be dispersed on an inert or active supporting medium.³ When supported, these active species can be a variety of materials, from organic molecules or enzymes (typically seen as homogeneous) anchored to the supporting material, to dispersed inorganic particles. The benefit of using bulk and supported heterogeneous catalysts is the easier separation from solution due to the different physical phases, using filtration or cyclones and using the solid catalyst in fixed or fluidised catalytic bed.¹¹ Some processes employ magnetic supports to further increase the ease the separation.¹² Another advantage of supported catalysts is the reduced quantity of catalytically active material, as the active phase is evenly dispersed which in turn reduces costs. By using specific supports, active phases, poisons and dopants, the catalytic process can be tailored to specific feedstocks and products, making it extremely versatile in industrial use.¹¹

A historic example of heterogeneous catalysis would be the Haber-Bosch process, which was developed in the early twentieth century, the mechanism of which is displayed below in **Figure 1.3**.¹³ In 1909, German chemists Fritz Haber and Carl Bosch synthesised ammonia from hydrogen and nitrogen in air using an iron-based catalyst, supported on iron oxide within a bed of aluminium, potassium, calcium and magnesium oxide promoters.¹³ It is estimated that without the Haber-Bosch process, current agricultural needs would require four times the land as currently used, which would equal half of all ice-free land on the planet.¹³

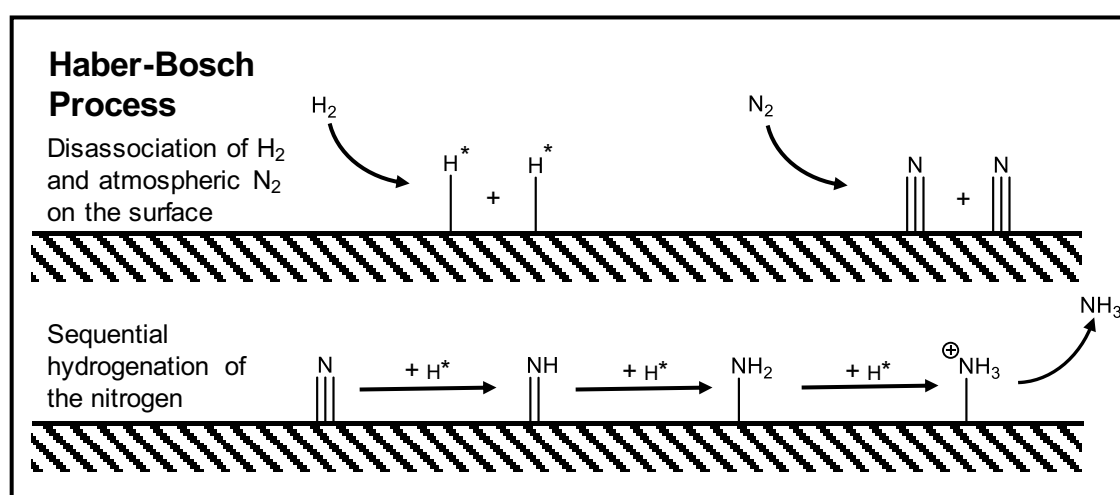


Figure 1.3. The reaction mechanism for the hydrogenation of nitrogen using the Haber-Bosch process. Redrawn from reference.¹⁴

A heterogeneously catalysed reaction typically occurs via seven steps,¹⁵ illustrated in **Figure 1.4**. It follows the journey of a substrate molecule diffusing from bulk fluid to external surface (1), internal diffusion from external surface to active site (2), adsorption from solution to active site (3), chemical transformation on the active site (4), desorption of product into solution (5), internal diffusion out to the external surface (6), and finally external diffusion of the product back into the bulk fluid (7).¹⁵

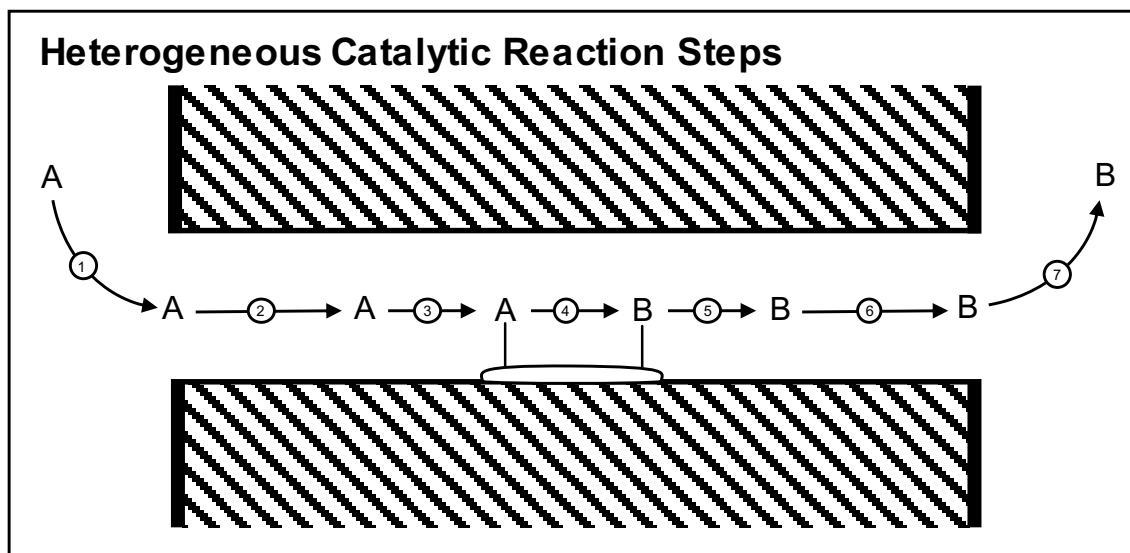


Figure 1.4. Reaction steps for heterogeneous catalytic reactions.¹⁵

The beginning and end of a catalytic process is the transfer (1) and removal (7) of reactants or products to/from the support external surface in a process called external diffusion. Rate limiting steps at this stage may take the form of mass transfer limitations, where the system's ability to diffuse reactant/product between the bulk fluid and the external surface is slower than the other steps. These limitations are rarely seen in academic studies, however, are prevalent in industrial catalysis.¹⁵ A typical range of activation energy for a process controlled by the external diffusion-limitations is below 20 kJ mol^{-1} .¹⁶

The next stage in a heterogeneous catalytic process is the internal diffusion of molecules in (2) or out (6) of the pore network, if the material is porous.¹⁵ These steps are of interest when employing a catalytic system with sterically hindered substrates or materials with small pores. Coking and other pore fouling mechanisms can also prove problematic at this stage. A characteristic range of activation energies when the reaction is controlled by internal diffusion-limitations is 20-60 kJ mol^{-1} .¹⁶

The crucial catalytic step in the process is the chemical transformation, which follows; the adsorption (3), transformation (4) and desorption (5) of compounds at the catalytic site.¹⁵ There are many established adsorption mechanism types of heterogeneous

catalysis;^{17, 18} Eley-Rideal,¹⁹ Langmuir-Hinshelwood-Hougen-Watson,²⁰ and the Mars van Krevelen. The Eley-Rideal mechanism proceeds via the adsorption of one molecule, which then reacts with the second in a non-adsorbed state. The Langmuir-Hinshelwood mechanism, however, proceeds via both reaction participants adsorbing to the surface, before reacting together followed by desorbing as the product.

The final mechanism often associated with metal oxide materials is the Mars van Krevelen mechanism. This mechanism is based on the notion of cyclic redox reactions occurring at the active site with gaseous oxygen. It follows the assumption that the oxygen interacting with the metal oxide lattice and therefore being taken up by the active site is equal to the oxygen being consumed in the reaction system. It assumes a steady state being achieved of active sites being reduced by the substrate, and these reduced active sites being oxidized by the catalyst. This mechanism promotes the idea of extremely high oxygen mobility. These mechanisms are pictured in **Figure 1.5**.

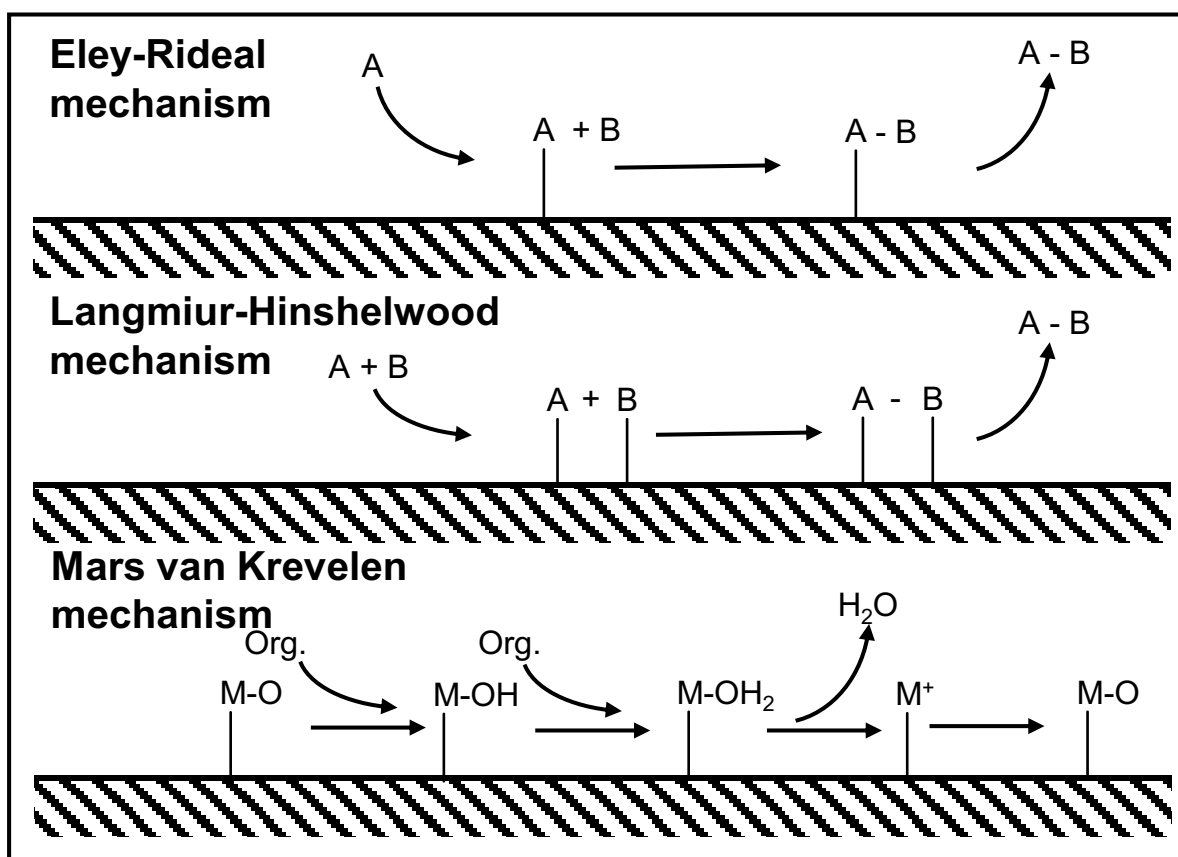


Figure 1.5. Different adsorption mechanisms for heterogeneous catalysis.

1.1.1.3 Electronic and Geometric Effects

A disadvantage of heterogeneous catalysts is the reaction only occurring at specific sites at the surface of the catalytically active component. This lowers the effective concentration of the catalyst, meaning heterogeneous reactions often require harsher

reaction temperatures and pressures to achieve conversion comparable to homogeneous species.³

As the substrate approaches the surface of the catalytic species it undergoes opposing electronic effects. Van der Waals forces attract the substrate and surface, however, this is opposed by the electrostatic interaction between the valence electrons on both parties repelling.²¹ The strength of this interaction determines the bonding strength of the two parties at adsorption. Strong interaction causes chemisorption to occur, where a chemical bond forms between substrate and surface, however, weak interaction causes physisorption to occur, where only weak electrostatic forces keep the substrate adsorbed. This is pictured in **Figure 1.6**.

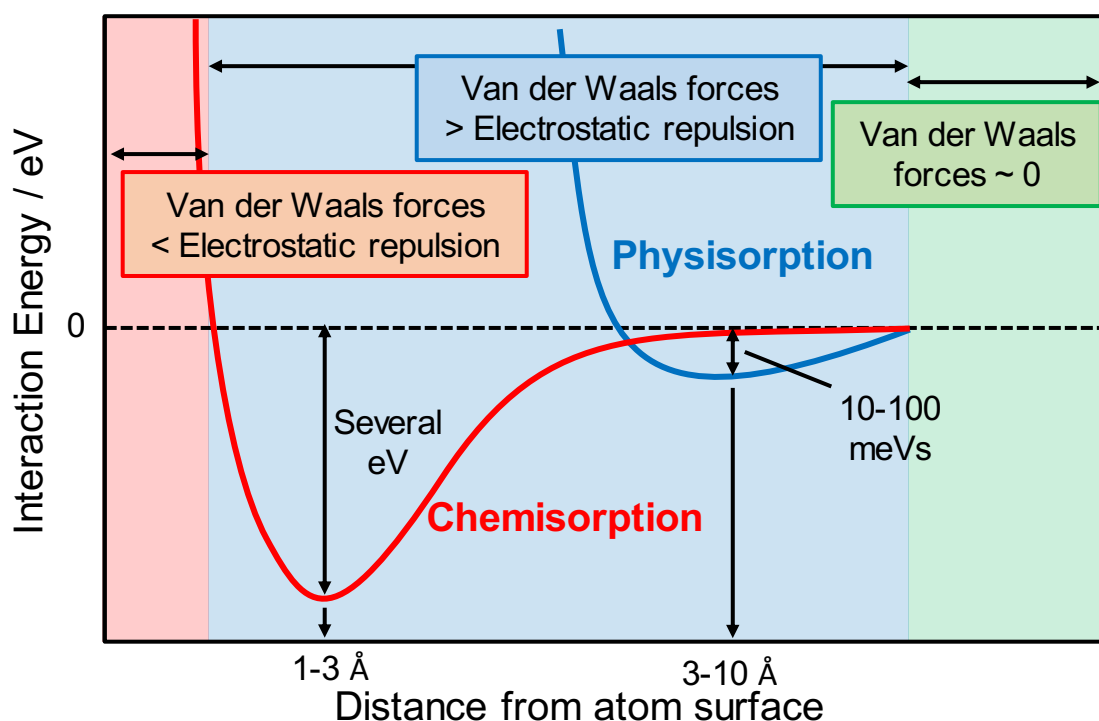


Figure 1.6. Physisorption and chemisorption interaction energy profiles as a function of distance from the surface, with different regions representing the strongest force with respect to the chemisorption profile.

Substrate adsorption occurs when an equilibrium between opposing forces at a specific distance is reached. The electronic properties of the catalytic species influence the adsorption strength between substrate and surface, which in turn alter the electron density of the substrate valence band, thereby making it susceptible to chemical change. The electronic environment of an active site can be probed through techniques such as XPS or XAFS, which highlight the local valence environment. When paired with other techniques, and accounting for other contributors to structure-property correlations

affecting catalytic performance, the localised electronic environment's contribution to catalytic ability can be observed.

Many factors can alter the electron density of both substrate and catalytic surface, which can help or hinder the substrate adsorption and subsequent reaction. These factors may be other reaction participants, dopants, poisons or in some cases the material that the catalytically active component is supported on.³ Historically, supports were thought of as an inert material merely acting as a high surface area medium for the catalytically active phase. Nevertheless, it was demonstrated by Tauster²² that in some cases, the supporting material can electronically interfere with the active phase. Platinum was found to cause the disassociation of H₂ when supported on TiO₂ but was unable to on other supporting materials.²² This is due to strong metal-support interaction (SMSI).

While electronic effects have a significant influence on the ability of a material for catalysis, geometric effects also play an extremely important role often in tandem.²³ When considering the two gold atoms in **Figure 1.6**, characterised fully in **Chapter 5.2.1**, the geometric differences of both particles can be explored. While the smaller particle has a surface area of less than half of the larger particle, it contains almost one fifth the quantity and volume of gold. This high surface area to volume ratio is indicative of small nanoparticles and results in an extremely large surface area of catalytically active surface per mole of the active phase. Above ten nanometres, however, the electronic inference is negligible, while geometric effects are still a large contributor to activity.²⁴

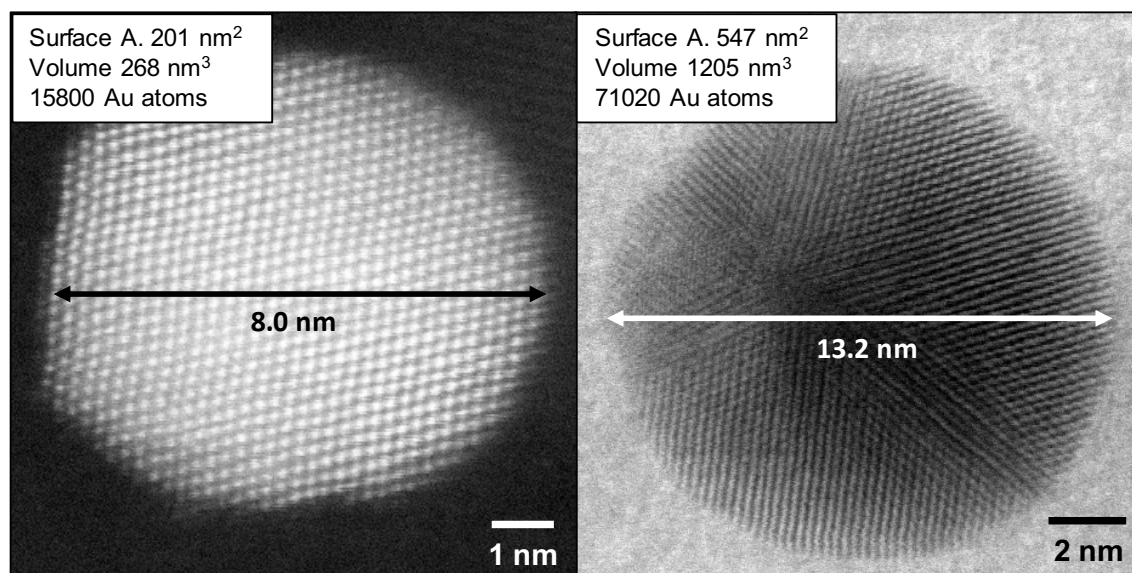


Figure 1.7. Gold nanoparticles synthesised using DIM methodology supported on nano-CaO. SA and volume approximated using a spherical particle assumption and using the lattice parameter of gold.

One model used to better explain the geometry of particles and heterogeneous catalytic surfaces is the terrace-ledge-kink model,²⁵ as shown in **Figure 1.8**. It displays a particle surface which contains 3 atom sites; terraces which represent a surface atom with one coordination site free, ledges which represent an edge of a surface resulting in two coordination sites, and lastly kinks which represent an atom with three coordination sites. Also, a site consisting of an atom on the surface with five coordination sites is referred to as an adatom. Both ledges and kinks are considered defects within the surface and increase in frequency as particle size decreases.²⁶ These defect sites often are the most electronically and geometrically favourable positions for adsorption to occur, which can often tie particle size to activity. Geometric orientated characterisation, using techniques such as TEM, can also highlight how the activity or selectivity of specific crystal planes can differ, allowing for smart design of catalytic sites.

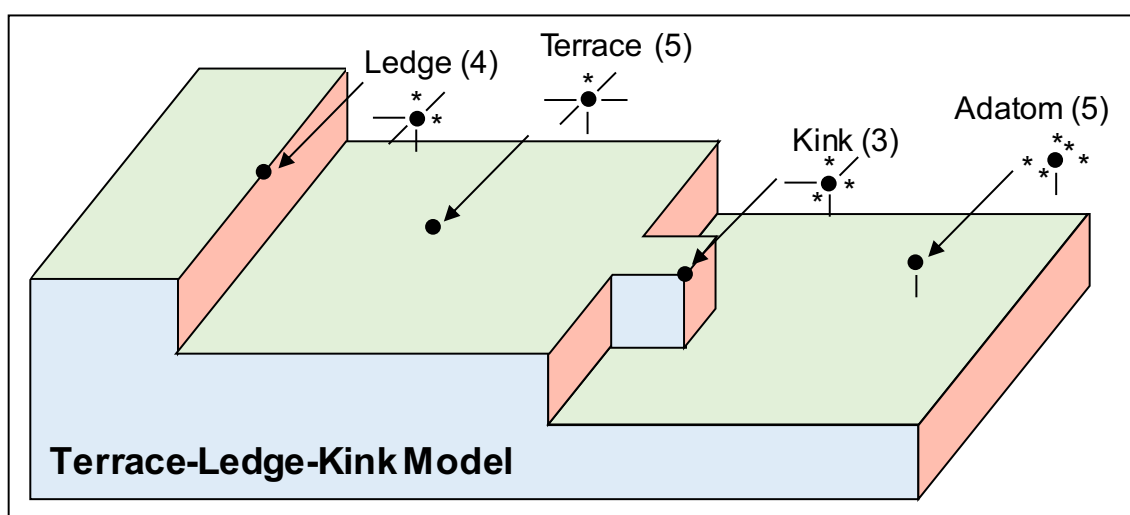


Figure 1.8. TLK model representing sites on a heterogeneous catalytic surface. Redrawn from reference.²⁷

It is often problematic to separate out electronic and geometric effects which contribute to altered catalytic ability, however the use of specific characterisation can help mitigate this. This allows for further analysis of this normalised data, allowing for other structure-performance correlations to be identified.

As previously mentioned, heterogeneous catalysis generally suffers from a lower effective concentration of active species relative to homogeneous routes. To mitigate this, catalytically active species are often dispersed over support materials, providing a bulk framework which reduces the quantity of active phase required. It is therefore very important for the catalytically active component to be supported on a large surface area material.

1.1.2 Support Materials

Surface area is achieved with porosity, with materials exhibiting different sizes and types of pores which are pictured in **Figure 1.9**. Voids within a material can be classified according to their pore size diameter into macro ($d_{\text{pore}} > 50 \text{ nm}$), meso ($50 > d_{\text{pore}} > 2 \text{ nm}$) and micropores ($d_{\text{pore}} < 2 \text{ nm}$).²⁸ These can be ink bottle, interconnected, through-pores or even created using a template.²⁹ Templated material can use either a hard or soft template, with the support materials formed around them, followed by template removal thermally or chemically.

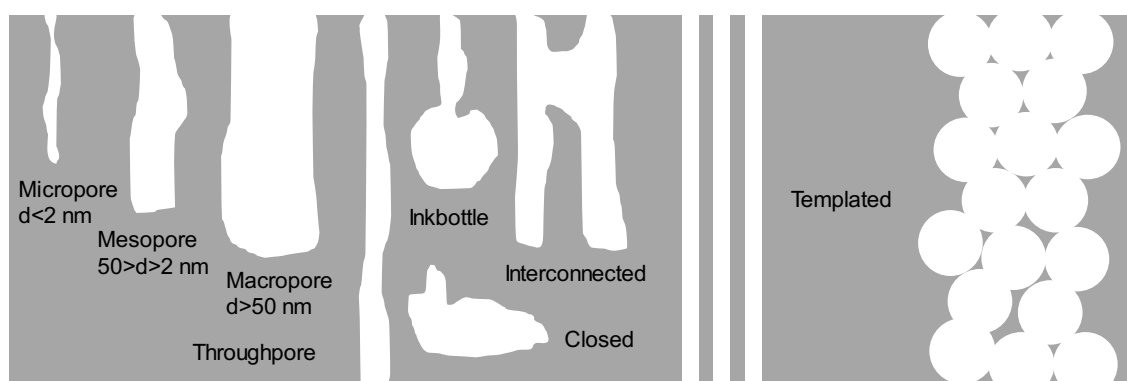


Figure 1.9. Different sizes and types of porosity. Redrawn from reference.²⁹

Hard templates can be a variety of materials, however, are typically synthesised to impart any shape in the nano-region. Polystyrene nanospheres have been employed to create a macroporous network in silica, as shown by Parlett *et al.*³⁰ This imparts easier diffusion throughout the material, along with functionalisation of the newly created voids.

1.1.2.1 Surfactant Soft Templates

Soft templates refer to the use of surfactants to form complex micelle structures in the nanoscale, thereby imparting porosity after removal.^{31, 32} The use of different soft templating agents and material precursors result in different types of template and therefore final material. Templating agents form liquid crystal structures, which stack in specific orientations depending on the solution conditions.³³

Liquid crystals are a state of matter, borrowing trends from both liquid phases and crystalline solids. There are three species of liquid crystal: thermotropic (dependant on temperature), lyotropic (dependant on monomer concentration and temperature), and metallotropic (dependant on monomer concentration, temperature and the inorganic-organic composition ratio).³⁴ Lyotropic liquid crystal structures are primarily used for mesoporous soft templating. The liquid crystal monomers are amphiphilic molecules, contain both hydrophobic and hydrophilic groups and are also referred to as surfactants.

The surfactant monomers diffuse into the solvent and adsorb at the interface between two phases,³ lowering the surface interfacial tension. In bulk solvents, surfactant monomers aggregate to form a more energy stable structures, such as micelles, which are monolayers of surfactant monomers encasing a second phase, or lamellar micelles, which are multiple layers of monomers forming a barrier at phases.³

These aggregations can only occur at specific conditions, the critical micelle concentration (CMC) and the Krafft temperature.³⁵ The shape of the resulting aggregate is dictated by the shape and size of the hydrophilic and hydrophobic tail groups, combined with the concentration and conditions. Other surfactant aggregates can be formed by varying the surfactant concentration, which is illustrated in **Figure 1.10**.

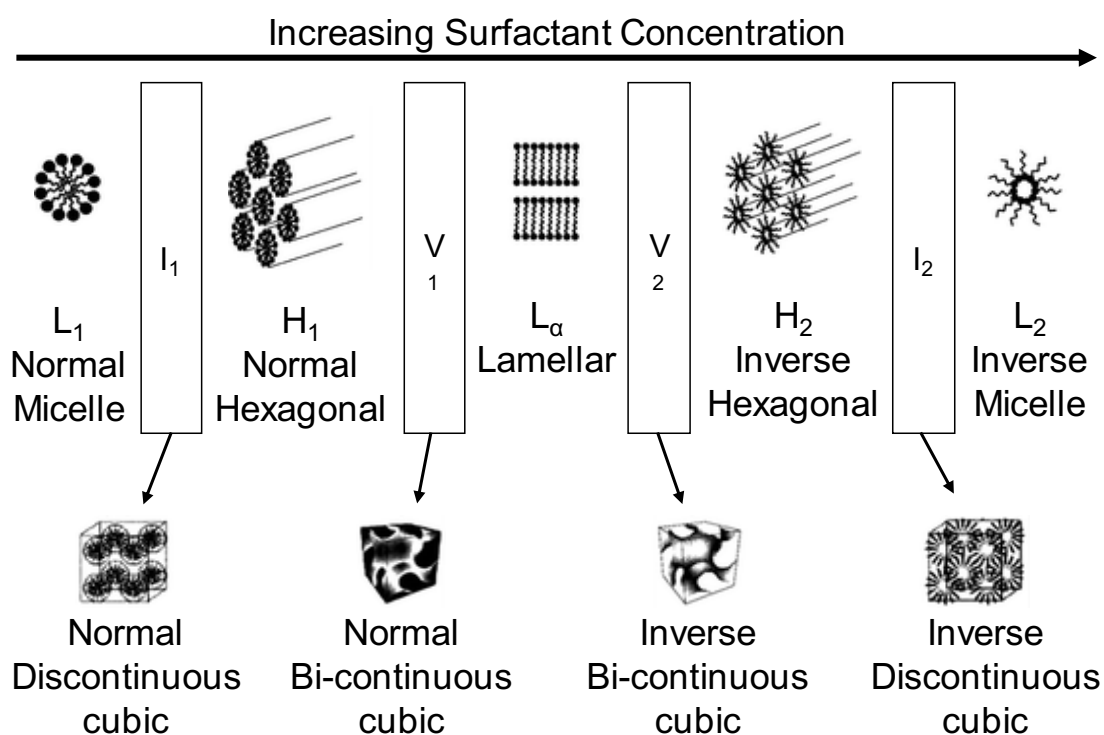


Figure 1.10. Diagram of surfactant lyotropic aggregates. Redrawn from references.^{3,34,36}

1.1.2.2 Templated Ordered Mesoporous Silica

One species of mesoporous material which has been the subject of recent study is SBA-15. First synthesised by Zhao *et al* in 1998,³⁷ Santa Barbara Amorphous 15 (SBA-15) is a long-range ordered mesoporous silica network, synthesised using a soft micelle template composed of the surfactant Pluronic P-123. P-123 is a triblock copolymer called a poloxamer, consisting of two hydrophilic poly(ethylene oxide) head groups connected by a hydrophobic poly(propylene oxide).³⁸ P123 refers to it being in paste form (P), 12 referring to the monomer molecular weight ($12 \times 300 = 3600 \text{ g mol}^{-1}$) and finally 3 referring to the percentage polyoxyethylene content ($3 \times 10 = 30\%$). An interesting

characteristic of this hydrophobic core is that it loses its hydrophobicity and becomes soluble in water at temperatures below 288 K (15 °C).³⁸ Below is the phase diagram of P-123 (**Figure 1.11**), showing both hexagonal and cubic phases of micelles aggregates at high concentrations.³³

Synthesising mesoporous materials with long-range ordered pores is a relatively recent development, beginning with MCM-41 type materials in the early 1990s.³⁹ The basic principle of these materials is the use of a sacrificial nano-template, around which the material precursor, such as alumina or silica, are deposited and polymerised.⁴⁰ Removal of the template can be achieved through solvent extraction or calcination.³⁷

The use of this mesoporous material as a catalytic support is advantageous for many reasons, primarily due to the large surface area to mass ratio typically between 700 to 1000 m².g⁻¹.⁴¹ The ordered nature of the pores, the diameter of which are readily modified through the application of carefully selected thermal treatments,³⁷ can allow for size exclusionary selectivity towards certain reactants.⁴² Another benefit is its high thermal stability, which is beneficial as many catalytic reactions require harsh temperatures.⁴³

The synthesis of SBA-15 requires the formation of hexagonally stacked micellar rods, which form a honeycomb-like structure after deposition of a silica precursor, typically tetramethoxysilane or tetraethoxysilane.³⁷ There are multiple synthesis routes to form the ordered mesoporous network, which result in materials with different physical properties.

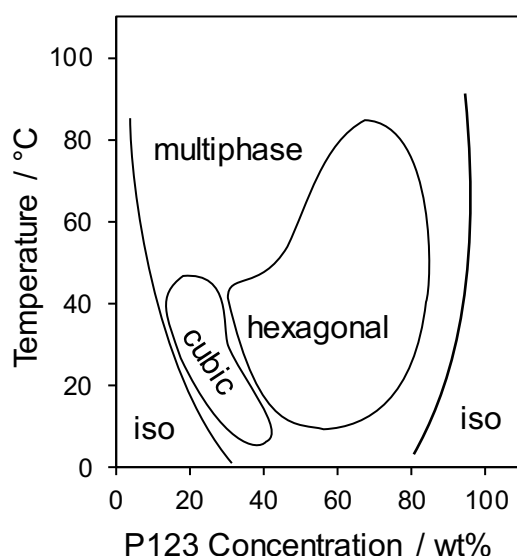


Figure 1.11. Phase diagram of Pluronic P-123. Redrawn from reference³⁸

The original synthesis route to produce SBA-15 is called Cooperative Self-Assembly, discovered by Zhao *et al.*³⁷ The surfactant soft template is dispersed in excess acidified

water, whereupon the addition of the silica precursor facilitates the assembly of the hexagonal micelle template. A more recent method is called True Liquid Crystal Templating (TLCT),⁴⁴ where the hexagonal micellar template forms as lyotropic liquid crystals prior to the silica precursor addition, after which the silica forms around the template. An advantage of using this method is reduced microporosity of the resulting silica material, which is beneficial as micropores are inaccessible to larger reactant molecules, representing the wasted surface area.^{34, 45} Calcination of the templated silica burns out the surfactant template, resulting in mesoporous silica.

An issue faced with SBA-15 as a catalytic support is the mesoporous pore size limited between 5-30 nm,³⁷ which can cause problems with larger molecules having diffusion limitations due to steric crowding by the silica porous structure. An example of these larger molecules would be triglyceride compounds present in bio-oil feedstocks. One solution is to create an expanded pore system. This can be achieved using a variety of methods, such as swelling the micellar soft templates using thermal treatments or poragens thereby increasing the volume of the void left after template removal.⁴⁶ Another route to greater diffusion throughout a material is the incorporation of macroporosity to give a hierarchical pore system. Hierarchical porous materials can be synthesised by utilising a combined sacrificial hard and soft template,⁴⁷ resulting in a material with greater diffusion properties. Polystyrene nanospheres have been used as a hard template, synthesised using an emulsifier free colloidal method.⁴⁸

By combining the synthesis and functionalisation of materials, costs can be reduced. SBA-15 has been used for a wide variety of scopes and has been shown repeatedly to be successfully synthesised and functionalised simultaneously. Organic one-pot functionalisation has been especially successful, for use in light absorption and emission,⁴⁹ CO₂ adsorption^{50, 51} and drug delivery.⁵² The major benefit of saturating the template with functionality is the selective placement after thermal template removal. This allows for uniform dispersion of functionality throughout the mesopore network, benefiting from both high surface area, thermal stability of the silica support and open macropores.

1.1.3 Biodiesel and its Catalytic Synthesis

Global transportation is enabled by the unsustainable consumption of finite petrochemical fuels which lead to global warming and climate change. The 2015 Paris Accords agreed to combat global temperature increases through the reduction of CO₂ emissions, one facet of which is the shift from petrochemical fuels.⁵³ Cleaner renewable alternatives, such as fuel cells and electric cars, offer promising alternatives to petroleum-based fuel transportation.

Most of these technologies are still in the development stage and have not been fully integrated into the current transportation infrastructure. Alternatively, biofuels offer a solution to greenhouse emissions as they can be derived from sustainably produced biomass. They may also be integrated into current vehicles without the need for alternative fuelling infrastructures, such as hydrogen fuel cells or electric vehicles. Moreover, the use of second-generation feedstock; non-virgin oils, waste material or biomass grown on non-arable land, eliminates the food vs. fuel debate.⁵⁴

1.1.3.1 Biodiesel and Transesterification

An incentive of utilising biomass as a source to produce biofuel is a closed CO₂ cycle. The vegetation and other sources from which biomass is derived from absorb CO₂ from the atmosphere through photosynthesis. Bio-oil can be utilised as a biofuel following further chemical refinement.⁵⁵ Combustion of the subsequent fuel releases CO₂ back into the atmosphere, which is in turn absorbed by vegetation, to be converted to biomass. The self-sustaining, carbon-neutral and renewable nature of biomass-derived fuels makes them an extremely innovative and exciting petroleum replacement technology.

A key stage in biofuel production is the chemical processing of bio-oil to form biodiesel, which requires a catalyst for these reactions to proceed at appreciable rates.⁵⁶ This chemical process is the transesterification of triglyceride compounds (TAG) producing fatty acid methyl esters (FAME) and glycerol as a by-product, when methanol (MeOH) is used. FAME can be used as a petrodiesel replacement, however, the glycerol can also find use in food and pharmaceutical industries, resulting in a theoretical fully atom economic reaction.⁵⁷

This reaction can be both acid and base catalysed shown in **Figure 1.12 (Reactions A1 and A2)**, with both routes have advantages and disadvantages over the other.⁵⁵ Typically the base route is favoured in industry, due to a less sterically hindered reaction pathway via an alkoxy intermediate resulting in an increased rate.⁵⁸ This increased activity comes at a cost, with base materials being susceptible to hydrolysis from water, producing free fatty acid (FFA) (**Figure 1.12 (Reaction B)**), which attacks the basic species causing

deactivation. Acid catalysis resolves this issue, as it can esterify the FFA to produce FAME. Unfortunately, the acidic reaction pathway requires the activation of the triglyceride molecule rather than the alcohol, meaning steric hindrance can play a huge role. In summary, acid catalysts can tolerate raw feedstocks, however, basic catalysts are extremely active and require feedstock pre-treatment to avoid deactivation.⁵⁶

Current industrial biodiesel synthesis uses homogeneous basic species, such as NaOH and KOMe,⁵⁹ using C₁₋₂ alcohols, however aqueous quenching and neutralisation steps are required.⁵⁵ These bases are vulnerable to saponification, where the metal ion attacks the FAME to form soap, as seen in **Figure 1.12 (Reaction C)**. The formation of soap can cause an issue with large scale synthesis, leading to emulsions and issues with separation. The use of heterogeneous materials which aren't susceptible to leaching may mitigate these issues. This would allow for easy separation between catalyst and products, allowing for material recycling and reuse.

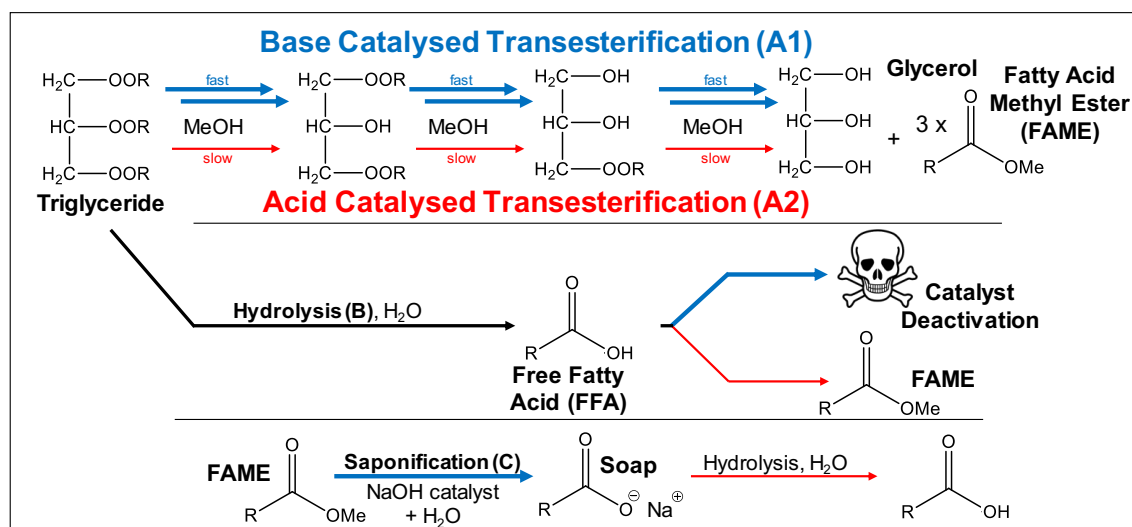


Figure 1.12. Reaction schematics for the transesterification of triglycerides using (A1) basic and (A2) acidic catalysis, (B) hydrolysis of FAME with water and (C) saponification of FAME to form soap. R=C₁₄₋₂₀ chain.

One of the key reasons to better characterise active sites within a catalytic material is to quantify the number of sites and subsequently their density within the catalyst. Raw reaction data can then be normalised to this data, allowing for a qualitative examination of how each specific active site performs. Referred to as a Turn-over Frequency (TOF), this normalised data is ideally representative of the entire catalytic material, thereby allowing for the comparison of individual active sites in different materials. It has been raised that some TOFs are not truly representative, as unidentified or wrongly identified

active sites contribute to the total density. When used with proper consideration for these pseudo-sites, however, they allow for greater understanding of the catalytic material.

Sites can be characterised in a number of ways, an example of which is using X-ray photoelectron spectroscopy to examine the surface environment of a material. A common technique used in multiple areas of science is titration, or the act to quantify an analyte using the interaction with a known species. For active site titration, this is done with a probe molecule, which will interact physically or chemically with the active site, with the probes subsequent consumption being detected and quantified. Carbon monoxide is predominantly used as a chemisorption probe for noble metal catalysts such as platinum or palladium, and solid acid materials often employ basic species; such as pyridine or phosphate organics. Solid base materials employ acid species to probe their sites, often using gaseous CO₂ or SO₂, or molecules in liquid form such as chloroform. This targeted probing allows for selective quantification of basic sites. This characterisation can be supplemented with further techniques, such as IR-spectroscopy, temperature programmed desorption and mass spectrometry, which determines the basic strength sites, bonded strength and density respectively.

This can be related to their catalytic performance. Raw reaction data can be normalised to the site density to give a TOF or examined as a function of site strength. This allows for direct comparison of similar materials through site performance.

Although solid base materials are the focus of this work, notable solid acid materials have also been used for the transesterification of triglycerides. Organic homogeneous species, such as sulphuric acid,⁵⁸ have been used on an industrial scale with great success. The dual esterification/transesterification is extremely desirable and has been replicated using organic acid groups grafted onto high surface area supports.^{60, 61} An issue faced by these materials is thermal sensitivity, meaning certain synthesis methods or thermal regeneration of the materials is not possible. Another family of materials with pronounced thermal sensitivity is acidic polymers⁶² and resins.⁶³ These materials display impressive activity for this reaction but are limited by temperature, limiting use to very mild conditions relative to those used for other materials.

Often associated with catalytic cracking of petroleum-derived crude oil, zeolites have been shown to be active for this process. Being microporous in nature, steric hindrance is a limiting factor in its catalytic ability. One route that proved effective was the seeding of the material with mesopores to ease diffusion.⁶⁴ Finally, zirconia is a material frequently used for photocatalytic water and air purification, however, its ability to support/promote acidic functionalities at its surface allows for its use in this reaction. Both

tungstated⁶⁵ and sulphated^{66, 67} zirconia have been shown extremely active for this reaction, while also tolerating high temperatures, unlike organic or resin acidic materials.

1.1.3.2 Heterogeneous Base Catalysed Transesterification

While solid acid materials can simultaneously transesterify triglycerides and esterify/hydrolyse feedstock impurities, they suffer from low activity when compared to solid base alternatives. This is due to a comparatively sterically challenged acid catalysed mechanism, therefore basic catalysts have been the focus of recent research as a more viable biodiesel catalyst.⁶⁸ The basic catalysed transesterification reaction mechanism proceeds via the deprotonation of the alcohol species by the basic catalyst. The subsequent alkoxide ion formed attacks the electron-deficient carbonyl carbon. Rearrangement of electron cleaves the C-O ester bond resulting in the formation of the fatty acid methyl ester and hydroxyl group on the glycerol backbone. This is illustrated in

Figure 1.13.⁶⁹

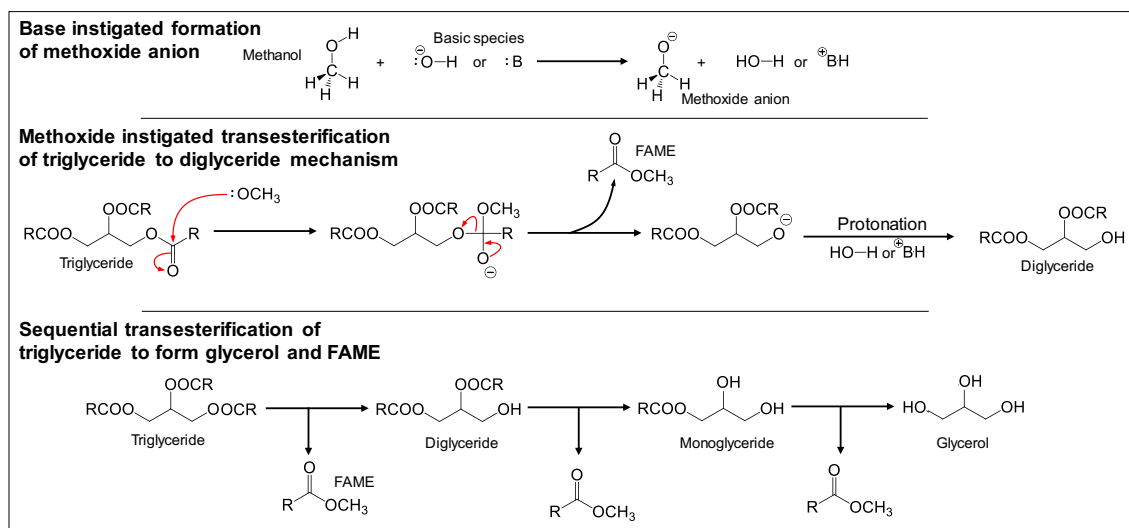


Figure 1.13. Diagram of (top) base instigated method formation, (middle) mechanism for the transesterification of triglycerides, and (bottom) reaction scheme for sequential reactions. Redrawn from reference.⁶⁹

One family of solid base catalyst that has been extensively studied for transesterification reactions are hydrotalcites.¹¹ These materials can be problematic due to leaching of the alkaline earth metal, which can falsify data due to the species reacting using a homogeneous pathway. Creasey *et al.*⁷⁰ provided a novel synthesis route that uses a nitrate and alkali-free method. The resulting catalysts outperformed conventional hydrotalcite, which was thought to be because of a greater proportion of accessible active sites.

1.1.3.3 Alkaline Earth Metal Oxides

Another family of solid base catalysts for transesterification which have been the subject of recent studies are alkaline earth metal oxides. These materials have been shown to catalyse a wide variety of reactions, due to their varying levels of basicity.⁷¹ This group consisting in part of magnesium, calcium, strontium, and barium oxides have been extensively studied as solid base catalysts.

The basicity of the resulting oxide increases with the increasing ionic radii, due to their decreasing electronegativity.⁷² Therefore the order of basicity is:

Order of Basicity: BaO < MgO < CaO < SrO

Calcium oxide catalysts have been extensively studied as solid base catalysts, due to their high activity, abundance and relatively inexpensive preparation. In 1999, Gryglewicz studied a variety of calcium species for the transesterification reaction, compared to the current homogeneous alternatives used by industry.⁷² It was observed that the basicity of calcium catalysts was directly correlated to their catalytic activity, and that oxide materials were superior to hydroxide species. A disadvantage of calcium oxide catalysis is leaching, which results in a homogeneous reaction pathway as seen with common hydrotalcite.⁷³ One way to mitigate this is through the use of mixed oxide materials, which have determined a decrease in calcium leaching.⁷⁴ It was proposed the mixed metal oxide disfavoured the loss of calcium through electronic interactions, thereby stabilising the calcium species at the surface.

More recent research has looked at ways of further reducing the cost of catalytic material from renewable sources. One avenue of study has been sourcing calcium oxide from eggshells and mollusc shells.⁷⁵ Another study looked at sourcing catalytic material from dolomite rock,⁷⁶ which consisted of both CaO (70%) and MgO(30%). Post calcination resulted in MgO nanoparticles dispersed on larger CaO particles used for the transesterification of short-chain triglyceride model compounds. This proposed synergetic relationship is interesting, however further study is needed to confirm at which species the reaction occurs. An insight into this relationship between mixed alkaline earth metal oxides is found in recent work by Li *et al*, which looked at varying ratios of calcium and strontium.⁷⁷ It was shown to be a viable catalyst for transesterification reactions, and X-ray diffraction revealed calcium-strontium carbonate crystallite present. XPS studies could be useful to determine the surface interactions between triglyceride compounds and mixed alkaline earth metal oxides catalytic species.

Dopants have also been used to further increase the basicity and subsequent activity of alkaline earth metal oxide materials. To date, there have been many dopants used, such

as organic promoters⁷⁸ and lanthanides,⁷⁹ however one of the most successful has been the use of alkaline metal dopants.⁸⁰ This has been shown to create super basic sites, which further increase the catalytic activity. This is thought to be caused by the incorporation of the alkaline metal cation into the oxide, which in turn generates ion pairs and oxygen vacancies.⁸¹ This is observed using Cs promoted nanocrystallites, which have a greatly enhanced base site densities and polarizabilities compared with undoped MgO nanocrystals.⁸² Magnesium Oxide (MgO) has also been comprehensively researched due to its low cost, abundance and reduced leaching.⁷² Montero found using heat treatments caused restructuring of the surface to reveal more basic 110 and 111 surface sites.⁸³ This study determined a clear correlation between strength of basic sites and activity, and suggesting 500-600 °C was the optimal heat treatment temperature to reveal the most basic facets at the MgO surface.

MgO functionalised SBA-15 has been shown to be extremely useful in a wide variety of procedures, either as the active phase or promoting species. A number of studies have used this material for drug delivery,⁸⁴ moisture sensitivity⁸⁵ and CO₂ adsorption.⁸⁶ CaO functionalised SBA-15 has been used⁸⁷⁻⁸⁹ for the transesterification of triglycerides, however, the use of MgO/SBA-15 is not as prevalent. Some attempts have been made to employ a one-pot synthesis of MgO, allowing the basic species to selectively be deposited inside the mesopore network, however, limited characterisation cannot confirm if this was successful.^{86, 90} As previously mentioned, when supported on micro or mesoporous materials, diffusion limitations appear to stunt the activity. Alternate routes have already been used with other catalytic species to improve the diffusion throughout the material, with a notable example being the incorporation of a macroporous network into a solid base material to increase accessibility of large chain triglycerides.⁹¹ By combining MgO one-pot functionalisation and macroporosity, a highly effective catalyst with reduced diffusion limitations would be created.

1.1.4 Nanoparticulate Gold and its Catalytic Applications

For thousands of years, metallic gold has been prized by civilisations throughout the world due to its attractive appearance and pliability. Its use in coinage and works of jewellery, some of which has been discovered intact after 7000 years, showcase its excellent stability, as gold oxide formation is not favoured.⁹² The first catalytic application of gold materials was discovered in 1823,^{93, 94} when Dulong and Thenard ran ammonia over the gold surface leading to decomposition. In 1856 Faraday synthesised the first nanoparticulate gold, which has been displayed in the royal society of chemistry to this day.⁹⁵ The vivid colours of nanoparticulate gold have led to their use in optical sensors,⁹⁶ and it caused by a phenomenon called surface plasmon resonance.⁹⁷ This is when surface electrons begin oscillating after exposure to light visible light. When they oscillate at the same frequency as a band of light, they absorb and scatter light characteristic of their size. The materials produced in this work are predominantly pink/red, indicating the gold particle size is below 20 nm.⁹⁸

In the late 1980s, the pioneering use of nanoparticulate gold for catalysis began, sparking the 'golden age' of Au catalysis. Two research groups who led by Masatake Haruta and Graham Hutchings, both independently developed gold species for two different reactions. In 1987 Haruta et al⁹⁹ demonstrated gold functionalised iron, cobalt and nickel oxide for the room temperature oxidation of carbon monoxide. Hutchins et al studied the standard reduction potential of metal chlorides for the synthesis of vinyl chloride,¹⁰⁰ hypothesised and subsequently proved gold to be the most effective species.¹⁰¹

A wide variety of gold species have been utilised to catalyse many diverse reactions, ranging from homogeneous gold complexes to single atom heterogeneous systems. This review is primarily focussed on heterogeneous systems ranging from single atoms to 10 nm nanoparticles.

1.1.4.1 Nanoparticulate Gold Species

As mentioned in **Section 1.1.1.3**, nanoparticulate functionalities benefit from an increased surface area to mass ratio compared to bulk species, allowing for increased surface interaction. Another benefit, most widely seen with single atoms or small clusters, is the altered electronic structure (**Figure 1.14**).¹⁰²

Single-atom catalysts have attracted attention in the past decade,^{23, 103} and have been found recently to be extremely effective for the oxidation of carbon monoxide.¹⁰⁴ The benefits of singular sites are increased activity and reduction in noble metal use, as theoretically the dispersion should be 100%. Stabilising these atoms is often problematic due to their high surface energy, as they are extremely mobile and prone to

agglomeration. Nitrogen doping and surface defect anchoring have been shown to increase stability.

In 1962, Kubo¹⁰⁵ suggested smaller nanoparticle clusters would behave very differently than their larger nanoparticle alternatives, due to a different valence band structure. It has been shown that nanoparticles have discrete energy bands within their valence bands in a similar manner to semiconductors. This is catalytically advantageous due to the valence band being susceptible to electronic interference from the support material in the form of strong metal-support interactions. This can electronically change the gold electronic environment, which may favour higher activity.

It was demonstrated by Landman that at eight Au atoms were required for catalytic energy,¹⁰⁶ thought to be due to 8 being the minimum number of required atoms to make a stable cluster. The d-band spin-orbital splitting increased between 8 to 100 atom clusters, from the atomic value to that of the bulk. This means clusters within this range have a different electronic structure to larger nanoparticles, which may result in greater catalytic performance. Certain morphologies of cluster have higher stability, these are Au₈, Au₁₁ and Au₅₅, however, a stabilising agent is typically still required.¹⁰⁷

Gold nanoparticles of intermediate sizes (2-5 nm) have been shown effective catalytic species for multiple reactions,¹⁰² thought to be the result of a combination of effects. The small nature of the particle results in a large proportion of defect or support boundary sites, as mentioned in **Section 1.1.1.3**. These sites have been shown to be preferential active sites, due to geometric or electronic effects. Electronic effects brought on by a discrete energy band in their valence band, as seen with clusters in **Figure 1.14**, can also affect these intermediate nanoparticles. This can lead to strong metal-support interactions (SMSI), however, these are not as strong as clusters due to the intermediate nanoparticle valence band having both discrete and continuous character.

Gold functionalised materials are extremely versatile catalytic systems, being able to enable multiple chemical transformations on its surface. Their use as catalysts is still relatively new compared to more traditional catalytic systems, however, gold shows great potential.

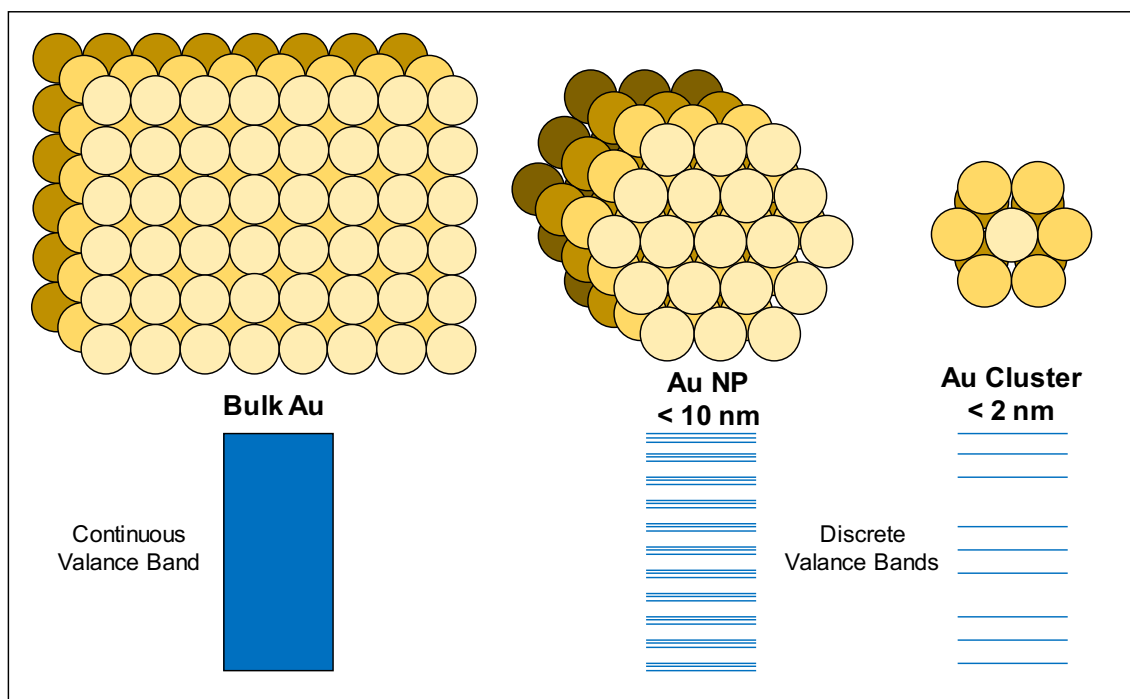


Figure 1.14. Diagram highlight the change in valance band with nanoparticles size, redrawn from reference.¹⁰²

1.1.4.2 Gold Catalysed Chemical Reactions

As previously mentioned, the catalytic performance of nanoparticulate gold was first realised using two industry-relevant reactions: the synthesis of the precursor to polyvinyl chlorate (PVC),¹⁰⁰ and the oxidation of carbon monoxide.⁹⁹

Vinyl chlorate is an important platform chemical used to produce polymer polyvinyl chloride.¹⁰⁰ The predominant production of its monomer is the thermal cracking of dichloroethane, which is advantageous due to the abundance and low cost of its feedstock. In China, however, abundant quantities of acetylene derived from huge coal reserves facilitated another route, the hydrochlorination of acetylene. Previous catalytic systems employed mercuric chloride on carbon,¹⁰⁷ which was extremely undesirable due to extreme toxicity, resulting in demand for cleaner and more active alternatives. Shinoda *et al.* tested a wide variety of metal chlorides,¹⁰⁸ however it was Hutchins that correlated their performance with the standard electron potential.¹⁰⁰ Gold chloride, with an electron potential of 1.4 eV, was predicted and experimentally proven to excel at this reaction.¹⁰¹

The production of carbon monoxide a clear problem in industrial and domestic sectors, such as mining and hydrocarbon combustion.¹⁰² Carbon monoxide inhalation can cause a variety of minor symptoms, however, excessive exposure can prove fatal.¹⁰⁹ Oxidation to the dioxide species is possible, however, can prove difficult due to the mild conditions set by its necessity in a domestic setting. A variety of catalysts were found to be partially

successful for this reaction, however, were unable to function at low temperatures and were susceptible to high water¹¹⁰ and CO concentration.^{111, 112} Haruta's gold materials exhibited excellent turn over frequency (TOFs) at low temperatures, with excellent tolerance to other species.⁹⁹ Other catalytic species have been utilised since 1987, however nanoparticulate gold continues to be a frontrunner.

Hydrogenation transformations are more commonly known to be catalysed by Pd or Pt species.¹¹³ There has been a notable precedent of nano-gold activity for this reaction, however historically this has not been studied extensively. Homogeneous systems have been widely researched, with excellent activity found using Au (I) and Au (III) complexes,¹¹⁴ however heterogeneous studies have not been as prevalent. While lacking the activity of other metals such as palladium,¹¹⁵ gold systems have been shown to demonstrate remarkable selectivity towards functional groups and partial hydrogenations.¹¹⁶ There is promising work on bimetallic gold materials, aiming to retain to the selectivity of gold and activity of the other metal.¹¹⁷

An oxidation reaction is a key chemical transformation in organic chemistry, one that gold has been found extremely active for. Epoxidation is the oxidation of an unsaturated compound to form a tricyclic C-O-C species, which due to the highly strained nature of this configuration is typically very reactive.¹¹⁸ The most industrially relevant substrates for epoxidation are ethene and propane, producing 15 and 3 Mt y⁻¹ of ethylene and propylene oxide respectively.¹¹⁹ Silver catalysts are often employed for ethylene oxide production, resulting in high activity, however, exhibit poor selectivity for propylene oxide synthesis, typically around <10%).^{120, 121} The use of gold functionalised materials has proved extremely selective at lower conversion, although selectivity is lost at high conversions. The use of hydrogen has been shown to further favour the epoxidation selectivity.^{122, 123}

Another oxidation process using industrially is the production of hydrogen peroxide.¹¹⁸ Current industrial methods are only viable on a huge scale, requiring the need to store vast quantities of the product which is extremely dangerous. A smaller-scale alternative is, therefore, an attractive possibility. Palladium based systems had been the focus of this research until gold's capacity for this reaction was demonstrated.¹²⁴ Further progress was made when Pd-Au alloys were employed resulting in a vast improvement to activity, although selectivity remained as poor as the Pd catalysts.¹²⁵ With the use of Fe₂O₃ and TiO₂ supports combined with short reaction lengths, selectivity and activity were maintained.

1.1.4.3 Selective Oxidation of Alcohols

A recurring theme when examining nanoparticulate gold catalysis is the impressive selective properties, either to functional groups or partial transformation. One of the most important compounds in cosmetic and flavour industries is benzaldehyde. Benzaldehyde has been produced via the hydrolysis of benzalchloride or toluene oxidation, however, organic chlorine and benzoic acid contamination are prevalent setting the requirement for an alternate route.¹²⁶ The selective oxidation of benzyl alcohol, sourced from biomass or derived from toluene, provides a pathway with reduced contaminants. Previously, the industrial production of aldehydes from alcohols employing often toxic stoichiometric oxidising agents¹²⁷ resulted in poor atom economy and large quantities of by-products. The selective oxidation of benzyl alcohol is a good example of where the design principles of green chemistry can be followed to implement less harmful reaction conditions.

By using environmentally benign oxidising agents, the ecological impact of an industrial process can be drastically reduced. Hydrogen peroxide¹²⁸ and tert-butyl hydroperoxide¹²⁹ have been shown to be effective, however, the use of abundant molecular oxygen^{130, 131} or air is preferential.¹³²⁻¹³⁴ The use of atmospheric pressures¹³⁵ and low temperatures¹³⁶⁻¹³⁸ has also been explored, which would further reduce the energy cost associated with synthesis. Other methods to improve the environmental impact include solvent-free,¹²⁹ photocatalytic,¹³⁹ microwave¹⁴⁰ and ultrasonic¹⁴¹ techniques.

Over oxidation can occur in the formation of a carboxyl acid species, with the subsequent coupling of acid-alcohol or aldehyde-alcohol forming an ester by-product displayed in **Figure 1.15**.¹⁴² This is why selectivity to the benzaldehyde product is key.

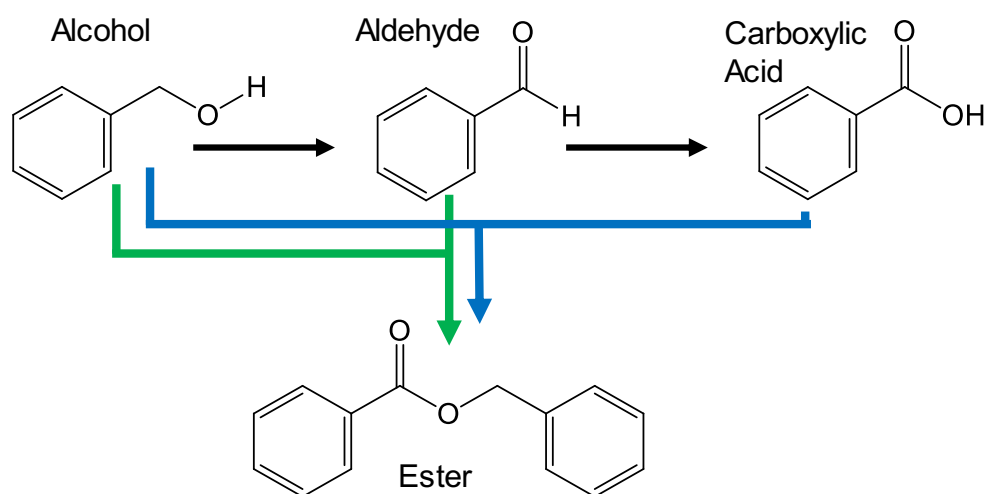


Figure 1.15. Coupling pathways to form benzyl benzoate for the selective oxidation of benzyl alcohol.¹⁴²

The selective oxidation is a base initiated deprotonation of the alcohol functional group, originating from either an organic reactant or a basic site on the support.^{142, 143} After the elimination of water, forming the benzyloxide anion, the molecule is bound to two neighbouring gold active sites. Further deprotonation results in benzaldehyde being desorbed. Further basic attack and adsorption to gold sites result in the over oxidation to form the unselective product benzoic acid. The regeneration of the gold sites occurs in this example through the oxidation of the surface-bound hydride species using adsorbed oxygen atoms. This mechanism is illustrated in **Figure 1.16**.

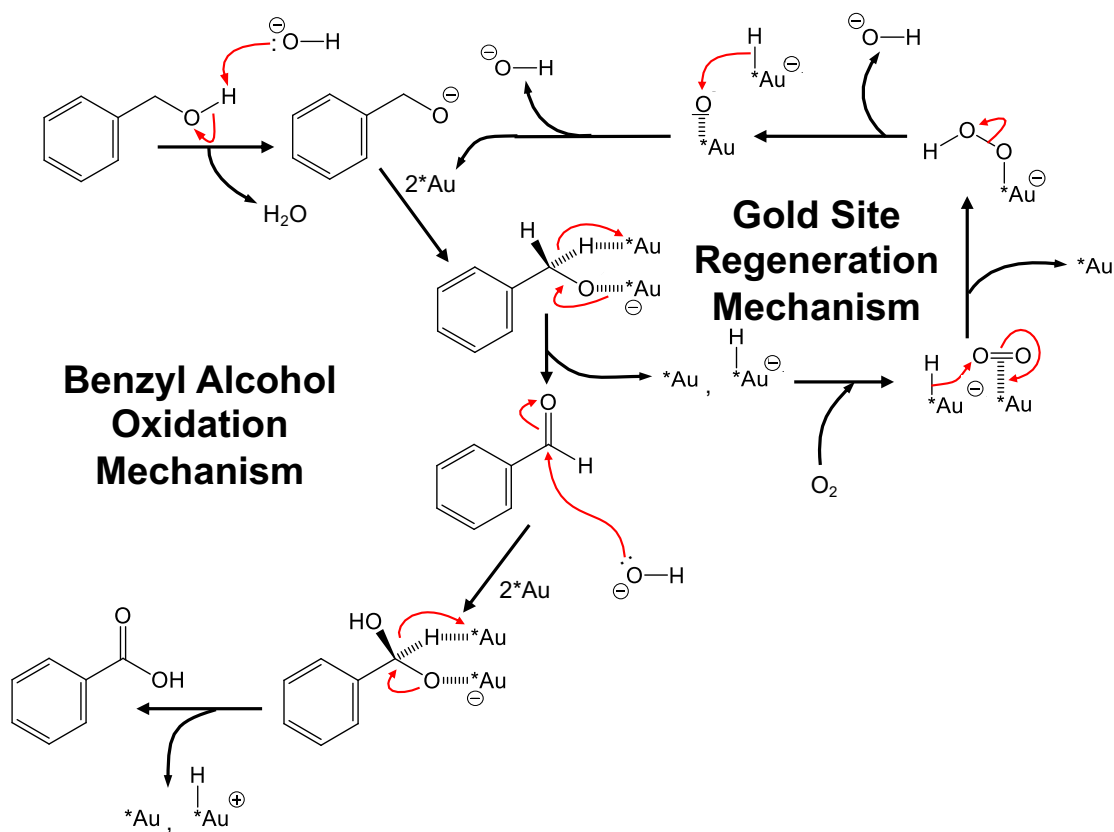


Figure 1.16. The mechanism for the oxidation of benzyl alcohol using heterogeneous gold catalysis with subsequent site regeneration, redrawn from reference.¹⁴³

Deactivation is observed often for this reaction when employing gold species and is thought to be a result of the acid unselective products and its derivatives.¹⁴³ Rodriguez-Reyes *et al* determined reduced oxygen was found to disfavour acid production however still showing ester formation.¹⁴² This proved that ester formation from the coupling of benzyl alcohol and benzaldehyde was occurring, as seen in the green pathway in **Figure 1.15**. Unfortunately, reaction profiles were not published, rendering a deduction to whether the lack of acid detected would prevent deactivation inconclusive. It is worth noting that in **Chapter 4**, benzoic acid production is not observed and deactivation does take place. This could indicate the ester product does play a part in deactivation.

1.1.4.4 Synthesis of Schiff Bases via Oxidative Coupling

The synthesis of imines, specifically Schiff Bases, is vital for a number of key applications. These family of compounds were discovered by Hugo Schiff in 1864,¹⁴⁴ and refer to an imine species with either a secondary ketimine or aldimine being present, with the nitrogen bound to another hydrocarbon species. The imine functional group within Schiff bases have been found to confer broad-spectrum biological activities resulting in an abundance of therapeutic applications, such as antimalarial,¹⁴⁵ antibacterial, antiviral and antifungal.¹⁴⁶ Schiff bases have also been used as ligands in coordination chemistry, binding the metal centre using the basic pi-accepting nitrogen in the imine functional group,¹⁴⁷ used in homogeneous catalysis¹⁴⁸ or acting as organometallic reactant.¹⁴⁹

Conventional synthesis¹⁵⁰ requires the condensation of amine and carbonyl-containing species, through nucleophilic addition resulting in the formation of a hemiaminal species, before subsequent dehydration to produce the imine as shown in **Figure 1.17**. The equilibrium of this reaction favours the reverse hydrolysis reaction, meaning the condensed water needs to be removed either through a drying agent, distillation or reaction conditions to push the equilibrium to favour the imine. It is reported this reaction may occur in the absence of a catalyst,¹⁵¹ however when the nucleophilic addition is disfavoured with an electron-donating group on the aldehyde/ketone species and an electron-withdrawing group on the amine species. In cases such as these, a Lewis acid is required.¹⁵² This is to promote the protonation and condensation of water from the hemiaminal hydroxyl species.

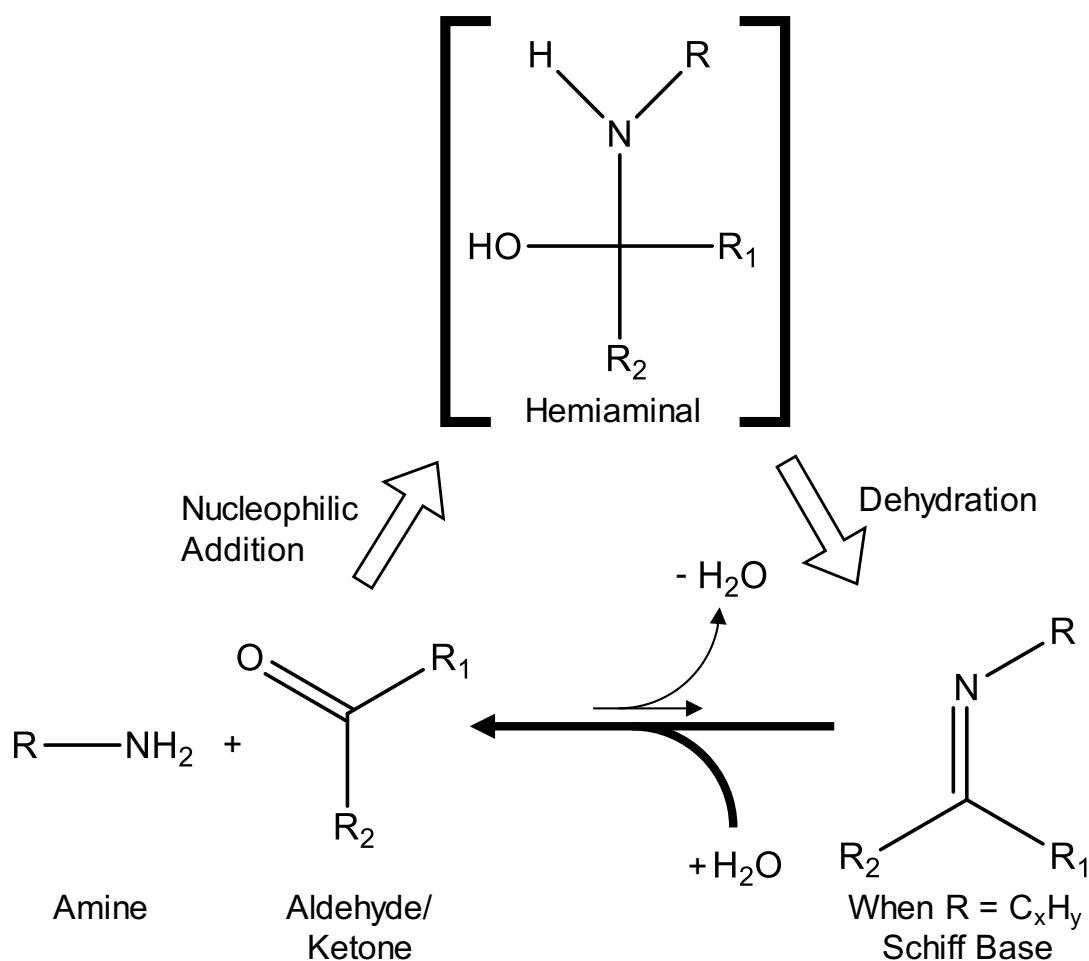


Figure 1.17. Reaction scheme for the conventional synthesis of an imine from an amine and carbonyl-containing compound via condensation reaction.¹⁵⁰

The complex aldehyde or ketone precursors required to form biologically active compounds often suffer from sensitivity to conditions or toxicity, resulting in poor yields and difficulty handling.¹⁴⁶ By starting with more benign substrates and using different one-pot reaction pathways, more environmentally friendly conditions can be employed, reducing energy cost, waste and purification steps.¹⁵³ Three different approaches to imine synthesis have shown great potential, being able to utilize greener conditions for a one-pot reaction.

The first route employs a secondary amine, which undergoes an oxidative dehydration reaction to form the imine species displayed in **Figure 1.18**.^{154, 155}

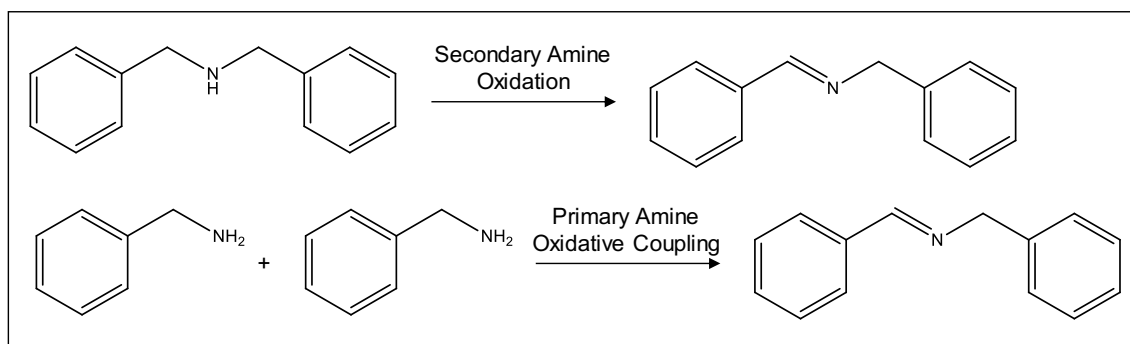


Figure 1.18. Reaction scheme for the synthesis of an imine from a secondary amine (top), and primary amine (bottom) via oxidative dehydration reaction.

These oxidative dehydration reactions have been performed using a wide variety of homogeneous species,¹⁵⁶ such as ruthenium,¹⁵⁷ cobalt,¹⁵⁸ copper¹⁵⁹ and vanadium¹⁶⁰ complexes. Heterogeneous gold catalytic systems have also been used, with activity found even in bulk gold however nanoparticulate gold was found a superior species.¹⁶¹ High selectivity to the secondary amine oxidation is often observed, with the resultant products having increased stability allowing for respectable yields.¹⁶² The reaction is however significantly influenced by the steric hindrance of the amide species, will very poor chemoselectivity for unsymmetrical substrates. The second route, a coupling of primary amines involved is also displayed in **Figure 1.18** (bottom).^{163, 164} Homocoupling results in excellent imine yield and selectivity, however, heterocoupled imines are much less selective as in a mixture of multiple species, substrates preferentially coupling to themselves.¹⁶³ There is also the concern that a number of by-products may be formed by the primary amine such as nitrile or amide species.^{165, 166}

Finally, the third route is the cascade of alcohol oxidation followed by aldehyde coupling with amines displayed in **Figure 1.19**.^{114, 167} This reaction is influenced by a range of parameters; concentration, steric/electronic effects, pH, temperature and solvent used. One of the more influential factors is the requirement of a low pH to enable the imine formation from its intermediate.¹⁵⁶ Catalysts with Lewis acid character have all been employed for this transformation,¹⁵⁶ enabling the dehydrogenation step which results in the imine.

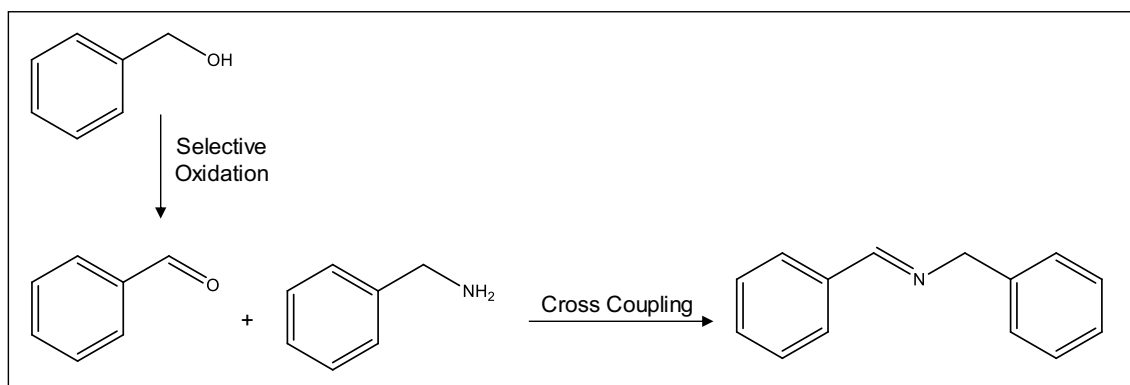


Figure 1.19. Reaction scheme for the synthesis of an imine from alcohol and amine via oxidative cross-coupling reaction.

This process allows for both symmetric and asymmetric imines, with water being the only product formed. Unfortunately, the major challenge with this method is achieving the first oxidative step using mild conditions.^{168, 169} As with processes mentioned earlier, homogeneous catalysis often results in difficulties with regard to separation and stability. Heterogeneous materials, while easily separated, were found to require harsh conditions and long reaction times.¹⁷⁰⁻¹⁷²

Gold was found to be extremely active for this reaction, which is attributed to its excellent performance in the selective oxidation step. Basic species were determined to be an essential addition to the reaction, and again this attributed to the effect of the base on the first step.^{173, 174} Other catalytic systems have been explored, such as alloys¹⁷⁵ and photocatalytically active supports.¹⁷⁶ A question not fully explored is the conflicting pH requirements for the two individual reactions. Basic conditions are required to promote or scavenge in the selective oxidation step, however, acidic conditions are required to eliminate water from the hemiaminal imine intermediate.¹⁶⁷ Coupling has been determined to occur instantaneously for certain substrates, however, with more complex reagents a dual functional system may be required for the base-acid steps.

1.2 Thesis Aims and Objectives

A gap in the literature has been identified regarding one-pot MgO functionalised SBA-15 materials in heterogeneous catalysis. Macroporous templating of SBA-15 has not been applied to these materials before and is thought to be beneficial in mitigating diffusion limitations resulting from sterically hindered substrates. Consequently, selective oxidation of benzyl alcohol and oxidative cross-coupling of benzyl alcohol and benzylamine have been found to require an added base to promote the reaction making the MgO/SBA-15 materials ideal support for another catalytic function. Different concentrations of the base have been found to influence the reaction differently. Base promoted reactions have been investigated, however, no basic SBA-15 has been used to the best of our knowledge. The objectives are therefore:

1. Synthesis, characterisation and screening of a one-pot TLCT mesoporous and hierarchical MgO/SBA-15 material for the transesterification of tributyrin (CHAPTER 3).
2. Investigate the incorporation of a macroporous network using the transesterification of larger chain triglyceride and other methods, to determine the effect on diffusion limitations (CHAPTER 3-5).
3. Functionalisation and characterisation of mesoporous and hierarchical MgO/SBA-15 with Au nanoparticles using a variety of impregnation techniques. Optimisation of the selective oxidation reaction conditions using chemometrics, and subsequent study on the effect of changing the most influential variables of the material to optimise the synthesis process further (CHAPTER 4).
4. Comparison of selective oxidation of Au@MgO/SBA-15 materials to bulk fumed silica (Au@MgO/SiO₂) and bulk alkaline (Au/MgO and Au/CaO) catalysts for the selective oxidation of benzyl alcohol and the oxidative cross-coupling of benzyl alcohol and benzylamine (CHAPTER 5).

1.3 References

1. B. A. de Marco, B. S. Rechelo, E. G. Tótolí, A. C. Kogawa and H. R. N. Salgado, Evolution of green chemistry and its multidimensional impacts: A review, *Saudi Pharmaceutical Journal*, 2019, **27**, 1-8.
2. J. H. Clark, R. Luque and A. S. Matharu, Green chemistry, biofuels and biorefinery, *Annual Review of Chemical and Biomolecular Engineering*, 2012, **3**, 183-207.
3. P. Atkins, J. de Paula and J. Keeler, *Physical Chemistry*, Oxford University Press, Great Britain, 8th edition, 2006.
4. D. E. Koshland Jr, The key-lock theory and the induced fit theory, *Angewandte Chemie International Edition in English*, 1995, **33**, 2375-2378.
5. J. You, Y. Guo, R. Guo and X. Liu, A review of visible light-active photocatalysts for water disinfection: Features and prospects, *Chemical Engineering Journal*, 2019, **373**, 624-641.
6. D. Bahnemann, Photocatalytic water treatment: solar energy applications, *Solar Energy*, 2004, **77**, 445-459.
7. J. Klosin, P. P. Fontaine and R. Figueroa, Development of Group IV molecular catalysts for high temperature ethylene- α -olefin copolymerization reactions, *Accounts of Chemical Research*, 2015, **48**, 2004-2016.
8. J. J. Eisch, Fifty Years of Ziegler-Natta Polymerization: From serendipity to science. a personal account, *Organometallics*, 2012, **31**, 4917-4932.
9. F. G. Helfferich, Comprehensive chemical kinetics, Chapter 8, Elsevier, 2004, **40**, 209-272.
10. S. A. Ashter, Thermoforming of single and multilayer laminates, William Andrew Publishing, Oxford, 2014, 123-145.
11. M. Weller, T. Overton, J. Rourke and F. Armstrong, Inorganic Chemistry, OUP Oxford, 2014.
12. Z. B. Shifrina and L. M. Bronstein, Magnetically recoverable catalysts: beyond magnetic separation, *Frontiers in Chemistry*, 2018, **6**, 298
13. T. Kandemir, M. E. Schuster, A. Senyshyn, M. Behrens and R. Schlögl, The Haber-Bosch process revisited: on the real structure and stability of "ammonia iron" under working conditions, *Angewandte Chemie International Edition*, 2013, **52**, 12723-12726.
14. C. J. M. van der Ham, M. T. M. Koper and D. G. H. Hetterscheid, Challenges in reduction of dinitrogen by proton and electron transfer, *Chemical Society Reviews*, 2014, **43**, 5183-5191.
15. R. Klaewkla, M. Arend and W. Hölderich, A review of mass transfer controlling the reaction rate in heterogeneous catalytic systems, *Mass Transfer - Advanced Aspects*, 2011, **29**.
16. S. R. Logan, Arrhenius activation energy of reactions that are almost diffusion-controlled, *Journal of the Chemical Society, Faraday Transactions 1: Physical Chemistry in Condensed Phases*, 1977, **73**, 592-595.
17. J. Wintterlin, S. Völkening, T. V. W. Janssens, T. Zambelli and G. Ertl, Atomic and macroscopic reaction rates of a surface-catalyzed reaction, *Science*, 1997, **278**, 1931-1934.

18. T. Waldmann, D. Künzel, H. E. Hoster, A. Groß and R. J. Behm, Oxidation of an organic adlayer: a bird's eye view, *J. Am. Chem. Soc.*, 2012, **134**, 8817-8822.
19. M. Gargaud, R. Amils, J. C. Quintanilla, H. J. Cleaves, W. M. Irvine, D. L. Pinti and M. Viso, *Encyclopedia of astrobiology*, Springer, Berlin, Heidelberg, 2011, 485.
20. K. J. Laidler and J. H. Meiser, *Physical chemistry*, Benjamin/Cummings Pub. Co., Menlo Park, California, 1982.
21. J. Bishop, C. J. Lobo, A. Martin, M. Ford, M. Phillips and M. Toth, Role of activated chemisorption in gas-mediated electron beam induced deposition, *Physical Review Letters*, 2012, **109**, 146103.
22. S. J. Tauster, Strong metal-support interactions, *Accounts of Chemical Research*, 1987, **20**, 389-394.
23. L. Liu and A. Corma, Metal catalysts for heterogeneous catalysis: from single atoms to nanoclusters and nanoparticles, *Chemical Reviews*, 2018, **118**, 4981-5079.
24. P. E. Strizhak, A. I. Trypolskyi, G. R. Kosmambetova, O. Z. Didenko and T. N. Gurnyk, Geometric and electronic approaches to size effects in heterogeneous catalysis, *Kinetics and Catalysis*, 2011, **52**, 128-138.
25. K. Oura, M. Katayama, A. V. Zotov, V. G. Lifshits and A. A. Saranin, *Surface Science: An Introduction*, Springer, Berlin, Heidelberg, 2003, pp. 229-260.
26. J. F. Nicholas, *Physics of Solid Surfaces*, Chapter 2.1.1.5.1 The terrace-ledge-kink (TLK) mode, Springer Materials, 1993, **24(A)**.
27. G. Zangari, Electrodeposition of Alloys and Compounds in the Era of Microelectronics and Energy Conversion Technology, *Coatings*, 2015, **5**, 195-218.
28. M. Thommes and K. A. Cychoz, Physical adsorption characterization of nanoporous materials: progress and challenges, *Adsorption*, 2014, **20**, 233-250.
29. Y. Li, L. Rong and Y. Li, Pore characteristics of porous NiTi alloy fabricated by combustion synthesis, *Journal of Alloys and Compounds*, 2001, **325**, 259-262.
30. Christopher M. A. Parlett, Mark A. Isaacs, Simon K. Beaumont, Laura M. Bingham, Nicole S. Hondow, K. Wilson and Adam F. Lee, Spatially orthogonal chemical functionalization of a hierarchical pore network for catalytic cascade reactions, *Nature Materials*, 2016, **15**, 178-182.
31. M. W. Matsen, Phase behavior of block copolymer/homopolymer blends, *Macromolecules*, 1995, **28**, 5765-5773.
32. D. Zhao, Q. Huo, J. Feng, B. F. Chmelka and G. D. Stucky, Nonionic triblock and star diblock copolymer and oligomeric surfactant syntheses of highly ordered, hydrothermally stable, mesoporous silica structures, *Journal of the American Chemical Society*, 1998, **120**, 6024-6036.
33. S. H. Tolbert, C. C. Landry, G. D. Stucky, B. F. Chmelka, P. Norby, J. C. Hanson and A. Monnier, Phase transitions in mesostructured silica/surfactant composites: surfactant packing and the role of charge density matching, *Chemistry of Materials*, 2001, **13**, 2247-2256.
34. T. Kaasgaard and C. J. Drummond, Ordered 2-D and 3-D nanostructured amphiphile self-assembly materials stable in excess solvent, *Physical Chemistry Chemical Physics*, 2006, **8**, 4957-4975.

35. A. Dominguez, A. Fernandez, N. Gonzalez, E. Iglesias and L. Montenegro, Determination of critical micelle concentration of some surfactants by three techniques, *Journal of Chemical Education*, 1997, **74**, 1227.
36. N. Garti, D. Libster and A. Aserin, Lipid polymorphism in lyotropic liquid crystals for triggered release of bioactives, *Food & Function*, 2012, **3**, 700-713.
37. D. Y. Zhao, J. L. Feng, Q. S. Huo, N. Melosh, G. H. Fredrickson, B. F. Chmelka and G. D. Stucky, Triblock copolymer syntheses of mesoporous silica with periodic 50 to 300 angstrom pores, *Science*, 1998, **279**, 548-552.
38. G. Wanka, H. Hoffmann and W. Ulbricht, Phase diagrams and aggregation behavior of poly(oxyethylene)-poly(oxypropylene)-poly(oxyethylene) triblock copolymers in aqueous solutions, *Macromolecules*, 1994, **27**, 4145-4159.
39. J. S. Beck, J. C. Vartuli, W. J. Roth, M. E. Leonowicz, C. T. Kresge, K. D. Schmitt, C. T. W. Chu, D. H. Olson, E. W. Sheppard, S. B. McCullen, J. B. Higgins and J. L. Schlenker, A new family of mesoporous molecular-sieves prepared with liquid-crystal templates, *Journal of the American Chemical Society*, 1992, **114**, 10834-10843.
40. A. Taguchi and F. Schuth, Ordered mesoporous materials in catalysis, *Microporous and Mesoporous Materials*, 2005, **77**, 1-45.
41. S. G. Wainwright, C. M. A. Parlett, R. A. Blackley, W. Zhou, A. F. Lee, K. Wilson and D. W. Bruce, True liquid crystal templating of SBA-15 with reduced microporosity, *Microporous and Mesoporous Materials*, 2013, **172**, 112-117.
42. A. Katiyar and N. G. Pinto, Visualization of size-selective protein separations on spherical mesoporous silicates, *Small*, 2006, **2**, 644-648.
43. P. Shah and V. Ramaswamy, Thermal stability of mesoporous SBA-15 and Sn-SBA-15 molecular sieves: an in situ HTXRD study, *Microporous and Mesoporous Materials*, 2008, **114**, 270-280.
44. G. S. Attard, J. C. Glyde and C. G. Goltner, Liquid-crystalline phases as templates for the synthesis of mesoporous silica, *Nature*, 1995, **378**, 366-368.
45. S. G. Wainwright, C. M. A. Parlett, R. A. Blackley, W. Z. Zhou, A. F. Lee, K. Wilson and D. W. Bruce, True liquid crystal templating of SBA-15 with reduced microporosity, *Microporous and Mesoporous Materials*, 2013, **172**, 112-117.
46. L. Huang and M. Kruk, Versatile surfactant/swelling-agent template for synthesis of large-pore ordered mesoporous silicas and related hollow nanoparticles, *Chemistry of Materials*, 2015, **27**, 679-689.
47. T. Sen, G. J. T. Tiddy, J. L. Casci and M. W. Anderson, Synthesis and characterization of hierarchically ordered porous silica materials, *Chemistry of Materials*, 2004, **16**, 2044-2054.
48. B. T. Holland, C. F. Blanford and A. Stein, Synthesis of macroporous minerals with highly ordered three-dimensional arrays of spheroidal voids, *Science*, 1998, **281**, 538-540.
49. A. Badiei, H. Goldooz, G. M. Ziarani and A. Abbasi, One pot synthesis of functionalized SBA-15 by using an 8-hydroxyquinoline-5-sulfonamide-modified organosilane as precursor, *Journal of Colloid and Interface Science*, 2011, **357**, 63-69.
50. S. Hao, H. Chang, Q. Xiao, Y. Zhong and W. Zhu, One-pot synthesis and CO₂ adsorption properties of ordered mesoporous SBA-15 materials functionalized with APTMS, *The Journal of Physical Chemistry C*, 2011, **115**, 12873-12882.

51. S. Hao, Q. Xiao, Y. Zhong, W. Zhu and H. Yang, One-Pot Synthesis of amino-functionalized SBA-15 and their CO₂ adsorption properties, *Chinese Journal of Inorganic Chemistry*, 2010, **26**, 982-988.
52. S. W. Song, K. Hidajat and S. Kawi, Functionalized SBA-15 materials as carriers for controlled drug delivery: influence of surface properties on matrix–drug interactions, *Langmuir*, 2005, **21**, 9568-9575.
53. United Nations Climate Change, Paris Agreement, 2015.
54. K. Wilson and A. F. Lee, Rational design of heterogeneous catalysts for biodiesel synthesis, *Catalysis Science & Technology*, 2012, **2**, 884.
55. A. Sivasamy, K. Y. Cheah, P. Fornasiero, F. Kemausuor, S. Zinoviev and S. Miertus, Catalytic applications in the production of biodiesel from vegetable oils, *Chemsuschem*, 2009, **2**, 278-300.
56. A. F. Lee, J. A. Bennett, J. C. Manayil and K. Wilson, Heterogeneous catalysis for sustainable biodiesel production via esterification and transesterification, *Chemistry Society Reviews*, 2014, **43**, 7887-7916.
57. J. A. Kenar, Glycerol as a platform chemical: Sweet opportunities on the horizon?, *Lipid Technology*, 2007, **19**, 249-253.
58. M. K. Lam, K. T. Lee and A. R. Mohamed, Homogeneous, heterogeneous and enzymatic catalysis for transesterification of high free fatty acid oil (waste cooking oil) to biodiesel: A review, *Biotechnology Advances*, 2010, **28**, 500-518.
59. J. M. Montero, D. R. Brown, P. L. Gai, A. F. Lee and K. Wilson, In situ studies of structure–reactivity relations in biodiesel synthesis over nanocrystalline MgO, *Chemical Engineering Journal*, 2010, **161**, 332-339.
60. I. K. Mbaraka, D. R. Radu, V. S. Y. Lin and B. H. Shanks, Organosulfonic acid-functionalized mesoporous silicas for the esterification of fatty acid, *Journal of Catalysis*, 2003, **219**, 329-336.
61. A. Martin, G. Morales, F. Martinez, R. van Grieken, L. Cao and M. Kruk, Acid hybrid catalysts from poly(styrenesulfonic acid) grafted onto ultra-large-pore SBA-15 silica using atom transfer radical polymerization, *Journal of Materials Chemistry*, 2010, **20**, 8026-8035.
62. P. Xia, F. Liu, C. Wang, S. Zuo and C. Qi, Efficient mesoporous polymer based solid acid with superior catalytic activities towards transesterification to biodiesel, *Catalysis Communications*, 2012, **26**, 140-143.
63. W. Liu, P. Yin, X. Liu, W. Chen, H. Chen, C. Liu, R. Qu and Q. Xu, Microwave assisted esterification of free fatty acid over a heterogeneous catalyst for biodiesel production, *Energy Conversion and Management*, 2013, **76**, 1009-1014.
64. A. Carrero, G. Vicente, R. Rodríguez, M. Linares and G. L. del Peso, Hierarchical zeolites as catalysts for biodiesel production from *Nannochloropsis* microalga oil, *Catalysis Today*, 2011, **167**, 148-153.
65. K. Ngaosuwan, X. H. Mo, J. G. Goodwin and P. Praserthdam, Effect of solvent on hydrolysis and transesterification reactions on tungstated zirconia, *Applied Catalysis a-General*, 2010, **380**, 81-86.
66. G. Morales, A. Osatiashtiani, B. Hernandez, J. Iglesias, J. A. Melero, M. Paniagua, D. Robert Brown, M. Granollers, A. F. Lee and K. Wilson, Conformal sulfated zirconia monolayer catalysts for the one-pot synthesis of ethyl levulinate from glucose, *Chemical Communications*, 2014, **50**, 11742-11745.

67. M. H. M. Yusoff and A. Z. Abdullah, Catalytic behavior of sulfated zirconia supported on SBA-15 as catalyst in selective glycerol esterification with palmitic acid to monopalmitin, *Journal of the Taiwan Institute of Chemical Engineers*, 2016, **60**, 199-204.
68. L. B. Sun, X. Q. Liu and H. C. Zhou, Design and fabrication of mesoporous heterogeneous basic catalysts, *Chemical Society Reviews*, 2015, **44**, 5092-5147.
69. U. Schuchardt, R. Sercheli and R. M. Vargas, Transesterification of vegetable oils: a review, *Journal of the Brazilian Chemical Society*, 1998, **9**, 199-210.
70. J. J. Creasey, A. Chierigato, J. C. Manayil, C. M. A. Parlett, K. Wilson and A. F. Lee, Alkali- and nitrate-free synthesis of highly active Mg-Al hydrotalcite-coated alumina for FAME production, *Catalysis Science & Technology*, 2014, **4**, 861-870.
71. K. Tanabe and Y. Fukuda, Basic properties of alkaline earth metal oxides and their catalytic activity in the decomposition of diacetone alcohol, *Reaction Kinetics and Catalysis Letters*, 1974, **1**, 21-24.
72. S. Gryglewicz, Rapeseed oil methyl esters preparation using heterogeneous catalysts, *Bioresource Technology*, 1999, **70**, 249-253.
73. M. Kouzu, S.-y. Yamanaka, J.-s. Hidaka and M. Tsunomori, Heterogeneous catalysis of calcium oxide used for transesterification of soybean oil with refluxing methanol, *Applied Catalysis A: General*, 2009, **355**, 94-99.
74. O. Kikhtyanin, L. Čapek, L. Smoláková, Z. Tišler, D. Kadlec, M. Lhotka, P. Diblíková and D. Kubička, Influence of Mg–Al mixed oxide compositions on their properties and performance in Aldol condensation, *Industrial & Engineering Chemistry Research*, 2017, **56**, 13411-13422.
75. G. Y. Chen, R. Shan, S. Y. Li and J. F. Shi, A biomimetic silicification approach to synthesize CaO-SiO₂ catalyst for the transesterification of palm oil into biodiesel, *Fuel*, 2015, **153**, 48-55.
76. K. Wilson, C. Hardacre, A. F. Lee, J. M. Montero and L. Shellard, The application of calcined natural dolomitic rock as a solid base catalyst in triglyceride transesterification for biodiesel synthesis, *Green Chemistry*, 2008, **10**, 654-659.
77. H. Li, S. L. Niu, C. M. Lu and J. Li, Calcium oxide functionalized with strontium as heterogeneous transesterification catalyst for biodiesel production, *Fuel*, 2016, **176**, 63-71.
78. H. Zhu, Z. Wu, Y. Chen, P. Zhang, S. Duan, X. Liu and Z. Mao, Preparation of biodiesel catalyzed by solid super base of calcium oxide and its refining process, *Chinese Journal of Catalysis*, 2006, **27**, 391-396.
79. T. L. Lohr, Z. Li and T. J. Marks, Thermodynamic strategies for C–O bond formation and cleavage via tandem catalysis, *Accounts of Chemical Research*, 2016, **49**, 824-834.
80. H. Matsushashi, M. Oikawa and K. Arata, Formation of superbase sites on alkaline earth metal oxides by doping of alkali metals, *Langmuir*, 2000, **16**, 8201-8205.
81. J. J. Woodford, C. M. A. Parlett, J.-P. Dacquin, G. Cibin, A. Dent, J. Montero, K. Wilson and A. F. Lee, Identifying the active phase in Cs-promoted MgO nanocatalysts for triglyceride transesterification, *Journal of Chemical Technology & Biotechnology*, 2014, **89**, 73-80.
82. J. M. Montero, K. Wilson and A. F. Lee, Cs promoted triglyceride transesterification over MgO nanocatalysts, *Topics in Catalysis*, 2010, **53**, 737-745.

83. J. M. Montero, P. Gai, K. Wilson and A. F. Lee, Structure-sensitive biodiesel synthesis over MgO nanocrystals, *Green Chemistry*, 2009, **11**, 265-268.
84. V. Fathi Vavsari, G. Mohammadi Ziarani and A. Badiei, The role of SBA-15 in drug delivery, *RSC Advances*, 2015, **5**, 91686-91707.
85. R. Wang, X. Liu, Y. He, Q. Yuan, X. Li, G. Lu and T. Zhang, The humidity-sensitive property of MgO-SBA-15 composites in one-pot synthesis, *Sensors and Actuators B-chemical*, 2010, **145**, 386-393.
86. Z. Y. Wu, Q. Jiang, Y. M. Wang, H. J. Wang, L. B. Sun, L. Y. Shi, J. H. Xu, Y. Wang, Y. Chun and J. H. Zhu, Generating superbasic sites on mesoporous silica SBA-15, *Chemistry of Materials*, 2006, **18**, 4600-4608.
87. H. Sun, J. Han, Y. Ding, W. Li, J. Duan, P. Chen, H. Lou and X. Zheng, One-pot synthesized mesoporous Ca/SBA-15 solid base for transesterification of sunflower oil with methanol, *Applied Catalysis A: General*, 2010, **390**, 26-34.
88. M. C. G. Albuquerque, I. Jimenez-Urbistondo, J. Santamaria-Gonzalez, J. M. Merida-Robles, R. Moreno-Tost, E. Rodriguez-Castellon, A. Jimenez-Lopez, D. C. S. Azevedo, C. L. Cavalcante and P. Maireles-Torres, CaO supported on mesoporous silicas as basic catalysts for transesterification reactions, *Applied Catalysis a-General*, 2008, **334**, 35-43.
89. W. Thitsartarn, T. Maneerung and S. Kawi, Highly active and durable Ca-doped Ce-SBA-15 catalyst for biodiesel production, *Energy*, 2015, **89**, 946-956.
90. Y. L. Wei, Y. M. Wang, J. H. Zhu and Z. Y. Wu, In-situ coating of SBA-15 with MgO: direct synthesis of mesoporous solid bases from strong acidic systems, *Advanced Materials*, 2003, **15**, 1943-1945.
91. J. J. Woodford, J.-P. Dacquin, K. Wilson and A. F. Lee, Better by design: nanoengineered macroporous hydrotalcites for enhanced catalytic biodiesel production, *Energy & Environmental Science*, 2012, **5**, 6145-6150.
92. P. G. Jones, H. Rumpel, G. M. Sheldrick and E. Schwarzmann, Gold(III) oxide and oxychloride, *Gold Bulletin*, 1980, **13**, 56-56.
93. P. Dulong and L. Thenard, Nouvelles observations sur la propriété dont jouissent certains corps de favoriser la combinaison des fluides élastiques, *Ann. Chim*, 1823, **2**, 380-387.
94. P. Dulong and L. Thenard, Note sur la propriété que possèdent quelques métaux de faciliter la combinaison des fluides élastiques, *Annanles de Chimie*, 1823, **2**, 440-444.
95. M. Faraday, X. The Bakerian Lecture. - Experimental relations of gold (and other metals) to light, *Philosophical Transactions of the Royal Society of London*, 1857, **147**, 145-181.
96. O. Loebich, The optical properties of gold, *Gold Bulletin*, 1972, **5**, 2-10.
97. S. K. Ghosh and T. Pal, Interparticle coupling effect on the surface plasmon resonance of gold nanoparticles: from theory to applications, *Chemical Reviews*, 2007, **107**, 4797-4862.
98. G. Frens, Controlled nucleation for the regulation of the particle size in monodisperse gold suspensions, *Nature Physical Science*, 1973, **241**, 20-22.
99. M. Haruta, T. Kobayashi, H. Sano and N. Yamada, Novel gold catalysts for the oxidation of carbon monoxide at a temperature far below 0 °C, *Chemistry Letters*, 1987, **16**, 405-408.

100. B. Nkosi, N. J. Coville and G. J. Hutchings, Vapour phase hydrochlorination of acetylene with group VIII and IB metal chloride catalysts, *Applied Catalysis*, 1988, **43**, 33-39.
101. B. Nkosi, N. J. Coville and G. J. Hutchings, Reactivation of a supported gold catalyst for acetylene hydrochlorination, *Journal of the Chemical Society, Chemical Communications*, 1988, 71-72.
102. M. Haruta, Spiers Memorial Lecture Role of perimeter interfaces in catalysis by gold nanoparticles, *Faraday Discussions*, 2011, **152**, 11-32.
103. G. Malta, S. A. Kondrat, S. J. Freakley, C. J. Davies, L. Lu, S. Dawson, A. Thefford, E. K. Gibson, D. J. Morgan, W. Jones, P. P. Wells, P. Johnston, C. R. A. Catlow, C. J. Kiely and G. J. Hutchings, Identification of single-site gold catalysis in acetylene hydrochlorination, *Science*, 2017, **355**, 1399.
104. B. Qiao, J.-X. Liang, A. Wang, J. Liu and T. Zhang, Single atom gold catalysts for low-temperature CO oxidation, *Chinese Journal of Catalysis*, 2016, **37**, 1580-1586.
105. R. Kubo, Electronic Properties of metallic fine particles. I, *Journal of the Physical Society of Japan*, 1962, **17**, 975-986.
106. U. Landman, B. Yoon, C. Zhang, U. Heiz and M. Arenz, Factors in gold nanocatalysis: oxidation of CO in the non-scalable size regime, *Topics in Catalysis*, 2007, **44**, 145-158.
107. G. J. Hutchings, Heterogeneous gold catalysis, *ACS Central Science*, 2018, **4**, 1095-1101.
108. K. Shinoda, The vapor-phase hydrochlorination of acetylene over metal chlorides supported on activated carbon, *Chemistry Letters*, 1975, **4**, 219-220.
109. A. Ernst and J. D. Zibrak, Carbon monoxide poisoning, *New England Journal of Medicine*, 1998, **339**, 1603-1608.
110. M. I. Brittan, H. Bliss and C. A. Walker, Kinetics of the hopcalite-catalyzed oxidation of carbon monoxide, *AIChE Journal*, 1970, **16**, 305-314.
111. J. P. Dauchot and J. P. Dath, Oxidation of carbon monoxide on thin film catalysts: Characterization by a critical temperature measurement, *Journal of Catalysis*, 1984, **86**, 373-383.
112. G. C. Bond, L. R. Molloy and M. J. Fuller, Oxidation of carbon monoxide over palladium–tin(IV) oxide catalysts: an example of spillover catalysis, *Journal of the Chemical Society, Chemical Communications*, 1975, 796-797.
113. B. Hammer and J. K. Norskov, Why gold is the noblest of all the metals, *Nature*, 1995, **376**, 238-240.
114. Y. Zhang, X. Cui, F. Shi and Y. Deng, Nano-gold catalysis in fine chemical synthesis, *Chemical Reviews*, 2012, **112**, 2467-2505.
115. A. S. K. Hashmi, Gold-catalyzed organic reactions, *Chemical Reviews*, 2007, **107**, 3180-3211.
116. A. C. Gluhoi, J. W. Bakker and B. E. Nieuwenhuys, Gold, still a surprising catalyst: Selective hydrogenation of acetylene to ethylene over Au nanoparticles, *Catalysis Today*, 2010, **154**, 13-20.
117. L. Piccolo, A. Piednoir and J.-C. Bertolini, Pd–Au single-crystal surfaces: Segregation properties and catalytic activity in the selective hydrogenation of 1,3-butadiene, *Surface Science*, 2005, **592**, 169-181.

118. M. Ali, M. Rahman, M. Sarkar and S. B. Abd Hamid, Heterogeneous metal catalysts for oxidation reactions, *Journal of Nanomaterials*, 2014, **2014**, 1-23.
119. A. S. K. Hashmi and G. J. Hutchings, Gold catalysis, *Angewandte Chemie International Edition*, 2006, **45**, 7896-7936.
120. T. Hayashi, K. Tanaka and M. Haruta, Selective vapor-phase epoxidation of propylene over Au/TiO₂ catalysts in the presence of oxygen and hydrogen, *Journal of Catalysis*, 1998, **178**, 566-575.
121. T. A. Nijhuis, M. Makkee, J. A. Moulijn and B. M. Weckhuysen, The production of propene oxide: catalytic processes and recent developments, *Industrial & Engineering Chemistry Research*, 2006, **45**, 3447-3459.
122. R. J. Davis, All that glitters is not Au⁰, *Science*, 2003, **301**, 926.
123. M. Comotti, C. Della Pina, R. Matarrese and M. Rossi, The catalytic activity of "naked" gold particles, *Angewandte Chemie International Edition*, 2004, **43**, 5812-5815.
124. G. Li, J. Edwards, A. F. Carley and G. J. Hutchings, Direct synthesis of hydrogen peroxide from H₂ and O₂ and in situ oxidation using zeolite-supported catalysts, *Catalysis Communications*, 2007, **8**, 247-250.
125. J. K. Edwards, A. Thomas, B. E. Solsona, P. Landon, A. F. Carley and G. J. Hutchings, Comparison of supports for the direct synthesis of hydrogen peroxide from H₂ and O₂ using Au–Pd catalysts, *Catalysis Today*, 2007, **122**, 397-402.
126. C. Della Pina, E. Falletta and M. Rossi, Highly selective oxidation of benzyl alcohol to benzaldehyde catalyzed by bimetallic gold–copper catalyst, *Journal of Catalysis*, 2008, **260**, 384-386.
127. S. Mandal, K. K. Bando, C. Santra, S. Maity, O. O. James, D. Mehta and B. Chowdhury, Sm-CeO₂ supported gold nanoparticle catalyst for benzyl alcohol oxidation using molecular O₂, *Applied Catalysis A: General*, 2013, **452**, 94-104.
128. F. Li, D. Hu, Y. Yuan, B. Luo, Y. Song, S. Xiao, G. Chen, Y. Fang and F. Lu, Zeolite Y encapsulated Cu (II) and Zn (II)-imidazole-salen catalysts for benzyl alcohol oxidation, *Molecular Catalysis*, 2018, **452**, 75-82.
129. V. R. Choudhary and D. K. Dumbre, Solvent-free selective oxidation of benzyl alcohol to benzaldehyde by tert-butyl hydroperoxide over U₃O₈-supported nano-gold catalysts, *Applied Catalysis A: General*, 2010, **375**, 252-257.
130. C. P. Ferraz, M. A. S. Garcia, É. Teixeira-Neto and L. M. Rossi, Oxidation of benzyl alcohol catalyzed by gold nanoparticles under alkaline conditions: weak vs. strong bases, *RSC Advances*, 2016, **6**, 25279-25285.
131. W. Guo, S. Niu, X. Ji, W. Yu, T.-W. Lin, Y. Wu, Y. Li and L. Shao, Doping carbon networks with phosphorus for supporting Pd in catalyzing selective oxidation of benzyl alcohol, *Journal of Nanoparticle Research*, 2018, **20**, 180.
132. V. V. Costa, M. Estrada, Y. Demidova, I. Prosvirin, V. Kriventsov, R. F. Cotta, S. Fuentes, A. Simakov and E. V. Gusevskaya, Gold nanoparticles supported on magnesium oxide as catalysts for the aerobic oxidation of alcohols under alkali-free conditions, *Journal of Catalysis*, 2012, **292**, 148-156.
133. T. Ishida, M. Nagaoka, T. Akita and M. Haruta, Deposition of gold clusters on porous coordination polymers by solid grinding and their catalytic activity in aerobic oxidation of alcohols, *Chemistry - A European Journal*, 2008, **14**, 8456-8460.

134. P. Sudarsanam, B. Mallesham, D. N. Durgasri and B. M. Reddy, Physicochemical and catalytic properties of nanosized Au/CeO₂ catalysts for eco-friendly oxidation of benzyl alcohol, *Journal of Industrial and Engineering Chemistry*, 2014, **20**, 3115-3121.
135. B. Qi, Y. Wang, L. Lou, Y. Yang and S. Liu, Solvent-free aerobic oxidation of benzyl alcohol over palladium catalysts supported on MnO_x prepared using an adsorption method, *Reaction Kinetics, Mechanisms and Catalysis*, 2013, **108**, 519-529.
136. G. Nagy, A. Beck, G. Sáfrán, Z. Schay, S. Liu, T. Li, B. Qiao, J. Wang and K. Lázár, Nanodisperse gold catalysts in oxidation of benzyl alcohol: comparison of various supports under different conditions, *Reaction Kinetics, Mechanisms and Catalysis*, 2019, **128**, 71-95.
137. T. Sato and T. Komanoya, Selective oxidation of alcohols with molecular oxygen catalyzed by Ru/MnO_x/CeO₂ under mild conditions, *Catalysis Communications*, 2009, **10**, 1095-1098.
138. M. J. Kim, Y. E. Jung, C. Y. Lee and J. Kim, HKUST-1/ABNO-catalyzed aerobic oxidation of secondary benzyl alcohols at room temperature, *Tetrahedron Letters*, 2018, **59**, 2722-2725.
139. S. Schünemann, M. v. Gastel and H. Tüysüz, A CsPbBr₃/TiO₂ composite for visible-light-driven photocatalytic benzyl alcohol oxidation, *ChemSusChem*, 2018, **11**, 2057-2061.
140. F. Mangin, P. Prinsen, A. Yopez, M. R. H. S. Gilani, G. Xu, C. Len and R. Luque, Microwave assisted benzyl alcohol oxidation using iron particles on furfuryl alcohol derived supports, *Catalysis Communications*, 2018, **104**, 67-70.
141. N. Mahamuni, P. Gogate and A. Pandit, Ultrasonic synthesis of benzaldehyde from benzyl alcohol using H₂O₂: role of ultrasound, *Industrial & Engineering Chemistry Research*, 2006, **45**, 98-108.
142. J. C. F. Rodríguez-Reyes, C. M. Friend and R. J. Madix, Origin of the selectivity in the gold-mediated oxidation of benzyl alcohol, *Surface Science*, 2012, **606**, 1129-1134.
143. E. Skupien, R. J. Berger, V. Santos, J. Gascon, M. Makkee, M. Kreutzer, P. Kooyman, J. A. Moulijn and F. Kapteijn, Inhibition of a gold-based catalyst in benzyl alcohol oxidation: Understanding and Remediation, *Catalysts*, 2014, **4**, 89-115.
144. H. Schiff, Mittheilungen aus dem Universitätslaboratorium in Pisa: Eine neue Reihe organischer Basen, *Justus Liebigs Annalen der Chemie*, 1864, **131**, 118-119.
145. C. M. da Silva, D. L. da Silva, L. V. Modolo, R. B. Alves, M. A. de Resende, C. V. B. Martins and Â. de Fátima, Schiff bases: A short review of their antimicrobial activities, *Journal of Advanced Research*, 2011, **2**, 1-8.
146. L. Blackburn and R. J. K. Taylor, In situ oxidation–imine formation–reduction routes from alcohols to amines, *Organic Letters*, 2001, **3**, 1637-1639.
147. R. Hernández-Molina and A. Mederos, *Comprehensive coordination chemistry II*, Chapter 1.19, Pergamon, Oxford, 2003, 411-446.
148. H. Nozaki, H. Takaya, S. Moriuti and R. Noyori, Homogeneous catalysis in the decomposition of diazo compounds by copper chelates: Asymmetric carbenoid reactions, *Tetrahedron*, 1968, **24**, 3655-3669.

149. G. C. Look, M. M. Murphy, D. A. Campbell and M. A. Gallop, Trimethylorthoformate: A mild and effective dehydrating reagent for solution and solid phase imine formation, *Tetrahedron Letters*, 1995, **36**, 2937-2940.
150. B. M. Stoltz, *Organic Syntheses*, **95**, J. Wiley and Sons, 2019.
151. F. Texier-Boullet, A simple, convenient and mild synthesis of imines on alumina surface without solvent, *Synthesis*, 1985, **1985**, 679-681.
152. A. K. Chakraborti, S. Bhagat and S. Rudrawar, Magnesium perchlorate as an efficient catalyst for the synthesis of imines and phenylhydrazones, *Tetrahedron Letters*, 2004, **45**, 7641-7644.
153. B. Chen, L. Wang and S. Gao, Recent advances in aerobic oxidation of alcohols and amines to imines, *ACS Catalysis*, 2015, **5**, 5851-5876.
154. P. K. Khatri, S. L. Jain, L. N. Sivakumar K and B. Sain, Polyethylene glycol clicked Co(II) Schiff base and its catalytic activity for the oxidative dehydrogenation of secondary amines, *Organic & Biomolecular Chemistry*, 2011, **9**, 3370-3374.
155. B. Zhu and R. J. Angelici, Non-nanogold catalyzed aerobic oxidation of secondary amines to imines, *Chemical Communications*, 2007, 2157-2159.
156. R. D. Patil and S. Adimurthy, Catalytic methods for imine synthesis, *Asian Journal of Organic Chemistry*, 2013, **2**, 726-744.
157. A. J. Bailey and B. R. James, Catalysed aerobic dehydrogenation of amines and an X-ray crystal structure of a bis(benzylamine) ruthenium(II) porphyrin species, *Chemical Communications*, 1996, 2343-2344.
158. P. A. Ganeshpure, A. Sudalai and S. Satish, Oxidation of primary amines with dioxygen catalysed by an oxygen carrier cobalt(II) Schiff base chelate, *Proceedings of the Indian Academy of Sciences - Chemical Sciences*, 1991, **103**, 741-745.
159. K. D. Karlin and Z. Tyeklar, *Bioinorganic chemistry of copper*, Springer Netherlands, 2012.
160. S. Kodama, J. Yoshida, A. Nomoto, Y. Ueta, S. Yano, M. Ueshima and A. Ogawa, Direct conversion of benzylamines to imines via atmospheric oxidation in the presence of VO(Hhpic)₂ catalyst, *Tetrahedron Letters*, 2010, **51**, 2450-2452.
161. B. Zhu, M. Lazar, B. G. Trewyn and R. J. Angelici, Aerobic oxidation of amines to imines catalyzed by bulk gold powder and by alumina-supported gold, *Journal of Catalysis*, 2008, **260**, 1-6.
162. T. Ishida, N. Kawakita, T. Akita and M. Haruta, One-pot N-alkylation of primary amines to secondary amines by gold clusters supported on porous coordination polymers, *Gold Bulletin*, 2009, **42**, 267-274.
163. L. Liu, S. Zhang, X. Fu and C.-H. Yan, Metal-free aerobic oxidative coupling of amines to imines, *Chemical Communications*, 2011, **47**, 10148-10150.
164. A. Grirrane, A. Corma and H. Garcia, Highly active and selective gold catalysts for the aerobic oxidative condensation of benzylamines to imines and one-pot, two-step synthesis of secondary benzylamines, *Journal of Catalysis*, 2009, **264**, 138-144.
165. S. Kamiguchi, A. Nakamura, A. Suzuki, M. Kodomari, M. Nomura, Y. Iwasawa and T. Chihara, Catalytic dehydrogenation of aliphatic amines to nitriles, imines, or vinylamines and dealkylation of tertiary aliphatic amines over halide cluster catalysts of group 5 and 6 transition metals, *Journal of Catalysis*, 2005, **230**, 204-213.

166. M. T. Schümperli, C. Hammond and I. Hermans, Developments in the aerobic oxidation of amines, *ACS Catalysis*, 2012, **2**, 1108-1117.
167. R. W. Layer, The chemistry of imines, *Chemical Reviews*, 1963, **63**, 489-510.
168. J. He, K. Yamaguchi and N. Mizuno, Selective synthesis of secondary amines via N-alkylation of primary amines and ammonia with alcohols by supported copper hydroxide catalysts, *Chemistry Letters*, 2010, **39**, 1182-1183.
169. S. Bähn, S. Imm, L. Neubert, M. Zhang, H. Neumann and M. Beller, The catalytic amination of alcohols, *ChemCatChem*, 2011, **3**, 1853-1864.
170. S. Sithambaram, R. Kumar, Y.-C. Son and S. L. Suib, Tandem catalysis: Direct catalytic synthesis of imines from alcohols using manganese octahedral molecular sieves, *Journal of Catalysis*, 2008, **253**, 269-277.
171. M. S. Kwon, S. Kim, S. Park, W. Bosco, R. K. Chidrala and J. Park, One-Pot synthesis of imines and secondary amines by Pd-catalyzed coupling of benzyl alcohols and primary amines, *The Journal of Organic Chemistry*, 2009, **74**, 2877-2879.
172. Q. Kang and Y. Zhang, Copper-catalyzed highly efficient aerobic oxidative synthesis of imines from alcohols and amines, *Green Chemistry*, 2012, **14**, 1016-1019.
173. S. Kegnæs, J. Mielby, U. V. Mentzel, C. H. Christensen and A. Riisager, Formation of imines by selective gold-catalysed aerobic oxidative coupling of alcohols and amines under ambient conditions, *Green Chemistry*, 2010, **12**, 1437-1441.
174. H. Sun, F.-Z. Su, J. Ni, Y. Cao, H.-Y. He and K.-N. Fan, Gold supported on hydroxyapatite as a versatile multifunctional catalyst for the direct tandem synthesis of imines and oximes, *Angewandte Chemie International Edition*, 2009, **48**, 4390-4393.
175. M. Li, F. Cárdenas-Lizana and M. A. Keane, Combined catalytic action of supported Cu and Au in imine production from coupled benzyl alcohol and nitrobenzene reactions, *Applied Catalysis A: General*, 2018, **557**, 145-153.
176. Y. Shiraishi, M. Ikeda, D. Tsukamoto, S. Tanaka and T. Hirai, One-pot synthesis of imines from alcohols and amines with TiO₂ loading Pt nanoparticles under UV irradiation, *Chemical Communications*, 2011, **47**, 4811-4813.

Chapter 2

Characterisation, Synthesis Methods, and Experimental Design



Au@MgO/SBA-15 mesoporous materials heat-treated between 100-800 °C

2.1 Chemical Table

The list of chemicals used for the catalyst synthesis, the characterisation and the reaction tests are summarised in **Table 2.1**.

Table 2.1. List of Chemicals for synthesis, characterisation and screening of catalysts.

	Chemical	Supplier	Purity
MATERIAL SYNTHESIS	Fumed SiO ₂	Sigma-Aldrich	99.8 %
	Gold (III) chloride trihydrate (HAuCl ₄ .3H ₂ O)	Alfa Aesar	99.99 %
	Hydrochloric acid (HCl)	VWR Chemicals	37 %
	Magnesium Nitrate Hexahydrate (Mg(NO ₃) ₂ .6H ₂ O)	Sigma-Aldrich	99 %
	Nano CaO	Sigma-Aldrich	98 %
	Nano MgO	Sigma-Aldrich	99 %
	Pluronic P123	Sigma-Aldrich	5800 g mol ⁻¹
	Potassium persulfate (K ₂ (SO ₄) ₂)	Sigma-Aldrich	99 %
	Sodium carbonate (Na ₂ CO ₃)	Sigma-Aldrich	99 %
	Sodium Hydroxide (NaOH)	Sigma-Aldrich	98 %
	Styrene	Sigma-Aldrich	99 %
	Tetraethoxysilane (TEOS)	Sigma-Aldrich	98 %
Tetramethoxysilane (TMOS)	Sigma-Aldrich	98 %	
CHARACT.	Ammonium Fluoride (NH ₄ F)	Sigma-Aldrich	98 %
	Boric Acid (H ₃ BO ₃)	Fluka	4 %
	Hydrochloric Acid (HCl)	Fisher	37 %
	Nitric Acid (HNO ₃)	VWR Chemicals	68 %
	Sulfuric Acid (H ₂ SO ₄)	Fisher	95 %
CATALYTIC TESTS	Anisole	Sigma-Aldrich	99 %
	Benzyl Alcohol	Sigma-Aldrich	99.8 %
	Benzyl Amine	Sigma-Aldrich	99.5 %
	Dihexyl ether	Sigma-Aldrich	97 %
	Methanol	VWR Chemicals	100 %
	Toluene	VWR Chemicals	100 %
	Tributyrin	Sigma-Aldrich	97 %
	Tricaprylin	Sigma-Aldrich	99 %
	Trilaurin	Alfa Aesar	95 %

2.2 Material Synthesis

The synthesis of various materials was performed with two processes to ensure reproducibility. Firstly, the synthesis methods used were taken from literature sources, and performed to the same standard and instruction. Secondly, the materials were repeatedly produced and characterised to ensure repeatability.

2.2.1 Typical preparation of MgO supported on Ordered Mesoporous SBA-15 using cooperative self-assembly (CSA)

Magnesium supported on SBA-15 using cooperative self-assembly (CSA) was synthesised using a similar method to Zhao *et al.*¹ The templating agent, Pluronic 123 (2.61 g) was combined with H₂O (82.3 ml) and HCl (15.4 ml), along with varying amounts of magnesium nitrate hexahydrate (Mg(NO₃)₂·6H₂O (0-2g). Tetraethyl orthosilicate (5.5 ml) (TEOS) was added to the mixture, which was stirred at 35 °C for 24 hours. The solution was then aged at 80 °C for a further 24 hours without agitation. The solution was filtered and washed with water (100 ml), then the resulting solid was calcined at 550 °C for 5 hours in the air (ramp rate 3 °C min⁻¹).

2.2.2 Typical preparation of MgO supported on Ordered Mesoporous SBA-15 using true liquid crystal templating (TLCT)

Magnesium supported on TLCT SBA-15 was synthesised using the liquid crystal templating method developed by Attard *et al.*² Pluronic P123 (2.00 g) was combined with H₂O (2.00 g) brought to pH 2 using HCl (37 %). Different amounts of magnesium nitrate hexahydrate were added to the mixture (0-2g), and subsequently, the mixture was agitated using a sonicating bath at 40 °C until a uniform gel was formed, whereupon tetramethyl orthosilicate (4.1 ml) (TMOS) was added. The uniform gel was aged at 40 °C under light vacuum (100 mbar) for 24 hours. The resulting solid was calcined at 550 °C for 5 hours in the air (ramp rate 3 °C min⁻¹).

2.2.3 Preparation of Polystyrene Nanosphere Hard Template:

Polystyrene colloidal nanospheres were synthesised using the method of Sen *et al.*³ Styrene (100 ml) was washed to remove the polymerisation inhibitor, using 0.1 M NaOH solution (5 x 100 ml) and further washing using H₂O (5 x 100 ml). Washed styrene was added to degassed water (1000 ml) and stirred at 300 RPM under nitrogen at 80 °C for 1 hour. Degassed potassium persulfate solution (K₂(SO₄)₂) (50 ml, 0.025 M) was added dropwise over 15 minutes. The mixture was then stirred at 300 RPM under N₂ overnight

at 80 °C. Polystyrene nanospheres were isolated via centrifugation at 10000 rpm for 15 minutes and dried at room temperature.

2.2.4 Typical Preparation of Ordered Hierarchical MgO/SBA-15 using true liquid crystal template (TLCT):

Magnesium supported on meso-macroporous SBA-15 was synthesised using a modified method to TLCT MgO/SBA-15, first used by Dhainaut et al.⁴ Hierarchical materials were synthesised using the same method as mesoporous SBA-15, where Polystyrene Colloidal Nanospheres (6.00 g) were incorporated into the mixture after addition of TMOS. This mixture was mixed until uniform, then aged at 40 °C under light vacuum (100 mbar) for 24 hours. The resulting solid was calcined at 550 °C for 5 hours in the air (ramp rate 3 °C min⁻¹).

2.2.5 Gold functionalisation of MgO/SBA-15 using double impregnation method (DIM)

Magnesium oxide functionalised SBA-15 and hierarchical SBA-15 support materials were impregnated with an aqueous solution of the gold precursor using an incipient wetness technique.^{5, 6} A gold (III) chloride trihydrate precursor (HAuCl₄·(3H₂O)) was added to the support in an aqueous solution (achieving a pH of approximately 6) with a volume half of that of the pore volume of the support, determined by nitrogen porosimetry. The mixture was stirred under sonication for 10 minutes to ensure uniform dispersion throughout the material. A 1 M solution of Na₂CO₃ was then added, with a volume of half of the pore volume, to ensure the minimum volume of impregnating solution possible. After subsequent stirring under sonication for 10 minutes, the impregnated supported was aged at room temperature for 24 hours, washed with 5 x 100 ml 0.14 M Na₂CO₃, followed by 5 x 100 ml H₂O and dried at 60 °C for two hours. Materials were subsequently heated under air to different temperatures using a 10 °C min⁻¹ ramp rate and held at the final temperature for 2 hours.

2.2.6 Gold functionalisation of MgO/SBA-15 using deposition precipitation (DP) method

An aqueous 100 ml gold (III) chloride trihydrate precursor (HAuCl₄·(3H₂O)) solution was brought to pH 9 using a 0.1 M NaOH solution, after which the support (2 g) was added and stirred for 1 hour, then subsequently aged for 12 at room temperature and pressure.^{5, 7} The resultant precipitate was filtered off and washed with 5 x 100 ml H₂O, followed by drying overnight at 110 °C. Materials were subsequently heated under air

to different temperatures using a $10\text{ }^{\circ}\text{C min}^{-1}$ ramp rate and held at the final temperature for 2 hours.

2.2.7 Gold functionalisation of MgO/SBA-15 using liquid phase deposition precipitation (LPRD) method

An aqueous (10 ml) gold (III) chloride trihydrate precursor ($\text{HAuCl}_4 \cdot (3\text{H}_2\text{O})$) solution was brought to pH 6 using a 0.02 M NaOH solution and aged in darkness for 24 hours with no agitation to complete the hydroxylation of Au^{3+} ions.^{5, 8} Support (2 g) was added, dispersed using an ultrasonic bath for 30 min, and subsequently aged at $100\text{ }^{\circ}\text{C}$ overnight. The solid was filtered, washed with $5 \times 100\text{ ml H}_2\text{O}$, and dried in the oven overnight at $110\text{ }^{\circ}\text{C}$. Materials were subsequently heated under air to different temperatures using a $10\text{ }^{\circ}\text{C min}^{-1}$ ramp rate and held at the final temperature for 2 hours.

2.2.8 Gold functionalisation of bulk materials using double impregnation method (DIM)

The bulk support material was impregnated with an aqueous solution of the gold precursor using the same methodology as the double impregnation technique previously described in section 2.2.5.

2.3 Material Characterisation

The materials were characterised by low and wide-angle X-Ray Diffraction (XRD), Inductively Coupled Plasma – Optical Emission Spectroscopy (ICP-OES), Nitrogen Porosimetry, Scanning Electron Microscopy (SEM), Scanning Transmission Electron Microscopy (STEM), X-Ray Photoelectric Spectroscopy (XPS), CO₂ Chemisorption-Mass Spectrometry and Temperature Programmed Desorption (CO₂ TPD).

2.3.1 X-Ray Diffraction (XRD)

X-ray diffraction is non-destructive, often used before other time-consuming analytical methods as a preliminary technique.⁹ This qualitative technique is extremely useful in determining the identity of different crystal phases in material, however, it can also be used to determine the size of nanoparticles.

A cathode ray filament is heated to produce electrons which are accelerated by an applied voltage to bombard a monochromatic Si (111) wafer, causing excitation of its inner shell electrons. The resultant X-rays produced when the Si inner electrons are dislodged contain multiple components, most commonly K α and K β . The X-rays are filtered through a nickel filter to give Cu K α (1.54 Å) wavelength X-rays, bombarding the homogeneously mixed sample causing diffraction. This diffracted electromagnetic radiation, depending on the incident beam angle, has been constructively or destructively interfered with, characteristic to specific crystal structures. The angle of the incident beam is rotated, causing the X-rays to diffract off different crystal planes within the material, causing different X-ray intensities which are recorded. This scattering process is elastic, meaning the wavelength of the X-rays is maintained. As a result, constructive interference can be understood by Bragg's Law,¹⁰ seen below as **Equation 2.1** and **Figure 2.1**.

$$n\lambda = 2d\sin\theta$$

Equation 2.1. Braggs law, where λ = wavelength of the X-ray. n = multiplication integer (order of reflection). d = interplanar distance. θ = diffraction angle at which the peak is associated.

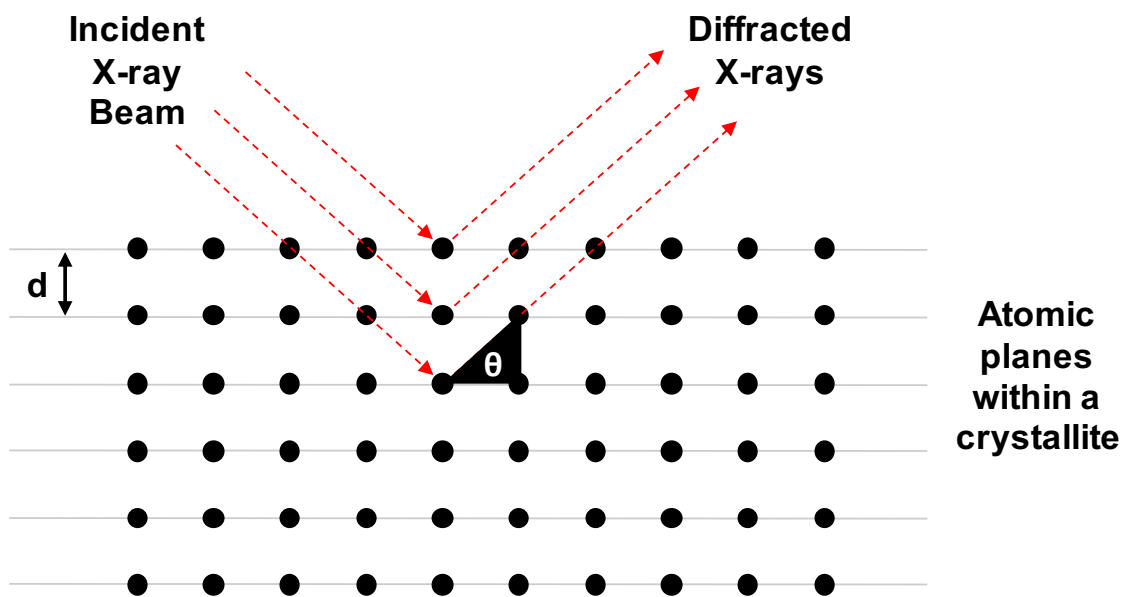


Figure 2.1. Illustration of Bragg's law.

The Scherrer equation¹¹ presented in **Equation 2.2** was used to estimate the average crystallite size of nanoparticles, utilising the inversely proportional relationship between crystallite size and peak broadening. By measuring the broadening of the peak at half the maximum intensity of the peak, the average crystallite size can be calculated. Particle size can only be calculated between 2.5-100 nm for a Cu K α X-ray source, as outside these parameters is outside the detection limit.¹¹ This can be problematic for characterising nanoparticle crystalline phases below this limit or to estimate the true particle size distribution if the material has different population of particles outside the XRD detection range.

$$\tau = \frac{K \cdot \lambda}{\beta \cdot \cos(\theta)}$$

Equation 2.2. Scherrer equation, where τ = mean size of the ordered crystalline domains. K = dimensionless shape factor, with a value close to unity. Typically, a value of 0.9 represents spherical particles. λ = X-ray wavelength β = line broadening at half the maximum intensity, FWHM. θ = Bragg angle (in radians).

X-ray diffractometry can also be used to investigate the long-range ordered porosity characteristic of surfactant templated mesoporous silica. At low 2θ angles, the X-rays diffract off the hexagonally ordered mesoporous channels, displayed in **Figure 2.2**, giving rise to the characteristic 10, 11 and 20 reflections. Low-angle reflections were adjusted using the method developed by Zhao et al,^{1, 12} where the 10 reflection distance was multiplied by $(2/\sqrt{3})$ due to the hexagonal pore arrangement.

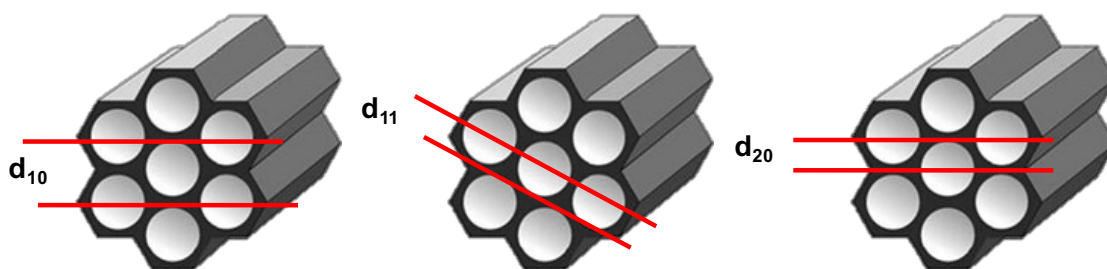


Figure 2.2. Low-angle X-rays diffracting off long-range ordered mesoporous silica.

X-ray diffraction patterns were recorded using a Bruker D8 diffractometer employing a Cu K α (1.54 Å) source fitted with a Lynx eye high-speed strip detector. Low-angle patterns were analysed using a variable knife-edge and crystallite phase was assigned using Reitveld refinement.

2.3.2 Inductively Coupled Plasma–Optical Emission Spectroscopy (ICP-OES)

This is a destructive analytical technique used to detect and quantify trace metals present in materials.¹³ Solid and liquid samples are digested using an acidic solution, before dilution and passing through a nebuliser (**Figure 2.3**). This causes the diluted sample solution to aerosolise into the spray chamber, which is then fed through a plasma flame. The process of ionisation from the plasma emits visible light that is characteristic to its parent element and is quantified using optical emission spectroscopy. The intensity of the optical radiation is used to quantify the concentration of an element when referenced to a calibration curve.

Optical emission spectroscopy was performed using a Thermo iCAP 7000 calibrated against a series of standards between 1 and 100 ppm. Samples (~10 mg) were digested using either hydrofluoric acid – a mixture of ammonium fluoride (100 mg), sulfuric acid (2 cm³), water (2 cm³) and nitric acid (5 cm³) prior to fluoride neutralisation with boric acid (3% solution, 1 cm³) – or Aqua regia – sulfuric acid (2 cm³, Fisher) hydrochloric acid (1 cm³), water (2 cm³) and nitric acid (5 cm³). Acid digestion mixtures were diluted 10% prior to analysis and measurements were repeated 3 times against at least 3 distinct wavelengths per element.

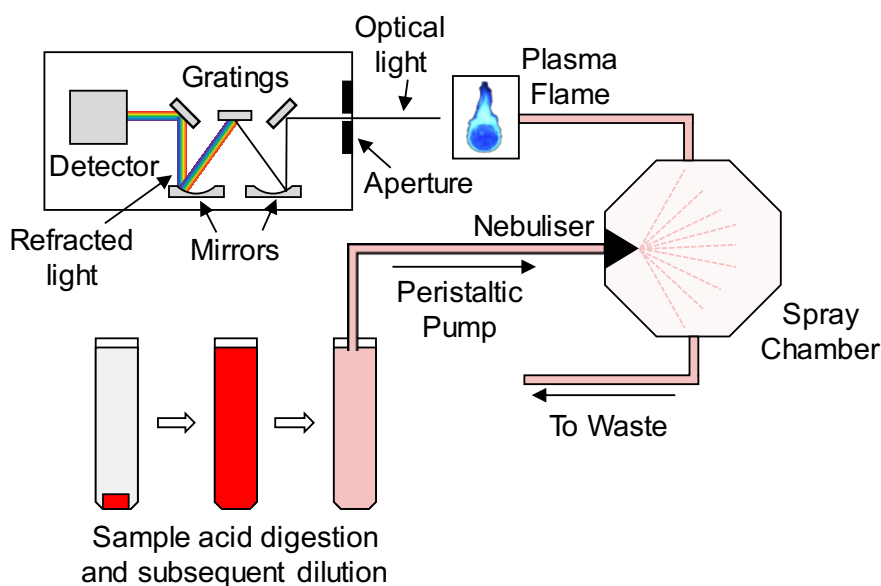


Figure 2.3. Typical ICP-OES schematic showing the process of the sample solution reaching the plasma torch and passing through the optical spectrometer. Redrawn from reference.¹⁴

2.3.3 Nitrogen Porosimetry

Nitrogen porosimetry is an extremely useful non-destructive technique used to determine physical properties and structural characteristics of materials.¹⁵⁻¹⁷ Material properties are determined by the deposition and removal of nitrogen at known pressures. Nitrogen is added incrementally to the void above the sample, with the amount of N_2 absorbed being measured at specific pressures. A vacuum is applied in stages, to cause the nitrogen to desorb from the surface, which is also quantified. Nitrogen and argon are commonly employed, although carbon monoxide and hydrogen can also be used. This technique relies on the Langmuir adsorption model, which follows a series of assumptions for the adsorbing of a gas onto a surface in an ideal system. The adsorption/desorption behaviour results in an isotherm, of which there are six types,^{18, 19} as seen in **Figure 2.4**, which are characteristic to the specific porous nature of the material.

- The first isotherm, Type I, is seen by microporous materials with strong interactions between adsorbent and adsorbate, such as zeolites.
- Type II isotherms are typically materials lacking porosity and having weak interactions with the adsorbate.
- Type III isotherms are very rare, having a weak interaction with the adsorbate.
- Type IV isotherms are characteristic of SBA-15 and other ordered mesoporous solids. They exhibit a hysteresis of the adsorption/desorption curve, which is

observed due to nitrogen bound in the mesopores being trapped by the nitrogen adsorbed at the pore entrance.

- Type V isotherms are often from mesoporous or macroporous solids with weak interactions.
- Type VI isotherms are characteristic of well-defined uniform non-porous solids.

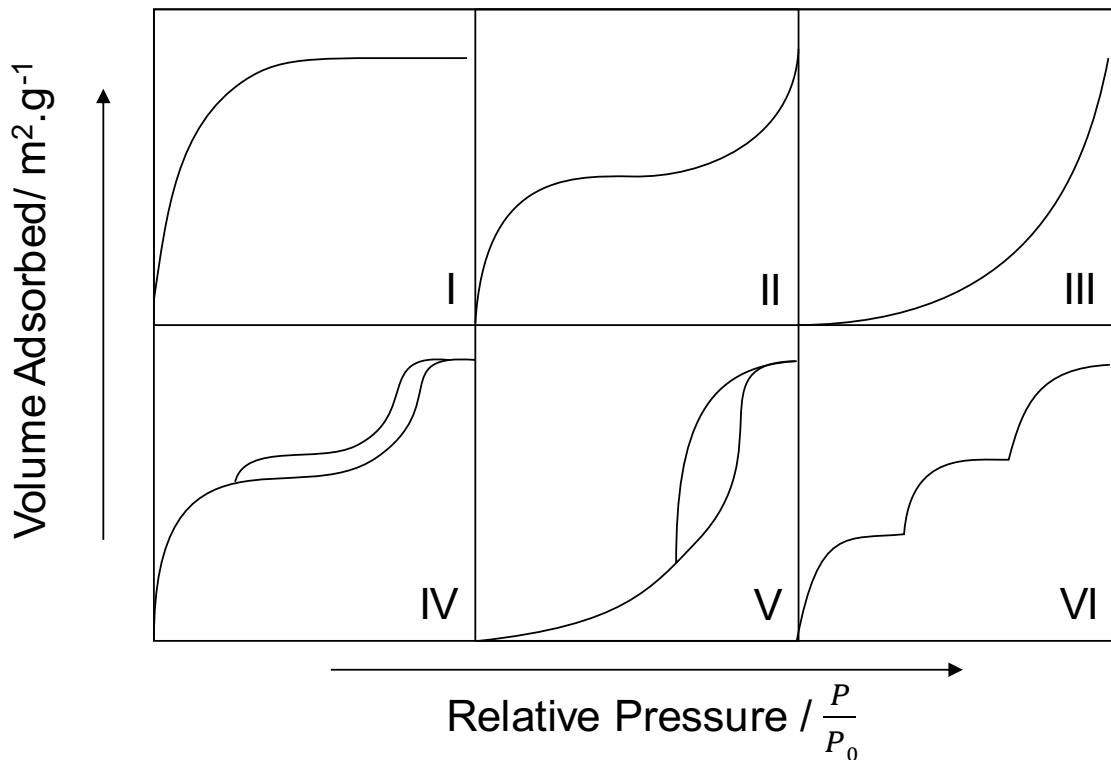


Figure 2.4. The six adsorption/desorption isotherms exhibited by porous materials as defined by IUPAC.

The hysteresis curves exhibited by the type IV isotherms are caused by the different rates of adsorption and desorption of the nitrogen.²⁰ This is caused by faster access to the entire pore during adsorption and reduced access during desorption illustrated in **Figure 2.5.**

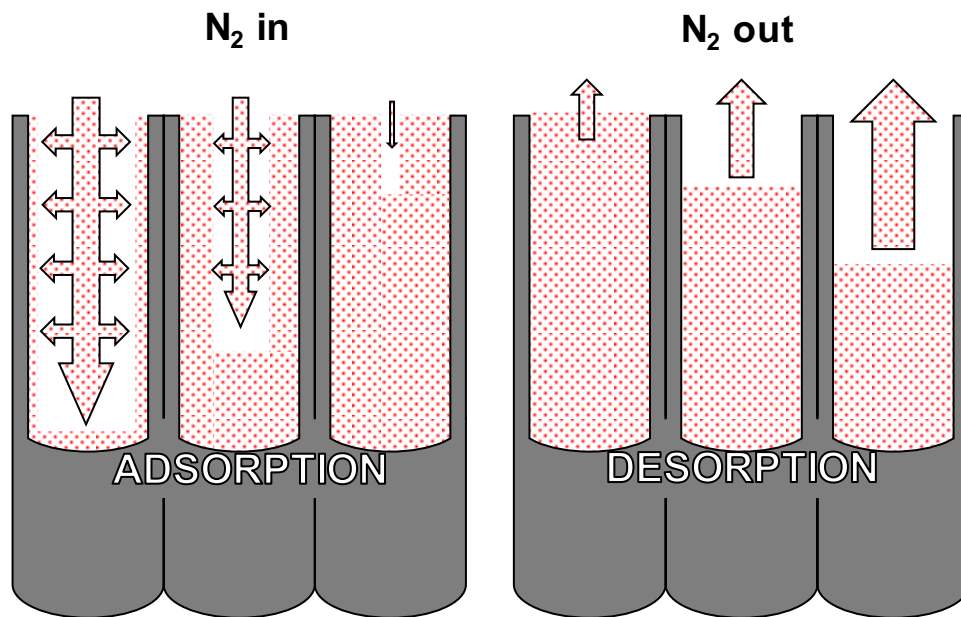


Figure 2.5. Nitrogen adsorption and desorption in a mesoporous material.

The hysteresis curve exhibited by type IV isotherm materials is heavily dependent on the uniformity of the pore network. Long-range ordered mesopores desorb at a very steady rate throughout the material due to its long honeycomb-like structured pores being similar in size and uniform throughout. This results in an H1 hysteresis curve which mirrors the adsorption curve, with longer desorption taking place because of the effect shown in **Figure 2.5**. Mesoporous materials with less uniformity in pore size or orientation have longer desorption, due to the inefficiencies removing the nitrogen, resulting in an H2 curve. Experimentally determined hysteresis profiles are displayed in **Figure 2.6** to illustrate the difference.

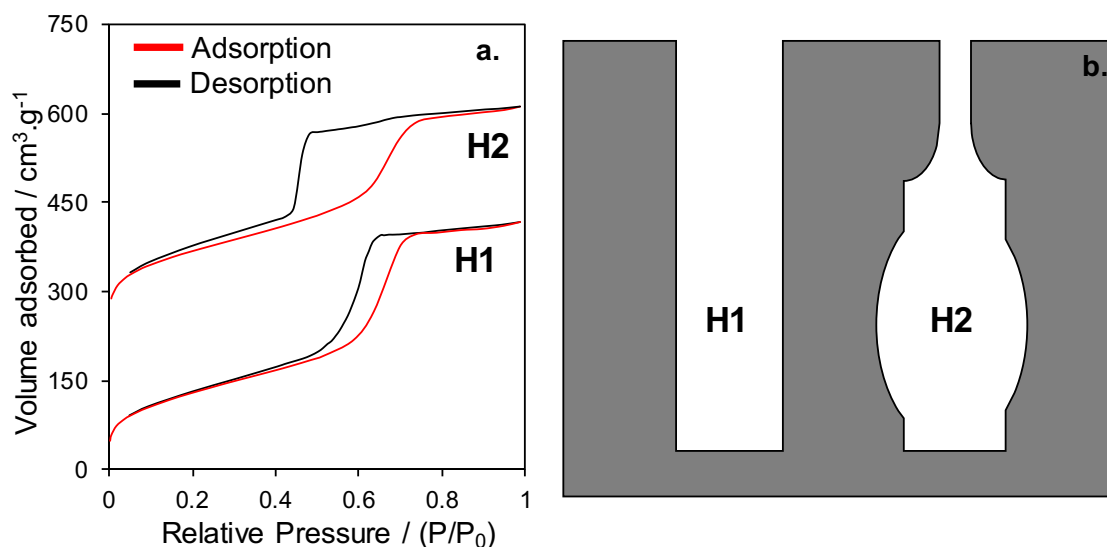


Figure 2.6. Nitrogen Porosimetry isotherm for SBA-15 type materials, showing (a) type IV isotherms with H1 and H2 hysteresis curves. An example structure of the pore networks that result in both hysteresis in also (b) illustrated.

The surface area is calculated using the Brunauer-Emmet-Teller (BET) equation,¹⁰ shown in (**Figure 2.7**), and is conducted at a constant temperature of 77.5 K. This equation is an expansion of the Langmuir equation and follows a series of assumptions;

1. Adsorbing gas molecules adsorb in layers infinitely
2. The adsorbent molecule only interacts with adjacent layers
3. The Langmuir theory can be applied to each layer
4. The enthalpy of adsorption for the first layer is constant and larger than subsequent layers.
5. The enthalpy of adsorption for the second and subsequent layers is the same as the enthalpy of liquefaction.

By plotting the relative pressure against the left-hand side of the equation (both of which are gathered experimentally during N₂ porosimetry), the slope and intercept can be calculated, giving information on the material physical properties.

$$\frac{1}{v \left[\left(\frac{P_0}{P} \right) - 1 \right]} = \frac{C - 1}{V_m \times C} \times \frac{P}{P_0} \times \frac{1}{V_m \times C}$$

BET Equation: Where P and P₀ are the equilibrium and the saturation pressure of adsorbates at the temperature of adsorption, v is the adsorbed gas quantity, and V_m is the monolayer adsorbed gas quantity c is the BET constant.

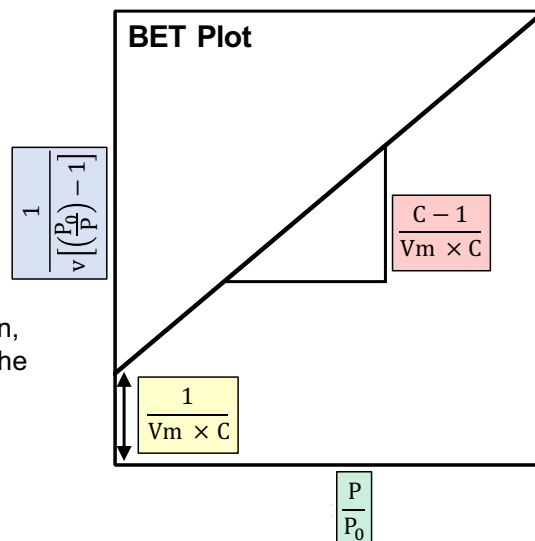


Figure 2.7. BET equation and plot.¹⁰

Nitrogen Adsorption analysis was undertaken using a Quantachrome Nova 1200 porosimeter. Samples were degassed at 120 °C for 2 h, prior to analysis. BET surface areas were calculated over the relative pressure range 0.01–0.2 (p/p₀), while pore size distributions were calculated using the Barrett–Joyner–Halenda (BJH) method applied to the desorption branch of the isotherm.

2.3.4 Scanning Electron Microscope – Energy Dispersive X-ray Analysis

Scanning electron microscopy (SEM) has many uses in biological and materials science, however for this work we used it to determine macropore structure and elemental analysis, with a schematic displayed in **Figure 2.8**.²¹ SEM uses a cathode filament to produce an electron beam, which is passed through a positively charged anode, followed by lenses and scan coils to focus and direct the electron beam respectively. In a process similar to X-ray photoelectron spectroscopy (**Section 2.3.6**), the electron beam strikes the sample expelling what is known as a secondary electron from the sample atom inner shell. This is identified and quantified using a positively charge secondary electron detector, with the number of electrons detected related to the shading of the specific pixel on the display. In a route similar to the relaxation process in Auger electron spectroscopy, the partially vacant inner shell is filled with an outer shell electron. This releases an X-ray photon with an energy characteristic to the sample atom element, which is detected in a process known as energy dispersive X-ray analysis (EDX). This second void is filled by a free electron, releasing more distinguishing photons. After the 'pixel' has been recorded, the scan coils move the beam to the next spot and the process

is repeated, resulting in an image of electron density, and an elemental map of the area. By utilising both of these techniques a coloured image of the material surface is calculated, with each colour representing different atoms.

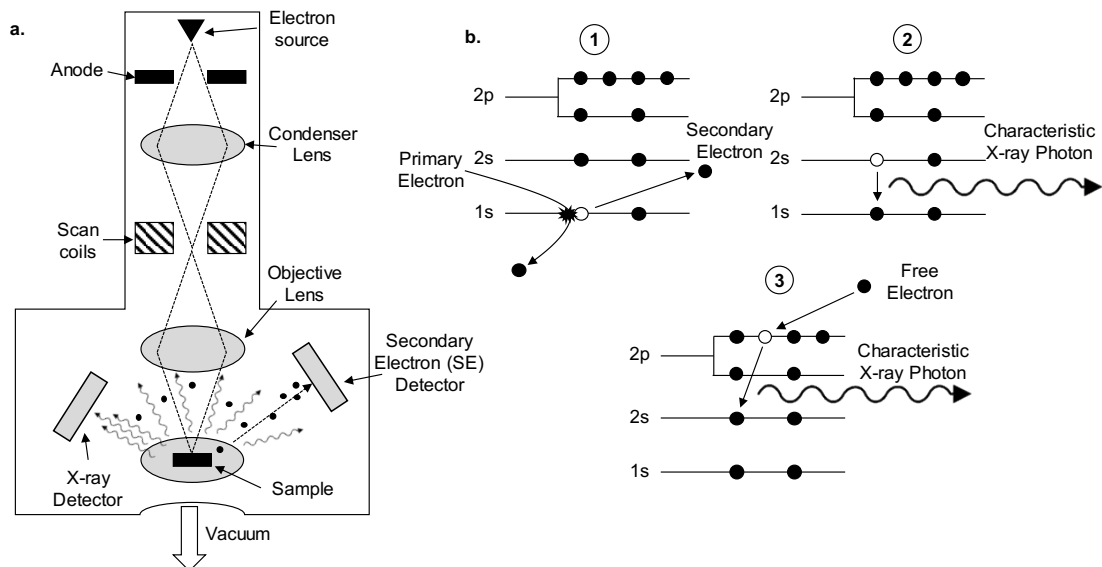


Figure 2.8. (a) SEM diagram and (b) electron shell interactions during SEM-EDX analysis. Redrawn from reference.²²

Scanning electron microscopy (SEM) images were recorded on a JSM-7800F Prime Field Emission Scanning Electron Microscope.

2.3.5 Scanning Transmission Electron Microscopy (STEM)

There are many types of transmission electron microscopy (TEM), including conventional, diffraction and spectroscopy, however, in this work, we utilise a scanning transmission electron microscope (STEM).²³ This is very similar to conventional transmission electron microscopy (CTEM), however, STEM focuses the electron beam into a fine point which is used to scan the sample, utilising scan coils also in SEM (**Section 2.3.4**). This allows for other techniques to be performed, such as Z-contrast annular dark-field imaging, and spectroscopic mapping by energy-dispersive X-ray (EDX) spectroscopy. This technique has a large array of uses, however, the applications for this work are imaging the pore size, structure and thickness, as well as particle size/shape and elemental characterisation.

Figure 2.9 is split into three stages;²⁴ firstly an electron beam is fired through a series of lenses followed by an aberration corrector,²⁵ which corrects the rays to focus on a singular point. The corrected electron beam then enters stage two, passing firstly through the sample followed by a second set of lenses. After this, the beam hits a series of detectors, including the bright field and high angle detector. The beam then enters the

third stage, is curved by a prism and detected using an electron energy loss spectrometer, which quantifies the energy loss and scattering angle. TEM differs from SEM, as it studies the transmitted beam through the sample, whereas SEM detects the secondary electrons. This is also used in TEM, however for darkfield analysis.

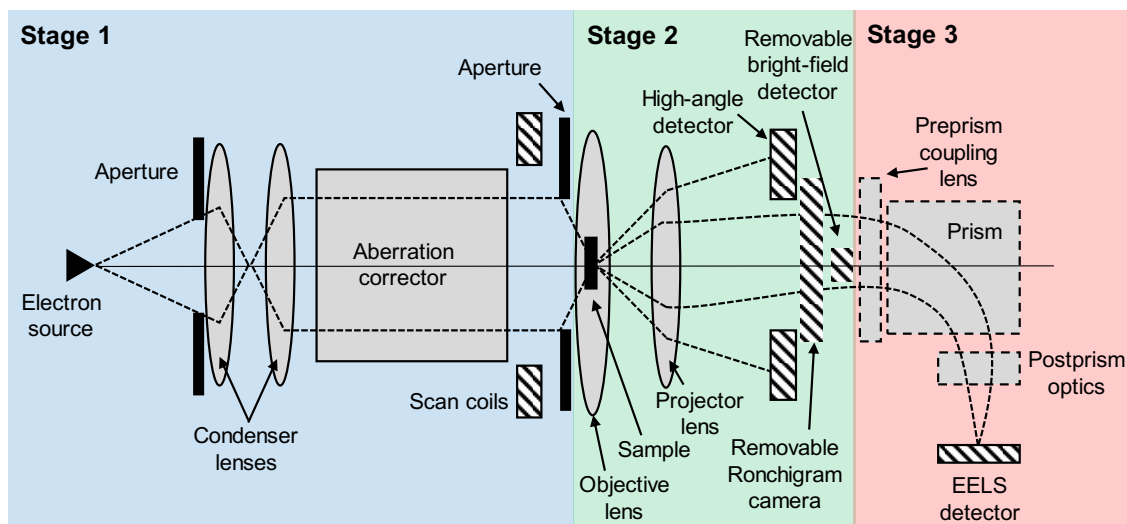


Figure 2.9. Basic schematic for a scanning transmission electron microscope (STEM). Redrawn from reference.²⁴

High-resolution scanning transmission electron microscopy (STEM) images were recorded on a JEOL 2100F FEG STEM operating at 200 keV and equipped with a spherical aberration probe corrector (CEOS GmbH) and a Bruker XFlash 5030 EDX. Samples were prepared for microscopy by dispersion in methanol and drop-casting onto a copper grid coated with a holey carbon support film (Agar Scientific). Images were analysed using ImageJ 1.41 software.

2.3.6 X-Ray Photoelectron Spectroscopy (XPS)

X-ray photoelectron spectroscopy is a non-destructive technique used to probe the chemical and physical interactions and states on the material surface from 1 to 10 nm.²⁶ Specific methodology can be used to examine different depths, however in this work we employed a basic methodology. Due to the material surface playing a crucial role in heterogeneous catalysis, this technique is vital to understanding the surface environment and how it interacts catalytically.

An X-ray source is excited, with the resultant X-ray beam directed to the material surface. This X-ray is absorbed by surface atoms, exciting inner shell electrons to the point where they are ejected. As the ejected inner shell electron, known as a photoelectron, passes through a magnetic field, it is curved relative to its speed which is related to the binding

energy (BE) and its photon energy ($h\nu$). This information reveals the identity of the parent element, orbital of the electron, and most importantly the chemical environment surrounding the atom. This is demonstrated in the figure below, **Figure 2.10**.

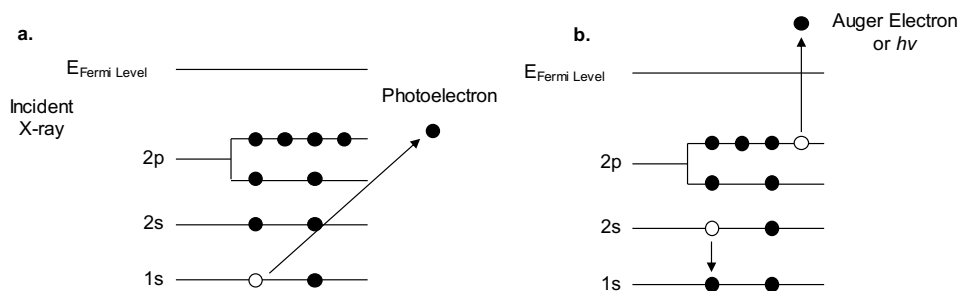


Figure 2.10. Diagram of (a) electron shells during the initial excitation and expulsion of the photoelectron, and (b) the subsequent relaxation and ejection of the Auger electron. Redrawn from reference.²⁷

To fill the hole left by the photoelectron departure, an electron from an outer shell drops down to fill the gap, known as the relaxation process. This produces energy, which is removed from the atom by the departure of a second electron or a photon, in a process known as Auger spectroscopy. It is important to perform experiments in a near-total vacuum, to stop electronic interference of organic contaminants.

XPS spectra were recorded using a Kratos Supra XPS fitted with a monochromated Al X-ray anode (1486.69 eV) and a charge neutraliser. All spectra were recorded with a base pressure below 1×10^8 Torr. Wide scans were recorded using a pass energy of 160 and high-resolution scans with a pass energy of 20. All spectra were calibrated to adventitious carbon (284.8 eV). All spectra were processed using CASA XPS v2.3.15 using Shirley background model for the baseline and the peak fit. Individual fittings will be explained further in the experimental work.

2.3.7 CO₂ Chemisorption-Mass Spectrometry and CO₂ TPD

Chemisorption is the process of a molecule chemically bonding to a surface and can be used as a tool to determine the strength and density of surface sites. Multiple gaseous compounds can be used molecular probes, such as NH₃ for acidic samples, CO₂ for basic, and CO for noble metals. This technique was used to probe the basic sites of the MgO/SBA-15 support, using carbon dioxide to titrate the sites, and temperature-programmed desorption to measure site strength. Known pulses of CO₂ were passed over a known outgassed sample until no more CO₂ is lost to chemisorption, illustrated in **Figure 2.11**. The molar quantity chemisorbed is proportional to the number of basic sites. This CO₂ saturated sample is then heated under an inert atmosphere, releasing its

chemisorbed CO₂ at different temperatures relative to how strongly bound it is to the site. This is quantified using mass spectrometry.

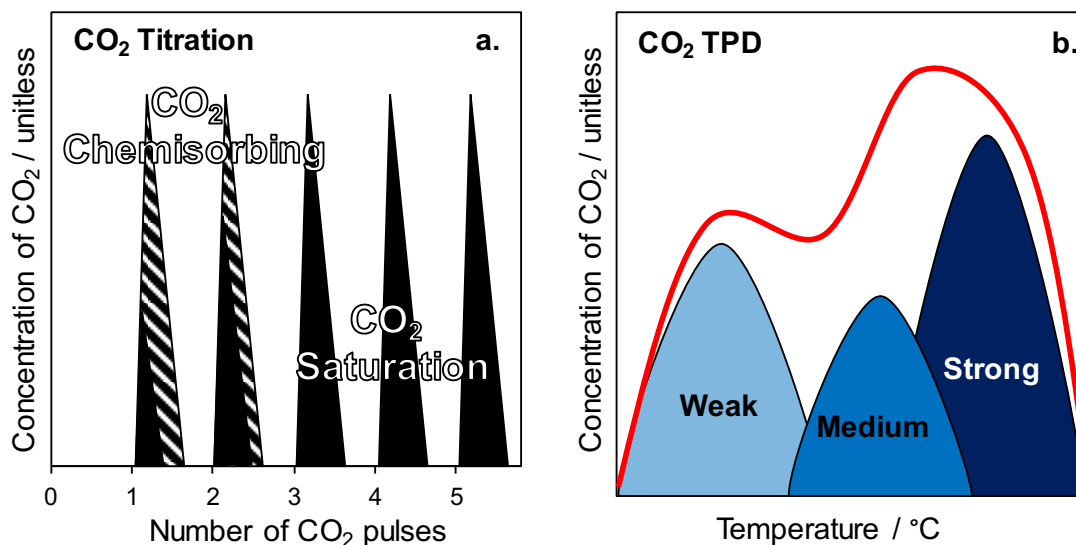


Figure 2.11. Illustration highlighting (a) CO₂ pulse titrations to calculate site density and (b) site strength derived by CO₂ TPD-MS.

CO₂ titrations were performed using a Quantachrome ChemBET 3000. Samples were outgassed at 400 °C under flowing helium (20 cm³.min⁻¹) for 1 hour prior to analysis. Titrations and temperature-programmed desorption were quantified using both a thermal conductivity detector and mass spectrometry.

2.3.8 Gas Chromatography – Flame Ionisation Detector

Gas chromatography (GC) is a chromatographic technique to separate compounds in the liquid or gaseous phase and quantify their amount using an internal standard. This technique was used to monitor the progress of the catalytic screening by taking periodic samples of the reaction mixture, which are then dispersed in an organic solvent to dilute the sample.

The GC sample is vaporised into the gas phase, with the excess sample being discarded to not overload the instrument. The gaseous sample is injected into a polar/nonpolar GC column and passed through the column using an inert carrier gas. Due to differing levels of affinity to the column, the molecules in the sample separate resulting in compounds eluting at different times. Other methods can be used to increase compound separation; such as temperature and flow ramps. The eluted compounds were in this work passed through a flame ionisation detector (FID). This acts to break up the compounds into their constituent ions, the electronic charge of which is detected and quantified. Other

techniques can be combined with GC such as mass spectrometry, which can identify the compounds without the use of standards.

When using GC to monitor a reaction, an internal standard was used to normalise the peak area, which can vary due to detector and injection volume fluctuation, to another compound of a known concentration. This is subsequently used to convert the normalised peak area, known as response factor, into molar concentrations. The methods used for each reaction are displayed in **Table 2.2**.

It is noted that the compound benzoic acid is detectable using the methods displayed below in **Table 2.2**. This is due to the temperature required to vapourise this species not being reached. Therefore, the molar balance of the reaction was calculated to ensure benzoic acid was not being produced.

Table 2.2. Gas chromatography methods for the transesterification of triglycerides, selective oxidation of aromatic primary alcohols and oxidative coupling of alcohols and amines.

Function	Inj. temp.	Column Heating Profile	GC model	Column
Transest. C4	250 °C	50 °C, 4 min 15 °C min ⁻¹ 280 °C, 5 min	Shimazu GC-2010	CP-Sil-5 (15 m × 0.25 mm × 0.25 µm)
Benzyl Alc. Selox + Cascade	250 °C	50 °C, 3 min 15 °C min ⁻¹ 280 °C, 3 min		
Transest. C8 & 12	50 °C 15 °C min ⁻¹ 270 °C	50 °C, 4 min 15 °C min ⁻¹ 280 °C, 5 min	Varian 450 GC	ZB-1HT Inferno (15 m × 0.53 mm × 0.15 µm)

2.4 Catalytic Testing

The reproducibility of all catalytic screening was ensured by triplicate reactions, with each sampling point being ran through the GC-FID also in triplicate. This ensured the data was displayed with the experimentally determined error.

2.4.1 Transesterification of tributyrin at 60 °C:

A mixture of triglyceride (10 mmol), magnesium oxide functionalised SBA-15 catalyst (50 mg), methanol (12 ml), and dihexyl ether (1 mmol) as internal standard were placed into a Radleys 12 plus carousel reactor, with the set up displayed in **Figure 2.13**. The resulting mixture was vigorously stirred at 60 °C in air at 700 RPM. Sampling from the reaction (0.25 ml) was performed at regular intervals up until 6 hours, after which samples were taken at 24 hours to calculate the maximum conversion. The reaction solution was diluted with dichloromethane (1.5 ml) and analysed using a calibrated Shimadzu GC-2010 fitted with a CP-Sil-5 column (15 m × 0.25 mm × 0.25 µm).

2.4.2 Transesterification of tributyrin, tricaprylin and trilaurin at 90 °C:

A mixture of triglyceride (10 mmol), magnesium oxide functionalised SBA-15 catalyst (100 mg), methanol (12 ml), and dihexyl ether (1 mmol) as internal standard were placed into 50 ml ACE pressure flasks fitted with sampling vents, displayed in **Figure 2.12**.



Figure 2.12. ACE pressure flasks used for transesterification of tributyrin, tricaprylin and trilaurin above the solvent boiling point.

The resulting mixture was vigorously stirred at 700 RPM at 90 °C. Sampling from the reaction (0.25 ml) was performed at regular intervals up until 6 hours, after which samples were taken at 24 hours to calculate the maximum conversion for tributyrin and tricaprylin. Start and endpoint samples were taken for trilaurin, due to the insoluble nature making the use of the sampling port difficult. The reaction solution was diluted with dichloromethane (1.5 ml) and analysed using a calibrated Shimadzu GC-2010 fitted with a CP-Sil-5 column (15 m × 0.25 mm × 0.25 μm) for tributyrin reactions. For tricaprylin and trilaurin; the reaction solution was diluted with dichloromethane (1:50) and analysed using a calibrated Varian 450 GC fitted with a ZB-1HT Inferno column (15 m × 0.53 mm × 0.15 μm).

2.4.3 Selective oxidation of benzyl alcohol

A mixture of benzyl alcohol (1 mmol), catalyst (50 mg), toluene (10 ml), and anisole (1 mmol) as internal standard were placed into a Radley 12 plus Carousel reactor, with the set up displayed in **Figure 2.13**.



Figure 2.13. Radleys 12 bed carousel reactor used for the selective oxidation of benzyl alcohol, and other reactions at atmospheric pressure.

Basic additives were added at this stage if required. The resulting headspace of the mixture was evacuated and replaced with a 1 bar oxygen atmosphere, vigorously stirred at 800 RPM and heated to the desired reaction temperature. Sampling from the reaction (0.25 ml) was performed at regular intervals up until 6 hours, after which samples were taken at 24 hours to calculate the maximum conversion. The reaction solution was diluted with dichloromethane (1.5 ml) and analysed using a calibrated Shimadzu GC-2010 fitted with a CP-Sil-5 column (15 m × 0.25 mm × 0.25 μm).

2.4.4 Selective oxidative coupling of benzyl alcohol and benzylamine

A mixture of benzyl alcohol (1 mmol), benzylamine (1 mmol), catalyst (50 mg), toluene (10 ml), and anisole (1 mmol) as internal standard were placed into a Radley 12 plus Carousel reactor, with the set up displayed in **Figure 2.13**. Basic additives were added at this stage if required. The resulting headspace of the mixture was evacuated and replaced with a 1 bar oxygen atmosphere, heated to the desired reaction temperature and vigorously stirred at 800 RPM. Sampling from the reaction (0.25 ml) was performed at regular intervals up until 6 hours, after which samples were taken at 24 hours to calculate the maximum conversion. The reaction solution was diluted with dichloromethane (1.5 ml) and analysed using a calibrated Shimadzu GC-2010 fitted with a CP-Sil-5 column (15 m × 0.25 mm × 0.25 μm).

2.4.5 Equations used for Screening

The conversion of reactants, initial reaction rate, selectivity of products and yield of products are calculated using **Equations 2.3 to 2.6**:

$$\text{Conversion (\%)} = 100 \times \frac{[S]_0 - [S]}{[S]_0}$$

Equation 2.3. Conversion of Substrate. Where: $[S]_0$ is initial concentration, $[S]$ is the concentration at time t .

$$\text{Rate (mmol.h}^{-1}\text{)} = \frac{[A] - [A]_0}{t - t_0}$$

Equation 2.4. Initial rate of reaction. Where: $[A]_0$ is the initial concentration at time t_0 , $[A]$ is the concentration at time t .

$$\text{Selectivity of N (\%)} = 100 \times \frac{[N]}{\sum_N [N]}$$

Equation 2.5. Selectivity to a product. Where: $[N]$ is the concentration of one of the products ($N = A, B, C, \dots$) at time t , and $\sum_N [N]$ is the sum of concentrations of all products at time t .

$$\text{Yield (\%)} = 100 \times \frac{[A]}{[A]_{\text{total}}}$$

Equation 2.6. The theoretical yield of a product. Where: $[A]$ is the concentration at time t , $[A]_{\text{total}}$ is the total concentration possible.

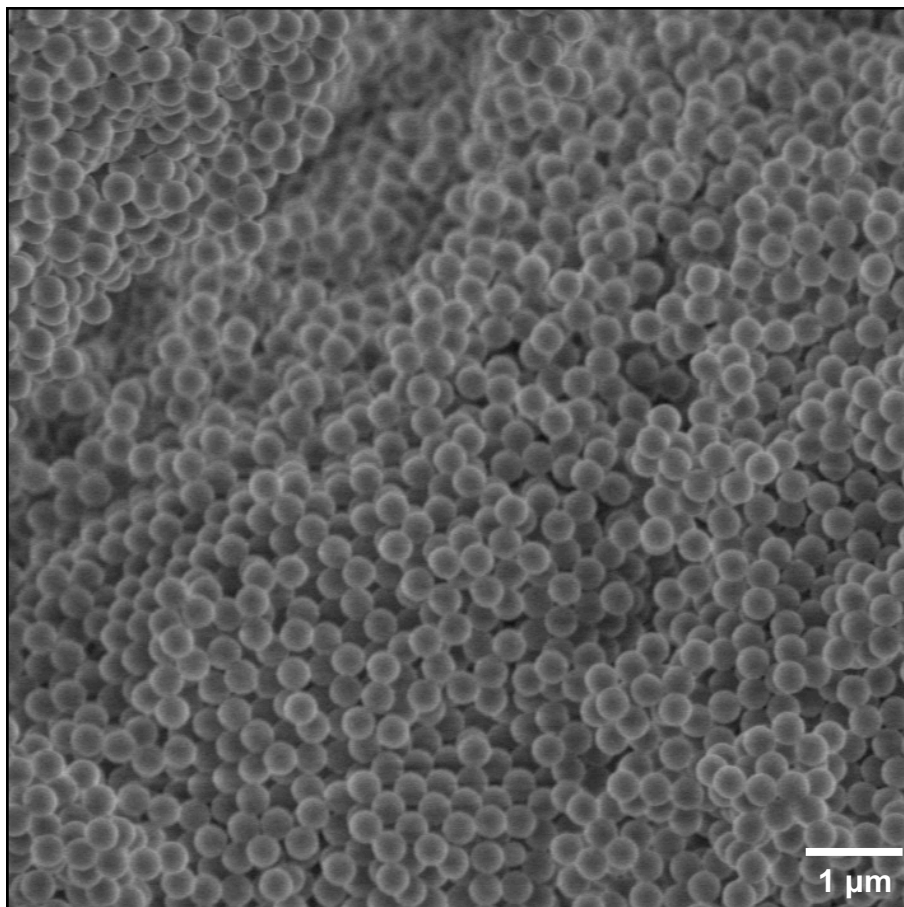
2.5 References

1. D. Y. Zhao, J. L. Feng, Q. S. Huo, N. Melosh, G. H. Fredrickson, B. F. Chmelka and G. D. Stucky, Triblock copolymer syntheses of mesoporous silica with periodic 50 to 300 angstrom pores, *Science*, 1998, **279**, 548-552.
2. G. S. Attard, J. C. Glyde and C. G. Goltner, Liquid-crystalline phases as templates for the synthesis of mesoporous silica, *Nature*, 1995, **378**, 366-368.
3. T. Sen, G. J. T. Tiddy, J. L. Casci and M. W. Anderson, Synthesis and characterization of hierarchically ordered porous silica materials, *Chemistry of Materials*, 2004, **16**, 2044-2054.
4. J. Dhainaut, J.-P. Dacquin, A. F. Lee and K. Wilson, Hierarchical macroporous-mesoporous SBA-15 sulfonic acid catalysts for biodiesel synthesis, *Green Chemistry*, 2010, **12**, 296-303.
5. P. Perez, M. A. Soria, S. A. C. Carabineiro, F. J. Maldonado-Hodar, A. Mendes and L. M. Madeira, Application of Au/TiO₂ catalysts in the low-temperature water-gas shift reaction, *International Journal of Hydrogen Energy*, 2016, **41**, 4670-4681.
6. M. Bowker, A. Nuhu and J. Soares, High activity supported gold catalysts by incipient wetness impregnation, *Catalysis Today*, 2007, **122**, 245-247.
7. F. Moreau, G. C. Bond and A. O. Taylor, Gold on titania catalysts for the oxidation of carbon monoxide: control of pH during preparation with various gold contents, *Journal of Catalysis*, 2005, **231**, 105-114.
8. Y. Sunagawa, K. Yamamoto, H. Takahashi and A. Muramatsu, Liquid-phase reductive deposition as a novel nanoparticle synthesis method and its application to supported noble metal catalyst preparation, *Catalysis Today*, 2008, **132**, 81-87.
9. G. R. Desiraju, J. J. Vittal and A. Ramanan, Crystal engineering: a textbook, World Scientific, 2011.
10. P. Atkins, J. de Paula and J. Keeler, Physical Chemistry, Oxford University Press, Great Britain, 8th edition, 2006.
11. A. L. Patterson, The Scherrer formula for X-Ray particle size determination, *Physical Review*, 1939, **56**, 978-982.
12. D. Zhao, Q. Huo, J. Feng, B. F. Chmelka and G. D. Stucky, Nonionic triblock and star diblock copolymer and oligomeric surfactant syntheses of highly ordered, hydrothermally stable, mesoporous silica structures, *Journal of the American Chemical Society*, 1998, **120**, 6024-6036.
13. J. W. Olesik, Elemental analysis using ICP-OES and ICP/MS, *Analytical Chemistry*, 1991, **63**, 12A-21A.
14. F. Caruso, S. Mantellato, M. Palacios and R. J. Flatt, ICP-OES method for the characterization of cement pore solutions and their modification by polycarboxylate-based superplasticizers, *Cement and Concrete Research*, 2017, **91**, 52-60.
15. K. A. Cychosz, R. Guillet-Nicolas, J. Garcia-Martinez and M. Thommes, Recent advances in the textural characterization of hierarchically structured nanoporous materials, *Chemical Society Reviews*, 2017, **46**, 389-414.
16. A. Galarneau, H. Cambon, F. Di Renzo, R. Ryoo, M. Choi and F. Fajula, Microporosity and connections between pores in SBA-15 mesostructured silicas

- as a function of the temperature of synthesis, *New Journal of Chemistry*, 2003, **27**, 73-79.
17. K. S. W. Sing, D. H. Everett, R. A. W. Haul, L. Moscou, R. A. Pierotti, J. Rouquérol, T. Siemieniewska, Reporting physisorption data for gas/solid systems with special reference to the determination of surface area and porosity, *Pure Applied Chemistry*, 1985, **57**, 603.
 18. H. Chon, S. I. Woo and S. E. Park, *Studies in surface science and catalysis*, Elsevier, 1996, **102**, 47-74.
 19. Z. Alothman, A review: fundamental aspects of silicate mesoporous materials, *Materials*, 2012, **5**, 2874-2902.
 20. S. Lowell, J. E. Shields, M. A. Thomas and M. Thommes, *Characterization of porous solids and powders: surface area, pore size and density*, Springer Netherlands, Dordrecht, 2004, 15-57.
 21. J. I. Goldstein, D. E. Newbury, J. R. Michael, N. W. M. Ritchie, J. H. J. Scott and D. C. Joy, *Scanning Electron Microscopy and X-Ray microanalysis*, Springer New York, 2017.
 22. S. Karan, Shape based characterization of nanoparticles – a fuzzy mathematical approach, *Proceedings of the Indian National Science Academy*, 2015, **81**.
 23. D. B. Williams and C. B. Carter, *Transmission electron microscopy: a textbook for materials science*, Springer US, 2009.
 24. N. Jonge, R. Sougrat, S. Pennycook, D. Peckys and A. Lupini, *Three-dimensional aberration-corrected scanning transmission electron microscopy for biology*, 2007.
 25. C. Hetherington, Aberration correction for TEM, *Materials Today*, 2004, **7**, 50-55.
 26. J. Chastain and J. F. Moulder, *Handbook of X-ray photoelectron spectroscopy: a reference book of standard spectra for identification and interpretation of XPS data*, ULVAC-PHI Incorporated, 1995.
 27. A. Hubin and H. Terry, *Comprehensive Analytical Chemistry*, Elsevier, 2004, **42**, 277-312.

Chapter 3

One-pot ordered mesoporous and hierarchically porous MgO/SBA-15 materials for the transesterification of triglycerides



SEM of Polystyrene Macropore hard template

3.1 Introduction

MgO functionalised SBA-15 has been studied extensively in literature,¹⁻⁴ however often these materials have been synthesised using the conventional co-operative self-assembly (CSA) method discovered by Zhao *et al.*⁵ This method leads to a highly microporous material, often resulting in larger substrates experiencing steric difficulties accessing these micropores. Other methods of synthesising SBA-15 have been developed, which reduce this wasted porosity, such as true liquid crystal templating.⁶

The use of an incorporated macroporous network has been previously used in hydrotalcite catalysts for biodiesel synthesis,⁷ and acts to reduce the travel length required through sterically hindered routes to access the catalytic sites. Therefore, by incorporating a hierarchical macro-mesopore network for biodiesel production, sterically hindered long mesopore channels will become broken up with a macroporous network. The literature on the transesterification of triglycerides has reported it to be a reaction susceptible to diffusion limitations, due to the relatively large size of the substrate molecules.^{8,9}

In this chapter, we aim to synthesise one-pot mesoporous and meso-macroporous MgO functionalised SBA-15 using a true liquid crystal templating technique. A polystyrene nanosphere hard template will be employed to incorporate the macropore network into the second materials. The second aim is to demonstrate how incorporating a hierarchical pore network into MgO functionalised SBA-15 can improve diffusion throughout the material. By introducing a macroporous bypass into the material, the path length travelled by the substrate will decrease and the support will provide easier access to the basic functionality. This will be demonstrated using the transesterification of model triglycerides (tributyrin (C₄), tricaprylin (C₈) and trilaurin (C₁₂)), which will enable us to compare the diffusion through the materials as the steric hindrance of the substrate size increases.

3.2 Results and Discussion

In this section we present the results of characterisation for the one-pot solid base functionalised SBA-15 materials, highlighting the differences among their physical and chemical properties, followed by the catalytic screening results using the transesterification of model triglycerides ($C_4 - C_{12}$), and the discussion of the effect of the catalyst properties on the reaction.

3.2.1 MgO functionalised CSA SBA-15

Similar work on functionalising SBA-15 with MgO using a cooperative self-assembly method has already been reported in the literature.⁵ The drawback of these studies are the lack of elemental analysis and diffractometry, which would identify the magnesium phase and loading. Therefore, it was decided to replicate this study as a starting point, with subsequent macropore incorporation if successful. The method used is described in **Section 2.2.1**.

3.2.1.1. X-ray Diffractometry

X-ray diffractometry was employed to examine the level of pore ordering and different crystalline phases within the material (**Figure 3.1**). As expected, when using the cooperative self-assembly method, highly defined low-angle peaks were observed (**Figure 3.1.a**). This is due to the nature of the synthesis, resulting in an extremely high surface area and uniformly ordered mesoporous network. No detectable change in low-angle reflections was observed, suggesting the apparent incorporation of magnesium oxide did not alter the material structure.

Wide-angle patterns (**Figure 3.1.b**) displayed the characteristic amorphous silica peak at 20-25°, with again no notable difference with Mg loading. The lack of reflections indicative of magnesium species was linked either to a negligible loading or to the presence of MgO as nano-species below the limit of XRD detection.

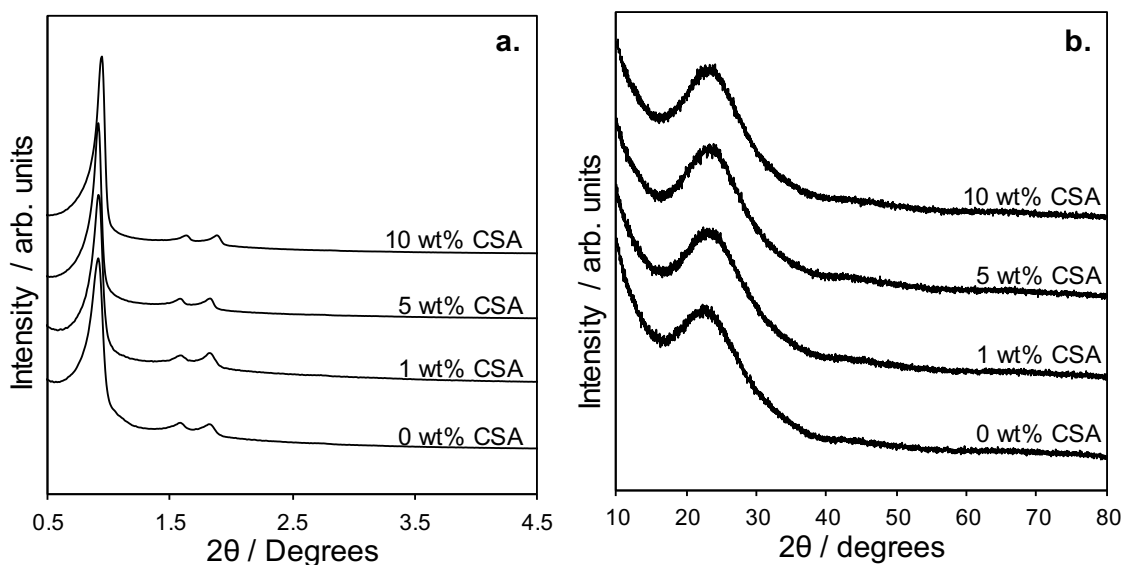


Figure 3.1. X-ray Diffraction Patterns of MgO functionalised SBA-15 synthesised using a one-pot cooperative self-assembly method, employing (a) low and (b) wide-angle scans.

3.2.1.2. Inductively coupled plasma with optical emission spectroscopy

Inductively coupled plasma optical emission spectroscopy was utilised to determine the atomic loading of magnesium within the material (**Figure 3.2**). ICP-OES showed loading was completely unsuccessful, with the black line representing a fully successful nominal loading. This indicated the one-pot impregnation was not suitable to transfer the $\text{Mg}(\text{NO}_3)_2$ from the aqueous phase to the solid material during the synthesis.

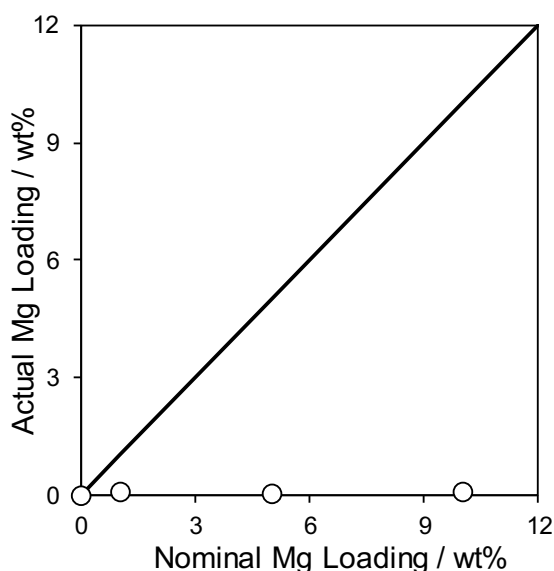


Figure 3.2. ICP-OES analysis of MgO impregnated on SBA-15 using a one-pot cooperative self-assembly method.

To verify the unsuccessful synthesis, the highest nominally loaded material was screened using the transesterification of tributyrin, employing conditions described in **Section 2.4.1**. These data, shown in **Appendix Figure 2.1**, demonstrated the absence of activity expected in unfunctionalised SBA-15 supports.

The unsuccessful synthesis method resembles a wet impregnation, where the functionalising species are retained within the solvent phase only to be discarded when the support is filtered off. Evaporation of the MgO-CSA solution would result in the retention of the magnesium species, as no filtering is required, however, would result in imprecise functionalisation throughout the entire material.

It was therefore decided to use a technique comparable to an incipient wetness impregnation called true liquid crystal templating (TLCT).⁶ This would form the soft template with the Mg²⁺ ion readily chelated to the Pluronic P123 core, before condensing the silica around the micellar template. The theoretical benefit of using a synthesis where the functionality is retained in the soft template is the targeted functionalisation solely within the mesoporous domain.

3.2.2 MgO functionalised TLCT SBA-15

The one-pot MgO impregnation of SBA-15 using TLCT was ultimately successful for both mesoporous and macro-mesoporous materials. In this section, the characterisation data for both material families are grouped together to give a better comparison between the two.

3.2.2.1. Inductively coupled plasma with optical emission spectroscopy

MgO/SBA-15 materials showed linear correlations between nominal and actual loading of Mg, as determined by ICP-OES (**Figure 3.3**), indicating a successful synthesis.

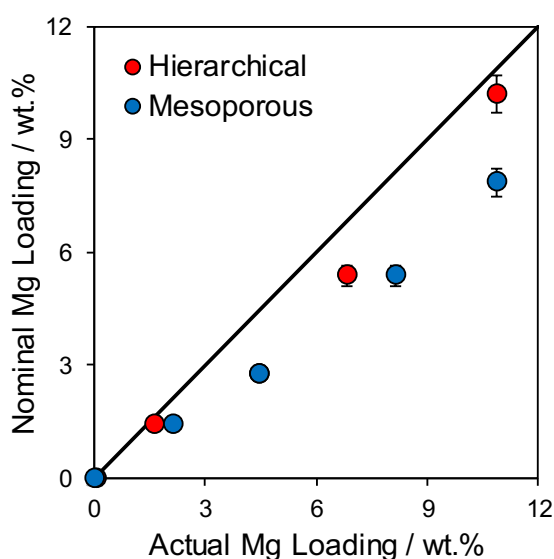


Figure 3.3. Actual versus nominal loading determined by ICP-OES.

While hierarchical materials closely matched the nominal loading, the mesoporous MgO/SBA-15 gave a higher actual loading when compared to the nominal. This may indicate either, the mesoporous materials retain more MgO, or the yield of SBA-15 support produced is lower than expected. We attributed this to the higher density of Mg²⁺ saturated P123 being lost in mesoporous synthesis, whereas the hierarchical Mg-P123 was diluted with the polystyrene hard template.

3.2.2.2. X-ray Diffractometry

Wide-angle XRD patterns for MgO/SBA-15 materials are presented in **Figure 3.4** and feature X-ray reflections indicative of different crystallite species which can be used to determine particle size.¹⁰

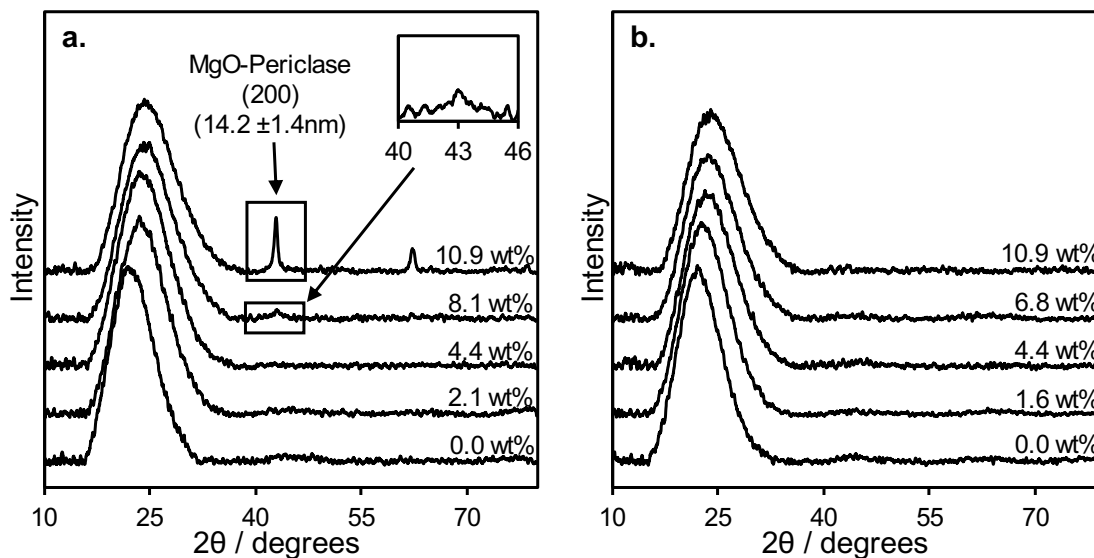


Figure 3.4. Wide-angle X-ray diffraction patterns of (a) mesoporous and (b) hierarchical SBA-15. Reflections present at approximately 42° and 63° are characteristic of periclase magnesium oxide.¹¹

Although ICP-EOS (**Figure 3.3**) confirmed the presence of magnesium as relatively abundant species, reflections indicative of periclase MgO were observed only in the two highest loading mesoporous samples. This was linked to two possible explanations: the size of MgO species was below the 2-2.5 nm detection limit of the X-ray diffractometer,¹² or MgO was as a non-crystalline phase. Crystalline magnesium oxide is typically in a rocksalt lattice structure,¹³ however amorphous MgO can be created using extreme pressure and temperature.¹³ The lack of either of these extreme conditions during the synthesis and further characterisation led to the conclusion that MgO species were crystalline and therefore below the XRD limit of detection.

The reflections observed for mesoporous 8.1 and 10.9 wt% were found to be approximately 15 nm in size using the Scherrer equation, which was confirmed later using TEM (**Figure 3.11**). This size of particle was too large to be retained within the mesopore domain (diameter 3-5 nm, **Figure 3.9**), indicating partial migration and deposition of the MgO outside the mesopore network. These results were interpreted as the presence of two MgO phases: a migrated 15-20 nm nanoparticle phase on the surface outside the mesopores, and a sub 2-2.5 nm MgO retained within the mesopore network.

Possible explanations for these particles outside the mesoporous network may be the saturation of the soft template, or feasibly the bleeding of basic functionality from the pore opening. While the appearance of the larger MgO phase seemed to be facilitated by increasing loading, this was not observed by the hierarchical materials. It is therefore proposed that by using a macroporous template, the migration of functionality during synthesis was prevented, as visualised in **Figure 3.5**.

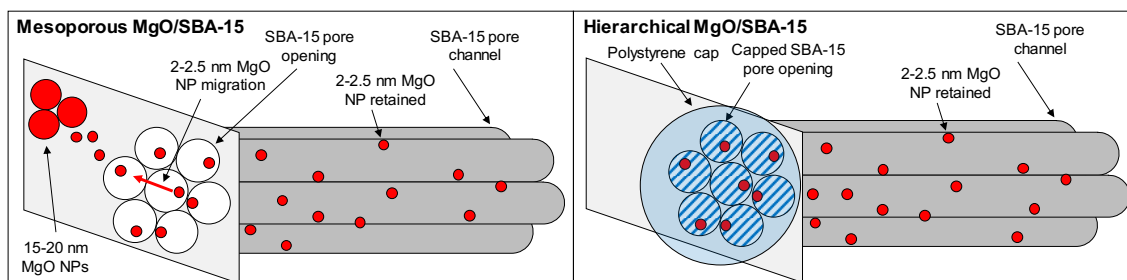


Figure 3.5. Diagram explaining the proposed migration of MgO nanoparticles to the surface and lack of migration in mesoporous and hierarchical MgO/SBA-15 respectively.

Another observation to be highlighted from **Figure 3.4** was the shifting of the amorphous silica peak ($20\text{-}25^\circ$), indicative of a change in the size of the silica unit cell.¹⁰ A trend was observed for both materials when comparing the decreasing lattice size with Mg loading (**Appendix Figure 2.1**), suggesting the presence of the Mg^{2+} or NO_3^{2-} ions were affecting the condensation of the silica. Nitrate anions have been known to interact with the P123 surfactant as salting in ion, described as the Hoffmeister anion effect.¹⁴ It may be that the nitrate could also affect the silica, or it may be another symptom of its effect on the template.

The low-angle reflections of both mesoporous and hierarchical materials are presented in **Figure 3.6**. The diffractograms showed three reflections (10, 11, and 20) characteristic of the pore diffraction planes present in ordered mesoporous SBA-15,⁵ which demonstrated the TLCT one-pot synthesis was successful in forming long-range ordered mesoporous silica.

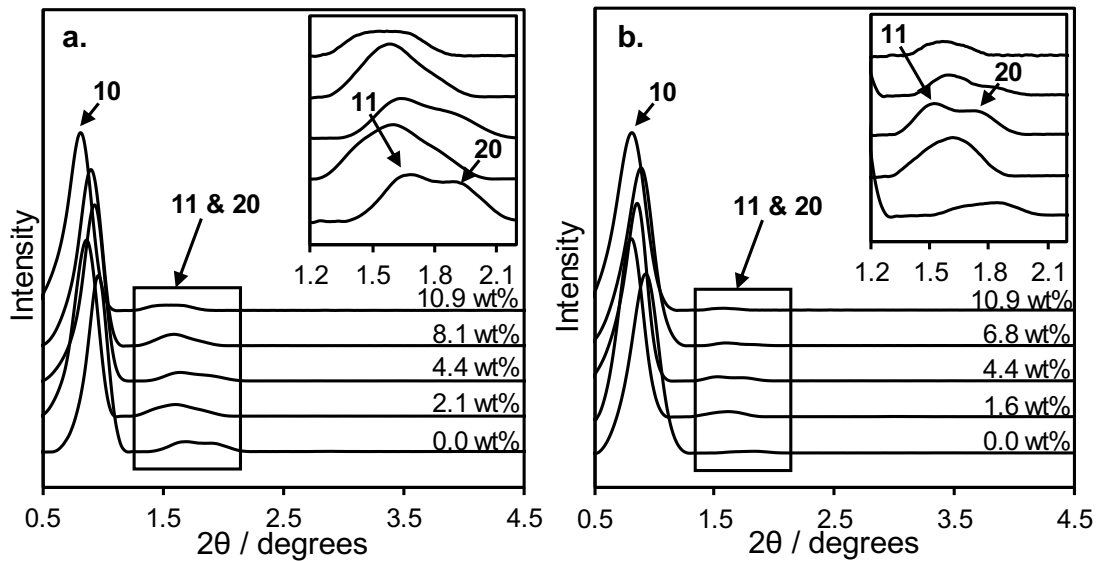


Figure 3.6. Low-angle X-ray diffraction patterns of (a) mesoporous and (b) hierarchical SBA-15. Inset shows the 11 and 20 low-angle reflections characteristic of SBA-15.

The inset patterns in **Figure 3.6** focuses on the 11 and 20 reflections for both materials from low to high Mg loading. It was noted that the hierarchical samples contained very weak 11 and 20 reflections, indicating reduced long-range order when compared to the purely mesoporous materials. This is thought to be caused by the macropore network breaking up the mesopore domain, and disrupting the long-range order.

It is worth mentioning that the highest loading was set at approximately 10 wt%, as at greater loadings the decreasing relative concentration of pluronic P123 altered the micellar phase.¹⁵ This caused the micellar system to verge on the phase boundary between hexagonal, cubic and multiphase micellar structures, which would cause disruption of the pore architecture.¹⁶ Finally, inter pore distances, calculated from the 10 reflections, remained constant at 10.9 ± 0.5 nm for all the materials. This suggested the pore structure of the materials was maintained, regardless of Mg impregnation or macropore incorporation (**Appendix Figure 2.2**).

3.2.2.3. Nitrogen Porosimetry

Both mesoporous and hierarchical materials exhibited type IV nitrogen porosimetry isotherms, as seen in **Figure 3.7**. This is characteristic of the ordered mesoporous domains observed in SBA-15 type materials,¹⁷ which suggests the synthesis of the materials was successful.

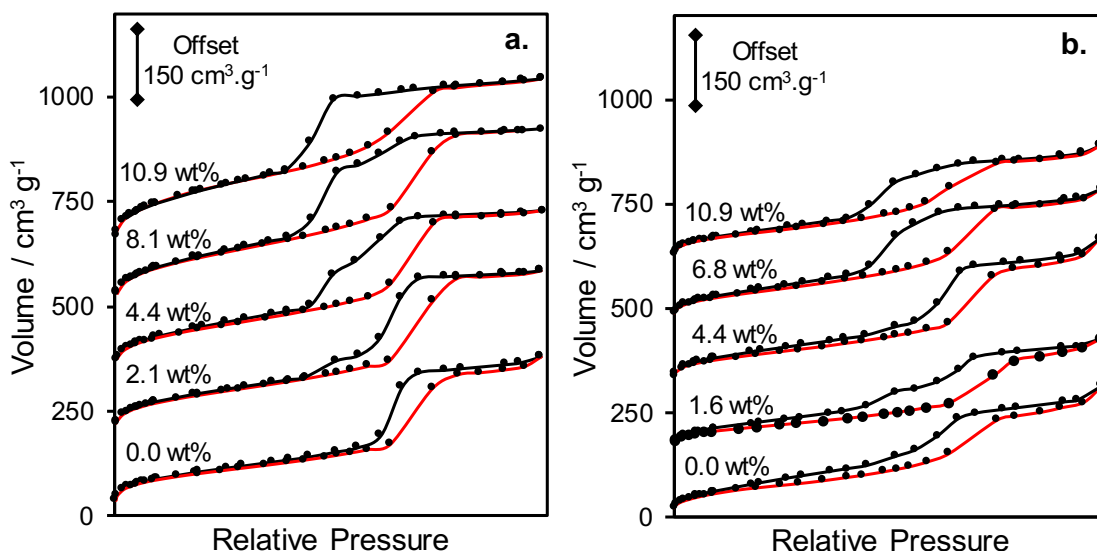


Figure 3.7. Nitrogen porosimetry isotherms of (a) mesoporous and (b) hierarchical materials.

It is noted that the shape of the isotherms changed with loading, specifically the hysteresis of both materials shifting from a type H1 to a H2.¹⁸ An H1 hysteresis curve is caused by the gradual evaporation of physisorbed liquid nitrogen from long-range ordered uniform pore channels, which is expected in SBA-15 materials.¹⁹ The shift of the hysteresis to H2 is caused by sporadic desorption from the non-uniform pore, which suggests the formation of irregularly distributed nanoparticles rather than a uniform wall coating. It was noted that the type H2 curves were more pronounced in the mesoporous materials, however, this observation may be more noticeable in the larger isotherms.

As expected, mesoporous materials exhibited a larger surface area than hierarchical materials (**Appendix Table 2.1**), due to their uninterrupted mesoporous domain. Microporosity in the mesoporous materials was also a key factor in the observed increase in total surface area (**Figure 3.8**). It is worth noting that TLCT mesoporous materials exhibited reduced microporosity relative to the co-operative self-assembly SBA-15 due to the synthesis method.⁶ The increased surface area may also be attributed to the nanoparticles forming on the material surface, however, this would be a minor increase if even detectable.

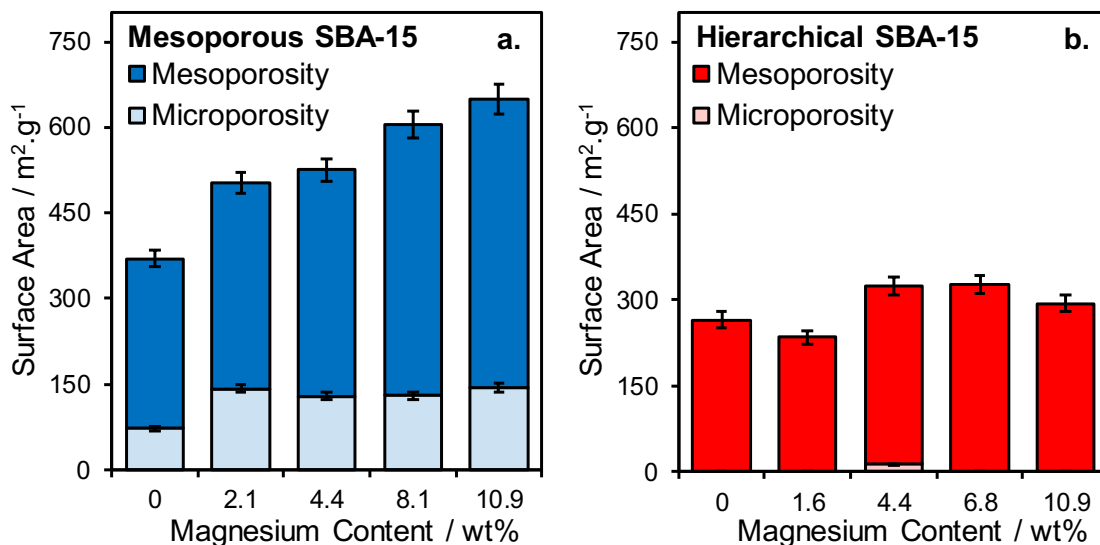


Figure 3.8. BET surface area for (a) mesoporous and (b) hierarchical MgO/SBA-15 materials, with mesoporous and microporous contributions determined using N₂ porosimetry.

Comparing the hierarchical materials to the mesoporous ones, the former showed relatively lower values of surface area in the range 250-300 m² g⁻¹, with small difference with the loading. The lower surface areas were attributed in part to the reduced mesoporosity, as a large volume is occupied by macropores. However, a reduction of microporosity was also observed in the hierarchical materials, which in turn contributed to the reduced surface area in these supports. Manayil *et al.* incorporated a macro-polystyrene template into cooperative self-assembly SBA-15,²⁰ and also perceived a reduction in the proportion of micropore area, however, their synthesis might not be directly comparable to this study due to the different synthesis method. A reduction of microporosity could, therefore, be a result of both incorporation of macroporosity and a modified synthesis.

In addition, a steady increase in surface area was observed with loading by the mesoporous materials from 375 to 650 m² g⁻¹ that was attributed to increased pore disorder. This may be caused by the nitrate Hofmeister anion, which alters the micellar structure of the soft template.¹⁴ The hierarchical materials did not experience this linear growth, suggesting the incorporation of the macropore template may have caused stabilisation of the material. Unfortunately, this observation has not been reported in the literature to the best of our knowledge, rendering the cause of changing porous structure and surface area unsubstantiated.

Pore size distributions determined via BJH calculations (**Appendix Table 2.1**), showed a decrease in average pore size with increased loading for both SBA-15 materials. A

linear decrease in the average pore size for both families of materials was observed with respect to the average pore distribution in the micro/mesopore regions (**Figure 3.9**), which could be due to the functionalisation of the mesoporous domain occupying the pores.

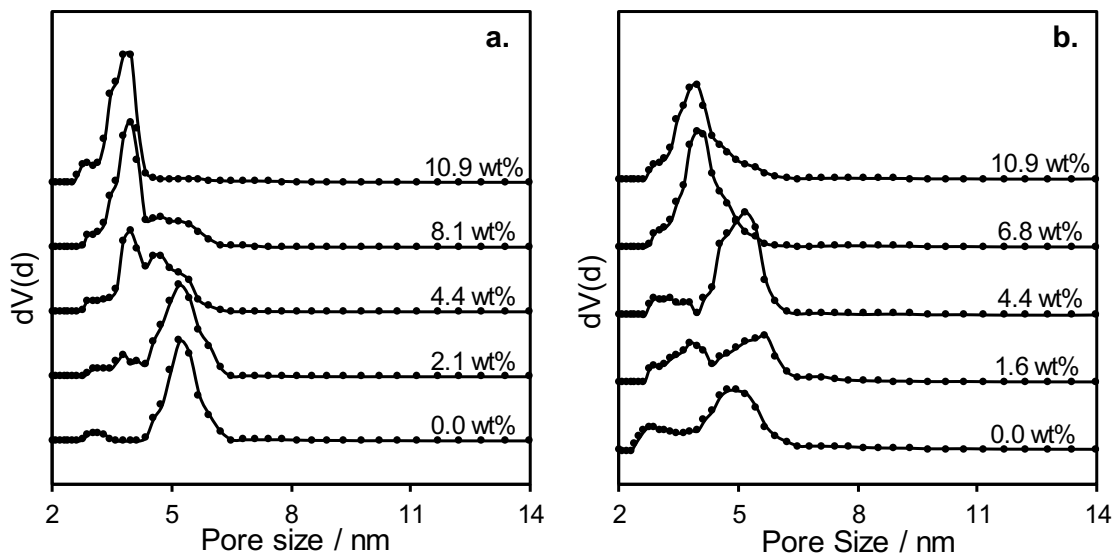


Figure 3.9. Pore size distributions for (a) mesoporous and (b) hierarchical MgO/SBA-15 materials determined using N₂ porosimetry.

Two distinct pore groups (filled and vacant), shifting in population with loading between at 3 and 5 nm, were observed instead of a gradual even functionalisation of MgO. Therefore, the average pore size calculation presented in **Appendix Table 2.1** is a poor representation of the real bimodal pore system present in the material. In conclusion, the porosimetry suggested that MgO nanoparticles were populating mesopores, with the two distinct vacant and filled changing in population.

3.2.2.4. Microscopy (SEM and TEM)

To determine macropore uniformity, scanning electron microscopy was used on the polystyrene hard template (**Figure 3.10a**) and the resultant hierarchical materials (**Figure 3.10b**). An even distribution was found, as a result of a proven highly modifiable and reliable synthesis.²¹

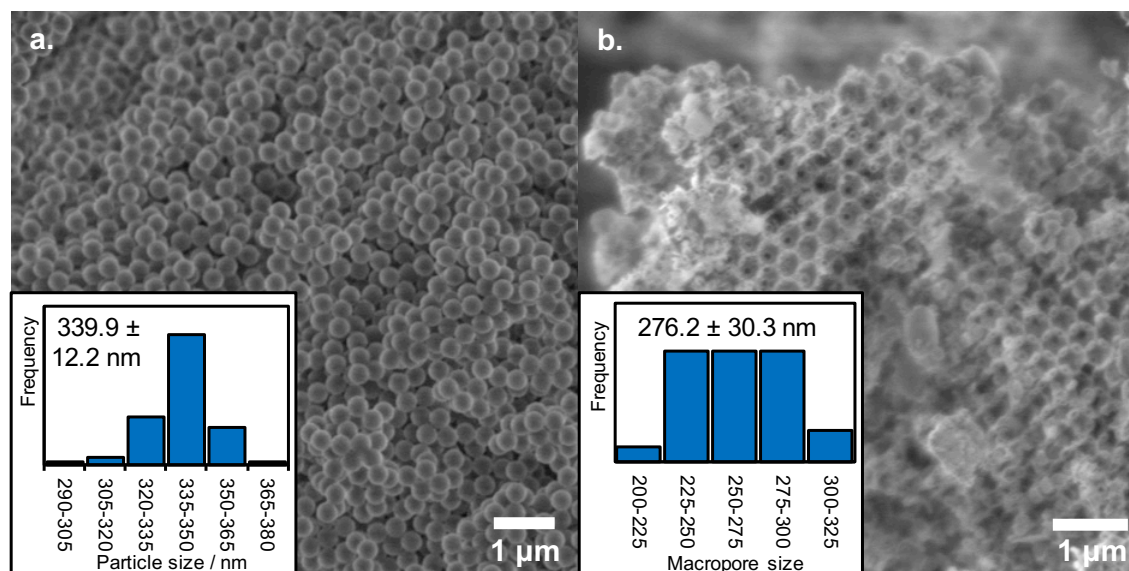


Figure 3.10. Scanning electron micrographs of (a) polystyrene nanospheres and (b) hierarchical MgO/SBA-15, with inset particle and pore size distribution histograms respectively.

The hexagonally stacked macropores in the hierarchical material (**Figure 3.10.b**) exhibited extensive interconnectivity, which is extremely attractive for catalytic supports.²² These materials had an average macropore size of 276 ± 30 nm, which when compared with the 340 ± 12 nm polystyrene nanosphere hard template, confirmed a pore contraction had taken place during calcination.²¹

Transmission electron microscopy was undertaken on both supports to confirm the successful templating of mesoporous and hierarchical pore domains (**Figure 3.11**). TEM was especially useful to corroborate findings from previous techniques.

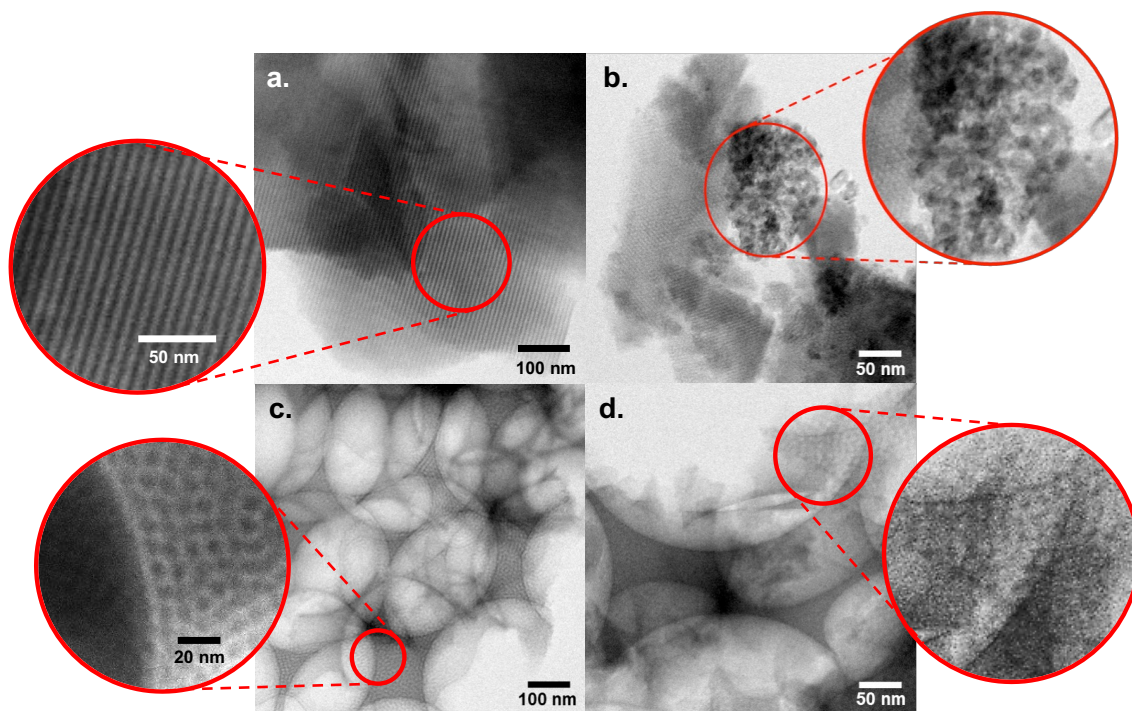


Figure 3.11. TEM images of magnesium oxide deposited on (a) 2.1 wt.% mesoporous SBA-15, (b) 10.9 wt.% mesoporous SBA-15, (c) 1.6 wt.% hierarchical SBA-15 and (d) 10.9 wt.% hierarchical SBA-15 materials.

The insets of **Figure 3.11** highlight the pore structure of the mesoporous domains (inset **Figure 3.11a**) and the nanoparticles build up on the surface of the 10.9 wt% mesoporous MgO/SBA-15 (inset **Figure 3.11b**). These nanoparticles were confirmed to be MgO by measuring a lattice parameter of 2.1 Å, which is in agreement with the periclase 200-crystallite plane (**Appendix Figure 2.3a**).²³ **Figure 3.11c** showed the mesoporous domain at the intersection between macropores, highlighting the extraordinarily well-interconnected nature of the dual pore material, in addition to the preservation of the ordered mesopores.

As seen in **Appendix Figure 2.4** and **Figure 3.11b**, the surface MgO phase appeared as both individual nanoparticles and a larger agglomeration, respectively. Particle sizes of the individual particles matched sizes calculated using the Scherrer equation in **Figure 3.4**, which may suggest these are the dominant species. This individual particle prevalence over clusters was not observed in the microscopy pictures for several potential reasons. Due to the similarity in Z contrast between Mg and Si, it was difficult to distinguish between MgO and silica phases. Because of this, the surface phases identified were predominantly MgO clusters, due to their noticeably different morphology.

3.2.2.5. X-ray Photoelectron Spectroscopy

X-ray photoelectron spectroscopy was used to identify the chemical nature of the species present in the materials and their interaction with each other. Three regions were examined: O 1s (to study the abundances of each oxide), Mg 2p (to examine which phases were present in the material), and Si 2p (to determine how the support was altered). The wide-angle of the MgO reference sample, produced from calcining the Mg precursor, was used as an XPS benchmark and is displayed in **Appendix Figure 2.4**

The Mg 2p spectra (**Figure 3.12**) showed three species of magnesium for both mesoporous and hierarchical materials: Mg-O-H (49.5 eV), Mg-O-Mg (49.8 eV) and Mg-O-Si (51.1 eV), which matched the spectra obtained from our MgO standard, as well as the spectra available in the literature for magnesium silicate.²⁴

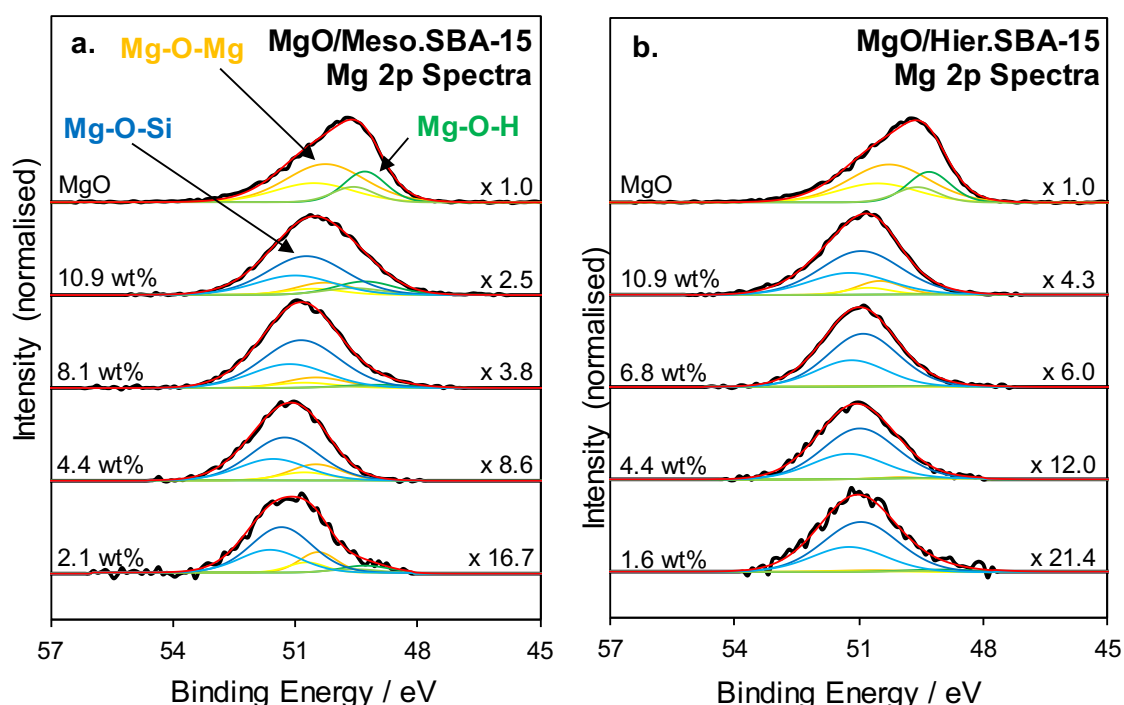


Figure 3.12. Mg 2p X-ray photoelectron spectroscopy of (a) mesoporous and (b) hierarchical MgO/SBA-15 normalised to show the appearance of new phases.

Magnesium silicate was found to be the major features of mesoporous materials, with the oxide component as strong secondary feature even at low loadings. The predominance of the oxide may indicate surface nanoparticles were present on the surface of all mesoporous MgO/SBA-15, however, were not detected at these low loadings (**Figure 3.12a**). Higher loaded hierarchical samples showed a slight increase in the MgO component, suggesting growth in particle size or, as indicated by porosimetry, in particle frequency. This can be supported when the normalisation factor is considered. As loading increased the ratio between components remained relatively stable, however,

the intensity of each component increased dramatically. This was caused by the increasing frequency of MgO NP occupying the mesopores, as shown by porosimetry in **Figure 3.8**. The reduced intensity of the hierarchical materials could also indicate less MgO present at the surface, suggesting better dispersion was occurring throughout the material.

The Si 2p spectra shown in **Figure 3.13** displayed 3 peaks at 102.5, 103.5 and 104.9 eV which correspond to Si-O-Mg, Si-O-Si and Si-O-H species, respectively.^{25, 26}

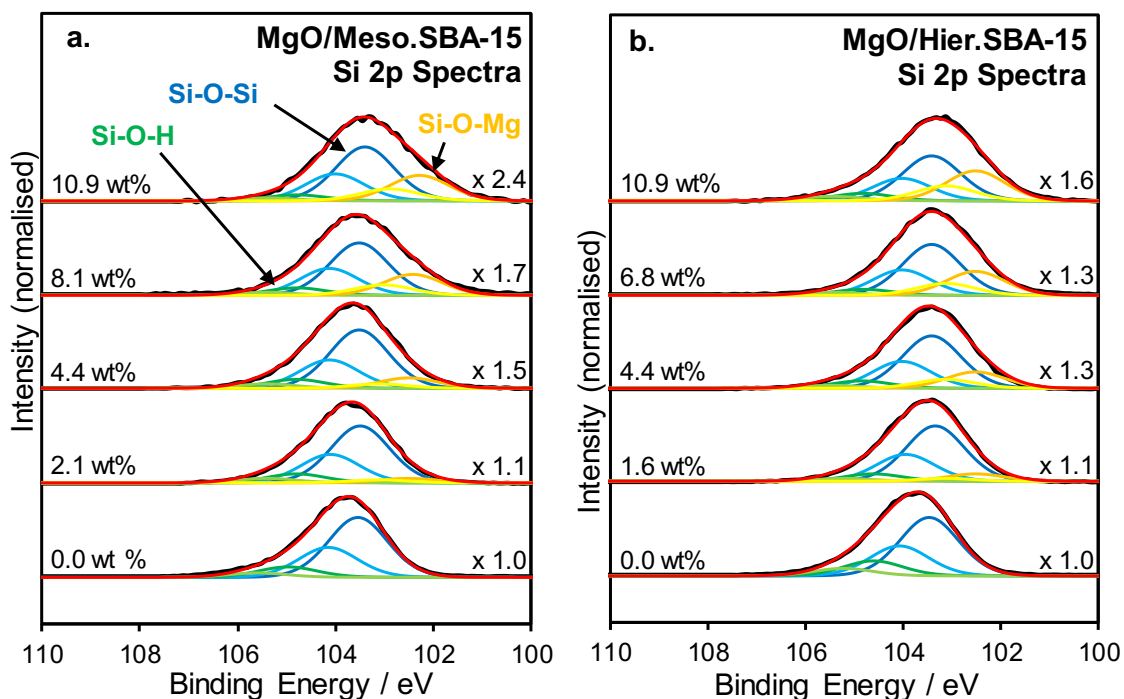


Figure 3.13. Si 2p X-ray photoelectron spectra of (a) mesoporous and (b) hierarchical MgO/SBA-15.

The large magnesium silicate component was observed for all materials and was indicative of the pore functionalisation taking place. It is noted that the hierarchical materials exhibited an increased Si-O-Mg feature throughout, suggesting a greater concentration of base functionality was interacting with the silica surface. This agrees with XRD, as an increased feature suggests small nanoparticles with greater support interaction, rather than larger nanoparticles on the surface, as seen with mesoporous materials. Surface hydroxides also appeared to be decreasing with loading, which may be attributed to the functionalisation of the surface sites with MgO.

Finally, the O 1s spectra (**Figure 3.14**) displayed three peaks at 530.1, 532.0 and 532.9 eV, which correspond to Mg-O-Mg, Si-O-Mg and Si-O-Si species, respectively.²⁷⁻²⁹

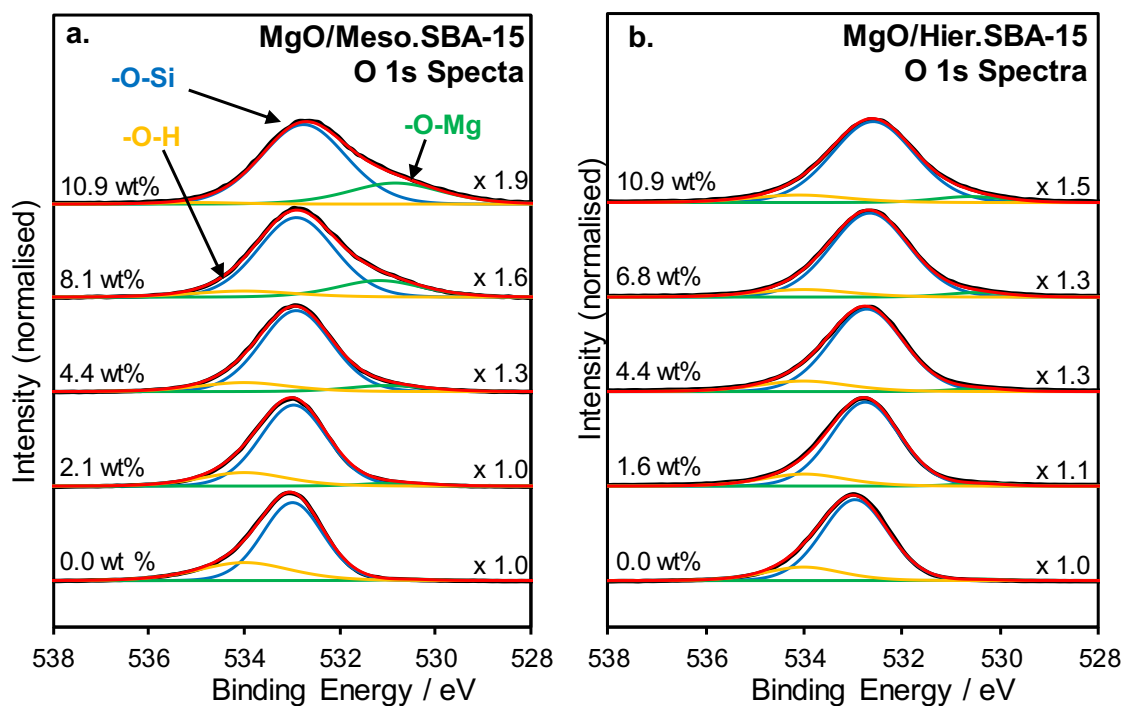


Figure 3.14. O 1s X-ray photoelectron spectra of (a) mesoporous and (b) hierarchical MgO/SBA-15.

The presence of Mg-O-Mg species in the O1s spectra again agreed with the Mg 2p, Si 2p, XRD and TEM, which all propose larger surface nanoparticles. The higher intensity of MgO in the mesoporous suggested a greater concentration at the surface of the material, and therefore poor dispersion.

To determine the location of MgO through the material, the loadings verified using ICP and XPS (**Figure 3.15**) were compared. As XPS is a surface-sensitive technique and ICP uses acid digestion and plasma to atomise and ionise the entire bulk of the material, comparing the two loadings would give the proportion of functionality at the surface.

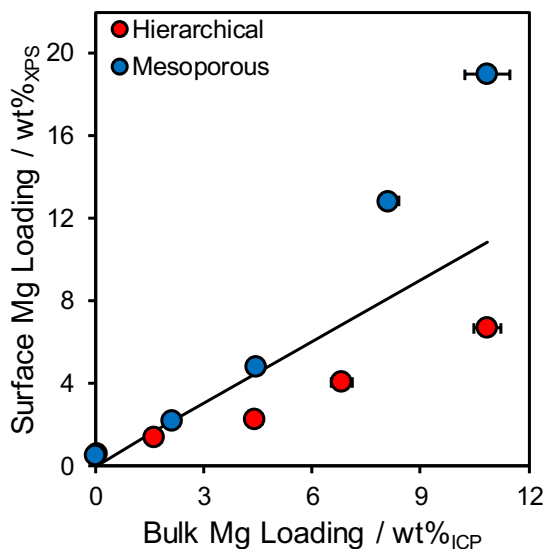


Figure 3.15. Surface versus bulk MgO loading determined by XPS and ICP-OES respectfully. A gradient of 1 (represented as a black line) would signify the surface Mg loading matching the bulk loading, representing even distribution throughout.

The hierarchical materials exhibited a reduced surface loading than expected; the majority of the MgO was retained within the bulk of the material suggesting negligible MgO migration to the surface. This supported the assumption that factors were causing the MgO functionality to remain in the pore channels during the synthesis of the hierarchical materials, suggested to be the macropore hard template. Conversely, mesoporous materials exhibited a higher surface loading, especially at the loadings previously determined to contain external MgO nanoparticles. This confirms that the mesoporous materials have a disproportionate concentration of base present at the surface.

The use of nuclear magnetic resonance spectroscopy (NMR) may have been beneficial to supplement this dataset. Two studies on magnesium oxide and magnesium oxide-silica systems highlight how NMR can support other techniques. Rimsza et al employed proton NMR to investigate the appearance of magnesium hydroxide from hydrated MgO barriers for subsurface waste isolation.³⁰ ¹H-NMR identified numerous hydroxide phases present, most of which were unidentified using WAXRD. This relates directly with the current work, as surface environments alter with loading, yet remain undetectable using XRD. C-NMR may also be employed to investigate the appearance of a carbonate phase, applicable also in the investigation of spent materials.

Secondly, work by Da Ros et al employs a MgO-SiO₂ support for ZrO₂ and ZnO catalysed ethanol to 1,3-butadiene conversion.³¹ Here, they use Si-NMR to identify the bonding environment of silica, and its interactions with its co-support MgO and active

phases. Interestingly, the absence of Si-O-Zr/Zn confirms the selective functionalisation of the basic surface with solid acid species. While not directly related to this chapter, the use of Si-NMR would be extremely useful to confirm the selective functionalisation of MgO in Chapter 4.

3.2.2.6. Active Site Probing

Probing of the active site was attempted using two methodologies, however, was ultimately unsuccessful. These experiments are displayed in **Appendix Figures 2.5-6**.

The basic sites were firstly degassed and probed using CO₂ titration, thereby calculating the density of basic sites per gram, which can be converted into the dispersion of sites compared to total MgO concentration. The results were found to be extremely irreproducible, and an order of magnitude lower than expected when using nano magnesia from the literature as a reference.¹¹

Base site density was found to remain constant with no new base surface created by the increase of loading. This suggested the propagation of layers of existing species in the form of added pore wall coating. This would mean that both materials were experiencing an increase in the coating layer thickness instead of creating a new surface. This disagreed with observations from the other characterisation techniques used thus far, which were:

- XPS found increasing concentrations of all spectra components, which was interpreted as increasing frequency of nanoparticles within the mesopores.
- Porosimetry found a bimodal pore system of empty and filled pores, which denied the idea of coating propagation and growth.
- Hysteresis curves altered with loading, shifting from long-range uniform pores to none uniformity, indicative of nanoparticles randomly dispersed throughout.
- All materials examined by TEM showed a pore size of 5 nm, indicating the pore constriction was not occurring throughout the channel, as would be expected with a uniform coating.

Therefore, a second attempt was made to measure the base site density using acrylic acid titrations. Unfortunately, this technique also proved to be plagued with inconsistencies and irreproducibility, providing this time dispersion values were an order of magnitude higher than expected.

The CO₂ titrated materials can be treated thermally to monitor the temperature of desorption of the different CO₂ molecules using a mass spectrometer or thermal conductivity. The temperature-programmed desorption profiles can be then used to

evaluate CO₂ desorption at different temperatures, which correlate higher temperatures to higher adsorption strength.³²⁻³⁵ As the higher adsorption strength could be correlated to the strength of the chemical adsorption bonding, these measurements could be used as an indication of the distribution of basic strength of the active sites present in the support. Unfortunately, the signal to noise ratio was extremely low, rendering any conclusions drawn inaccurate.

The disappointing results of site titrations and temperature-programmed desorption could be attributed to the age of the materials and exposure of the materials to atmospheric CO₂ and H₂O. As magnesium oxide is a relatively weak solid base, it could be argued that using weak acid probes would only result in binding to strong sites and chemisorption. By using a stronger probe, such as sulphur dioxide, this might have been overcome resulting in all sites being chemisorbed. Finally, the use of IR-spectroscopy could elucidate the type of probe molecule adsorption, allowing for greater understanding of the basic strength of the material.

3.2.2.7. Characterisation summary

In summary, a variety of techniques were used to elucidate the chemical and physical properties of mesoporous and hierarchical MgO/SBA-15 materials. TLCT materials were found to be successfully synthesised with magnesium oxide, with ICP-OES determining both followed a linear trend with nominal loading.

X-ray diffraction was used to investigate the crystallite species within the material. Low-angle diffraction patterns found the long-range ordering of the mesopores was maintained, although hierarchical materials did exhibit reduced reflections, thought to be caused by interruption of the mesoporous phase by macroporosity. Wide-angle XRD also indicated the presence of two phases of MgO: sub 2.5 nm (in mesopore and hierarchical materials) and 15-20 nm in the highest loaded mesoporous SBA-15 (only present in mesoporous materials). This was confirmed using microscopy and X-ray photoelectron spectroscopy. These results indicated that while the hierarchical synthesis contained the functionalisation within the mesopores, the mesoporous synthesis with high loading experienced migration of MgO to the surface and the subsequent formation of larger particles outside the mesopores.

Nitrogen porosimetry was employed to probe the pore structure, with all materials exhibiting type IV isotherms indicative of ordered mesoporous silica. The materials experienced a shift in the hysteresis curve with loading, from H1 to H2. This was thought to be caused by the formation of non-uniform pores as a result of sub 2.5 nm MgO nanoparticle formation within the mesoporous domain. Pore size distribution determined a bimodal pore size, empty and filled, whose population shifted as loading increased. This result supported the assumption of randomly distributed nanoparticles <2.5 nm phase within the pore network, instead of the formation of a uniform wall coating. In addition, mesoporous materials exhibited changes such as increased surface area and poor dispersion of MgO. Conversely, hierarchical materials' surface areas were not affected, which could be attributed to the polystyrene hard template acting to maintain the structure and cap the mesopores during synthesis.

Finally, efforts to probe the basic sites and basic strength were unsuccessful. Base site densities and CO₂ desorption profiles were found irreproducible, in some cases an order of magnitude lower than expected values. A repeat was attempted using an acrylic acid titration, however again reproducibility proved problematic. It was concluded that the low concentration of sites and the age of the material were possible causes for extreme irreproducibility.

3.2.3 Catalytic Screening Experiments

The catalytic activity and selectivity of the MgO/SBA-15 materials were screened using the transesterification as triglycerides with three model compounds (tributylin (C₄), tricaprylin (C₈) and trilaurin (C₁₂)), to represent three different sterically bulky triglyceride feedstock. The substrate, intermediates and products were monitored using gas chromatography, with the methyl ester and triglyceride been the only ones calibrated. The approximate diameter of tributyrin was calculated as 1.06 nm using Chemdraw (**Appendix Figure 2.7**), meaning this model molecule has already the potential to cause a steric hindrance when accessing the mesopore domain.³⁶

3.2.3.1 Tributyrin (C₄) Screening at 60 °C

Both families of materials were screened at 60 °C for a period of 24 hours, with the initial rate of consumption and final conversion of tributyrin being displayed in **Figure 3.16**.

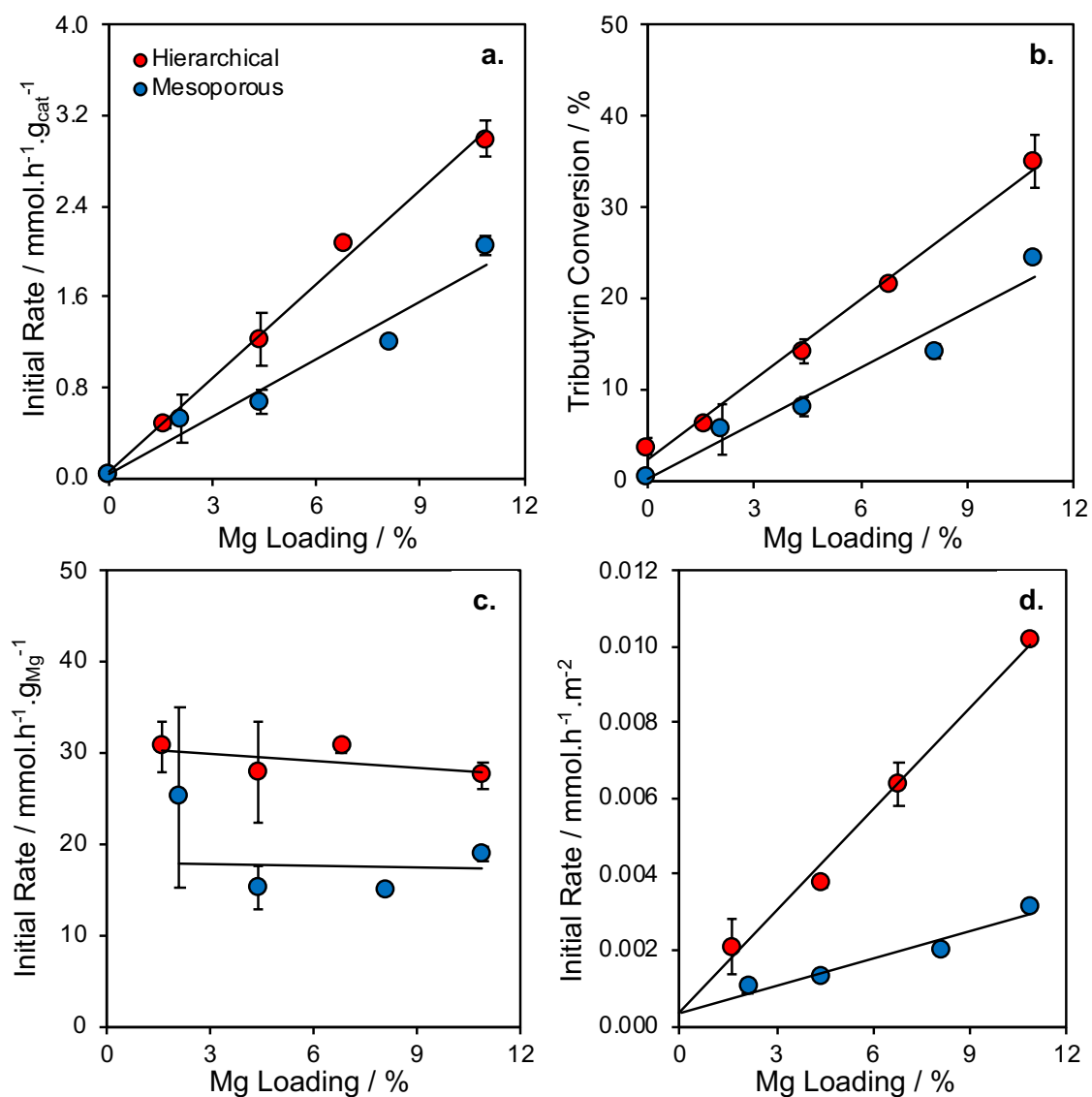


Figure 3.16. Tributyrin conversion versus magnesium loading, (a) initial rate of tributyrin consumption normalised to the mass of catalyst, (b) total tributyrin conversion after 24 hours for both materials, (c) initial rate of tributyrin consumption normalised to the mass of magnesium, (d) initial rate of tributyrin consumption normalised to surface area.

In the absence of functionality, both SBA-15 supports showed non-significant conversion of tributyrin after 24 hours, which may be a result of the acidic nature of the silica surface, as seen with the CSA samples in **Appendix Figure 2.8**.³⁷ A blank reaction was also run, resulting in no conversion detected. A linear increase in both rate (**Figure 3.16a**) and conversion (**Figure 3.16b**) was observed following the increasing magnesium loading. XPS suggests this may be caused by increasing frequency of the basic sites, with

porosimetry supporting this. When normalised to magnesium loading (**Figure 3.16c**), as determined using ICP-OES, both trends plateau with hierarchical materials displaying approximately twice the activity as the mesoporous materials. Surface area normalised rate (**Figure 3.16d**) gives no such plateaux, suggesting it is not strongly correlated to the activity. This correlates with literature, which states the importance of base concentration in the reaction.^{38, 39} It is also noted the relative similarities in surface area, with both materials containing similar pore networks. It can therefore not be concluded that surface area and other physical descriptors of the materials do not play a significant role. Further investigations need to be made using materials with different physical properties and larger substrates.

It is also worth noting that benchmark materials (MgO and hydrated magnesium silicate) were also screened (**Appendix Figure 2.9**) and normalised to magnesium content. The hierarchical material had initial productivity almost 15 times the nano-MgO, while the magnesium-silicate material exhibited negligible activity, which proves the effectiveness of the SBA-15 type catalyst. Reaction data was also normalised to base site density to give a turnover frequency (**Appendix Figure 2.10**), resulting in both materials following a similar linear trend to the reaction data, however, this data is not conclusive due to the poor quality of the site density characterisation.

The superior performance of the hierarchical materials, at almost a 50% increase for the triglyceride conversion, is thought to be caused by a less sterically hindered route to the basic functionality in the mesopores, either through more open access or reduced path length. To investigate this further, the activation energy was calculated to determine if diffusion limitations were at play.

3.2.3.2 Tributyrin Kinetic Study

To determine if the materials were diffusion or kinetically limited, a kinetic study was undertaken, displayed in **Figure 3.17**. This was performed by screening the materials at 40, 50 and 60 °C, plotting the gradient in an $\ln(\text{rate})$ vs temperature^{-1} graph. By using the Arrhenius equation, the gradient can be used to give the activation energy of the reaction.

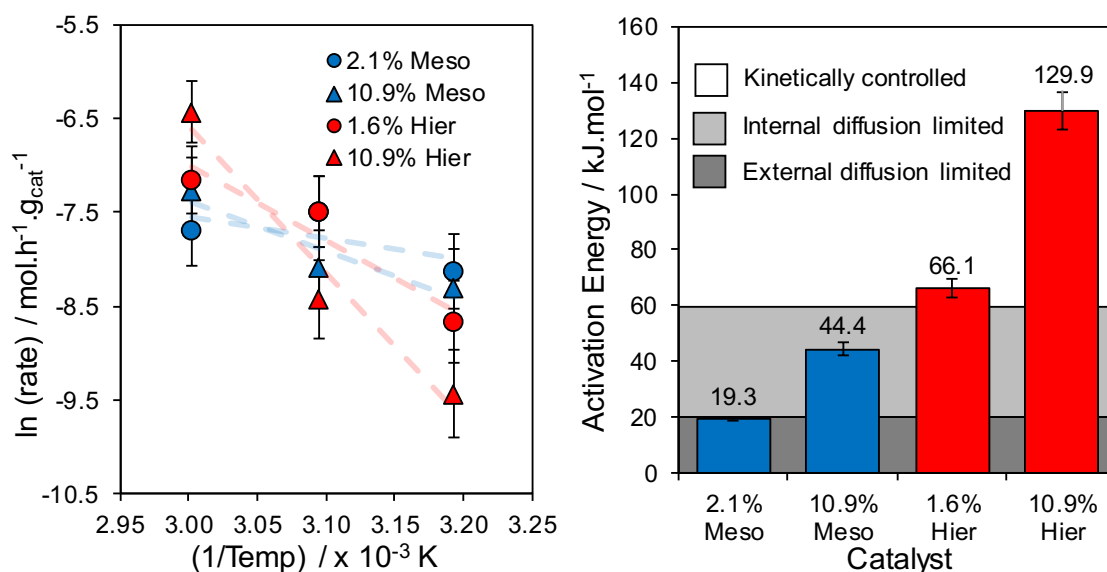


Figure 3.17. Arrhenius plot (a) of the lowest and highest loaded SBA-15 type materials and subsequent (b) activation energy of each catalyst.

Considering the substrate dimensions, solvation sphere and the mesopore channel diameter, a diffusion limitation was deemed likely. Using an Arrhenius plot (**Figure 3.17a**) it was determined mesoporous materials exhibited small activation energy (**Figure 3.17b**), indicative of a diffusion-limited material.

Activation energy at approximately 20 kJ mol^{-1} observed in the low loaded mesoporous material was symptomatic of possible internal or external diffusion limitations as the E_a was situated at the boundary. High loaded mesoporous materials exhibited increased activation energy, however, it still exhibited diffusion limitations. It is thought that this increase in activation energy was caused by the sterically unhindered 15-20 nm MgO nanoparticles, therefore rendering the E_a of 44 kJ mol^{-1} an averaging effect of the diffusion-limited mesopore sites and sterically unhindered surface sites.

The presence of a macroporous domain overcame the diffusion limitations, with the hierarchical materials exhibiting activation energies within the expected range for kinetically controlled reactions (above 60 kJ mol^{-1}).⁴⁰⁻⁴⁵ The high activation energy observed for the 10.9 wt% hierarchical material could indicate a weaker active site, however, this value of 130 kJ mol^{-1} is still within the range expected for this reaction.

This kinetic study proves the mesoporous materials were stunted by diffusion limitations, whereas the hierarchical materials were kinetically controlled. As this study was performed with a relatively small triglyceride (tributylin), larger triglycerides were screened to perceive the effect of increasing substrate chain length on activity.

3.2.3.3 Tributyrin (C₄), Tricaprylin (C₈) and Trilaurin (C₁₂) Screening at 90 °C

As activation energies proved the existence of diffusion limitations for mesoporous materials when screening small model substrates, larger triglycerides were subsequently screened. This was performed to determine if hierarchical materials continued to alleviate internal diffusion limitation as substrate size increased. The materials were screened at 90 °C, displayed in **Figure 3.18**, as at lower temperatures the larger triglycerides were insoluble. The 4.4 wt% materials were chosen due to similar magnesium content and the lack of external MgO nanoparticles on the mesoporous materials, screening only the MgO phase ideally within the mesopore domain.

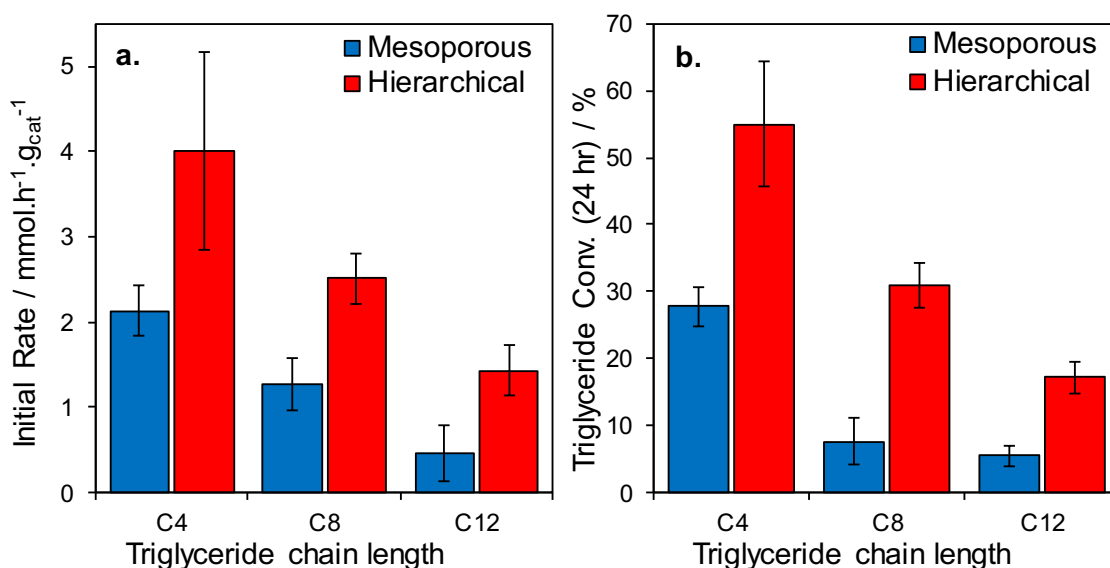


Figure 3.18. Screening data for the transesterification of triglycerides of different sizes, (a) initial rate of triglyceride consumption normalised to catalyst mass and (b) total conversion after 24 hours.

A decrease in initial activity was observed for both materials as the chain length of the triglyceride was increased (**Figure 3.18a**). However, when compared to the final conversion (**Figure 3.18b**), the hierarchical materials significantly outperformed the mesoporous materials, resulting in an almost fourfold conversion increase when screening with trilaurin (C₁₂). Turn over frequencies were calculated for this screening data, with the subsequent TOF enhancement from hierarchical pore architecture both displayed in **Appendix Figure 2.11**, however, the error associated renders the data inconclusive.

While a loss in activity was experienced for both supports, the mesoporous support was affected to a greater degree. The effectiveness of a meso-macroporous network has been demonstrated, however the results also highlight that functionalising within the

mesopore creates diffusion limitations that ultimately reduce the catalytic performance. When using larger triglycerides, the diffusion limitation is the accessing of the mesopore, therefore any material with functionality solely located there will suffer likewise. One route to mitigate this is through an expansion of the mesopores either using hydrothermal treatment⁴⁶ or swelling agents.¹⁹ These techniques might allow less hindered mesoporous access, which when combined with a macroporous network would result in highly effective industrially viable material.

3.2.3.4 Methanol:Tributyrin Ratio Study

Typical industrial base catalysed biodiesel production employs a 9-12:1 ratio for reduced solvent usage and altering viscosity.^{47, 48} Different ratios of methanol to tributyrin were screened to determine what effect the substrate concentration had (**Figure 3.19**).

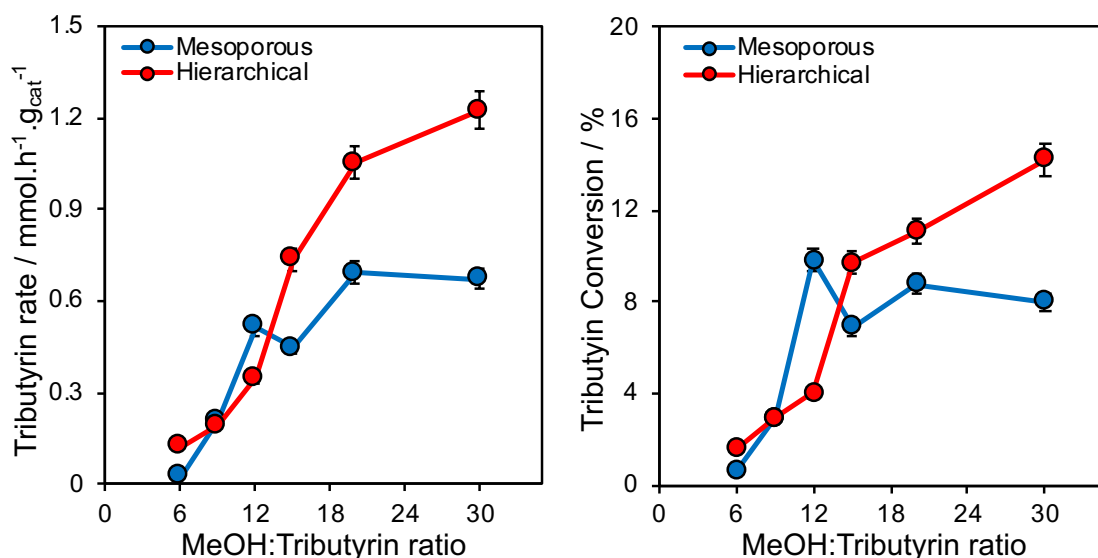


Figure 3.19. (a) Initial rate of triglyceride consumption and (b) final conversion after 24 hours as a function of methanol to tributyrin ratio for mesoporous and hierarchical 4.4 wt% MgO/SBA-15.

The results displayed in **Figure 3.19** showed the 30:1 ratio, employed in all previous screening studies, was the optimum tested. Viscosity is often a problem when scaled up to industrial capacity, meaning the reactant ratios must be altered between different feedstocks to allow for optimum diffusion and activity.

Both mesoporous and hierarchical MgO/SBA-15 showed an increased initial rate and final conversion with increased methanol to tributyrin ratio. This could be linked to the increased viscosity of the reaction mixture at low ratios. This is unlikely, however, as tributyrin is a low viscosity triglyceride. A more likely cause of the decreased activity is the effect of the ratio on the methoxide formation equilibrium.

The trends observed here are likely an effect of the transesterification equilibrium being pushed in favour of the products. As Le Chatelier's principle dictates: if a constraint (in this case concentration of a reactant) is applied to a system in equilibrium, the equilibrium will shift so as to tend to counteract the effect of the constraint.⁴⁹ By increasing the methanol concentration, the methoxide concentration also increases, causing the subsequent equilibrium shift to counteract this.

While hierarchical materials showed a sustained increase in activity with ratio, mesoporous materials plateaued above 15-20:1. It could be that above this ratio, the increased concentrations effect on the equilibrium is negligible, however, the opposite is seen with hierarchical materials. One possible explanation is that above this ratio, the concentration of tributyrin is too low, causing the methanol to preferentially situate in the mesopores. Due to the steric hindrance, the tributyrin may not easily interact with the subsequent methoxide, causing the activity to become stunted. This is not observed in the hierarchical materials, as the macropores allow the methoxide filled mesopores to interact with the tributyrin.

3.2.3.5 Recycling Study at 60 °C

Lastly, the longevity of the catalyst was determined by sequential recovery and reuse of the spent mesoporous material, displayed in **Figure 3.20**. Recovery was performed using vacuum filtration followed by washing with methanol to remove any substrate or product physisorbed to the surface. The resultant powder was either dried at room temperature and pressure for 12 hours or calcined at 380 °C for 5 hours to decompose MgCO_3 and Mg(OH)_2 . By comparing dried versus calcination, the gradual build-up of magnesium hydroxide and carbonate was compared. The initial rate was used as the transesterification reaction is an equilibrium driven reaction.

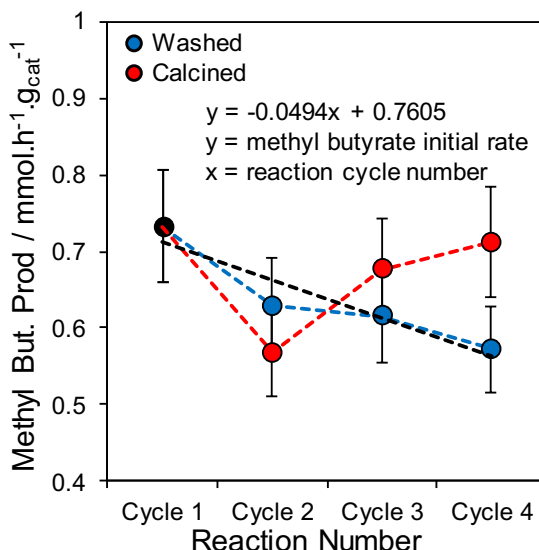


Figure 3.20. Methyl butyrate initial productivity as a function of sequential reaction cycles for mesoporous 4.4 wt% MgO/SBA-15, recovered and regenerated using washing or calcination.

Firstly, it was noted that regardless of the recovery procedure, activity was maintained to a large degree. A gradual drop was observed for the initial productivity of methyl butyrate with respect to the washed samples as the cycle number increased, whereas calcined materials retained their activity. This could indicate the presence of atmospheric or reactant poisoning on the washed samples causing a drop in basicity and therefore activity.

The loss in initial rate may suggest the poisoning Mg phases decreased the catalytic performance gradually, with ICP confirming leaching was not the cause. It was estimated using the equation in **Figure 3.20** a complete loss of activity after approximately 15 cycles if methanol washing was used, however further cycles are required to confirm this. While this does correlate with typical atmosphere sensitive catalytic species, the error associated with this recycling study is too large to draw solid conclusions. Further experiments are required to confirm this observation.

3.2.3.6 Catalytic Screening Summary

The materials synthesised and characterised in **Section 3.2.2** were screened using several transesterification experiments. The two clear conclusions were: activity increased in a linear trend with loading, and hierarchical material outperformed their mesoporous counterparts.

The cause of the increased activity with loading is thought to be caused by increased functionalisation of mesopores with MgO nanoparticles below 2.5 nm. This is supported by porosimetry and XPS, by comparing hysteresis curves, pore size distributions and component intensities.

Hierarchical materials were found to give superior catalytic activity relative to the mesoporous materials, shown using the Arrhenius equation and screening with larger triglycerides to be decreased diffusion limitations. The viscosity of the substrate was also investigated by varying the reactant ratio, however, it was determined that the substrate viscosity was too low to be of any effect. It is thought that at higher viscosities, diffusion limitations would separate the activities of mesoporous and hierarchical catalysts, however, this is unsupported.

The materials were recovered and reused, maintaining a large component of their activity. It was decided that atmospheric or reaction compound contamination could be a major concern, and therefore half of the recovered catalyst was calcined to remove these poisons. Calcined materials appeared to retain their activity to a greater degree, however further catalytic cycles would be required to confirm this.

3.3 Conclusions and Recommendations for Further Work

One-pot true liquid crystal templated mesoporous and hierarchical MgO/SBA-15 has been successfully synthesised and their activity for the transesterification of tributyrin and larger triglycerides has been demonstrated. It was determined using TEM and XPS that 15-20 nm MgO nanoparticles formed outside the pore network of the mesoporous materials above 8 wt% Mg. By contrast, hierarchical MgO/SBA-15 was found to retain MgO within the material, with XPS and ICP showing the uniform distribution of Mg. It's theorised that the macroporous template acts to cap the mesopores thereby preventing the bleeding of the magnesium species onto the surface, but also enables the retention of pore structure within the material, however, these claims are unconfirmed.

Long-range pore ordering was observed using porosimetry, LAXRD and TEM, with a change in N₂ porosimetry isotherm from type IV H1 to type IV H2 attributed to the mesopores changing from uniform to none uniform. This suggests that the mesoporous situated MgO is in the form of randomly distributed nanoparticles rather than a uniform pore wall coating, which is supported with XPS. Site titrations were performed with little success, primarily due to irreproducibility.

All materials were screened for the transesterification of tributyrin as a model reaction. It was found that the hierarchical materials exhibited a higher conversion and initial methyl butyrate productivity than the mesoporous materials. Kinetic studies determined the cause of this differing activity was internal diffusion limitations present within the mesoporous material. Further screening with larger chain triglycerides demonstrated the superior performance of the hierarchical catalysts, highlighting the benefits of a meso-macroporous network embedded in a catalytic system designed for reactions with large substrate feedstocks. Ultimately, the drawback of using a mesoporous restricted functionality meant diffusion limitations were still at play at higher triglyceride size.

The ratio between alcohol and substrate was also investigated, finding a reduced activity at lower ratios. This is thought to be caused by an equilibrium shift as the concentration of methanol is reduced. Recycling studies established spent materials retained their activity to a major degree, however, a slight deactivation was observed for materials washed with methanol, attributed to a build-up of contaminants at the surface.

Finally, if this work was continued there are many available routes. More accurate site characterisation would be a priority, combined with elemental mapping of the active phase using EDX. Mercury porosimetry would also be very useful in probing the

macroporous regions. This has been impractical to achieve during the project, primarily due to equipment error and time limitations. Secondly, industrially relevant reactions should be explored, such as a tributyrin scale up, using industrial feedstocks or shifting to a flow reactor. Time constraints have not allowed for these experiments. Considering the results, further material optimisation may be required before viability for industrial applications is reached.

From a materials standpoint, there are many avenues of further advancement. While MgO has been shown to be effective as a base functionality for SBA-15, there is potential to further functionalise SBA-15 with other alkaline earth metal oxides.⁵⁰⁻⁵³ Leaching is a major concern with CaO and SrO,⁵⁴ however work with mixed metal oxides has been shown to mitigate this.^{55, 56} Work with Ca mixed oxides has also been shown to dramatically increase basicity as has doping with alkali metals.^{3, 55, 57-62} The catalytic materials synthesised in this chapter have high time and monetary costs associated with its synthesis, and effort needs to be made to mitigate this. Recycled materials have been used previously,⁶³ however finding a suitable recycled material as a nano-sized macropore template will be extremely difficult.

Bifunctionality is an excellent opportunity to utilise the proven basicity of this material while retaining the increased diffusion of material that comes with macropore incorporation. Further functionalisation of the MgO/SBA-15 material with gold nanoparticles was therefore pursued in subsequent chapters. These bifunctional catalysts will be used in the selective oxidation of alcohols and subsequent coupling with amines to imines. These transformations have been found extremely favoured under basic conditions, meaning if the catalyst has basic sites combined with a noble metal, base additives may not be required. This is beneficial, as the reduction of separation steps for base recovery and product purification reduces energy and time costs of the process.

3.4 References

1. Y. L. Wei, Y. M. Wang, J. H. Zhu and Z. Y. Wu, In-situ coating of SBA-15 with MgO: direct synthesis of mesoporous solid bases from strong acidic systems, *Advanced Materials*, 2003, **15**, 1943-1945.
2. R. Wang, X. Liu, Y. He, Q. Yuan, X. Li, G. Lu and T. Zhang, The humidity-sensitive property of MgO-SBA-15 composites in one-pot synthesis, *Sensors and Actuators B: Chemical*, 2010, **145**, 386-393.
3. Z. Y. Wu, Q. Jiang, Y. M. Wang, H. J. Wang, L. B. Sun, L. Y. Shi, J. H. Xu, Y. Wang, Y. Chun and J. H. Zhu, Generating superbasic sites on mesoporous silica SBA-15, *Chemistry of Materials*, 2006, **18**, 4600-4608.
4. Y. M. Wang, Z. Y. Wu, Y. L. Wei and J. H. Zhu, In situ coating metal oxide on SBA-15 in one-pot synthesis, *Microporous and Mesoporous Materials*, 2005, **84**, 127-136.
5. D. Y. Zhao, J. L. Feng, Q. S. Huo, N. Melosh, G. H. Fredrickson, B. F. Chmelka and G. D. Stucky, Triblock copolymer syntheses of mesoporous silica with periodic 50 to 300 angstrom pores, *Science*, 1998, **279**, 548-552.
6. S. G. Wainwright, C. M. A. Parlett, R. A. Blackley, W. Z. Zhou, A. F. Lee, K. Wilson and D. W. Bruce, True liquid crystal templating of SBA-15 with reduced microporosity, *Microporous and Mesoporous Materials*, 2013, **172**, 112-117.
7. J. J. Creasey, C. M. A. Parlett, J. C. Manayil, M. A. Isaacs, K. Wilson and A. F. Lee, Facile route to conformal hydrotalcite coatings over complex architectures: a hierarchically ordered nanoporous base catalyst for FAME production, *Green Chemistry*, 2015, **17**, 2398-2405.
8. K. Narasimharao, A. Lee and K. Wilson, Catalysts in Production of Biodiesel: A Review, *Journal of Biobased Materials and Bioenergy*, 2007, **1**, 19-30.
9. L. B. Sun, X. Q. Liu and H. C. Zhou, Design and fabrication of mesoporous heterogeneous basic catalysts, *Chemical Society Reviews*, 2015, **44**, 5092-5147.
10. C. Suryanarayana and M. G. Norton, X-Ray Diffraction: A Practical Approach, Springer US, 1998.
11. J. M. Montero, P. Gai, K. Wilson and A. F. Lee, Structure-sensitive biodiesel synthesis over MgO nanocrystals, *Green Chemistry*, 2009, **11**, 265-268.
12. K. O'Connell and J. R. Regalbuto, High sensitivity silicon slit detectors for 1 nm powder XRD size detection limit, *Catalysis Letters*, 2015, **145**, 777-783.
13. M. Durandurdu, Ferromagnetism in amorphous MgO, *Philosophical Magazine*, 2017, **97**, 2129-2141.
14. B. Bharatiya, G. Ghosh, P. Bahadur and J. Mata, The effects of salts and ionic surfactants on the micellar structure of tri-block copolymer PEO-PPO-PEO in aqueous solution, *Journal of Dispersion Science and Technology*, 2008, **29**, 696-701.
15. G. Wanka, H. Hoffmann and W. Ulbricht, Phase diagrams and aggregation behavior of poly(oxyethylene)-poly(oxypropylene)-poly(oxyethylene) triblock copolymers in aqueous solutions, *Macromolecules*, 1994, **27**, 4145-4159.
16. A. Galarneau, H. Cambon, F. Di Renzo, R. Ryoo, M. Choi and F. Fajula, Microporosity and connections between pores in SBA-15 mesostructured silicas as a function of the temperature of synthesis, *New Journal of Chemistry*, 2003, **27**, 73-79.

17. M. Thommes and K. A. Cychoz, Physical adsorption characterization of nanoporous materials: progress and challenges, *Adsorption*, 2014, **20**, 233-250.
18. K. A. Cychoz, R. Guillet-Nicolas, J. Garcia-Martinez and M. Thommes, Recent advances in the textural characterization of hierarchically structured nanoporous materials, *Chemical Society Reviews*, 2017, **46**, 389-414.
19. S.-Y. Chen, Y.-T. Chen, J.-J. Lee and S. Cheng, Tuning pore diameter of platelet SBA-15 materials with short mesochannels for enzyme adsorption, *Journal of Materials Chemistry*, 2011, **21**, 5693-5703.
20. J. C. Manayil, A. Osatiashtiani, A. Mendoza, C. M. A. Parlett, M. A. Isaacs, L. J. Durndell, C. Michailof, E. Heracleous, A. Lappas, A. F. Lee and K. Wilson, Impact of macroporosity on catalytic upgrading of fast pyrolysis bio-oil by esterification over silica sulfonic acids, *ChemSusChem*, 2017, **10**, 3506-3511.
21. T. Sen, G. J. T. Tiddy, J. L. Casci and M. W. Anderson, Synthesis and characterization of hierarchically ordered porous silica materials, *Chemistry of Materials*, 2004, **16**, 2044-2054.
22. C. M. A. Parlett, M. A. Isaacs, S. K. Beaumont, L. M. Bingham, N. S. Hondow, K. Wilson and A. F. Lee, Spatially orthogonal chemical functionalization of a hierarchical pore network for catalytic cascade reactions, *Nature Materials*, 2016, **15**, 178.
23. Z. Liu, Z. Yin, C. Cox, M. Bosman, X. Qian, N. Li, H. Zhao, Y. Du, J. Li and D. G. Nocera, Room temperature stable CO_x free H₂ production from methanol with magnesium oxide nanophotocatalysts, *Science Advances*, 2016, **2**.
24. S. Seal, S. Krezoski, S. E. Hardcastle, T. L. Barr, D. H. Petering, C. F. Cheng, J. Klinowski and P. H. Evans, Investigations of the surface chemistry of pathogenic silicates, *Journal of Vacuum Science & Technology A*, 1995, **13**, 1260-1266.
25. Y. S. Jin, Q. J. Yan, Z. R. Yin and Y. Chen, Secondary ion mass spectrometry and X-ray photoelectron spectroscopy of Na₂MoO₄/SiO₂ catalysts for methane oxidative coupling, *Journal of the Chemical Society, Faraday Transactions*, 1995, **91**, 381-384.
26. K. S. Seal S., Barr T.L., Petering D.H., Klinowski J., and Evans P.H., *Proceedings of the Royal Society B: Biological Sciences*, 1996, **263**.
27. E. Paparazzo, XPS analysis of oxides, *Surface and Interface Analysis*, 1988, **12**, 115-118.
28. H. Seyama and M. Soma, Bonding-state characterization of the constituent elements of silicate minerals by X-ray photoelectron spectroscopy, *Journal of the Chemical Society, Faraday Transactions 1: Physical Chemistry in Condensed Phases*, 1985, **81**, 485-495.
29. J. A. N. C. Haider, Jr., W. E. Swartz, Jr., Valence and core electron spectra of Mg in MgO in evaporated thin films, *Zeitschrift für Naturforschung A*, 1975, **30a**.
30. J.M. Rimsza, E.G. Sorte, and T.M. Alam, Hydration and Hydroxylation of MgO in Solution: NMR Identification of Proton-Containing Intermediate Phases, *ACS Omega*, 2019, **4**, 1033-1044.
31. S. Da Ros, M. D. Jones, D. Mattia, J. C. Pinto, M. Schwaab, F. B. Noronha, S. A. Kondrat, T. C. Clarke, S. H. Taylor, Ethanol to 1,3-Butadiene Conversion by using ZrZn-Containing MgO/SiO₂ Systems Prepared by Co-precipitation and Effect of Catalyst Acidity Modification, *ChemCatChem*, 2016, **8**, 2376.

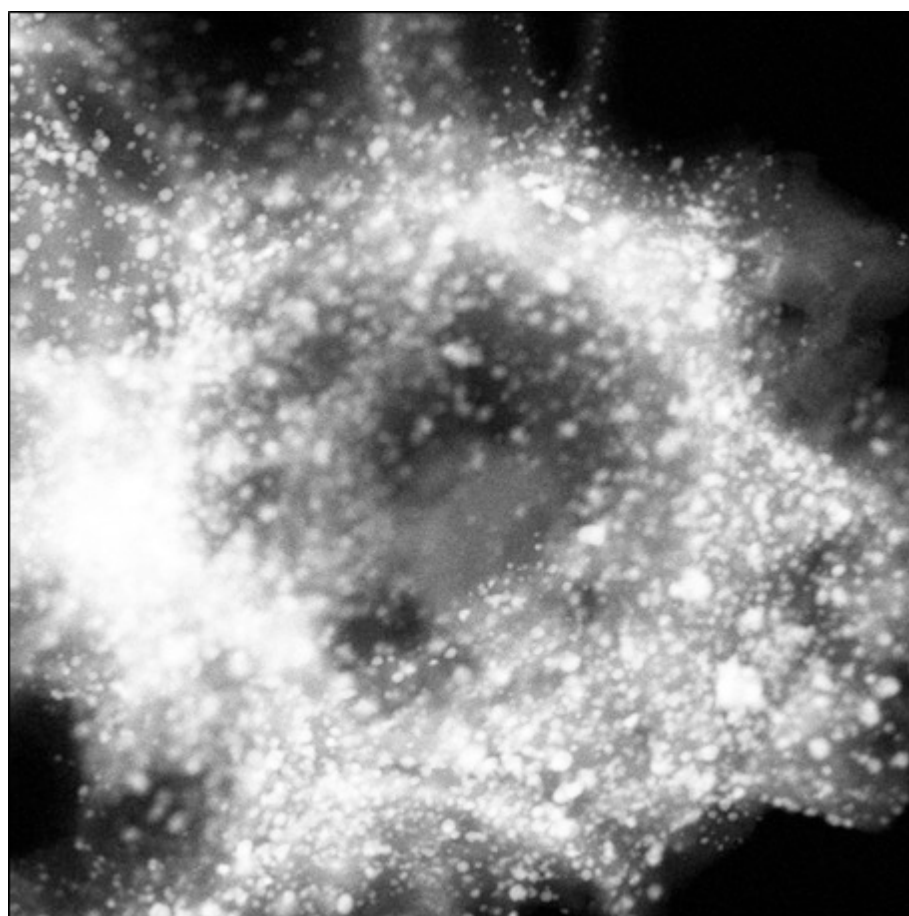
32. J. I. Di Cosimo, V. K. Díez, C. Ferretti and C. R. Apesteguía, *Catalysis: Volume 26, Chapter 1*, The Royal Society of Chemistry, 2014, **26**, 1-28.
33. T. Selvamani, A. Sinhamahapatra, D. Bhattacharjya and I. Mukhopadhyay, Rectangular MgO microsheets with strong catalytic activity, *Materials Chemistry and Physics*, 2011, **129**, 853-861.
34. L. She, J. Li, Y. Wan, X. Yao, B. Tu and D. Zhao, Synthesis of ordered mesoporous MgO/carbon composites by a one-pot assembly of amphiphilic triblock copolymers, *Journal of Materials Chemistry*, 2011, **21**, 795-800.
35. X. Fu, N. Zhao, J. Li, F. Xiao, W. Wei and Y. Sun, Carbon dioxide capture by MgO-modified MCM-41 materials, *Adsorption Science & Technology*, 2009, **27**, 593-601.
36. H. D. Hanh, N. T. Dong, K. Okitsu, R. Nishimura and Y. Maeda, Biodiesel production through transesterification of triolein with various alcohols in an ultrasonic field, *Renewable Energy*, 2009, **34**, 766-768.
37. M. Weller, T. Overton, J. Rourke and F. Armstrong, *Inorganic Chemistry*, OUP Oxford, 2014.
38. N. Boz and M. Kara, Solid Base Catalyzed Transesterification of Canola Oil, *Chemical Engineering Communications*, 2008, **196**, 80-92.
39. W. Zhou, S.K. Konar, and D.G.B. Boocock, Ethyl esters from the single-phase base-catalyzed ethanolysis of vegetable oils, *Journal of the American Oil Chemist's Society*, 2003, **80**, 367-371.
40. M. D. Kostić, A. Bazargan, O. S. Stamenković, V. B. Veljković and G. McKay, Optimization and kinetics of sunflower oil methanolysis catalyzed by calcium oxide-based catalyst derived from palm kernel shell biochar, *Fuel*, 2016, **163**, 304-313.
41. T. Maneerung, S. Kawi, Y. Dai and C.-H. Wang, Sustainable biodiesel production via transesterification of waste cooking oil by using CaO catalysts prepared from chicken manure, *Energy Conversion and Management*, 2016, **123**, 487-497.
42. S. Niu, Y. Zhou, H. Li, C. Lu and L. Liu, An investigation on the catalytic capability of the modified white mud after activation in transesterification and kinetic calculation, *Energy*, 2015, **89**, 982-989.
43. S. H. Teo, A. Islam and Y. H. Taufiq-Yap, Algae derived biodiesel using nanocatalytic transesterification process, *Chemical Engineering Research and Design*, 2016, **111**, 362-370.
44. N. Y. Yahya, N. Ngadi, S. Wong and O. Hassan, Transesterification of used cooking oil (UCO) catalyzed by mesoporous calcium titanate: Kinetic and thermodynamic studies, *Energy Conversion and Management*, 2018, **164**, 210-218.
45. L. Zhao, Z. Qiu and S. M. Stagg-Williams, Transesterification of canola oil catalyzed by nanopowder calcium oxide, *Fuel Processing Technology*, 2013, **114**, 154-162.
46. D. Zhao, Q. Huo, J. Feng, B. F. Chmelka and G. D. Stucky, Nonionic triblock and star diblock copolymer and oligomeric surfactant syntheses of highly ordered, hydrothermally stable, mesoporous silica structures, *Journal of the American Chemistry Society*, 1998, **120**, 6024-6036.
47. M. Elkady, A. Zaatout and O. Balbaa, Production of biodiesel from waste vegetable oil via KM micromixer, *Journal of Chemistry*, 2015, **2015**, 1-9.

48. A. Matassoli, I. Corrêa, M. Portilho, C. Veloso and M. Langone, Enzymatic synthesis of biodiesel via alcoholysis of palm oil, *Applied biochemistry and biotechnology*, 2008, **155**, 347-355.
49. P. Atkins, J. de Paula and J. Keeler, *Physical Chemistry*, Oxford University Press, Great Britain, 8th edition, 2006.
50. M. C. G. Albuquerque, I. Jimenez-Urbistondo, J. Santamaria-Gonzalez, J. M. Merida-Robles, R. Moreno-Tost, E. Rodriguez-Castellon, A. Jimenez-Lopez, D. C. S. Azevedo, C. L. Cavalcante and P. Maireles-Torres, CaO supported on mesoporous silicas as basic catalysts for transesterification reactions, *Applied Catalysis A-General*, 2008, **334**, 35-43.
51. C. H. Huang, K. P. Chang, C. T. Yu, P. C. Chiang and C. F. Wang, Development of high-temperature CO₂ sorbents made of CaO-based mesoporous silica, *Chemical Engineering Journal*, 2010, **161**, 129-135.
52. H. Sun, J. X. Han, Y. Q. Ding, W. Li, J. Z. Duan, P. Chen, H. Lou and X. M. Zheng, One-pot synthesized mesoporous Ca/SBA-15 solid base for transesterification of sunflower oil with methanol, *Applied Catalysis A-General*, 2010, **390**, 26-34.
53. A. Tangy, I. N. Pulidindi and A. Gedanken, SiO₂ beads decorated with SrO nanoparticles for biodiesel production from waste cooking oil using microwave irradiation, *Energy & Fuels*, 2016, **30**, 3151-3160.
54. M. L. Granados, D. M. Alonso, I. Sádaba, R. Mariscal and P. Ocón, Leaching and homogeneous contribution in liquid phase reaction catalysed by solids: The case of triglycerides methanolysis using CaO, *Applied Catalysis B: Environmental*, 2009, **89**, 265-272.
55. H. Li, S. L. Niu, C. M. Lu and J. Li, Calcium oxide functionalized with strontium as heterogeneous transesterification catalyst for biodiesel production, *Fuel*, 2016, **176**, 63-71.
56. O. Kikhtyanin, L. Čapek, L. Smoláková, Z. Tišler, D. Kadlec, M. Lhotka, P. Diblíková and D. Kubička, Influence of Mg–Al mixed oxide compositions on their properties and performance in Aldol condensation, *Industrial & Engineering Chemistry Research*, 2017, **56**, 13411-13422.
57. J. M. Montero, K. Wilson and A. F. Lee, Cs Promoted Triglyceride Transesterification Over MgO Nanocatalysts, *Topics in Catalysis*, 2010, **53**, 737-745.
58. R. S. Watkins, A. F. Lee and K. Wilson, Li–CaO catalysed tri-glyceride transesterification for biodiesel applications, *Green Chemistry*, 2004, **6**, 335-340.
59. Z. Z. Wen, X. H. Yu, S. T. Tu, J. Y. Yan and E. Dahlquist, Synthesis of biodiesel from vegetable oil with methanol catalyzed by Li-doped magnesium oxide catalysts, *Applied Energy*, 2010, **87**, 743-748.
60. P. S. Varbanov, J. J. Klemes, S. R. W. Alwi, J. Y. Yong and X. Liu, Process integration, modelling and optimisation for energy saving and pollution reduction, Milano, 2015, **45**, 1291-1296.
61. S. H. Teo, Alumina supported/unsupported mixed oxides of Ca and Mg as heterogeneous catalysts for transesterification of *Nannochloropsis* sp. microalga's oil, *Energy conversion and management*, 2014, **88**, 1193-1199
62. S. Limmanee, T. Naree, K. Bunyakiat and C. Ngamcharussrivichai, Mixed oxides of Ca, Mg and Zn as heterogeneous base catalysts for the synthesis of palm kernel oil methyl esters, *Chemical Engineering Journal*, 2013, **225**, 616-624.

63. G. Y. Chen, R. Shan, S. Y. Li and J. F. Shi, A biomimetic silicification approach to synthesize CaO-SiO₂ catalyst for the transesterification of palm oil into biodiesel, *Fuel*, 2015, **153**, 48-55.

Chapter 4

Gold functionalised MgO/SBA-15 mesoporous and hierarchical materials for the selective oxidation of benzyl alcohol



Hierarchical SBA-15 supported gold nanoparticle

4.1 Introduction

As mentioned in **Section 1.1.4.3**, one issue faced with the selective oxidation of benzyl alcohol is maintaining selectivity towards the benzaldehyde product, preventing the over oxidation to the acid or ester coupling product.

In the previous chapter, materials were developed displaying excellent basicity and reduced diffusion limitations (shown using the transesterification of triglycerides). While effective catalysts in their own right, it was decided to use them as high surface area basic supports for the selective oxidation of benzyl alcohol. Green chemistry dictates the move to more sustainable reactions, with the selective oxidation of benzyl alcohol being a prime candidate. Typical synthesis requires the use of a base additive, however by employing a solid base material we hope to omit this requirement.

The initial goals for this chapter are therefore finding a suitable synthesis to impregnate gold nanoparticles within the mesopore network of MgO/SBA-15 material investigated in the previous chapter. A concern faced by many studies is an unselective gold species obtained when chlorine is present in the gold precursor species.¹⁻⁴ To avoid this, many methods utilise strong basic reducing agents to hydrolyse the gold complex to form $\text{Au}(\text{OH})_x^-$ with the number of hydroxyls dependant on the pH. Of these methods, the most promising are deposition precipitation, double impregnation method and liquid phase reductive deposition.^{5, 6} An added benefit of using these methods is exploiting the isoelectric point of the surfaces in the MgO/SBA-15 materials. Using a pH between 6-9, we aim to selectively functionalise the MgO species, encouraging synergistic interactions.

After a suitable gold synthesis has been chosen, the model reaction conditions must be optimised. This will be achieved by using chemometrics, a common methodology used in the chemical industry. Finally, the materials will be investigated, altering variables in their production to better understand where the activity is derived from.

4.2 Results and Discussion

The previous chapter was a large in-depth study of the materials using a wide variety of characterisation techniques. This was useful in determining as much about the chemical and physical characteristics of the materials as possible. However, it severely limited the number of materials studied.

The following experimental chapter is using a more efficient approach to characterisation, omitting SEM and site titration, due to the continued use of TEM and the inaccuracy of site titration respectively. This efficient characterisation sequence allows for a larger range of materials to be investigated, as well as multiple variables.

Because of this streamlined mind-set, it was possible to investigate:

- Multiple synthesis methods from the literature (DIM, DP, LPRD) described in **Section 2.2.5-7**
- Optimising reaction conditions instead of using literature conditions.
- The influence of different variables on the reaction (Reaction temperature, stirring speed, substrate concentration, porosity, heat treatment).
- The effect of different heat treatments on the materials.
- The temperature dependence of materials.
- The effect of Mg and Au loading.
- Possible causes of deactivation.
- The use of greener and industrially relevant conditions.

4.2.1 Preliminary Synthesis Study

The following section will investigate suitable synthesis methods of gold nanoparticles deposited onto base functionalised ordered mesoporous and hierarchically porous silica, reaction optimisation using chemometrics, exploring heating treatments, and exploring different causes of catalytic deactivation.

4.2.1.1 Preliminary Study Characterisation

The three synthesis methods explained in **Section 2.2.5-7** were used to impregnate gold into mesoporous and hierarchical MgO/SBA-15. To determine if the gold functionalisation was successful, ICP-OES was employed to determine the loading of both magnesium (**Figure 4.1a**) and gold (**Figure 4.1b**) functionalities. It was observed that materials retained their Mg content post impregnation to a large extent with a small amount lost into solution. With a theoretical loading of one weight percent, the gold impregnation ranged from partially successful to unsuccessful. Literature has reported the poor loading generated when deposition precipitation (DP) procedure is used,^{5, 6} which was verified in this work. Both liquid phase reductive deposition (LPRD) and double impregnation method (DIM) showed approximately half the nominal loading. This was, however, an order of magnitude better than DP materials. It could be argued the DIM materials exhibit a higher loading than the LPRD materials, although the difference is within error.

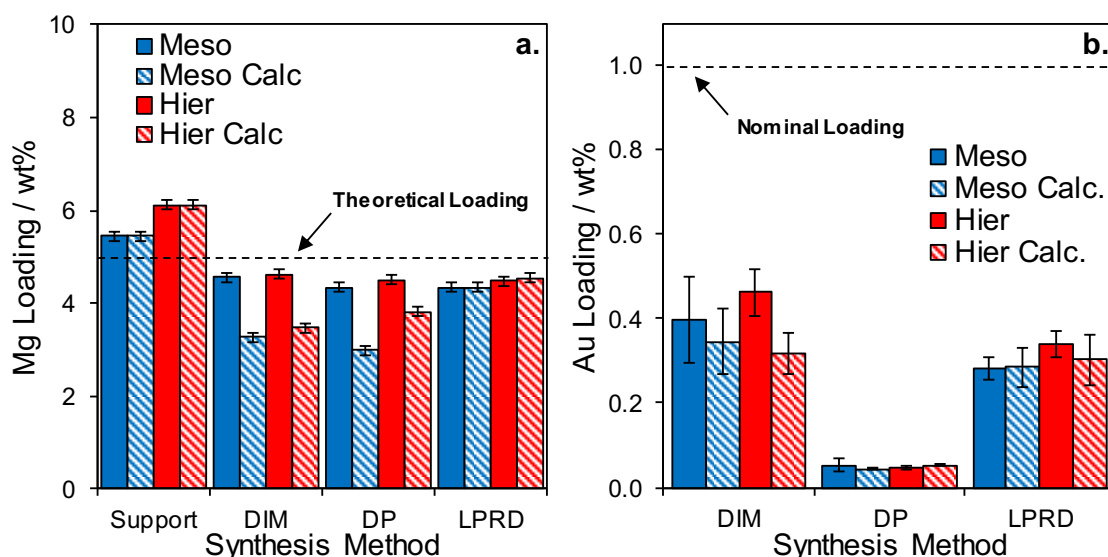


Figure 4.1. ICP-OES atomic weight percentages of (a) magnesium and (b) gold for DP, DIM and LPRD methods.

One of the larger difficulties faced when impregnating silica-based catalysts with gold is the mildly acidic nature of the support. This hinders the successful deposition of gold

onto the silica surface. As previously mentioned in **Section 4.1**, the ligands of the precursor are hydrolysed to form $\text{Au}(\text{OH})_x^-$ which has been shown to increase the selectivity of the resultant materials.⁶ A requirement of this is an alteration of the pH, which changes the surface environment of the support. The isoelectric point of a support material, in an aqueous solution, is the pH at which surface-bound hydroxyls (M-OH) are neutral.^{7, 8} At a pH above $(\text{M}-\text{O})^-$ or below $(\text{M}-\text{OH}_2)^+$ this point the surface becomes electronically charged.⁹ The resultant negatively charged Au complex approaching the surface would, therefore, become repelled if a surface was at a pH above its isoelectric point.

This is, unfortunately, the case with silica, which has an isoelectric point of 2-5.^{10, 11} All three synthesis methods employ a pH of between 6 to 9, therefore the adsorption and subsequent impregnation are electronically disfavoured. This is another benefit of using a support already functionalised with MgO, which has an isoelectric point of 10.5,¹² thereby preferentially favouring the impregnation specifically to the $\text{Mg}-\text{OH}_2^+$ surface. This allows for greater synergistic interactions between the two species, and also benefits from the fantastic physical properties of SBA-15 without being hindered by the acidity of the silica surface.

This, in turn, may explain the poor loading of DP versus LPRD materials, both using methods which call for the filtering of reaction solution from the impregnated material. DP uses a sodium hydroxide solution to increase the pH to 9, whereas the LPRD method uses a less concentrated solution to reach pH 6. It is suggested that at pH 9, the MgO surface has a weaker positive charge, thereby not causing as strong interaction between itself and the gold complex, resulting in poor loading.

Wide and low-angle X-ray diffraction patterns of mesoporous and hierarchical MgO/SBA-15 are displayed in **Figure 4.2**. The wide-angle pattern backgrounds have been subtracted and the amorphous silica peak at 22-25° removed to better stack the patterns for comparison.

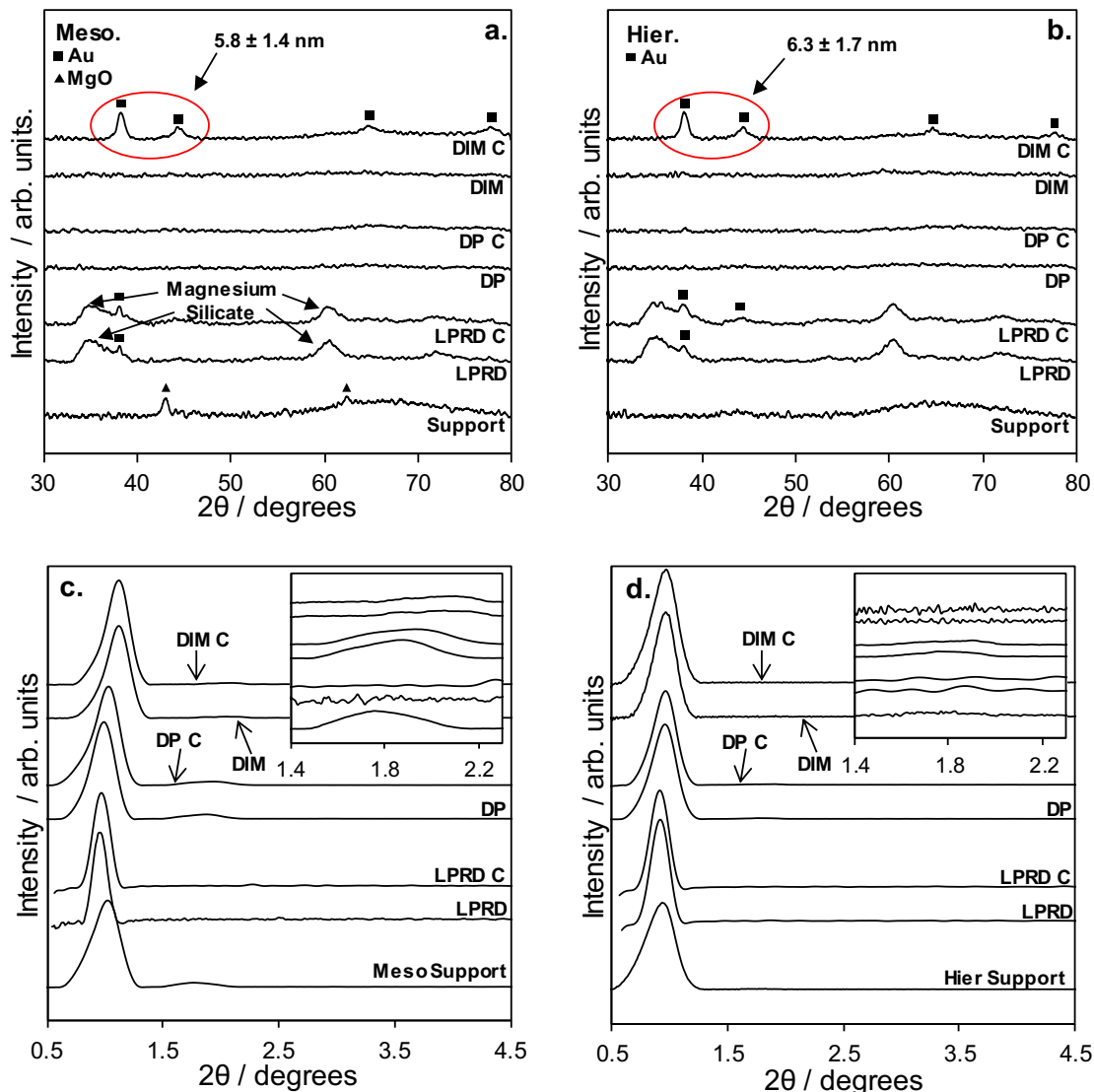


Figure 4.2. Wide-angle X-ray diffraction patterns for (a) mesoporous and (b) hierarchical materials impregnated using the three techniques. Low-angle X-ray diffraction patterns for (c) mesoporous and (d) hierarchical materials with inset of 11 and 20 reflections.

Wide X-ray showed 3 clear features. The first feature was the gold reflection, with the most prominent peak at approximately 38° representing $\text{Au}_{111,13}$ visible in the LPRD before and post heat-treatment, and DIM only post heat treatment. No reflections were observed for DP synthesis, which was expected due to the extremely small loading. Interestingly LPRD displayed Au reflection before and after heat treatment, with other features making it difficult to approximate particle size using the Scherrer equation. The appearance of gold reflections implies that the particle size exceeds the X-ray diffractometer detection limit, which is approximately 2-2.5 nm in size.¹⁴ As the pore size of previously synthesised MgO/SBA-15 materials in the previous chapter was between 3-5 nm in size, the likelihood of these particles remaining in the pore network is unlikely.

The DIM materials exhibited gold reflections only after heat treatment, suggesting particle agglomeration and growth through thermal treating. The particles for both mesoporous and hierarchical materials were approximately 6 nm in size post calcination, again suggesting materials were outside the pore network. It is probable that a significant proportion of gold particles were still below the detection limit within the pore network, and therefore the Scherrer¹⁵ calculated values are an overestimation. TEM and XPS analysis were required to determine a more accurate particle size, and distribution of Au throughout the materials.

The second feature observed was the MgO reflections at approximately 43 and 62 °,¹⁶ which was only displayed in the mesoporous parent support. The previous chapter demonstrated how at lower loadings MgO/SBA-15 showed no MgO reflection in the wide-angle, however for loadings 8 weight percent and above, the MgO peaks began to appear. The parent supports used were on the cusp of this boundary; therefore, the mesoporous material exhibited very small peaks.

Finally, the remaining features in the LPRD patterns were from a magnesium silicate species,¹⁷ likely created during the aqueous gold impregnation. This new phase was disadvantageous, as the previous chapter demonstrated the poor basic strength of magnesium silicate over the proven basicity of the MgO functionality. In addition, it is detrimental that the gold impregnation alters the parent support in such a way that would change its crystallite structure.

Regarding low-angle X-ray diffraction, patterns are interpreted the same way as the previous chapter, with the three peaks (10, 11 and 20)¹⁸ indicating the order in the repeating pore structure. The patterns displayed in **Figure 4.2c-d** showed a strong 10 reflection, confirming the presence of long-range ordered mesoporosity indicative of SBA-15. The mesoporous parent support low-angle pattern displayed a poorly defined 11 and 20 reflection, which again was indicative of TLCT SBA-15.¹⁹ This pore integrity was strongly maintained in the DP, and less preserved for the DIM materials. For the LPRD materials, no reflections were observed; suggesting pore ordering had been disrupted. Hierarchical materials, as seen with the previous chapter, did not exhibit strong 11 or 20 reflections, again thought to be due to the macroporous voids breaking up the long-range ordering of the mesopores.

The wide and low-angle patterns of LPRD materials suggested the integrity of the support was compromised by the synthesis, both chemically (with a change to a magnesium silicate), and structurally (with a disruption of the pore network). This is disadvantageous, as the benefit of using MgO/SBA-15 is its high surface area caused

by its mesoporous domain and the basicity of the MgO functionality. Nitrogen porosimetry was used to confirm any irregularities in the physical properties of the support.

Nitrogen Porosimetry (**Figure 4.3**) exhibited type IV isotherms with H2 hysteresis curves, suggesting the synthesis of long-range ordered mesoporous materials was mostly successful.²⁰ The parent support isotherms agreed with the previous chapter, which revealed that increasing the Mg loading caused the typical mesoporous materials containing uniform cylindrical pores to shift to H2. This implied more complex pore systems, lacking uniformity and poor pore size distribution.²¹

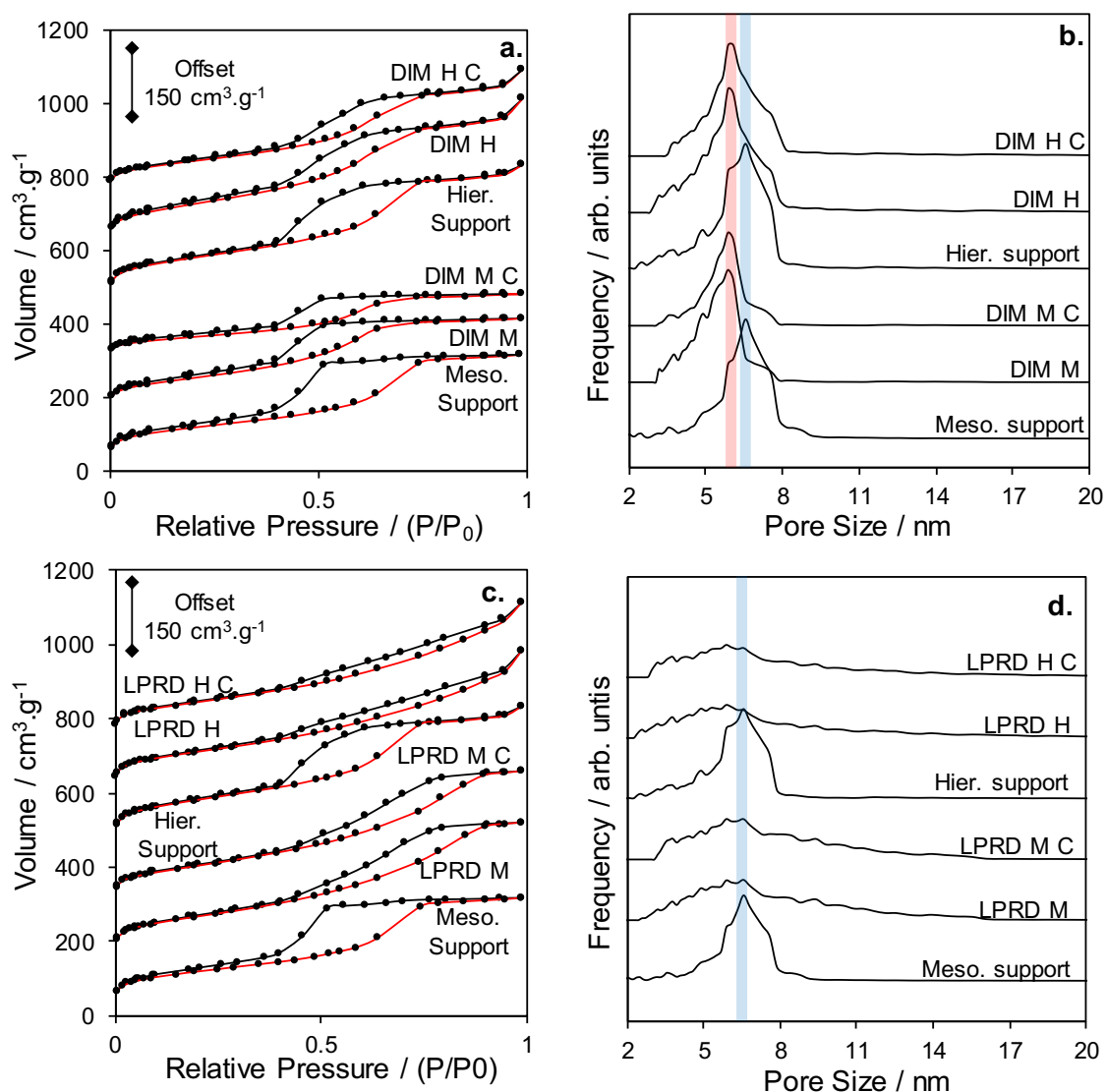


Figure 4.3. Nitrogen porosimetry isotherm for (a) DIM and (c) LPRD materials, with calculated pore size distributions for (b) DIM and (d) LPRD.

All DIM materials displaying H2 isotherms retained most of the physical characteristics of SBA-15, with defined porosity and uniformity (**Figure 4.3a**). However, it was observed smaller hysteresis curves and a reduced pore size distribution for the materials after impregnation.²⁰ This could suggest the material pore structure contracted because of the aqueous gold impregnation, resulting in smaller pores and a smaller surface area. On the other hand, LPRD materials displayed a dramatically altered isotherm post impregnation (**Figure 4.3c**). The isotherm, although still type IV, displayed characteristics of H3-5 hysteresis curves, suggesting the materials were dramatically altered during synthesis. The pore size distribution was significantly reduced in intensity and sharpness, further suggesting pore integrity and uniformity were compromised. It was concluded from these isotherms that DIM impregnation had a minor effect on the physical properties of the support, while the LPRD synthesis had a major destructive effect on the integrity and uniformity of the material. This is extremely disadvantageous, as the high surface area and uniformity of the mesopore network is the most desirable quality when using SBA-15 materials as catalytic supports.

As the three methods accomplished the deposition of Au on the catalyst regardless the physical changes, the three synthesis candidates were tested in the selective oxidation of benzyl alcohol, to determine the most effective method to continue with. This reaction was selected because it has been reported to be effectively catalyzed by gold species and benefited by the presence of bases.²²

4.2.1.2 Preliminary Study Screening

Literature conditions for the selective oxidation of benzyl alcohol were chosen to compare the catalytic activity of the three synthesis methods in this preliminary experiment.^{23, 24}

As presented in **Figure 4.4**, all three materials were active in this reaction to some degree, with the hierarchical materials outperforming their mesoporous counterparts, as seen in **Section 3.2.3**. Unsurprisingly, due to their limited Au loading, DP materials displayed extremely poor activity and final conversion, even when normalised to gold mass instead of to catalyst mass.

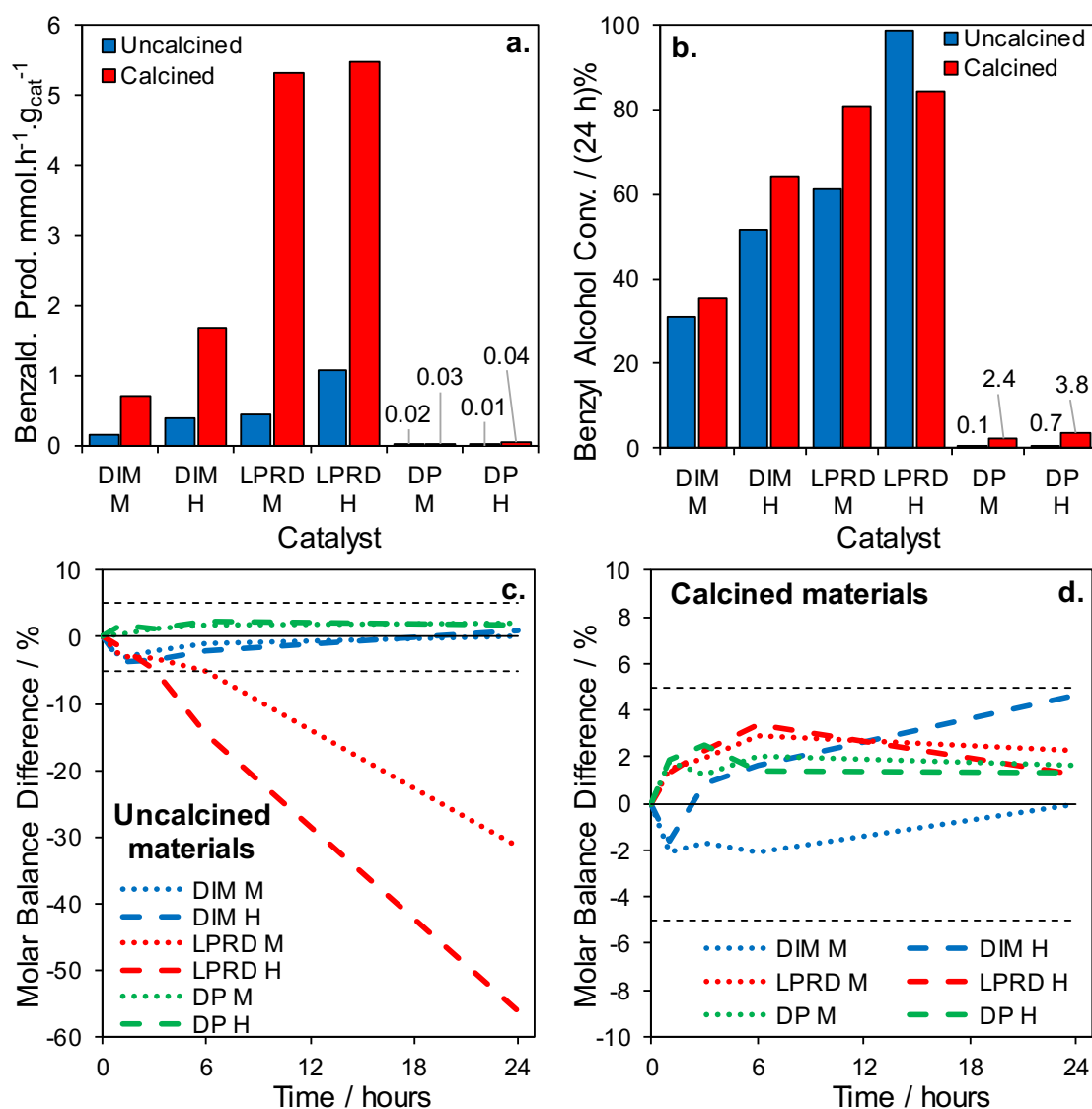


Figure 4.4. Reaction data for the screening of three preliminary synthesis materials using the selective oxidation of benzyl alcohol. Initial rate of selective product (a) normalised to catalyst mass and (b) final conversion of the substrate after 24 hours. The molar balance was determined of (c) pre- and (d) post-heat treated materials, and the relative standard deviations are displayed. Reaction conditions were determined from literature; 100 °C, 800 RPM, O₂ headspace at 1 bar.

Surprisingly, LPRD showed higher activity than DIM materials, despite porosimetry and X-ray diffractometry suggested these materials had suffered pore destruction/disordering and chemical transformation of the basic functionality. In general, the calcined the materials increased the initial productivity, final conversion and selectivity to the product. Although particle size characterisation was problematic due to poorly defined WAXRD reflections, it could be reasoned that this activity increase was caused in part by Au particle growth.

Although LPRD materials exhibited a comparatively fantastic initial activity, they did not achieve total conversion after 24h, indicating deactivation has occurred. Literature has shown the basicity of the reaction has a large effect on the rate of deactivation of the catalyst.²⁵ Reaction deactivation suggests the altered basic species in LPRD do not have the capability to prevent deactivation whereas DIM materials, with reduced activity and final conversion, are more resistant to deactivation. This suggests the DIM basic functionality is less active but more stable, allowing the reaction to progress more consistently.

To determine the selectivity of the reaction, a molar balance was calculated from the known products and substrate, with the relative standard deviation being displayed in **Figure 4.4c-d**. A tolerance of 5% was allowed, with respect to the error associated with the GC and error of the multiple injections of the same sample. It was determined that DIM and DP materials remained under the 5% barrier, suggesting they remained selective throughout the reaction. LPRD pre-heated materials displayed a significant molar loss as the reaction progressed, which suggested the catalysts were over oxidising to form other molecules not included in the calibration. This is highly detrimental as the selective product benzaldehyde is consumed at nearly an identical rate to its production. This was not observed for the heat-treated materials, suggesting that activity and selectivity are temperature dependant for the Au or Mg-Si species.

4.2.1.3 Preliminary Study Summary

In summary, Au@MgO/SBA-15 was successfully synthesised to varying degrees of success. ICP-OES analysis determined that both DIM and LPRD retained the majority of the basic functionality while impregnating an acceptable loading of gold. DP impregnation was not found to be as successful, with a loading 20 times smaller than nominal, thought to be caused by the pH of synthesis. X-ray diffractometry also highlighted the low concentration of gold in the DP materials, with no gold or MgO reflections observed. DIM materials gave gold reflections post calcination, suggesting particle sintering by thermal treatment, while LPRD materials exhibited gold peaks for pre- and post-heat treatment, as well as magnesium silicate species, suggesting the support was drastically altered. Low-angle X-ray diffraction was used to examine the pore ordering of the materials. The mesoporous materials appeared to be more uniformly ordered, however, the LPRD samples exhibited reduced pore ordering. Porosimetry confirmed this, with DIM materials retaining their pore integrity post impregnation, and LPRD losing their pore ordering.

The reaction data confirmed that the DP materials were poor catalyst candidates, displaying low activity and conversion. LPRD method displayed an impressive initial activity and the highest overall conversions after 24 h, but the catalyst deactivated earlier than DIM materials or were over oxidizing the desired product. This is thought to be caused by the weaker basicity provided by the magnesium silicate species. Finally, DIM materials exhibited lower activity but more stability than LPRD catalysts due to the MgO functionality.

DP and LPRD materials were discarded for further investigation. DP because, despite retaining the chemical and physical properties of the parent support, they showed poor impregnation and activity to the reaction. With regards to LPRD materials, they exhibited an extremely large activity, but at the cost of poor selectivity and expedited deactivation, as well as altered physical and chemical characteristics. Therefore, the DIM materials were chosen as the synthesis method to continue with, because they retained the properties of the parent support, and gave adequate activity, conversion, selectivity and reduced deactivation. In addition, WAXRD indicated a potential increase in particle size with temperature for DIM materials, suggesting a possible topic of investigation to optimise activity through particle size tuning.

The choice to continue using the double impregnation method is in part due to its catalytic performance and subsequent longevity, however, is primarily due to its effect on catalytic descriptors. Examples of these desirable properties are an ordered mesoporous network (characterised using LAXRD and microscopy), and MgO nanoparticle decorated

mesopores (quantified using WAXRD and nitrogen porosimetry). Both liquid phase reductive deposition and deposition precipitation methodologies gives less control to achieve the desired loading^{5, 6} and pore destruction, which are extremely undesirable. For this reaction, the proven basicity and physical properties of the material (shown in the previous chapter) are key for utilisation as effective catalytic supports.

4.2.2 Chemometrics Study

For most comparative chemical studies, reaction conditions are taken from the literature to better compare materials. This is often a poor representation of the performance of the material, as individual candidates will have specific optimum conditions of operation. Because of this issue, studies sometimes conduct optimisation reactions, varying conditions such as reaction temperature, substrate concentration and pressure among other factors. This is important as some variables can be affected by physical properties of heterogeneous catalysts, e.g. porous materials can encounter a mass transport limitation at low stirring speed.

In industrial chemical engineering, the use of chemometrics, or design of experiments, is used to examine the influence of each variable, if its influence is significant, and if there are synergistic effects between variables. This is the use of mathematical and statistical methods to optimise the conditions while gaining the maximum understanding from a data set. Its use in academic chemistry is limited, however, is becoming more widely used as its benefits are more understood.²⁶⁻²⁸

4.2.2.1 Chemometrics Experimental design

To optimise the experiment, three responses were chosen to be measured in order to follow the progress of the reaction, and guide the catalytic performance to a better result.²⁹ The responses chosen were: benzyl alcohol conversion, benzaldehyde initial rate and benzyl benzoate selectivity. These were chosen considering the consumption of substrate is paramount, high activity is required to be industrially relevant, and low selectivity to the unwanted over oxidation is preferred. Throughout the study, certain factors were kept constant, to omit them from varying the catalytic performance. These constants were:

1. Reactor volume and type
2. Solvent
3. Solvent volume
4. Reaction pressure
5. Stirrer bar
6. Catalyst mass
7. Internal standard

The factors to investigate were chosen to probe the physical and chemical characteristics of the materials. In total 5 were chosen at two levels:

1. Reaction temperature (60 and 80 °C)

The activation energy (E_a) value is indicative of the reaction dependence with temperature and the material used as a catalyst. Low E_a can be characteristic of low-temperature dependence and mass transfer limitations, which can be brought about from using mesoporous materials. Higher E_a indicates weaker sites.

2. Substrate concentration (0.1 and 0.2 M)

A larger concentration on one side of the chemical equation (i.e. substrate), can push the reaction rate value to be higher. This, in turn, can cause the further over oxidations to occur, thereby increasing selectivity to subsequent undesired products.

3. Stirring speed (600 and 800 RPM)

As previously mentioned, external diffusion limitations can be often investigated using different stirring speeds. While this was deemed unlikely, a higher RPM was included to confirm the lack of external diffusion limitations within the range tested.

4. Pore network of the catalyst (mesoporous and hierarchical)

As previously shown, the use of a macroporous network facilitates easy access through the material to the sterically hindered mesopores. This was demonstrated using a relatively large substrate, tributyrin, however, it is worth investigating whether a smaller substrate also benefits from this.

5. Catalyst heat treatment (no heat treatment, 550 °C, 2 h, 10 °C.min⁻¹)

Benzyl alcohol selective oxidation has been shown in the literature to be most active when gold nanoparticles are within 2-5 nm.³ Using a heat treatment of the material, the gold species can sinter and form larger particles. This pre-treatment variable is investigating if the gold particle size is likely to affect activity. The chosen temperature is the same used during the parent support synthesis.

As there are five factors with two levels each, 2⁵ experiments are required. Therefore 32 reactions were performed. A step by step guide is displayed in **Appendix 3a**.

4.2.2.2 Chemometrics Results and Discussion

The influence of factors in the responses selected are represented in a simplified manner in **Figure 4.5**. It was determined that stirring speed was the only factor to give an influence below error. To see the complete set of data and the level influence of the factors on the observed responses, please refer to **Appendix Table 3a.1** and **Appendix Figures 3a.1-3**.

	Reaction Temperature	Reaction Stir speed	Porous network	Benzyl Alcohol Conc.	Heat Treatment
Benzyl Alcohol Conversion / %	↑	—	—	—	—
Benzaldehyde Productivity / $\text{mmol}\cdot\text{h}^{-1}\cdot\text{g}_{\text{cat}}^{-1}$	—	—	—	—	↑
Benzyl Benzoate Selectivity / %	↓	—	↑	↑	↓

Figure 4.5. Influence of factors on the responses monitored for the selective oxidation of benzyl alcohol. Green upwards and red downwards represents a significant increase/decrease in response when the increased level of the factor is used.

It was established that both conversion and activity were influenced significantly by individual factors without displaying any synergistic effect. The conversion was mainly influenced by the reaction temperature, which was expected, as reactions tend to progress faster with added heat. The activity was mostly influenced by the heat treatment, which suggested that the effect of the treatment on the basicity of the support and/or the Au particle size, were promoting the desired reaction.

On the contrary, the selectivity to the unwanted ester product was influenced by all the factors except the stirring speed. According to the rule of temperature in Levenspiel's 'Chemical Reaction Engineering',³⁰ the increase of temperature favours the reaction with the highest activation energy. As ester selectivity decreases with increased temperature, this suggests the over oxidation and coupling may not be the reaction with higher activation energy in this reaction system. The heat-treatment caused a decrease in selectivity, suggesting larger nanoparticles are disfavoured the over oxidation reactions. Substrate concentration increased the ester selectivity, suggesting the increased concentration facilitated the probability of over oxidation. Ester selectivity was also increased when using a hierarchical network, which could be a by-product of the increased activity relative to the mesoporous materials. It was observed that the more active materials lose selectivity to benzaldehyde as they progress further into the reaction, as an increased benzaldehyde concentration pushes the unselective reaction

forward. No conclusive results were obtained during the examination of the synergistic influence of factors on ester selectivity, as they were under the limit of accuracy degree for the selectivity.

4.2.2.3 Chemometrics Summary

The chemometric study determined an expected effect of the temperature on the consumption of substrate, while it was interesting to observe that the heat treatment promoted the rate of benzaldehyde productivity, and the pore structure affects the selectivity. With the aim to further explore the effect of the heat treatment, the conditions 100 °C, 800 RPM and 0.1 M Benzyl Alcohol were then fixed in a subsequent and more expanded study on the heat treatment temperature for the different porosity supports.

The temperature of 100 °C was chosen to better compare results to literature, and as the reaction is very temperature-dependent with these materials, increase overall activity. The higher RPM was chosen to avoid any diffusion limitations that may occur, however unlikely. The lower concentration of benzyl alcohol was selected to reduce the over oxidation and coupling reactions. Varying the porosity was decided to be kept because an improvement in performance was still observed for these relatively small substrate molecules. The main aim of next section was to tune the particle size and the basicity of the support by changing the temperature used in the heat treatment and assess whether the effects of increasing conversion, increasing of activity and reduction of benzyl benzoate selectivity remain unchanged for a wider range of heat treatment temperatures in both types of supports.

4.2.3 Heat-Treatment Study

During the preliminary study, it was determined that heating DIM materials caused an increase in particle size, which was followed by an increase in their catalytic performance. This was expected, as it is widely known that nanoparticulate gold is stable up to 300 °C and will agglomerate above this temperature.³¹ Bulk gold has a Hüttig temperature of 319 °C,³² where surface particles become mobile, although the literature has determined that nanoparticulate gold is susceptible to melting at even lower temperatures.³³ To investigate these further, batches of mesoporous and hierarchical MgO/SBA-15 were impregnated with gold using the DIM synthesis. The materials were then heated using a 10 °C min⁻¹ ramp to 100, 200, 300, 400, 500, 600, 700 or 800 °C, and held for 2 hours under air. The subsequent materials were characterised using a variety of techniques, revealing information on the chemical and physical properties of the material, specifically the nanoparticulate gold species. All materials were then screened for the selective oxidation of benzyl alcohol using the conditions optimised via chemometrics.

4.2.3.1 Heat-Treatment Study Characterisation

ICP-OES data in **Figure 4.6** confirmed the successful impregnation of gold onto the MgO/SBA-15, both for mesoporous and hierarchical supports. After achieving a loading half of the nominal in the preliminary study, a larger nominal loading of 1.5 wt% was chosen to try and reach around 1 wt% loading.

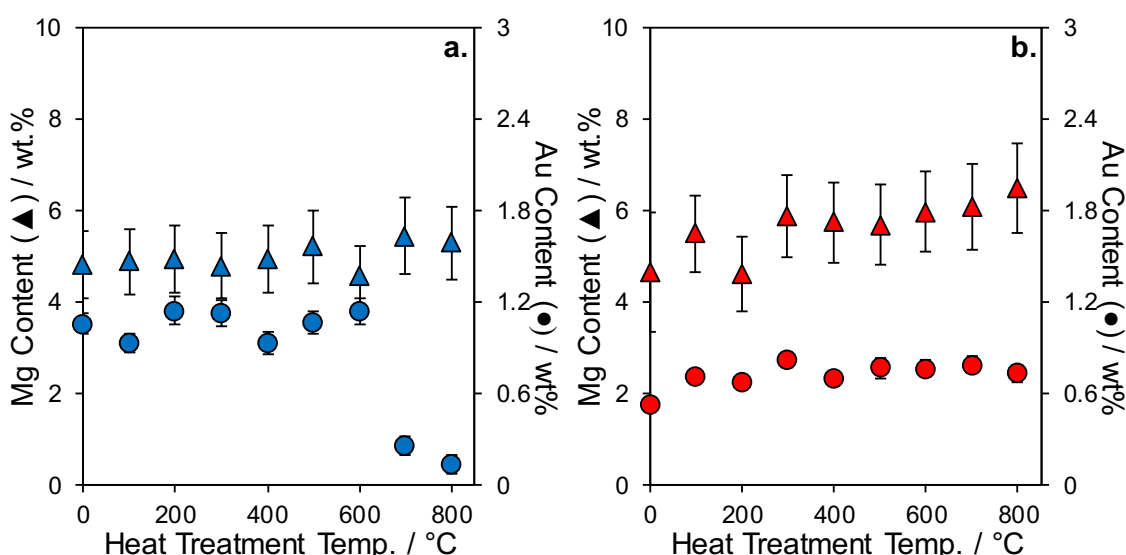


Figure 4.6. Magnesium and gold loadings determined using inductively coupled plasma optical emission spectroscopy (ICP-OES) for (a) mesoporous and (b) hierarchical materials.

Both supports showed a consistent magnesium loading of approximately 5-6 wt% which remained constant regardless of the heat treatment temperature. This indicated that the magnesium functionality was stable in the materials up to 800 °C. It could be argued that the hierarchical supports had a slightly higher magnesium loading (**Figure 4.6a**), which would corroborate what was observed in the previous chapter. The opposite was seen with respect the gold functionality, with mesoporous supports retaining an increased concentration relative to the hierarchical. At 700 °C, the gold loading decreased (**Figure 4.6b**), which could be due to the destruction of the pore structure, seen with SBA-15 materials treated with high temperature.³⁴ This was not observed in the hierarchical supports, suggesting the macropore network stabilised the mesoporous domain. The hierarchical supports exhibited a reduced loading of 0.6-0.7 wt%, maintained for all temperatures, suggesting a reduced ability to retain gold within the support.

Low-angle X-ray diffraction, displayed in **Figure 4.7**, mirrored what was observed in the previous chapter and the preliminary study. It was hypothesised that the hierarchical mesopores differ from the conventional long-range ordered hexagonally stacked mesoporous materials. The hierarchical mesopores curved round the macropores, increasing the destructive interference of diffracted X-rays. All three low-angle reflections indicative of SBA-15 were visible, with the primary 10 reflections being the most intense and 11 and 20 reflections being well defined. There was an interesting shift for the 11 and 20 peaks in both supports, suggesting a change in the inter-pore distance (calculated in **Appendix Figure 3b.1**), which could signify a swelling of the material with heat treatments. As previously observed with the hierarchical supports, the low-angle reflections were not as defined, with the 11 and 20 peaks indistinguishable, explained in **Section 3.2.2.2**. The temperatures chosen ran from 100 to 800 °C, however it was found that at the highest temperature, the low-angle and wide reflections displayed different peaks, suggesting both the physical structure and chemical composition of the materials could not withstand this high heat. The identity of these reflections is not known, but the wide-angle is suspected to be a gold-magnesium phase.³⁵ The altered physical structure and chemical composition, confirmed by porosimetry, is the reason why the upper temperature of materials catalytically screened was limited to 700 °C.

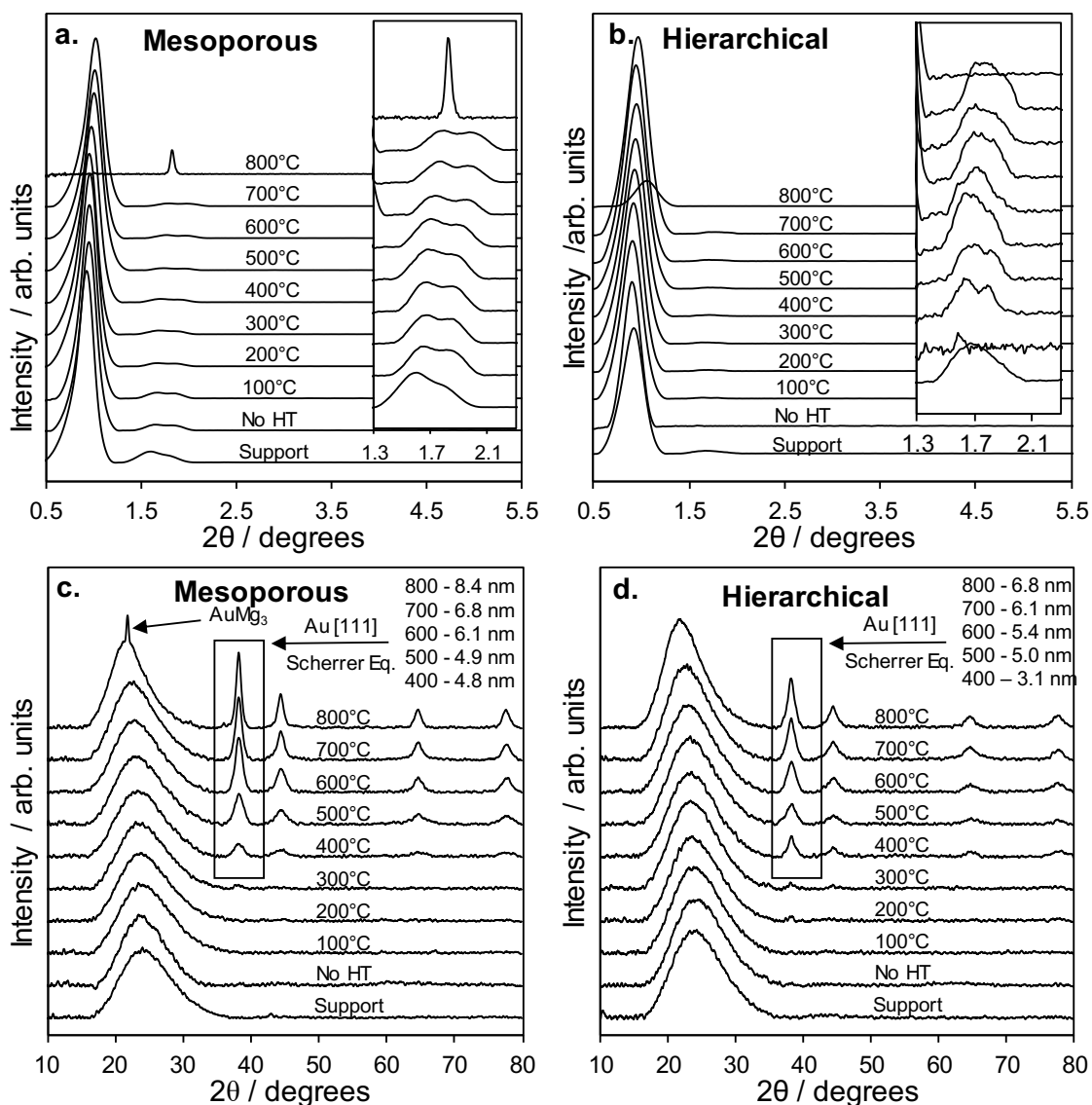


Figure 4.7. Low-angle X-ray diffractometry patterns for (a) mesoporous and (b) hierarchical materials, and wide-angle X-ray diffractometry patterns for (c) mesoporous and (d) hierarchical materials.

The wide-angle X-ray diffraction patterns for the mesoporous and hierarchical materials are also observed in **Figure 4.7**. Two features were clearly visible in both patterns, the amorphous silica hump from the SBA-15 support, and the gold feature, which increased in intensity as the heat treatment temperature increased. Using the Scherrer equation, we estimated the particle size of the gold functionality (**Appendix Figure 3b.1**). A clear increase of particle size was observed in relation to temperature, which corroborated the findings from the preliminary study. Gold was not visible for both materials below approximately 300 °C, which agrees with the literature that states gold nanoparticles are thermally stable up to 300 °C.³¹ As both supports showed increasing gold nanoparticle

size with temperature, it could be reasoned that below 300 °C the particle size was below the detection limit (2-2.5 nm).¹⁴

The physical properties of the mesoporous and hierarchical materials determined through nitrogen porosimetry (**Figure 4.8**) confirmed what was shown in XRD. Both parent supports were correctly synthesised, displaying Type IV H2 isotherms and hysteresis curves first seen in the previous chapter (**Figure 3.7**), and the subsequent materials loaded with gold retained their mesopore structure and pore size distribution. A drop in surface area was observed, which continued to decrease with temperature. This could be due to a combination of pore destruction and Au particle agglomeration.

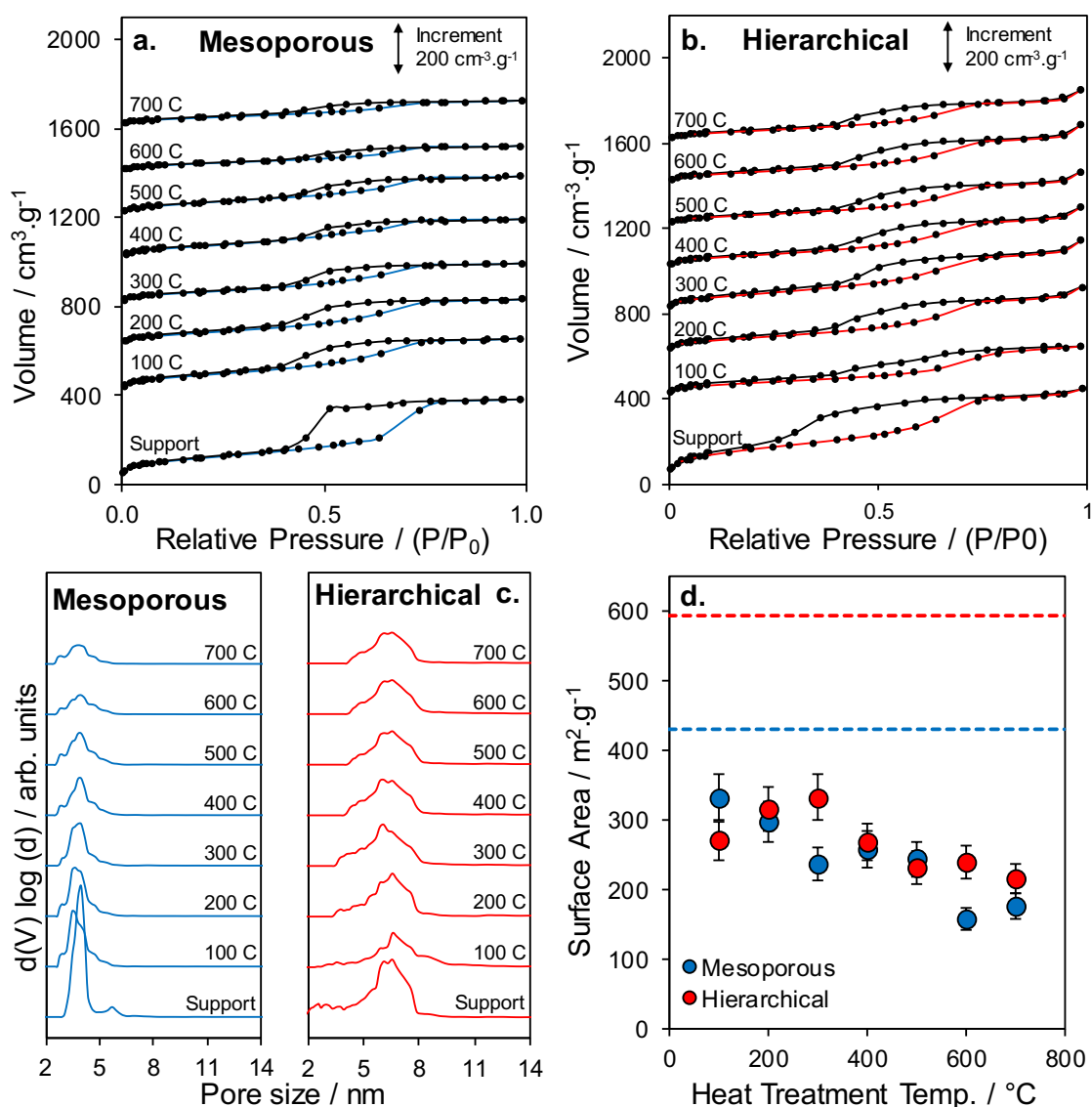


Figure 4.8. Nitrogen Porosimetry isotherms for (a) mesoporous and (b) hierarchical materials, with subsequent (c) pore size distributions and (d) surface area (lines represent the parent support).

The initial Au impregnation altered the isotherm. While still displaying a type IV isotherm, the adsorption isotherm climbed at a reduced rate to a smaller volume, suggesting some pore destruction and loss of surface area. When the heat treatment temperature increased, the isotherm did not change dramatically in shape, however, both supports experienced a flattening, indicating a decreasing surface area, which was confirmed using BET. Both supports retained their pore size, however, they lost the broad peak as temperature increased.

X-ray photoelectron spectroscopy was used to probe the functionality environments of the materials and determine the effect of heat treatment. The Mg 2p spectra shown in **Appendix Figure 3b.2** displayed 3 doublet peaks at 49.1, 50.1 and 51.0 eV which correspond to Mg(OH)₂, MgO and Mg-O-Si respectively. This was very similar to the Mg 2p spectra of the parent supports seen in the previous chapter. However, the Mg-O-Si component was shifted to higher BE, indicating a lower electron density in the species, possibly caused by the presence of gold.

Both materials exhibited no real change in their respective components as a function of temperature, observed in **Figure 4.9**. The MgO component for the mesoporous materials was larger than the hierarchical, suggesting a larger nanoparticle species had been formed in lieu of a silica pore wall coating, as also observed in the previous chapter. A large drop in the MgO feature was observed for the M700 material, inversely correlated to a rise in Mg-O-Si.

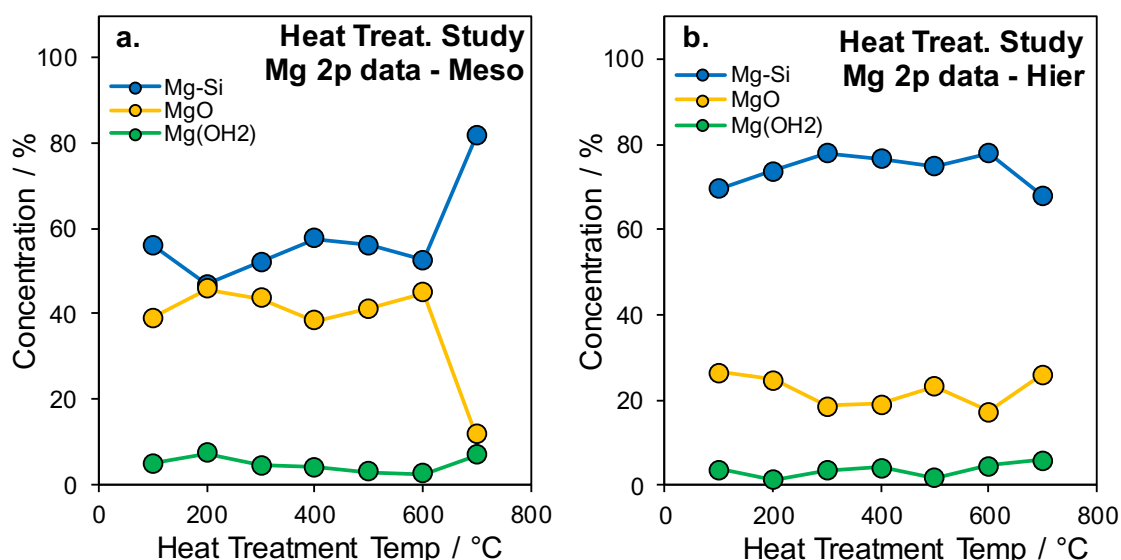


Figure 4.9. Mg 2p distribution of features for (a) mesoporous and (b) hierarchical materials.

The O 1s spectra shown in **Appendix Figure 3b.3** displayed 3 peaks at 530.4, 532.5 and 534.4 eV which correspond to MgO and organic contaminants, SiO₂ and hydroxyl species bound to the silica surface respectively.³⁶ The respective intensities of these features are displayed in **Figure 4.10**. Both supports exhibited no real change in component position or relative intensity with increasing heat treatment temperature. The only notable point was the increased concentration of the hierarchical MgO/Organic component relative to the parent support seen in the previous chapter. This could be a by-product of the gold impregnation, possibly due to the organic component of the sodium carbonate reducing agent.

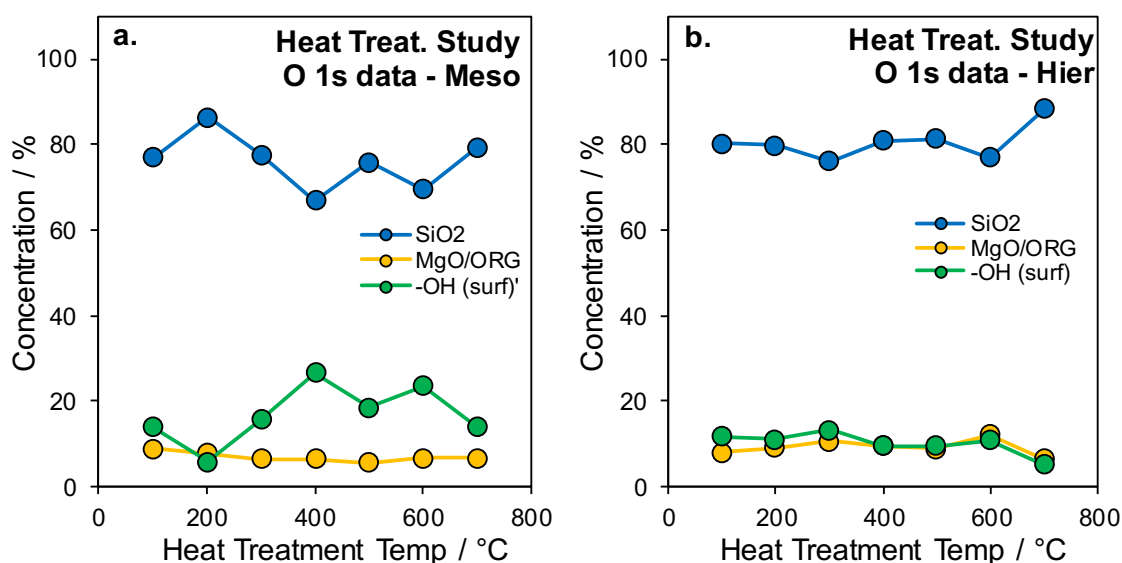


Figure 4.10. O 1s distribution of features for (a) mesoporous and (b) hierarchical materials.

As seen with the previous chapter, the MgO/SBA-15 materials resulted in three doublet components in the Si 2p spectra in **Appendix Figure 3b.4**, at 101.9, 103.2 and 105.2 eV which corresponded to Si-O-Mg/organic contaminants, SiO₂ and chemisorbed species bound to the silica surface respectively. The respective concentration of each of these components is displayed in **Figure 4.11**.

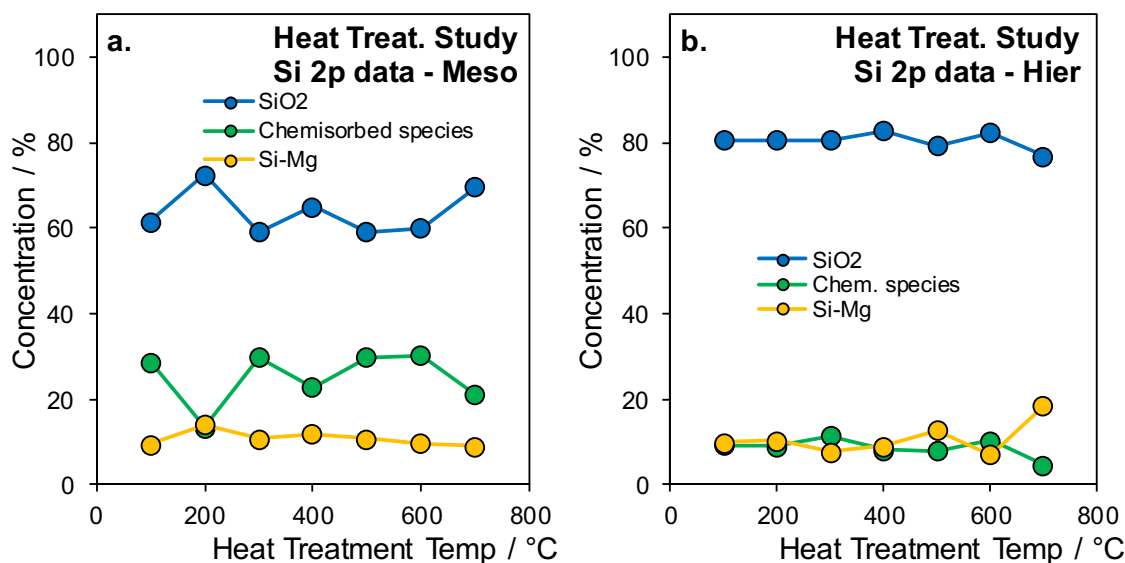


Figure 4.11. Si 2p distribution of features for (a) mesoporous and (b) hierarchical materials.

Both mesoporous and hierarchical materials showed a very similar distribution of components, with silica being the prevalent peak, with Si-O-Mg and chemisorbed species both being approximately half the peak area. The surprising feature of both supports was the prevalence of surface-bound chemisorbed species, which differed from the previous chapter in the absence of gold. This could be due to the methodology of the gold impregnation. The mesoporous material exhibited an increased concentration of chemisorbed species, possibly due to the reduced uniformity of the MgO coating, as seen with the previous chapter. This, in turn, would present a larger surface area for contaminants to chemisorb to the bare silica surface.

The Au 4f spectra shown in **Figure 4.12** was more complex than spectra previously presented. The Au 4f region overlapped with the Mg 2s region, making it impossible to isolate the more subtle Mg and Au components, such as Mg(OH)₂, MgCO₃ and Au³⁺. The magnesium components reported were therefore simplified to a single feature, and the possible Au³⁺ component was omitted. There were 3 peaks displayed, two doublet peaks at approximately 84 and 86 eV which corresponded to metallic (Au⁰) and cationic gold (Au⁺), and the single MgO peak at 90 eV.

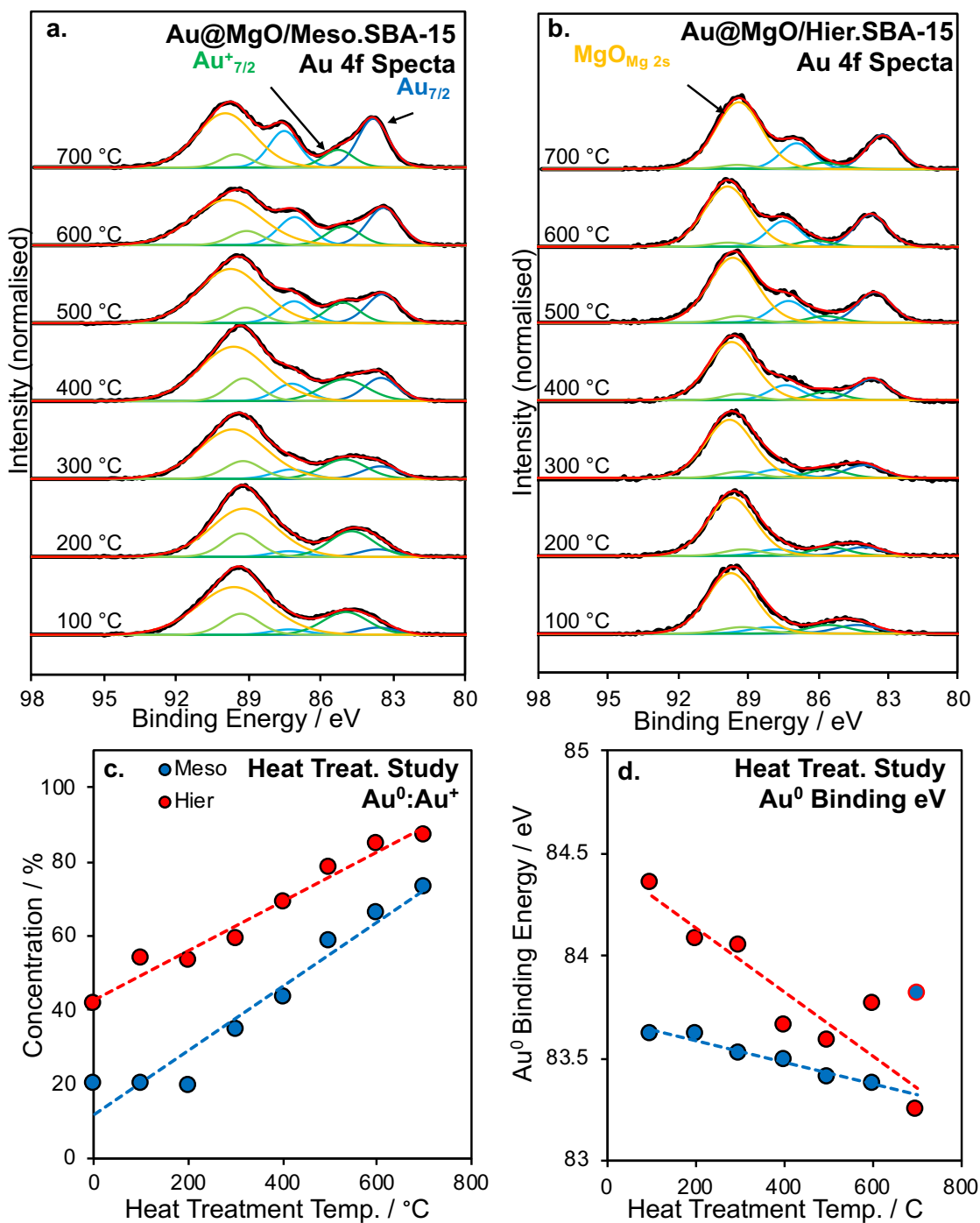


Figure 4.12. Au 4f X-ray photoelectron spectra of (a) mesoporous and (b) hierarchical materials, (c) the ratio of metallic to cationic gold and (d) $Au^0_{7/2}$ Binding energy.

There are three conclusions to be drawn from the Au 4f region, the first related to the Au metallic to cationic ratio, the second to the $Au^0_{7/2}$ binding energy shift, and the third to the increasing peak area relative to the Mg 2s component. The shift from predominantly cationic to metallic gold followed a similar trend to Au NP size, suggesting the particle size may have a direct influence on the charge of the Au sites, perhaps the geometric shape of the particle holds influence on the charge its surface exhibits. Both mesoporous

and hierarchical followed this trend, suggesting particle size again may be the cause. A shift to lower binding energy was observed as temperature increased which has been shown in previous work to be caused by a more basic environment, and it is a well-known effect that heat-treating MgO can expose more basic facets. It is proposed that the heating caused more basicity to be exhibited up to 400-500 °C, however above this level may be more a result of the Au phase.^{22, 37} Increasing Au intensity relative to Mg 2s suggested more Au-Au interactions in the material. This could be a migration of Au to the surface of the material, which was not observed with TEM, or more likely, sintering of particles with temperature, which was supported by TEM, WAXRD and change in the colour (**Appendix Figure 3b.5**).

Transmission electron micrographs displayed in **Figure 4.13** and **Appendix Figure 3b.6** confirmed the successful synthesis of the SBA-15 mesoporous and hierarchical structure, supporting the data and conclusions from WAXRD and Porosimetry. In addition, the somewhat destroyed pore structure, especially evident in M200 (**Appendix Figure 3b.6, left-middle**), was also clearly shown for the mesoporous materials, whereas hierarchical materials appear to retain both their mesoporous and macropore structure. This agrees with nitrogen porosimetry, which found a decreasing surface area and altered isotherm, which was more deviated from the parent support in the case of the mesoporous materials.

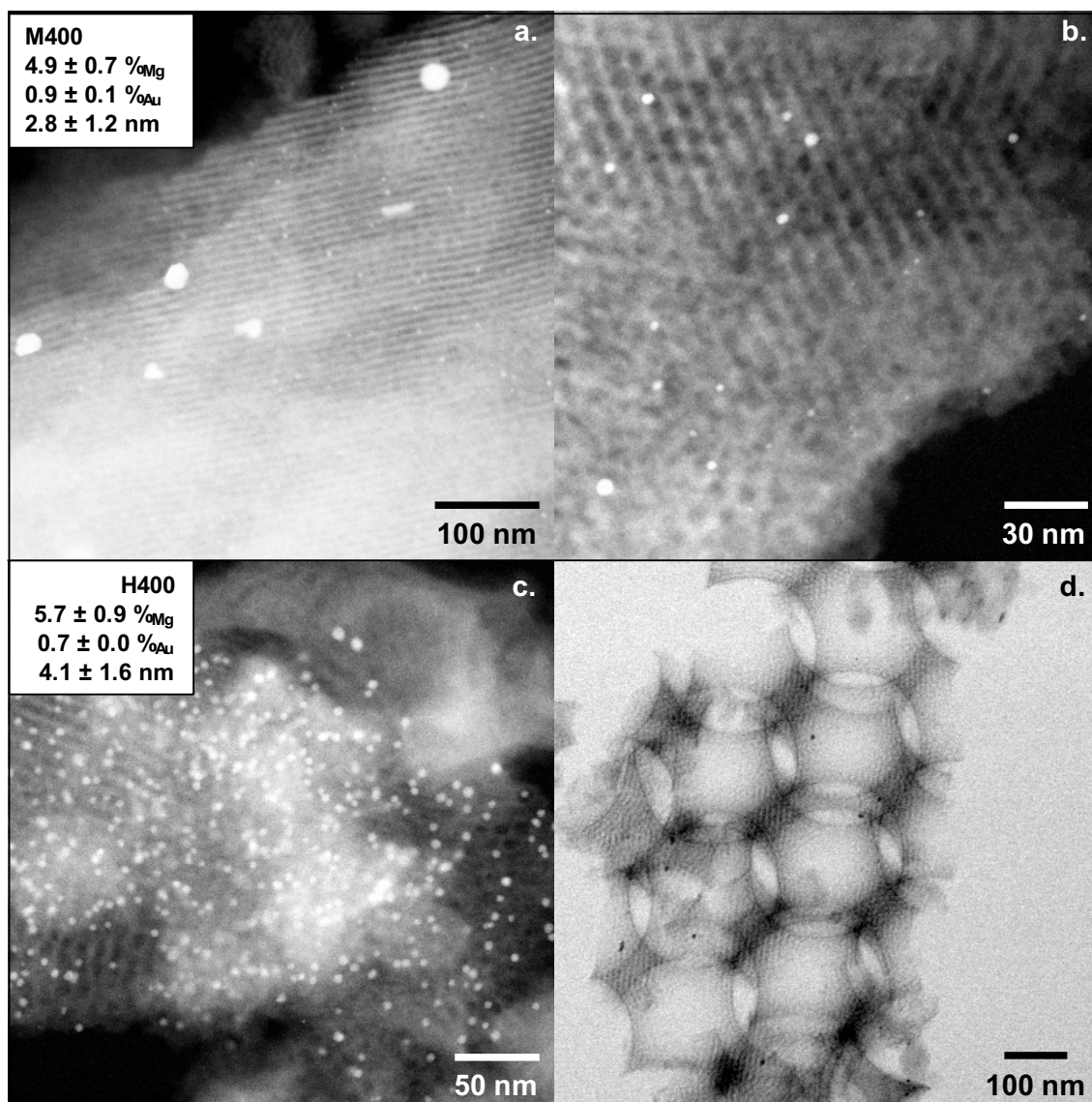


Figure 4.13. Transmission electron microscopy micrographs of (a,b) mesoporous and (c,d) hierarchical Au@MgO/SBA-15 materials, heat-treated at 400 °C.

Most importantly, there was a lack of particle uniformity observed, with sub 5 nm NPs inside the mesopore network, and larger gold particles around 20-50 nm. While it is widely understood that it is the former species being responsible for the catalytic activity, it proved problematic to estimate particle size from WAXRD in future studies. This was due to the significant number of particles undetected by the X-ray diffractometer, as they were outside the detection limit. What can be concluded from the raw micrographs is the retention of the support structure, and partial success synthesising nanoparticles within the pore network.

It could be theorised that an altered synthesis could be employed in the future, using pre-prepared capped nanoparticles to ensure particle uniformity. By using a stronger basic

functionality such as CaO, and an organic capping agent with an acidic head group, the gold could be selectively functionalised within the mesopores. Thermal treatment could then be employed to remove the head group, resulting in a more selective functionalisation.

Using the method of Wu et al,³⁸ it is possible to use the calculated particle size to estimate other properties; such as site density and dispersion. As this method uses approximations based on the gold unit cell, there are assumptions that must be made;

- Particles are completely spherical
- Each surface gold atom has the potential to be an active site
- The unit cell is that of metallic gold

The nanoparticle size distributions, shown in **Figure 4.14**, displayed growth in hierarchical nanoparticles from 2 nm to 4 nm, from very monodisperse to poorly dispersed particles. This trend continued linearly with respect to the particle size calculated using the Scherrer equation for samples treated at 500 – 700 °C. This was not observed for the mesoporous materials, which had a calculated size of approximately 4-5 nm for materials treated at 100-400 °C, with all materials displaying poor size uniformity. After that point, the Scherrer equation was used, showing the mesoporous materials followed the trend of the hierarchical materials and increased linearly with temperature.

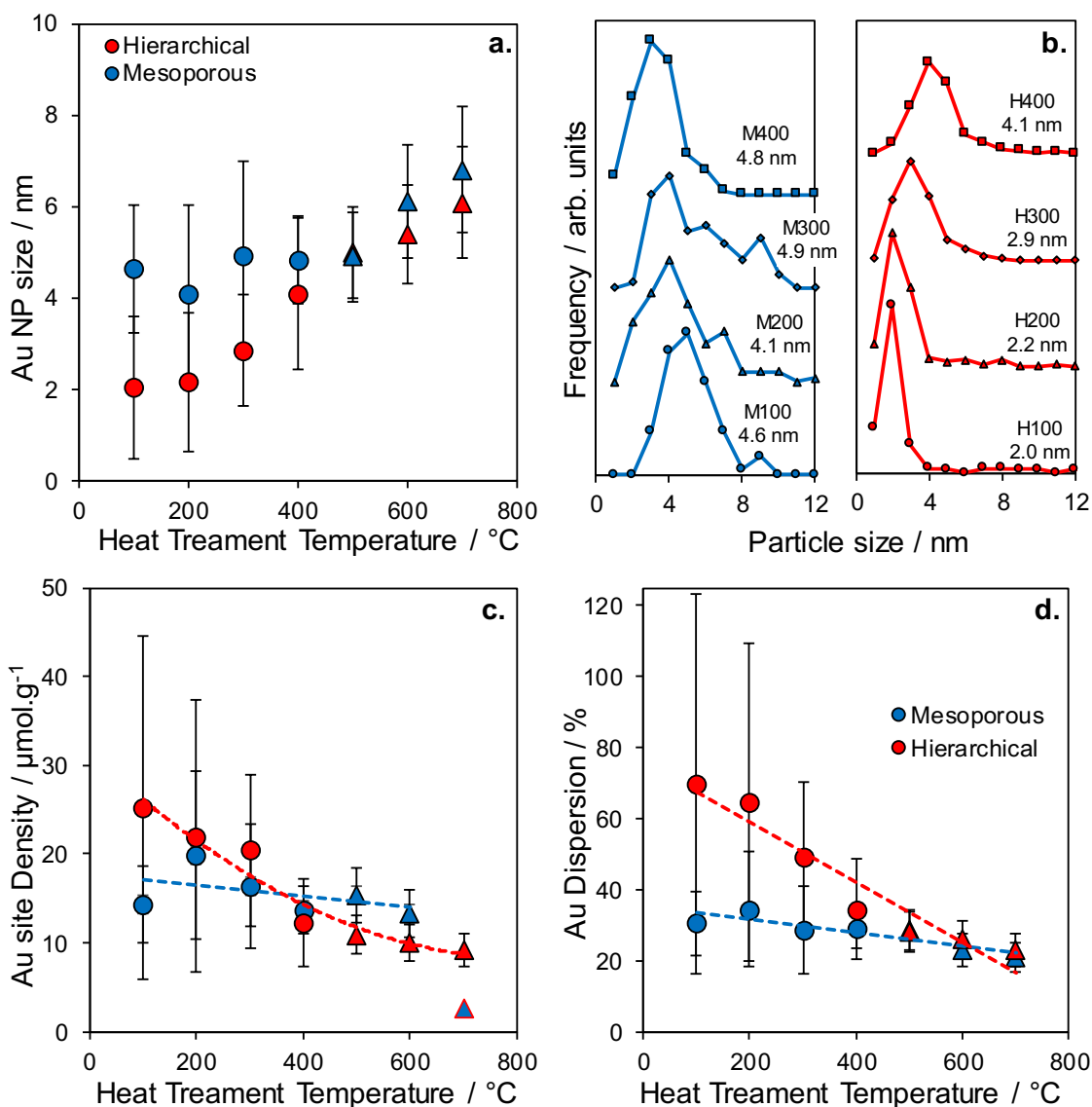


Figure 4.14. Average gold (a) particle size, gold particle size (b) distributions, (c) site density and (d) gold dispersion derived from transmission electron microscopy micrographs (●) and WAXRD Scherrer equation (▲).

An unfortunate consequence of using particle size calculated from TEM micrographs was the extremely large error associated with the lack of particle size uniformity. This is reflected in the data derived from the TEM particle sizes (**Figure 4.14a**). Hierarchical materials showed a decrease in site density as particle size increased, which is to be expected, as their surface area normalised to gold mass decreased with increasing size. Interestingly the mesoporous materials did not match this trend, exhibiting a flat linear trend. This could be caused by the smaller shift in particle size observed from M100 to M400, but most likely as a result of the large error associated with the data.

A similar trend was observed when considering the hierarchical dispersion, observing a decreased dispersion in tandem with an increase in particle size. The mesoporous

materials did not follow the trend of their site density, with dispersion decreasing with increasing heat treatment temperature. This was an expected response to increasing particle size.

After characterisation, the two families of materials were screened using the selective oxidation of benzyl alcohol, using the conditions optimized in **Section 4.2.2**.

4.2.3.2 Heat-Treatment Study Screening

The catalytic screening results of heat-treated materials are displayed in **Figure 4.15**. As for the preliminary study, catalytic activity changed with heat treatment. This wider study showed also that both supports exhibited volcano plots for productivity and conversion.

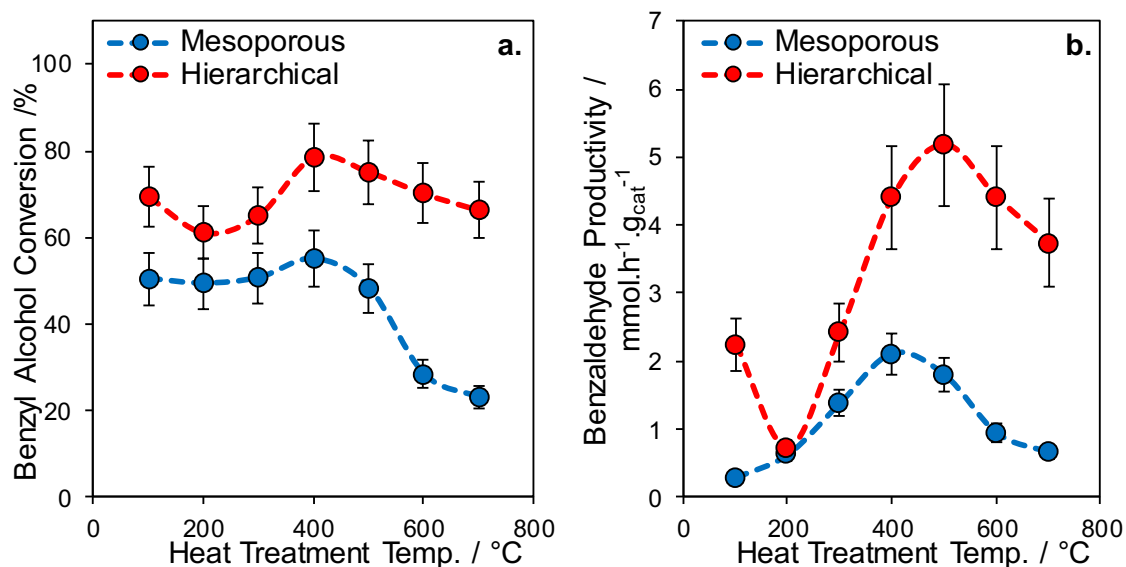


Figure 4.15. The final conversion of benzyl alcohol after (a) 24 hours and (b) initial rate of productivity of the selective product benzaldehyde using the optimised conditions determined using chemometrics.

Both mesoporous and hierarchical materials followed the same trend when comparing the conversion of benzyl alcohol, reaching a maximum at 400 °C and decreasing as the temperature further increased. The same trend was observed when considering the initial productivity of the mesoporous materials, however, the hierarchical materials reached maximum productivity at 500 °C. As the hierarchical materials reached a maximum conversion and rate at different treatment temperature, it can be concluded that materials H400 and H500 were deactivating at different rates. By having a faster initial rate but lower final conversion, it can be assumed that H500 was deactivating faster. From a practical viewpoint, that would make H400 the superior material when operated in continuous flow, as it hypothetically would have a longer lifespan.

After the maxima were reached for both conversion and rate, both materials exhibited a drop off in activity and final conversion. This may be caused by increasing particle size, or a change in the basic functionality, as the optimal temperature of 400-600 °C caused higher basic facets to occur.²² Another cause of activity loss could be pore structure and surface area degradation, therefore the decrease in activity after 400-500 °C could be caused by reduced access to the mesoporous domain and catalytic species within.

Turnover frequencies (TOFs), displayed in **Appendix Figure 3b.7**, showed a similar trend to the raw initial rate data, with both materials displaying a volcano plot reaching a maximum at M400 and H500. This could reflect how dependant these materials were on the gold particle size. The approximated nature of the TOF calculation was unfortunate, as it did not consider the true number of sites, only the estimated number.

The mesoporous and hierarchical materials were also screened at 60 and 80 °C, (**Appendix Figure 3b.8**), to observe the temperature dependence and therefore calculate activation energy. One of the primary conclusions of the previous chapter was the diffusion limitations exhibited by mesoporous MgO/SBA-15, and a literature search shown in **Appendix Table 3b.1** and **Appendix Figure 3b.9** confirmed diffusion limitation played a large role in most studies concerning the selective oxidation of benzyl alcohol.

Both materials followed the same general trend when comparing activation energy (E_a), decreasing with heat-treatment temperature (**Figure 4.16a**) and decreasing with particle size (**Figure 4.16b**). The particle size vs. E_a plot can be split into three regions: The two points with the highest activation energy, H100 and H200, suggested the need to provide energy, by increasing the reaction temperature, in order to activate the reaction on these materials. From this dataset, it can, therefore, be concluded that below 3 nm the gold species site was weak, relying instead on a greater temperature dependence. This was observed directly in **Appendix Figure 3b.8**, where very little activity was observed for these materials until enough heat energy was introduced into the system.

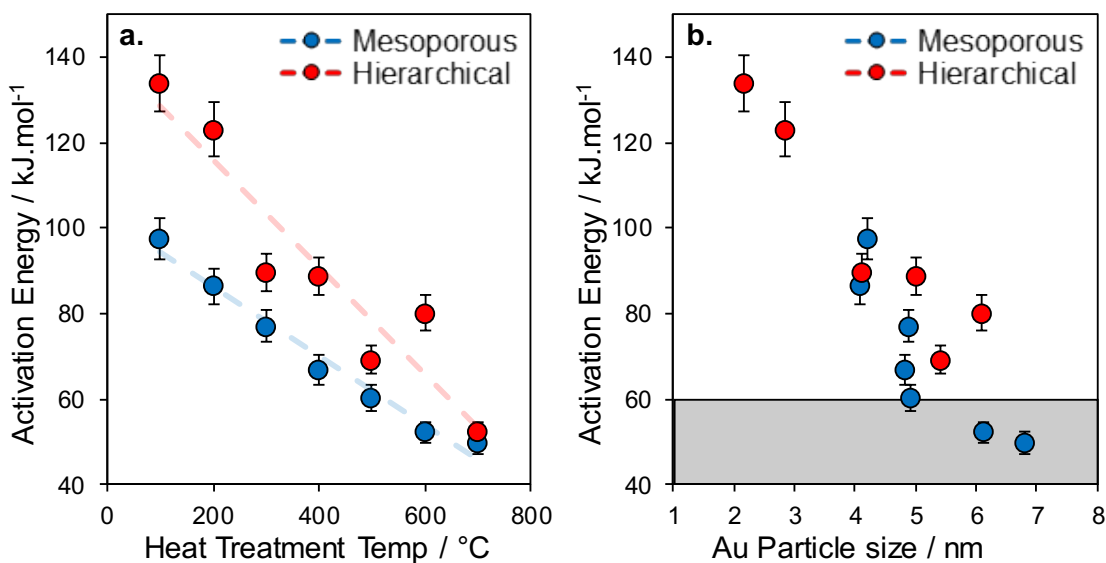


Figure 4.16. Activation energy versus (a) heat treatment temperature and (b) particle size determined using TEM and WAXRD for mesoporous and hierarchical materials.

Between 3-6 nm were the gold materials with kinetically controlled activity, but low activation energy between 60-100 kJ mol⁻¹. These were the best performing materials, with sites strong enough to reduce the need for heat energy input. Optimal materials for mesoporous and hierarchical (M400 and H400) were within this range.

In **Figure 4.16b**, the greyed-out region represents the beginning of diffusion limitations and the end of kinetic control. Three materials were within this region: M600, M700 and H700, all containing gold particle sizes above 6 nm. There are multiple reasons why these materials may be outside of kinetic control: This could be an effect of a degrading pore network (confirmed by porosimetry), causing reduced access to the gold particles trapped in the mesoporous network. This is unlikely, however, as this was not observed with the H600 material. A more likely cause is the geometric change occurring from gold nanoparticle growth. Due to the experimental error associated with TEM, we consider this a very close fit to the literature values.

With a maximum pore size of 5 nm, the SBA-15 produced in this work may experience issues accessing these gold particles; with potential pore blockage, surface migration or steric issues accessing the gold within the pores. With decreasing, activation energy with particle size diffusion limitations of the substrate into the mesopores may be occurring, and activation energy above the diffusion limit of ~60 kJ mol⁻¹ may be an averaging of surface gold E_a with diffusion-limited E_a . Further TEM and screening could be used to prove this, and increasing mesopore size through a pore swelling may alleviate it.

One of the key observations seen for all materials, regardless of temperature, synthesis method or heat treatment, was the deactivation over the course of the reaction. There are many reasons why this might occur, and it is often observed in the literature.²⁵ A clear representation of this deactivation is plotting rate vs conversion, as shown in **Figure 4.17**, which enables the comparison of reaction rate among experiments at the same level of reactant concentrations. Both mesoporous and hierarchical exhibited a hyperbolic curve from 400 to 700 °C, showing the same shape but exhibiting different initial rates and final conversions. The curve deviated from the hyperbolic curve as heat treatment temperature decreased. This suggests that regardless of the catalytic activity, deactivation occurred at the same rate over the same period of time from 400 to 700 °C.

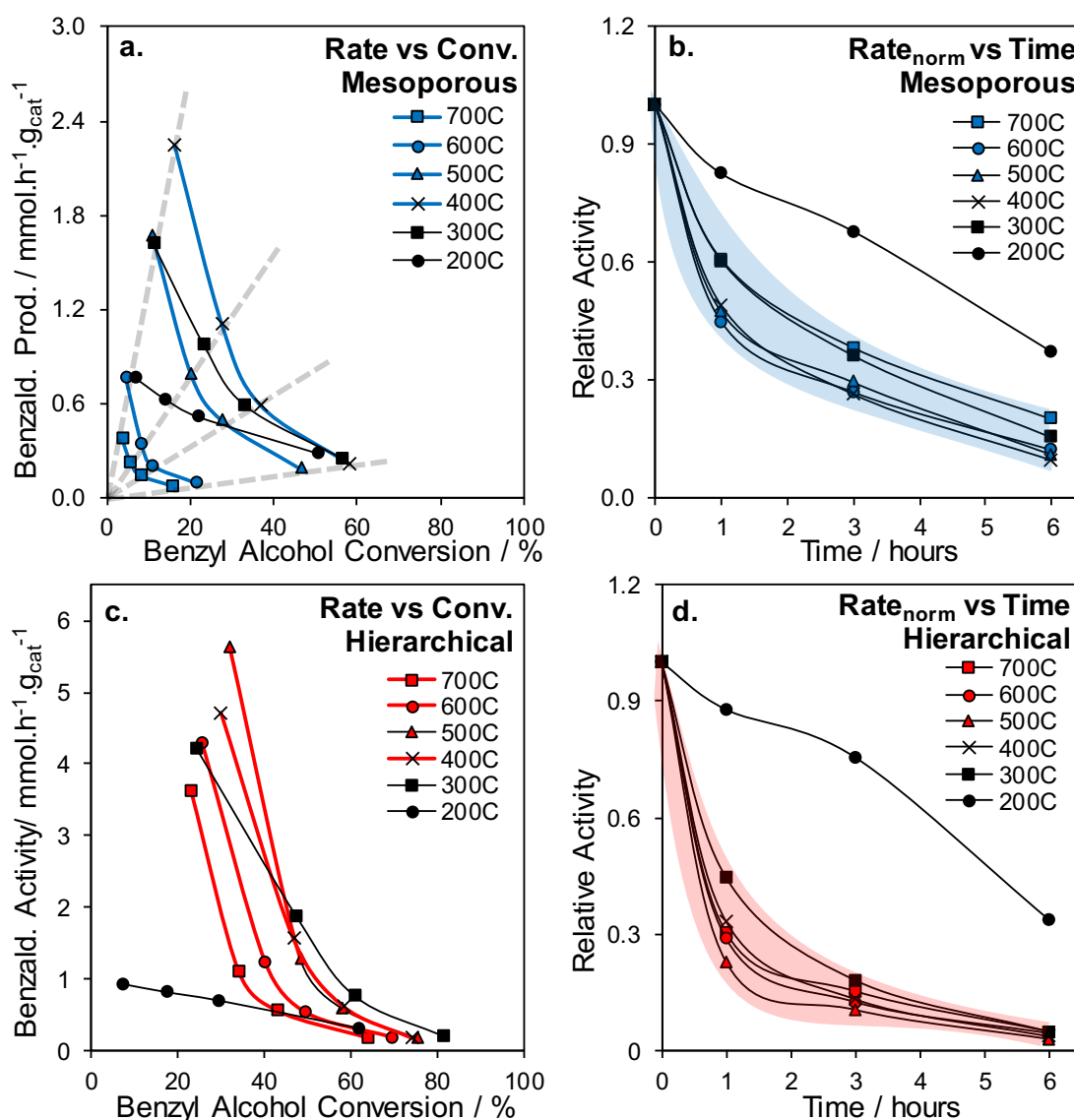


Figure 4.17. Benzaldehyde productivity versus benzyl alcohol conversion plots between (a) mesoporous and (c) hierarchical materials and relative activity versus time plots between (b) mesoporous and (d) hierarchical materials.

This was further highlighted in **Figure 4.17b and 4.17d** when normalised rate vs time was depicted, showing the mesoporous and hierarchical materials followed the same deactivation trend. The cause of this is thought to be benzoic acid or ester coupling product, potentially suggesting that even a minor concentration can cause site inhibition.³⁹

4.2.3.3 Heat-Treatment Study Summary

In summary, ICP-OES, nitrogen porosimetry and XRD showed the synthesis of the support and subsequent gold impregnation and heat treatment was successful. TEM and XPS determined gold remaining stable up to 400 °C, shifting to larger nanoparticles. Literature has revealed that temperature has a large influence on the MgO basicity, through the exposure of basic facets on the surface. Therefore, it is hypothesised that 100-500 °C materials had increasing basicity with temperature. Above this range, the basicity remained constant. It can be considered therefore that, excluding the physical structure of the support, the material performance was dictated by basicity and particle size below 500 °C, and solely particle size above 500 °C, shown in **Figure 4.18**.

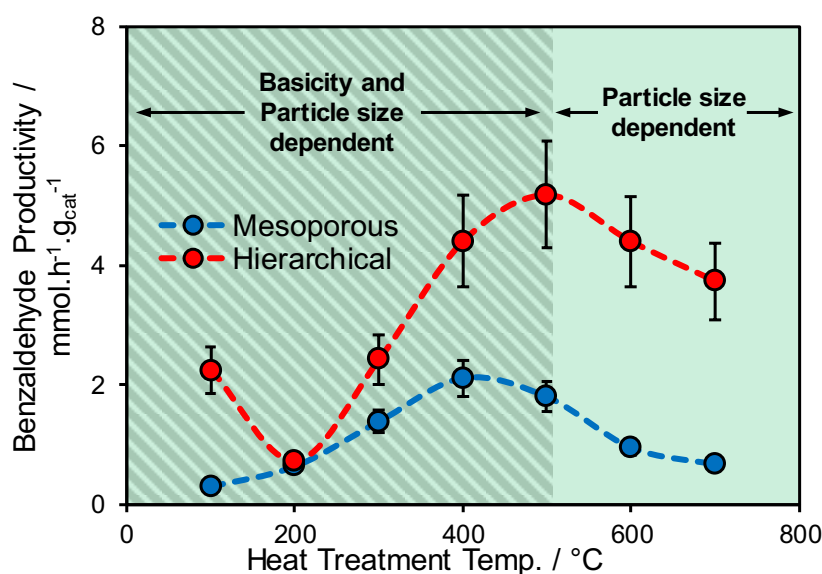


Figure 4.18. Mesoporous and hierarchical initial productivity of benzaldehyde, displaying regions under the influence of basicity and particle size.

Screening using the selective oxidation of benzyl alcohol at different temperatures showed a volcano plot of activity, peaking at M400 and H500. Arrhenius plots showed no steric hindrance. When normalised to site density (approximated from particle size), the turnover frequencies showed a peak at 500 °C, which was also the temperature with the highest basicity but relatively small Au NPs.

Deactivation was a large concern for this reaction (further explored in **Section 4.2.4**), therefore the reaction rate was plotted against conversion to highlight the rate of deactivation. The heat treatment temperature with the highest conversion (400 °C) was therefore chosen, as it would hold onto activity for longer, ensuring the longest lifespan and consequently the most viable for real-world use.

Two variables which were investigated, but not displayed here, were the effect of Au loading and Mg Loading. It was initially thought that altering Au loading would change only the particle size of the Au NPs while retaining constant basic concentration and changing Mg loading would ideally keep constant Au functionality, whilst varying levels of basic concentration. Unfortunately, it was not possible to solely change these variables without altering others, resulting in materials that neither displayed basicity trends nor different sized gold nanoparticles as desired. These two studies are in **Appendix 3c and 3d**.

From the two studies, it was determined that the variation of magnesium loading unexpectedly altered the effectiveness of gold impregnation onto the support, which is thought to be due to the Au precursor preferentially favouring the basic sites. Subsequently, microscopy and X-ray diffraction determined the average particle size and distribution changed with Mg loading. Also, X-ray photoelectron spectroscopy of the Au 4f region determined that the Au⁰ component did not shift, suggesting basicity of the materials was not altered. It was however noted that deactivation occurred at a faster rate in absence of basic phase, suggesting the MgO functionality helped retain activity for longer. The gold variation resulted in a roughly linear relationship with respect to activity and loading, however, microscopy and X-ray diffraction gave no change in particle size. This is unfortunate, as literature points to varied loadings being correlated to particle size.⁴⁰

A possible solution to both studies issues could have been synthesising the gold functionality beforehand, utilizing potentially a polyol methodology. Both studies revealed inconsistencies with the gold impregnation, suggesting the synthesis may need to be refined to guarantee reproducibility.

4.2.4 Deactivation and Green Conditions Study

The materials produced in this chapter confirmed to be active for the model reaction, however, all experienced deactivation to some degree. There are many studies in the literature that employ greener conditions to optimise their catalytic materials for reactions at lower temperatures, and using less environmentally harmful compounds.⁴¹⁻⁴⁴

This study investigates possible causes of deactivation and features standalone experiments determining the suitability of the Au@MgO/SBA-15 materials for greener reaction conditions.

4.2.4.1 Deactivation Investigation

The literature points to the unwanted oxidation product, benzoic acid and its ester coupling product inhibiting the active site,³⁹ however there are many other common causes of deactivation that need to be excluded.^{25, 45}

Many noble metal and solid base catalytic systems have been known to leach into solution.⁴⁶ This is disadvantageous, as it could cause the active solid phase to slowly dissolve away into solution, deactivating the reaction. It can also prove problematic, as the active component in the reaction is unknown, the homogeneous gold species or the solid nanoparticle. Separation and recycling are challenging; however, these are concerns more from an industrial perspective. ICP-OES analysis of fresh and spent material in **Figure 4.19** showed no loss of either Au or Mg content, within error. This proved both gold and MgO functionalities were remaining within the material.

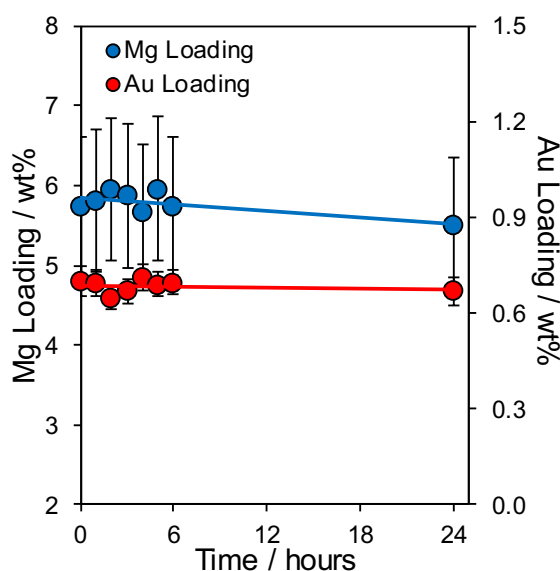


Figure 4.19. ICP-OES analysis of Au@MgO/hierarchical SBA-15 catalytic material taken at periodic intervals during selective oxidation of benzyl alcohol test, to check for functionality leaching.

Another concern when using noble metals as a nano-catalyst is the agglomeration and growth during the reaction. This would occur in a similar way to the heat treatment XRD patterns in **Figure 4.7**. Wide-angle X-ray diffraction patterns of fresh and spent material in **Figure 4.20** showed no change in particle size within error, using the Scherrer equation on 100 and 220 reflections and taking the average. This result was expected as the recovered material displayed no change in colour, which was a visual indication of the changes in gold particle size. This confirmed that both particle size agglomeration and leaching were not occurring.

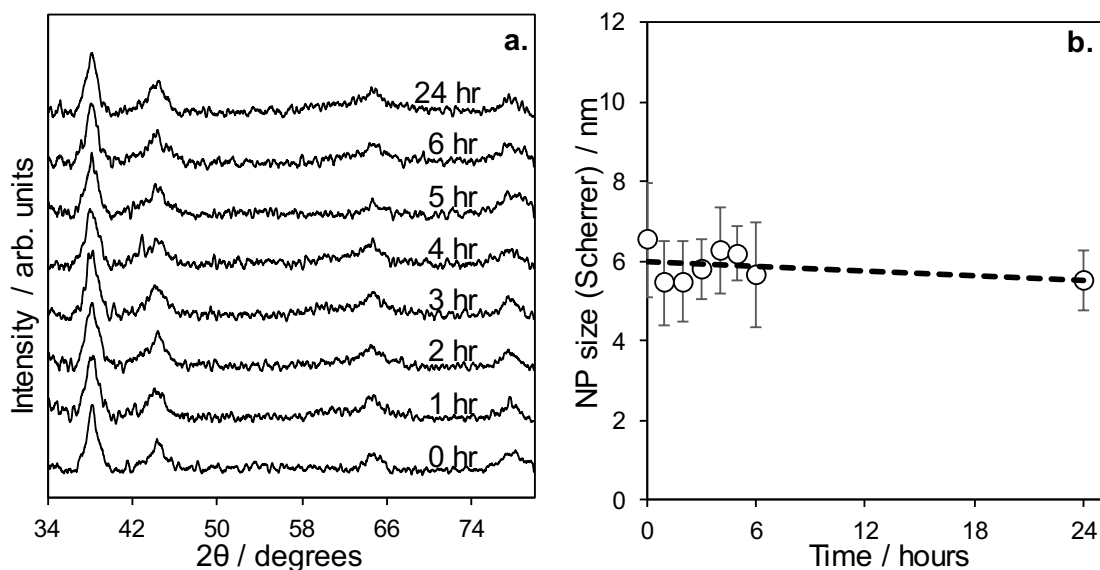


Figure 4.20. Wide-angle X-ray diffraction (a) patterns and the associated (b) particle sizes (calculated using the Scherrer equation) of Au@MgO/hierarchical SBA-15 catalytic material taken at periodic intervals during selective oxidation of benzyl alcohol test, to check for gold particle size propagation.

Diminishing substrate concentration could be causing reduced interactions with active sites, causing the observed decrease in activity as the reaction progresses. Le Chatelier's Principle⁴⁷ dictates for a reaction at equilibrium, the loss of the substrate (benzyl alcohol) will cause the equilibrium to shift to the reverse reaction. The deactivation could be caused by a potentially reduced likelihood of substrate-site interaction, or a shift in the equilibrium from changing concentrations. To determine this, 1 mmol of the substrate was added to the reaction system after 3 hours to replenish the concentration.

Both mesoporous and hierarchical materials did not exhibit a significant improvement in rate with the added substrate, displayed in **Figure 4.21**. After 3 hours, when the extra substrate was added, no clear improvement was observed, clearly expressed on the reaction profiles in **Appendix Figure 3e.1**. An improvement was observed between 4-5

hours, however, this was within the error of the measurement. This proves that decreasing substrate concentration was not the cause of deactivation and other factors were at play.

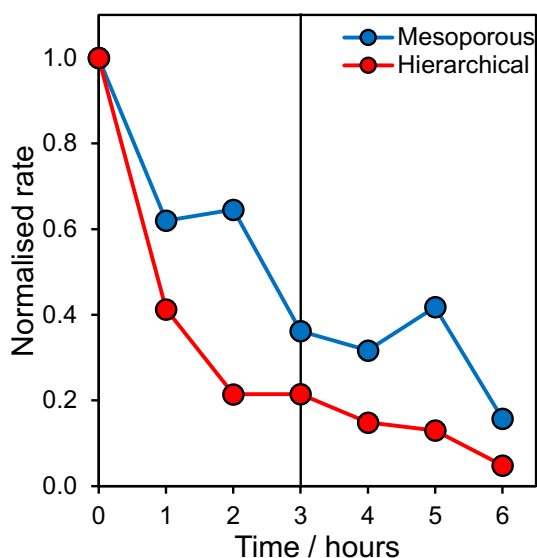


Figure 4.21. Normalised rate loss as a function of time for Au@MgO/SBA-15 materials during selective oxidation of benzyl alcohol test.

It was noted during the catalytic screening that at the endpoint of the reaction a reduced pressure was found in some of the sealed reaction vessels. It was thought that oxygen consumption, as the green oxidising agent, was depleting the headspace. To investigate whether it had a significant effect on activity, the best performing mesoporous and hierarchical materials were screened whilst under oxygen flow, the conversion profiles of which are displayed in **Figure 4.22**.

Both mesoporous and hierarchical materials exhibited similar conversion profiles regardless of using O₂ headspace or O₂ flow. Both materials resulted in a reduced conversion when using flow, which could be linked to multiple reasons. A flaw with the experimental design was the changing of reaction environment, as the oxygen was introduced via a needle to the reaction solution. A catalyst build-up was observed on this needle for both materials, which may be the cause for this drop in activity. Therefore, the results were deemed inconclusive due to experimental error but were judged unlikely that the reduced pressure was causing deactivation.

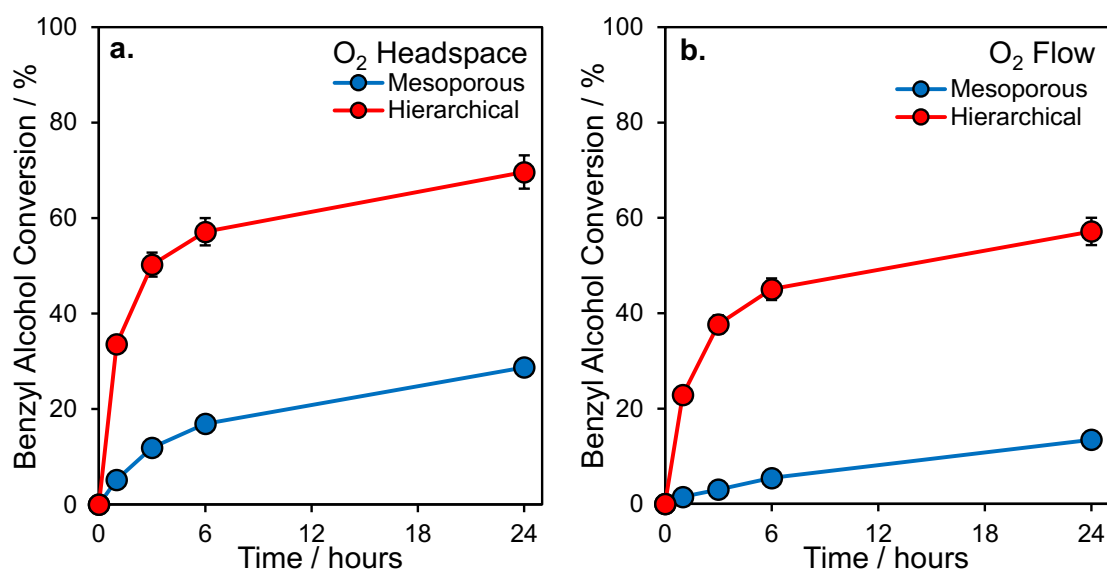


Figure 4.22. Benzyl alcohol conversion as a function of time for mesoporous and hierarchical materials screening for the selective oxidation of benzyl alcohol using an (a) oxygen-rich headspace and (b) under O₂ flow.

All the previous factors could potentially cause a loss of activity over the course of the reaction, however, were unlikely to be the true cause. As previously mentioned, the literature points to the unwanted product benzoic acid or benzyl benzoate causing the deactivation,³⁹ bindings to the gold sites and inhibiting them.²⁵ To confirm this was occurring for the mesoporous and hierarchical materials, the catalysts were screened using a weak and strong base to act as benzoic acid scavengers, displayed in **Figure 4.23**.

It was determined that both base additives decreased the rate of deactivation to a different degree. The stronger base, potassium carbonate, was found to maintain activity for a longer time, which was expected from the literature.²⁵ This resulted in near-total conversion after a mere six hours. The sodium carbonate screening tests were also successful in decreasing deactivation, more so with the mesoporous material, however not near the same degree as with potassium carbonate additive.

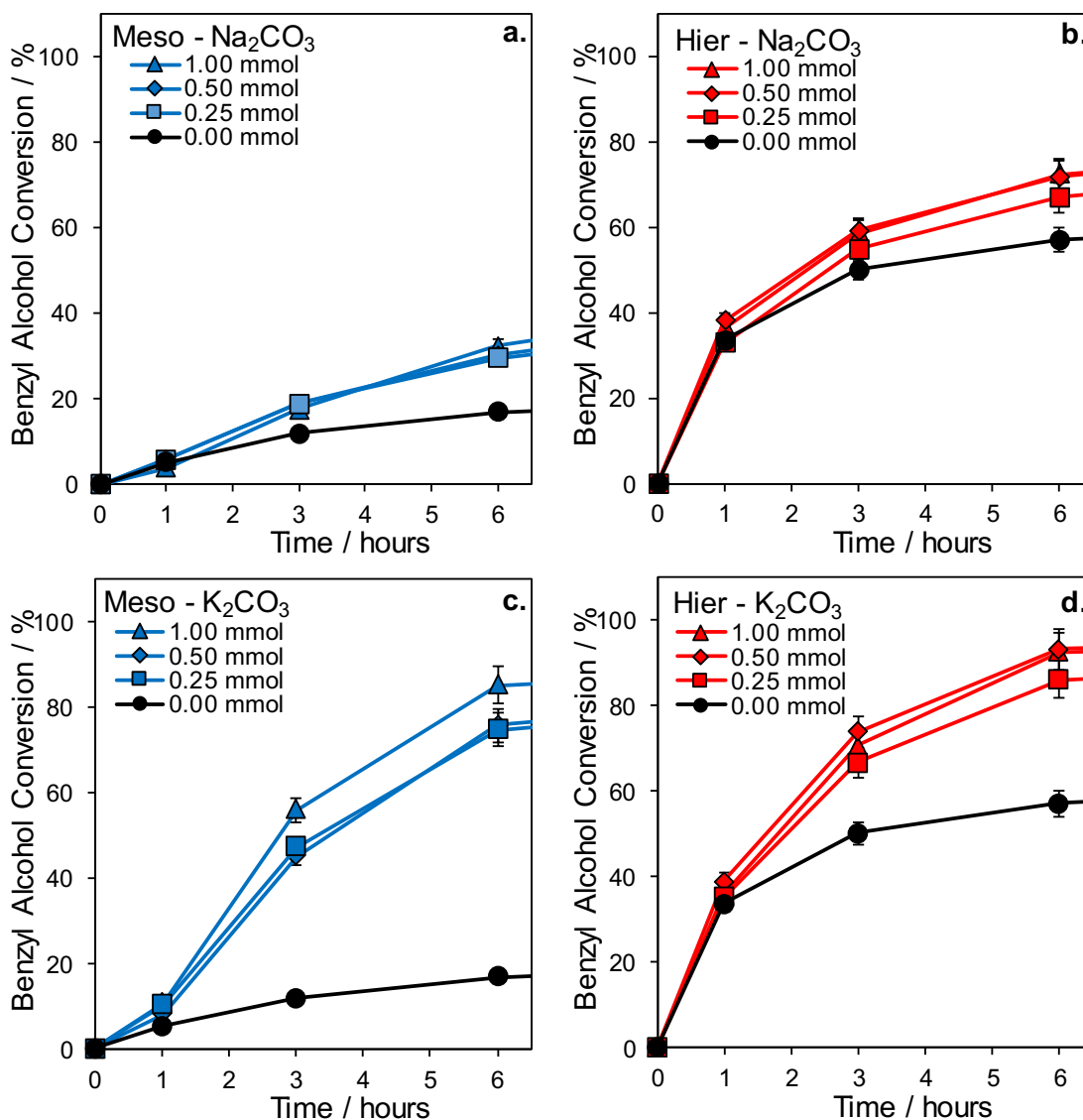


Figure 4.23. Substrate conversion as a function of time for (a,c) mesoporous and (b,d) hierarchical in the presence of varying concentration of sodium and potassium carbonate.

Benzaldehyde productivity, displayed in **Figure 4.24**, was constant for the hierarchical material within error, irrespective of base additive, suggesting activity towards the production of benzaldehyde was not boosted by the base additive. On the contrary, the conversion was dramatically increased when potassium carbonate was employed. Mesoporous materials did exhibit a slight increase in activity, which may be attributed to reduced deactivation at the beginning of the reaction. A dramatic increase in conversion was observed with basic additives, regardless of the concentration of added base. The large boost in conversion, without significant change in initial rate, confirmed the inhibition of active site was prevented by the scavenging nature of the base additive.

Some literature has found the addition of base promotes the reaction by inhibiting the coupling of benzyl alcohol and benzoic acid,^{25, 48} however other works have stated it promotes the coupling of benzaldehyde and benzyl alcohol.⁴⁹ As no notable increase in activity was observed for either base at any concentration, it is therefore suspected that no promotion was occurring. It could be theorised that increasing the basic strength of the added base may cause a promotion effect as seen in the literature.⁴⁹ What is clear, however, is the reduction in product inhibition, evident with the increased six-hour and final conversion.

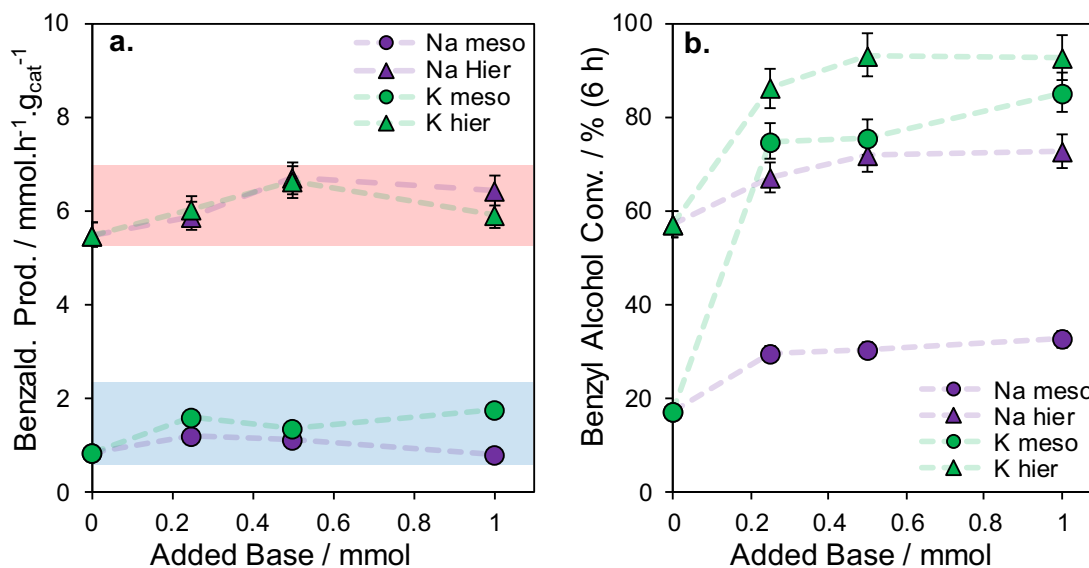


Figure 4.24. Change in (a) rate and (b) substrate conversion through the addition of base.

4.2.4.2 Green Conditions

Many studies in the literature have employed greener conditions and compounds to reduce the energy and environmental impact.⁵⁰⁻⁵² A part of this was the decision to employ an oxygen-rich headspace, instead of a more environmentally unfavourable oxidant, and low temperature 60 °C reactions. Different conditions of oxygen concentration and flow were explored to determine the catalytic activity using greener conditions. Additionally, one of the most energy-intensive tasks in industry is the removal of reaction compounds from the solvent. It is therefore highly desirable to reduce the volume or completely omit solvents.

Solvent-free conditions, the use of oxygen-rich headspace, oxygen flow and aerobic headspace were tested and compared in **Figure 4.25**, resulting in a large increase of selectivity to the benzyl benzoate for the solvent-free conditions. A massive increase in rate was also observed for the solvent-free conditions, which is to be expected, due to the increased likelihood of collisions between substrate and site. This was an interesting

observation, as using the current experimental design it showed how ineffective the catalytic materials would be in the absence of a solvent. Further screening using sacrificial bases or stronger basic supports could prove effective for this condition.

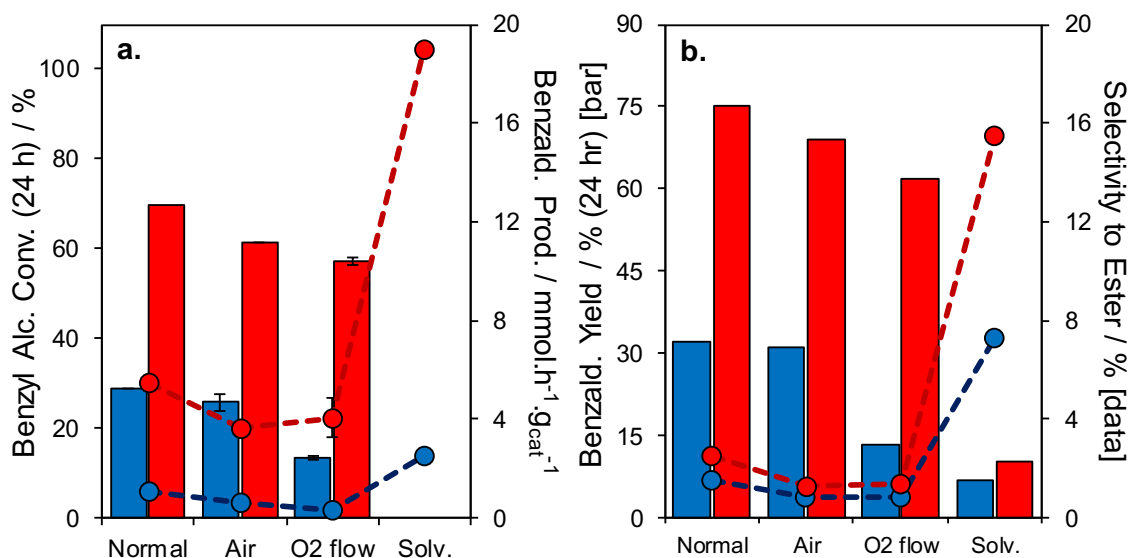


Figure 4.25. (a) Final conversion and rate and (b) final product yield and selectivity to the unwanted product of mesoporous (blue) and hierarchical (red) Au@MgO/SBA-15 materials screened in the absence of solvent.

Comparing the different oxygen feeding conditions, it was found that the use of flowing oxygen or the reaction open to air resulted in a slightly decreased conversion and a drop-in activity. This is expected under aerobic conditions due to the decreased concentration of O₂, however, under O₂ flow, it was expected the easier oxygen diffusion into solution would facilitate a more efficient reaction. This was not the case, however, as it was previously discussed to be likely due to error with the experimental design. The highest conversion and activity were found to be for oxygen-rich headspace when considering the different conditions introducing oxygen into the system. This could be due to either a slightly increased pressure in the headspace or more oxygen dissolving into the reaction mixture. Although aerobic headspace was slightly lower in conversion and activity than rich oxygen headspace, the reaction profiles were similar (**Figure 4.6**), which was an indication that the concentration of oxygen in the air was sufficient to provide enough O₂ oxidant within the solvent phase to facilitate the reaction.

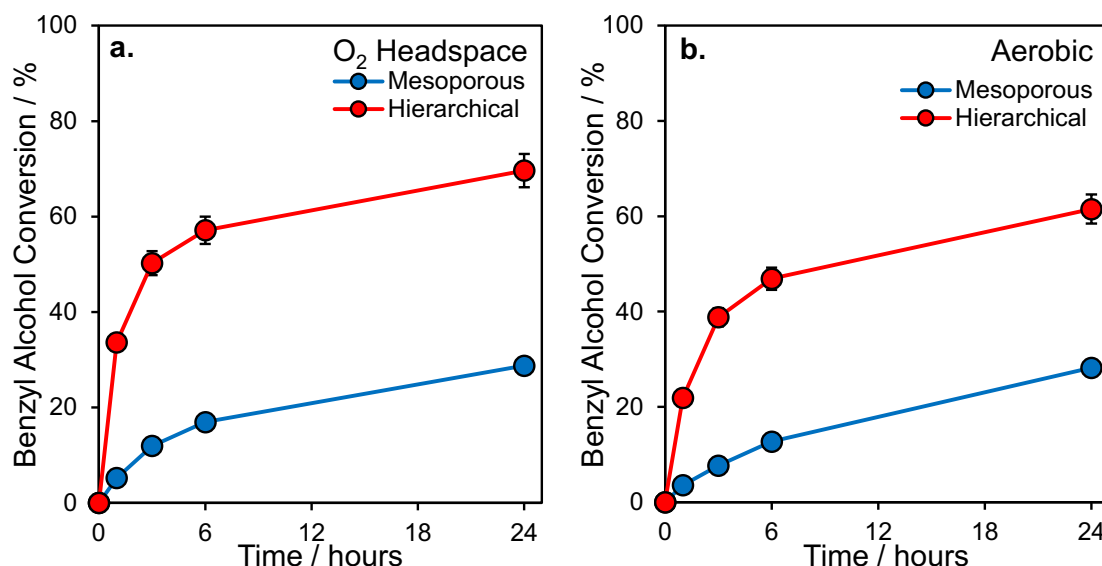


Figure 4.26. Substrate conversion profile as a function of time for mesoporous and hierarchical materials screened with an (a) oxygen headspace and (b) in air.

To determine the activation energy during the heat treatment study, the materials were screened at lower temperatures, displayed in **Figure 4.27**. At 60 °C, the hierarchy of activity of the materials reversed, due to the higher temperature dependence of the hierarchical materials. The drop in temperature caused a significant activity loss. However, it did confirm that both materials exhibited activity at lower energy-intensive reaction conditions.

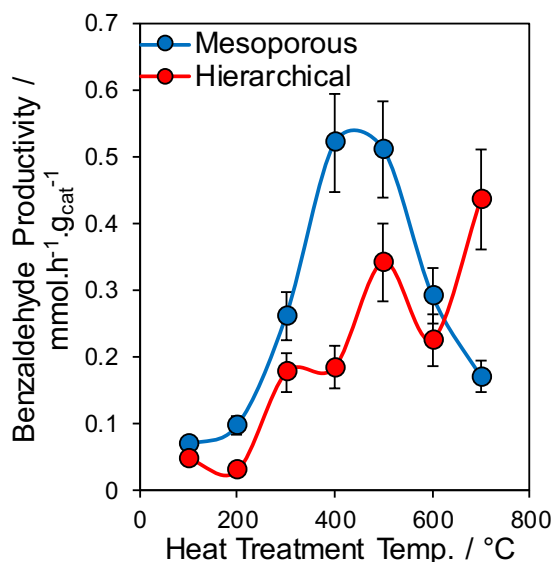


Figure 4.27. Mesoporous and hierarchical materials heated to different temperatures screened for the selective oxidation of benzyl alcohol at a reaction temperature of 60 °C.

Two final experiments were carried out for catalyst recovery and reuse, and for the comparison of fresh and ‘old’ materials. Both of these experiments showed how viable the materials are from an industrial standpoint.

The recycling study in **Figure 4.28** showed a near-total loss of initial activity after the first use, with the conversion gradually decreasing with use. This is interesting, as it suggests site inhibition was causing the deactivation of incredibly active sites on the material immediately, whereas a reserve of less active sites continued to remain active for longer (illustrated by the materials continued ability to convert). Regardless, the data showed that with continued use, the material was almost completely dead after three uses. Literature has shown the deactivation prevention with the use of base additive (also seen in this chapter), and with the regeneration of the sites.²⁵ It could also be hypothesised that heating to above the decomposition temperature of benzoic acid could also regenerate activity.

Due to the time constraints of catalytic synthesis, characterisation, and screening, there was a four-month gap between the initial testing in the temperature study and the first repeat of the deactivation study. A loss in activity, shown in **Figure 4.28**, was observed and thought to be caused by the exposure of materials to atmospheric CO₂ and water, causing the formation of carbonates and hydroxide. The effect of prolonged exposure on gold is not known. The materials were subsequently remade and screened for the second repeat of the deactivation study, but it is worth mentioning the lack of stability of these materials if not stored correctly.

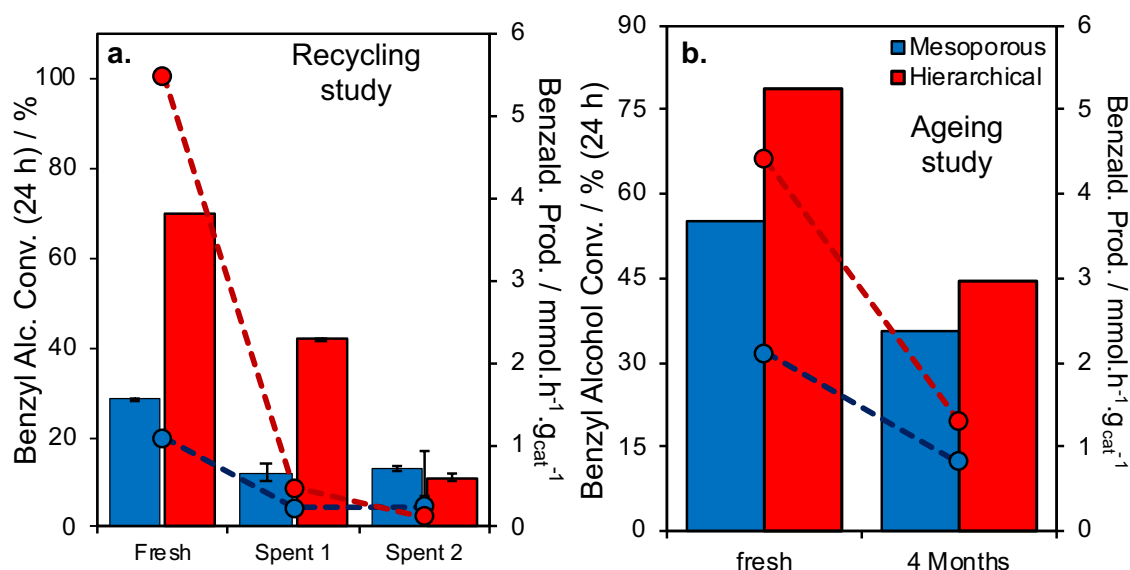


Figure 4.28. (a) Final substrate conversion and initial productivity of fresh and spent materials and (b) fresh and older material.

4.2.4.3 Deactivation and Green Conditions Summary

Multiple experiments were run to both determine and rule out the cause of deactivation. It was determined that the gold particles were stable throughout the reaction, with no leaching or particle agglomeration observed. Factors such as decreasing substrate concentration/equilibrium being reached, and low O₂ pressure headspace, did not influence the rate of deactivation. Reaction deactivation was determined to be caused by the production of a site inhibitor. The use of a 'scavenger' base hoovered up this inhibitor as it was produced, which was observed by the increased conversion. Of the two bases investigated, the stronger base (potassium carbonate) prolonged activity for longer.

Different reaction conditions were investigated, comparing an oxygen-rich headspace, oxygen flow, air headspace and solvent-free. The three different oxidant conditions showed slight differences in performance; with the best performing condition the oxygen headspace. Solvent-free conditions showed a huge increase in activity, likely brought on the very concentrated substrate. This, however, came with a cost, as selectivity to the unwanted ester was nearly an order of magnitude higher than other conditions tested. The activity was lost when the catalyst was recovered and reused, with literature pointing to an inhibiting product building up on the surface.²⁵ As no acid is detected, the inhibiting species is thought to be the benzyl benzoate coupling product. It was also noted that the catalyst had degraded in the four months since its synthesis, thought to be caused by UV exposure.

In summary, both mesoporous and hierarchical materials were active for this reaction, however, a stronger basic material is required to prevent the adsorption of the inhibiting products on the site. To this end, stronger bulk solid bases will be loaded with gold using the DIM synthesis in the next chapter and screened to see if their activity is maintained for longer.

4.3 Conclusions and Recommendations for Further Work

To conclude, gold nanoparticles have been impregnated on a known solid base functionalised support. Preliminary studies determined double impregnation method was the most suitable synthesis, due to its moderate activity and capacity to maintain the pore network.

Chemometrics was used to determine the optimum reaction conditions, as well as variables that may interact with the reaction singularly or synergistically. The reaction temperature was found to exert significant influence on final conversion and to a lesser extent rate. Selectivity was found to be influenced by a variety of factors, the most predominant being level of porosity and substrate concentration. Heat treatment was found to be extremely influencing on benzaldehyde productivity, prompting a study into the effect of different heat treatments.

Studying the effect of different heat treatments determined optimum heating of 400 °C, which was thought to be dependent on both changing gold environment and magnesium oxide environment. As the materials were heated, the gold agglomerated together into larger particles, resulting in different catalytic behaviour. Also facilitated by increasing temperature, the MgO surface underwent rearrangement to reveal more strongly basic facets. To isolate the effect of both these variables, two studies were undertaken: varying the loading of MgO and Au, to vary the basicity and gold particle size independent of each other respectively. Both studies revealed inconsistencies in the synthesis method, thought to be in the first stage one-pot synthesis of the MgO/SBA-15 support. It was also determined it was not possible to change the desired variable without altering others.

One of the most enjoyable aspects of this experimental chapter is the potential for expansion of this work. One of the avenues it could be taken is pivoting the study to a more industrially viable material, by using a flow reactor, and experimenting with different reactivation methods, such as base washing or thermally decomposing the inhibitor. Unfortunately, time constraints prevented these studies in the present thesis.

As mentioned in the previous chapter, MgO is considered a weak solid base when compared to other alkaline earth metal oxides, therefore there is potential to use a stronger solid basic functionality. Other alkaline earth metal oxides have the ability to further decrease deactivation, however, other base functionalities could also be used. Furthermore, regarding the support, there are significant monetary and time costs associated with using ordered mesoporous templated silica, combined with the poor

performance of SiO₂ as a gold support. These are the primary reasons for the use of bulk solid base supports in the last experimental chapter. Replicating the success of this work, at a reduced time and monetary cost. Furthermore, the use of noble metal alloys have been shown to be very promising,⁵³ and the use of a cheaper co-metal, such as copper or nickel, as the major phase would further dramatically reduce costs and alter catalytic activity.

4.4 References

1. M. Haruta, Spiers Memorial Lecture: Role of perimeter interfaces in catalysis by gold nanoparticles, *Faraday Discussions*, 2011, **152**, 11-32.
2. M. E. Ali, M. M. Rahman, S. M. Sarkar and S. B. A. Hamid, Heterogeneous metal catalysts for oxidation reactions, *Journal of Nanomaterials*, 2014, **2014**, 23.
3. G. J. Hutchings, Heterogeneous gold catalysis, *ACS Central Science*, 2018, **4**, 1095-1101.
4. A. S. K. Hashmi and G. J. Hutchings, Gold catalysis, *Angewandte Chemie International Edition*, 2006, **45**, 7896-7936.
5. M. Bowker, A. Nuhu and J. Soares, High activity supported gold catalysts by incipient wetness impregnation, *Catalysis Today*, 2007, **122**, 245-247.
6. P. Perez, M. A. Soria, S. A. C. Carabineiro, F. J. Maldonado-Hodar, A. Mendes and L. M. Madeira, Application of Au/TiO₂ catalysts in the low-temperature water-gas shift reaction, *International Journal of Hydrogen Energy*, 2016, **41**, 4670-4681.
7. G. A. Parks, The isoelectric points of solid oxides, solid hydroxides, and aqueous hydroxo complex systems, *Chemical Reviews*, 1965, **65**, 177-198.
8. M. A. Brown, M. Arrigoni, F. Héroguel, A. Belouqui Redondo, L. Giordano, J. A. van Bokhoven and G. Pacchioni, pH dependent electronic and geometric structures at the water-silica nanoparticle interface, *The Journal of Physical Chemistry C*, 2014, **118**, 29007-29016.
9. M. Haruta, Nanoparticulate gold catalysts for low-temperature CO oxidation, *Journal of New Materials for Electrochemical Systems*, 2004, **7**, 163-172.
10. X. Cui, W.-C. Zin, W.-J. Cho and C.-S. Ha, Nonionic triblock copolymer synthesis of SBA-15 above the isoelectric point of silica (pH=2-5), *Materials Letters*, 2005, **59**, 2257-2261.
11. S. T. Moerz and P. Huber, pH-dependent selective protein adsorption into mesoporous silica, *The Journal of Physical Chemistry C*, 2015, **119**, 27072-27079.
12. B. Wang, X. Xiong, H. Ren and Z. Huang, Preparation of MgO nanocrystals and catalytic mechanism on phenol ozonation, *RSC Advances*, 2017, **7**, 43464-43473.
13. K. Sneha, A. Esterle, N. Sharma and S. Sahi, Yucca-derived synthesis of gold nanomaterial and their catalytic potential, *Nanoscale research letters*, 2014, **9**, 627.
14. K. O'Connell and J. R. Regalbuto, High sensitivity silicon slit detectors for 1 nm powder XRD size detection limit, *Catalysis Letters*, 2015, **145**, 777-783.
15. A. L. Patterson, The Scherrer formula for X-Ray particle size determination, *Physical Review*, 1939, **56**, 978-982.
16. J. Malinowski, G. Dercz, K. Prusik, L. Pajak, R. Pielaszek and W. Pudlo, Structure studies on nanocrystalline powder of MgO xerogel prepared by sol-gel method, *Materials Science-Poland*, 2009, **27**, 201-207.
17. Z. Sun, X. Duan, C. Srinivasakannan and J. Liang, Preparation of magnesium silicate/carbon composite for adsorption of rhodamine B, *RSC Advances*, 2018, **8**, 7873-7882.

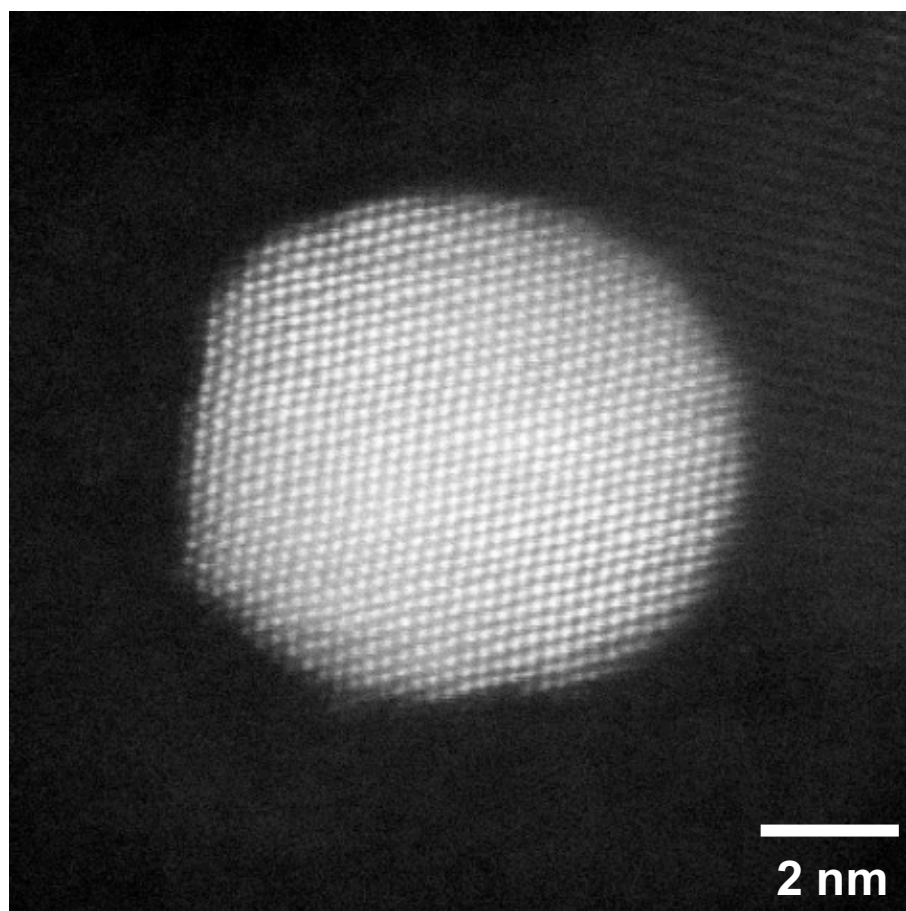
18. D. Y. Zhao, J. L. Feng, Q. S. Huo, N. Melosh, G. H. Fredrickson, B. F. Chmelka and G. D. Stucky, Triblock copolymer syntheses of mesoporous silica with periodic 50 to 300 angstrom pores, *Science*, 1998, **279**, 548-552.
19. S. G. Wainwright, C. M. A. Parlett, R. A. Blackley, W. Z. Zhou, A. F. Lee, K. Wilson and D. W. Bruce, True liquid crystal templating of SBA-15 with reduced microporosity, *Microporous and Mesoporous Materials*, 2013, **172**, 112-117.
20. Z. Alothman, A Review: Fundamental aspects of silicate mesoporous materials, *Materials*, 2012, **5**, 2874-2902.
21. K. A. Cychosz, R. Guillet-Nicolas, J. García-Martínez and M. Thommes, Recent advances in the textural characterization of hierarchically structured nanoporous materials, *Chemical Society Reviews*, 2017, **46**, 389-414.
22. Y. Song, J. K. Mobley, A. H. Motagamwala, M. Isaacs, J. A. Dumesic, J. Ralph, A. F. Lee, K. Wilson and M. Crocker, Gold-catalyzed conversion of lignin to low molecular weight aromatics, *Chemical Science*, 2018, **9**, 8127-8133.
23. R. Poreddy, C. Engelbrekt and A. Riisager, Copper oxide as efficient catalyst for oxidative dehydrogenation of alcohols with air, *Catalysis Science & Technology*, 2015.
24. T. Silva, E. Teixeira Neto, N. López and L. Rossi, Volcano-like behavior of Au-Pd core-shell nanoparticles in the selective oxidation of alcohols, *Nature*, 2015, **4**, 5766.
25. E. Skupien, J. R. Berger, P. V. Santos, J. Gascon, M. Makkee, T. M. Kreutzer, J. P. Kooyman, A. J. Moulijn and F. Kapteijn, Inhibition of a gold-based catalyst in benzyl alcohol oxidation: understanding and remediation, *Catalysts*, 2014, **4**.
26. W.-Y. Yu, G. M. Mullen and C. B. Mullins, Hydrogen adsorption and absorption with Pd-Au bimetallic surfaces, *The Journal of Physical Chemistry C*, 2013, **117**, 19535-19543.
27. D. Pugliese, F. Bella, V. Cauda, A. Lamberti, A. Sacco, E. Tresso and S. Bianco, A Chemometric Approach for the Sensitization Procedure of ZnO flowerlike microstructures for dye-sensitized solar cells, *ACS Applied Materials & Interfaces*, 2013, **5**, 11288-11295.
28. F. Bella, D. Pugliese, J. R. Nair, A. Sacco, S. Bianco, C. Gerbaldi, C. Barolo and R. Bongiovanni, A UV-crosslinked polymer electrolyte membrane for quasi-solid dye-sensitized solar cells with excellent efficiency and durability, *Physical Chemistry Chemical Physics*, 2013, **15**, 3706-3711.
29. G. E. P. Box, J. S. Hunter and W. G. Hunter, *Statistics for experimenters: design, innovation, and discovery*, Wiley-Interscience, 2005.
30. *Chemical reaction engineering - 3rd Edition*, Wiley India Pvt. Limited, 2006.
31. N. Masoud, T. Partsch, K. P. de Jong and P. E. de Jongh, Thermal stability of oxide-supported gold nanoparticles, *Gold Bulletin*, 2019, **52**, 105-114.
32. S. Yang, F. Xu, S. Ostendorp, G. Wilde, H. Zhao and Y. Lei, Template-confined dewetting process to surface nanopatterns: fabrication, structural tunability, and structure-related properties, *Advanced Functional Materials*, 2011, **21**, 2446-2455.
33. K. Dick, T. Dhanasekaran, Z. Zhang and D. Meisel, Size-dependent melting of silica-encapsulated gold nanoparticles, *Journal of the American Chemical Society*, 2002, **124**, 2312-2317.

34. J. B. Lowe and R. T. Baker, Deformation of ordered mesoporous silica structures on exposure to high temperatures, *Journal of Nanomaterials*, 2014, **2014**, 13.
35. V. S. Cvetković, N. Jovičević, J. S. Stevanović, M. G. Pavlović, N. M. Vukičević, Z. Stevanović and J. N. Jovičević, Magnesium–gold alloy formation by underpotential deposition of magnesium onto gold from nitrate melts, *Metals*, 2017, **7**, 95.
36. H.-L. Lu, S.-J. Ding and D. W. Zhang, Investigation of thermal stability of atomic-layer-deposited MgO thin films on Si(100) using X-Ray photoelectron spectroscopy, *Electrochemical and Solid-State Letters*, 2010, **13**, G25-G28.
37. J. M. Montero, P. Gai, K. Wilson and A. F. Lee, Structure-sensitive biodiesel synthesis over MgO nanocrystals, *Green Chemistry*, 2009, **11**, 265-268.
38. Z. Y. Wu, Q. Jiang, Y. M. Wang, H. J. Wang, L. B. Sun, L. Y. Shi, J. H. Xu, Y. Wang, Y. Chun and J. H. Zhu, Generating superbasic sites on mesoporous silica SBA-15, *Chemistry of Materials*, 2006, **18**, 4600-4608.
39. J. C. F. Rodríguez-Reyes, C. M. Friend and R. J. Madix, Origin of the selectivity in the gold-mediated oxidation of benzyl alcohol, *Surface Science*, 2012, **606**, 1129-1134.
40. P. Suchomel, L. Kvitek, R. Pucek, A. Panacek, A. Halder, S. Vajda and R. Zboril, Simple size-controlled synthesis of Au nanoparticles and their size-dependent catalytic activity, *Scientific Reports*, 2018, **8**, 4589.
41. N. M. JamJam, Y. H. Taufiq Yap, E. N. Muhamad, M. Izham Saiman and T. A. Saleh, Free solvent oxidation of molecular benzyl alcohol by newly synthesized AuPd/titania catalysts, *Inorganic Chemistry Communications*, 2019, **107**, 107471.
42. V. R. Choudhary, A. Dhar, P. Jana, R. Jha and B. S. Uphade, A green process for chlorine-free benzaldehyde from the solvent-free oxidation of benzyl alcohol with molecular oxygen over a supported nano-size gold catalyst, *Green Chemistry*, 2005, **7**, 768-770.
43. S. Said and M. Riad, Oxidation of benzyl alcohol through eco-friendly processes using Fe-doped cryptomelane catalysts, *Solid State Sciences*, 2019, **94**, 145-154.
44. E. N. Kolobova, A. N. Pestryakov, N. Bogdanchikova and V. Cortés Corberán, Silver catalysts for liquid-phase oxidation of alcohols in green chemistry: Challenges and outlook, *Catalysis Today*, 2019, **333**, 81-88.
45. A. Kumar, V. P. Kumar, A. Srikanth, V. Vishwanathan and K. V. R. Chary, Vapor phase oxidation of benzyl alcohol over nano Au/SBA-15 catalysts: effect of preparation methods, *Catalysis Letters*, 2016, **146**, 35-46.
46. G. I. Almerindo, L. F. D. Probst, C. E. M. Campos, R. M. de Almeida, S. M. P. Meneghetti, M. R. Meneghetti, J.-M. Clacens and H. V. Fajardo, Magnesium oxide prepared via metal–chitosan complexation method: Application as catalyst for transesterification of soybean oil and catalyst deactivation studies, *Journal of Power Sources*, 2011, **196**, 8057-8063.
47. P. Atkins, J. de Paula and J. Keeler, *Physical Chemistry*, Oxford University Press, Great Britain, 8th edition, 2006.
48. S. K. Klitgaard, A. T. DeLa Riva, S. Helveg, R. M. Werchmeister and C. H. Christensen, Aerobic oxidation of alcohols over gold catalysts: role of acid and base, *Catalysis Letters*, 2008, **126**, 213-217.

49. C. P. Ferraz, M. A. S. Garcia, É. Teixeira-Neto and L. M. Rossi, Oxidation of benzyl alcohol catalyzed by gold nanoparticles under alkaline conditions: weak vs. strong bases, *RSC Advances*, 2016, **6**, 25279-25285.
50. M. Du, G. Zeng, J. Huang, D. Sun, Q. Li, G. Wang and X. Li, Green photocatalytic oxidation of benzyl alcohol over noble-metal-modified H₂Ti₃O₇ nanowires, *ACS Sustainable Chemistry & Engineering*, 2019, **7**, 9717-9726.
51. J. Liu, S. Zou, J. Wu, H. Kobayashi, H. Zhao and J. Fan, Green catalytic oxidation of benzyl alcohol over Pt/ZnO in base-free aqueous medium at room temperature, *Chinese Journal of Catalysis*, 2018, **39**, 1081-1089.
52. L. M. Chevallier, S. Dessolin, F. Serres, L. Bruyas and G. Chatel, Effect of ultrasound on the green selective oxidation of benzyl alcohol to benzaldehyde, *Molecules*, 2019, **24**.
53. K. Heidkamp, M. Aytemir, K.-D. Vorlop and U. Prüße, Ceria supported gold–platinum catalysts for the selective oxidation of alkyl ethoxylates, *Catalysis Science & Technology*, 2013, **3**, 2984-2992.

Chapter 5

Gold functionalised SiO_2 , MgO and CaO supports for the selective oxidation of benzyl alcohol and oxidative cross-coupling of benzyl alcohol and benzylamine.



Gold nanoparticle from Au/CaO(400) sample.

5.1 Introduction

In the previous chapter, gold functionalised MgO/SBA-15 was investigated for the selective oxidation of benzyl alcohol. It was determined how different heat treatments, loadings and reaction conditions resulted in significant deviations to the material and activity. It was also determined that deactivation was occurring via the inhibition of the gold species from most likely benzyl benzoate.

To alleviate this deactivation, nano-alkaline earth metal oxide supports and silica support will be functionalised and compared to the mesoporous and hierarchical materials produced in the previous chapter. The materials will be screened for the oxidative cross-coupling of benzyl alcohol and benzylamine, to study their scavenger capacity to prevent deactivation of the intrinsic basicity, and compare if the support nature and/or the support architecture plays an important role in this type of reaction.

5.2 Results and Discussion

As with previous chapters, multiple characterisation techniques were employed to determine the physical and chemical properties of the materials. These involve quantitative techniques, such as inductively coupled plasma-optical emission spectroscopy (ICP-OES) and nitrogen porosimetry, and qualitative techniques including X-ray photoelectron spectroscopy (XPS), scanning transmission electron microscopy (STEM) and X-ray diffraction (XRD).

As with the Au@MgO/SBA-15 materials, Au/Bulk materials were screened for the selective oxidation of benzyl alcohol, investigating the effect of added base. Further screening for oxidative cross-coupling of benzyl alcohol and benzylamine was undertaken, as it is an extremely useful chemical transformation for processes with toxic or unstable aldehyde intermediates, as mentioned in **Chapter 1.1.4.4**.

5.2.1 Au/Bulk Materials Characterisation

The atomic loading of the bulk supports was determined using ICP-OES analysis, displayed in **Figure 5.1** as a function of heat treatment temperature. The loading differed between supports, seemingly as a result of their basicity or isoelectric point.

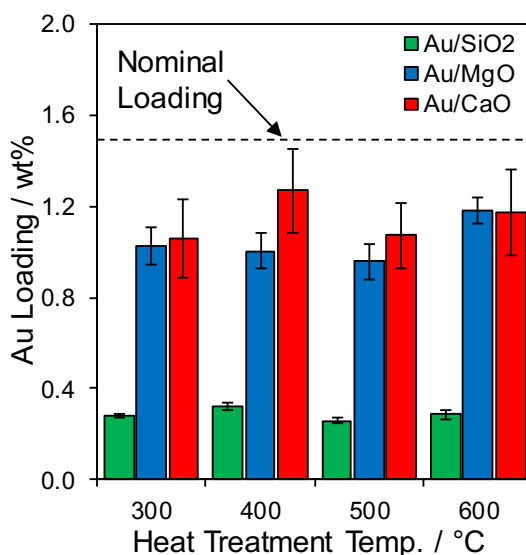


Figure 5.1. Inductively coupled plasma – optical emission spectroscopy of the gold content of Au functionalised bulk supports as a function of heat treatment temperature.

The lowest loaded materials, Au/SiO₂, gave a gold content approximately five times smaller than the nominal. Au/MgO and Au/CaO gave an improved loading, similar to those of the Au@MgO/SBA-15. As mentioned in **Chapter 4.2.1**, the support's isoelectric point plays an important role in successful impregnations.^{1, 2}

The lowest loaded support, fumed silica, has an isoelectric point of between a pH of 2 and 5.^{3, 4} As the pH of the DIM impregnation is approximately 6,⁵ this means the silica surface is negatively charged, thereby disfavoring the impregnation. MgO, and to a greater extent CaO, have a higher isoelectric point, 10.5⁶ and 12.3⁷ respectively. This means the alkaline earth metal oxides will have a positively charged surface during the synthesis, thereby favouring impregnation. The increased loading of Au/CaO materials is therefore likely the result of an increased isoelectric point and therefore greater positively charged surface.

5.2.1.1 Wide and Diffractometry

Wide-angle X-ray diffraction (Figures 5.2 to 5.4) was employed to ascertain the crystalline species within the material and to estimate the crystallite size of the gold functionality. The previous chapter determined that calculating the crystallite size using solely the Scherrer equation proved inaccurate, primarily due to particles below the limit of detection being omitted.

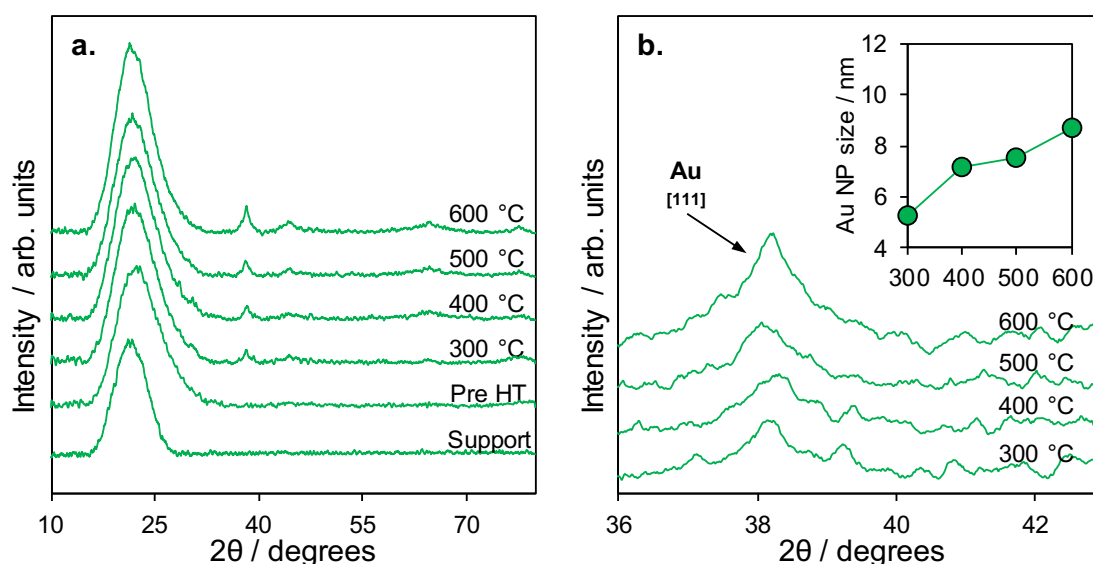


Figure 5.2. Wide-angle X-ray diffraction patterns of Au/SiO₂ materials heat-treated at different temperatures, displaying the (a) full pattern and (b) the Au [111] reflection.

XRD analysis of the Au/SiO₂ materials discovered an amorphous silica reflection between 20-25°, characteristic of fumed silica.⁸ Both parent support and preheat treated materials showed no gold reflections, suggesting the gold particles post impregnation were below the limit of detection of 2-2.5 nm.⁹ Heat-treated materials showed the reflections indicative of metallic gold, with the most prominent peak being the gold₁₁₁ reflection at approximately 38°. Particle size determined using the Scherrer equation showed a linear increase with temperature, which was comparable with Au@MgO/SBA-15 materials.

The analysis of the parent support in **Figure 5.3** revealed a mixture of majorly MgO¹¹ and a minority of Mg(OH)₂¹², which is common to atmosphere sensitive solid base materials. Post impregnation materials shifted to an almost complete hydroxide phase, likely resulting from the aqueous gold impregnation method. This pattern was comparable for the Au/MgO 300 °C sample, as the decomposition temperature of 332 °C¹² for the hydroxide species was not reached. Gold reflections were not visible for pre heat-treated and 300 °C samples, suggesting the gold species were potentially below the detection limit, thereby requiring microscopy to accurately characterise.

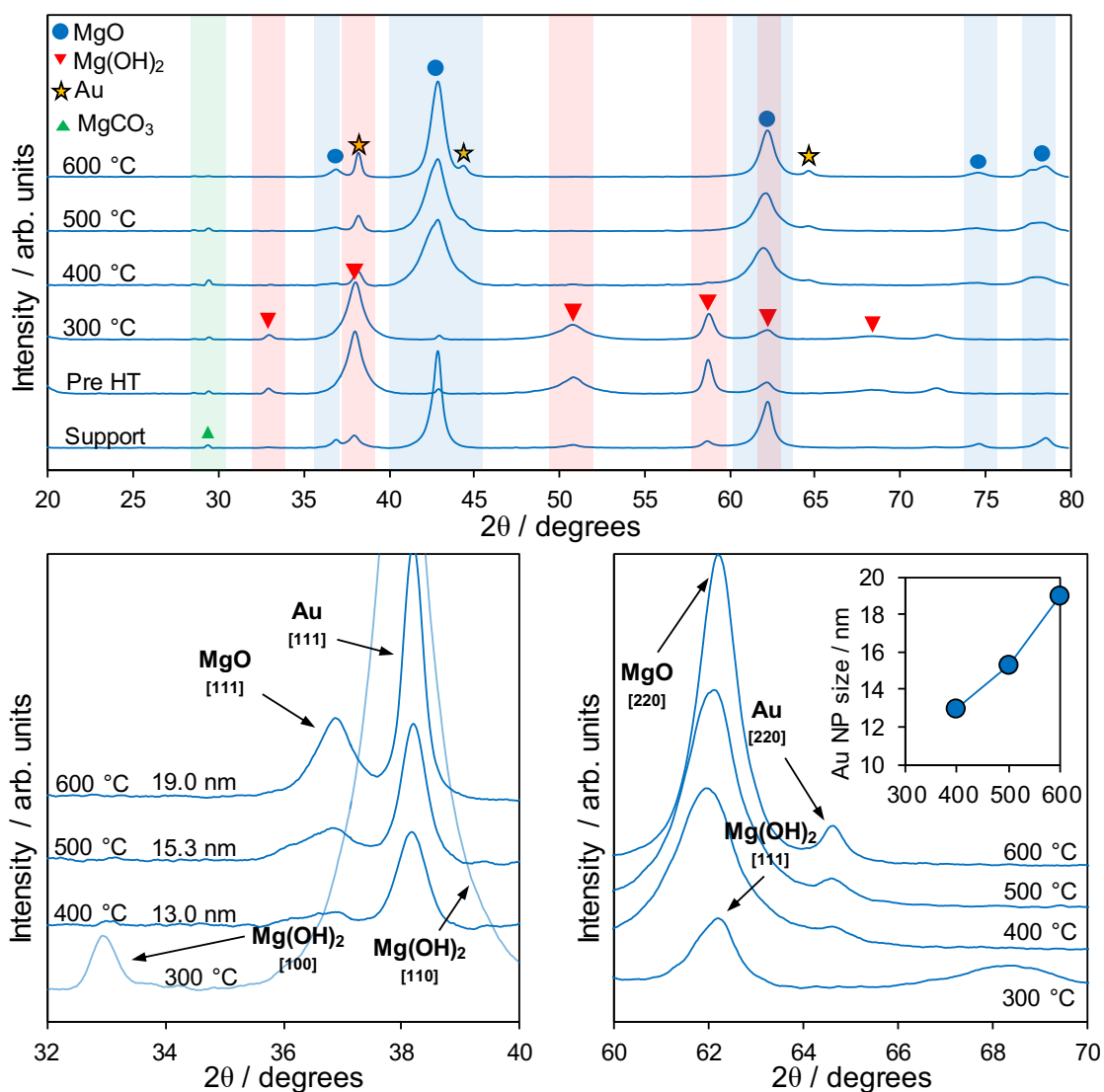


Figure 5.3. Wide-angle X-ray diffraction patterns of Au/MgO materials heat-treated at different temperatures, displaying the full pattern (top), the Au and MgO [111] reflection (bottom left), as well as the Au [220] reflection (bottom right).

Materials calcined at 400 °C and higher indicated no hydroxide reflections, suggesting total decomposition back to MgO. Gold reflections within the range of 13-19 nm became

visible above this temperature although, as discussed previously this figure, likely omits sub 2.5 nm gold particles. The heat treatment temperature increase caused the MgO reflections to become sharper and less distributed, evident in the MgO₁₁₁ reflection. This may suggest the support was reforming into more crystalline species. A small MgCO₃ reflection was observed at 28-29° even above the decomposition temperature of 350 °C.¹² This may be caused by the decomposition not taking place until 600 °C, or because heat-treating in air could cause atmospheric CO₂ to chemisorb back to the vacant sites upon cooling. This could be prevented by initially treating the materials under pure oxygen flow, or treating the current materials at above 350 °C in an inert/O₂ atmosphere.

Similar to MgO supported materials, the Au/CaO XRD patterns (**Figure 5.4**) showed a mixture of phases across all samples, and the parent support exhibiting calcium oxide as the major phase with smaller hydroxide and carbonate impurities.¹³ The pre heat-treated sample shifted completely from the oxide to hydroxide phase, which was expected as the gold impregnation was aqueous. However, carbonate was also a large component of the pattern. Gold is not visible for the pre heat-treated material, suggesting the gold was below the detection limit.

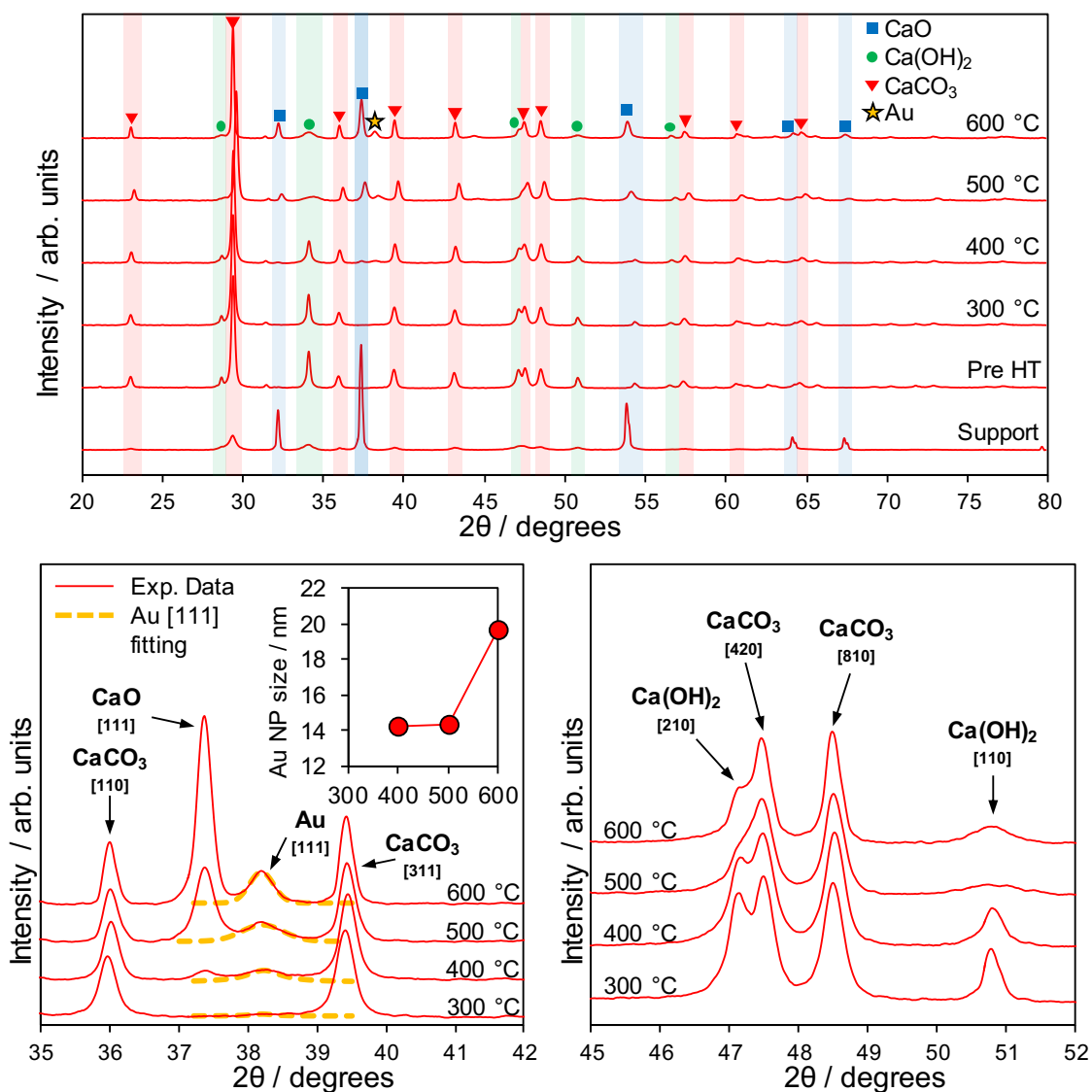


Figure 5.4. Wide-angle X-ray diffraction patterns of Au/CaO materials heat treated at different temperatures, displaying the full pattern (top), the Au and CaO [111] reflection (bottom left), as well as the Ca(OH)₂ reflections (bottom right).

When the heat treatment temperature increased up to 400 °C and above, the intensity of the calcium hydroxide phase decreased, suggesting decomposition back to the oxide species was occurring. This was supported by the appearance of CaO at 400 °C, which suggested Ca(OH)₂ begins decomposing under the reported temperature of 520 °C.¹⁴ On the contrary, the CaCO₃ phase remained constant, since the decomposition is initiated above 700-800 °C.¹⁵ Gold reflections were observed at 400 °C with a particle size ranging from 14-20 nm, further supporting that the Au nanoparticles are stable up to 300 °C.¹⁶

5.2.1.2. Nitrogen Porosimetry

Nitrogen Porosimetry was undertaken for all Au/Bulk supports to determine their physical properties. Regardless of the heat treatment temperature, each sample from the same support showed very little isotherm shape deviation with temperature.

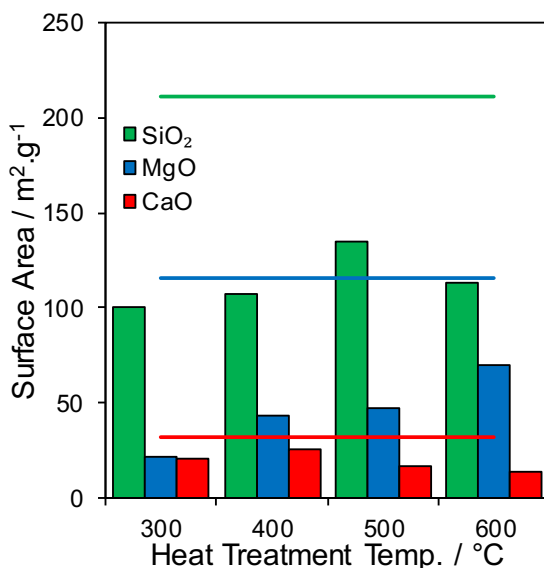


Figure 5.5. Surface area for gold functionalised bulk supports as a function of heat treatment temperature, with parent support surface area represented by lines.

Fumed silica displayed a broad pore size distribution (**Appendix Figure 4a.1**), with very little porosity below 15 nm, except for the 500 °C sample. However, this is most likely an anomalous result. Nano-MgO materials porosity was contained within the range 5-20 nm (**Appendix Figure 4a.2**), with a shift in distribution from lower to larger pore size as temperature increased. Nano-CaO materials (**Appendix Figure 4a.3**) displayed pore tendencies from both SiO₂ and MgO. They showed both, a sharp distribution of sub 10 nm pores and a large distribution of 15 nm and above, with the relative distribution of both being unaffected by temperature. It could be reasoned the fumed silica support remained stable due to its high thermal stability,¹⁷ whereas the MgO, and to a lesser extent CaO, experienced decomposition of hydroxide and carbonate species that caused changes within the structure.

All materials exhibited a drop in surface area of over 50% compared to the parent supports and treated materials (**Figure 5.5**). This was also observed in the SBA-15 materials (**Figure 4.8**), suggesting the decrease could be caused by the aqueous nature of the impregnation. The change in surface area observed with the heat treatment was attributed to the atmospheric impurity decomposition. Magnesium oxide experienced the highest decomposition of its atomically poisoned derivative, with a steady linear increase

of surface area with heat treatment temperature. On the contrary, silica and calcium oxide remained relatively constant within error.

5.2.1.3. X-ray Photoelectron Spectroscopy

XPS analysis was carried out to elucidate the surface species and their changing concentrations with temperature. The results for fumed silica (**Figure 5.6** to **Figure 5.7**), MgO (**Figure 5.8** to **Figure 5.9**) and CaO (**Figure 5.10** to **Figure 5.11**) are presented in this section.

As seen with the heat treatment study (**Chapter 4.2.3.1**), there are two components at 103.0 and 103.3 eV (**Figure 5.6a**), which correspond to SiO₂ and chemisorbed species¹⁸ bound to the silica surface respectively. No changes appeared in either feature binding energy or relative intensity. This is thought to be due to the relatively high thermal stability of silica.

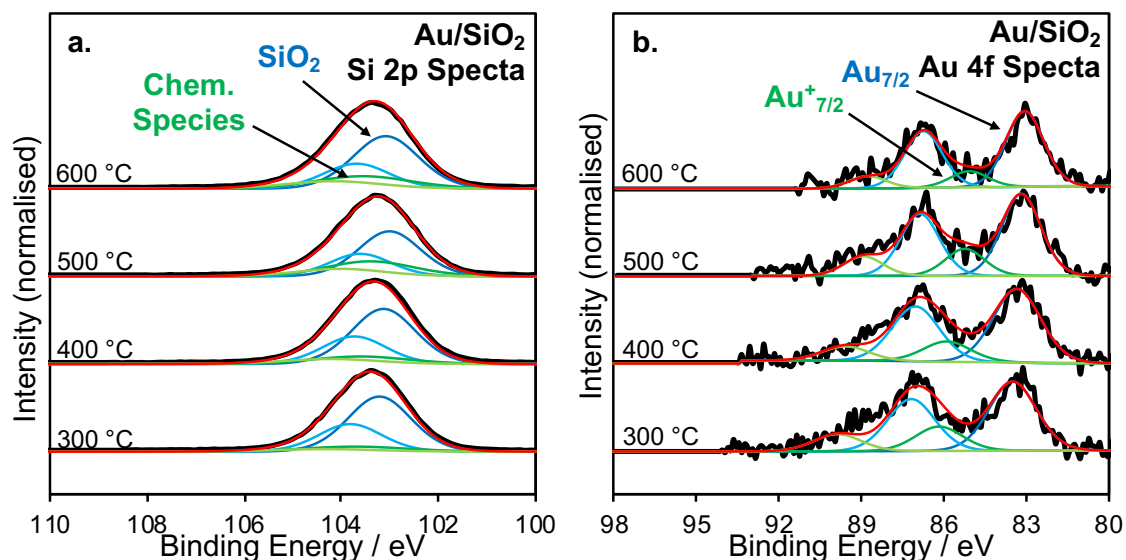


Figure 5.6. X-ray photoelectron spectra of (a) Si 2p and (b) Au 4f for Au/SiO₂ materials heat treated at different temperatures.

Two small doublet peaks were visible in the Au 4f spectra at 83-84 and 86 eV (**Figure 5.6b**), corresponding to Au⁰ and Au⁺, respectively.¹⁹ There appears to be a slight shift in features, which is unusual considering the silica having no significant basicity. The ratio between metallic and cationic gold remained relatively constant, with the principal species being metallic.

The O 1s spectra shown in **Figure 5.7** displayed 3 peaks at 530.4, 532.5 and 534.4 eV which correspond to organic contaminants, SiO₂ and hydroxyl species²⁰ bound to the silica surface, respectively. There appears to be no major change in either feature binding energy or relative intensity. This is thought to be due to the relatively high thermal

stability of silica. It could be argued there was a slight decrease in organic contaminants, which may have been thermally decomposed by the heat treatments. This could result in a slight uptake of the hydroxyl feature, benefiting from the vacated surface sites.

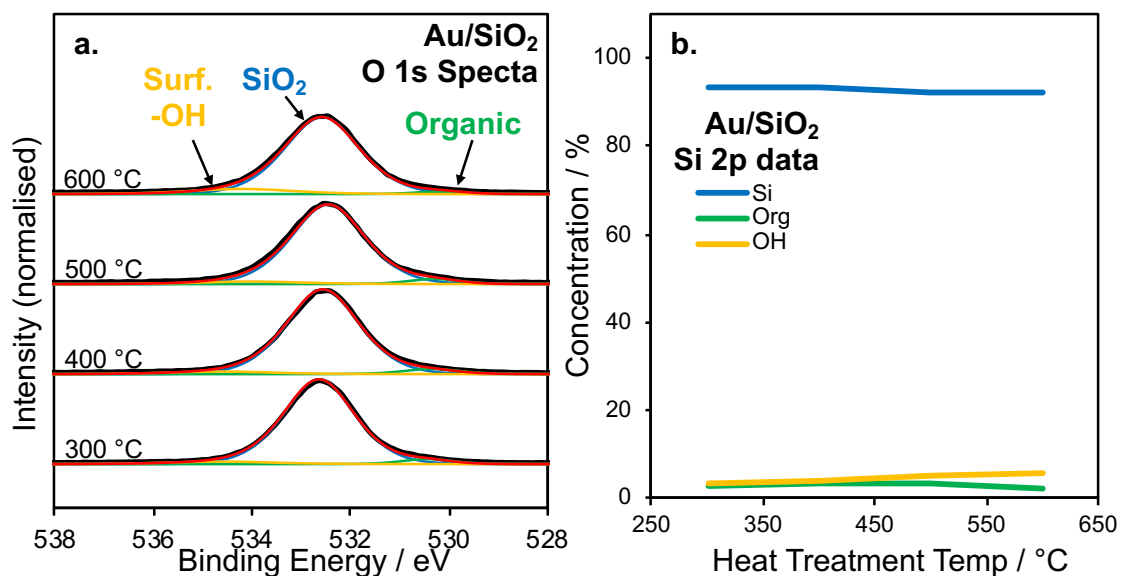


Figure 5.7. X-ray photoelectron spectrum of (a) O1s and (b) relative component concentrations for Au/SiO₂ materials heat-treated at different temperatures.

The Au/SiO₂ XPS revealed a very stable material, with no significant change with temperature. The lack of change in the Si 2p region was attributed to the relatively high thermal stability of the support. The gold functionality appeared to be shifting to lower binding energies, an effect previously thought to be caused by increasing basicity.

The Mg 2p spectra shown in **Figure 5.8**, displayed 3 doublet peaks at 49.1, 50.3 and 52.0 eV, which correspond to MgO, Mg(OH)₂ and MgCO₃, respectively.^{20, 21}

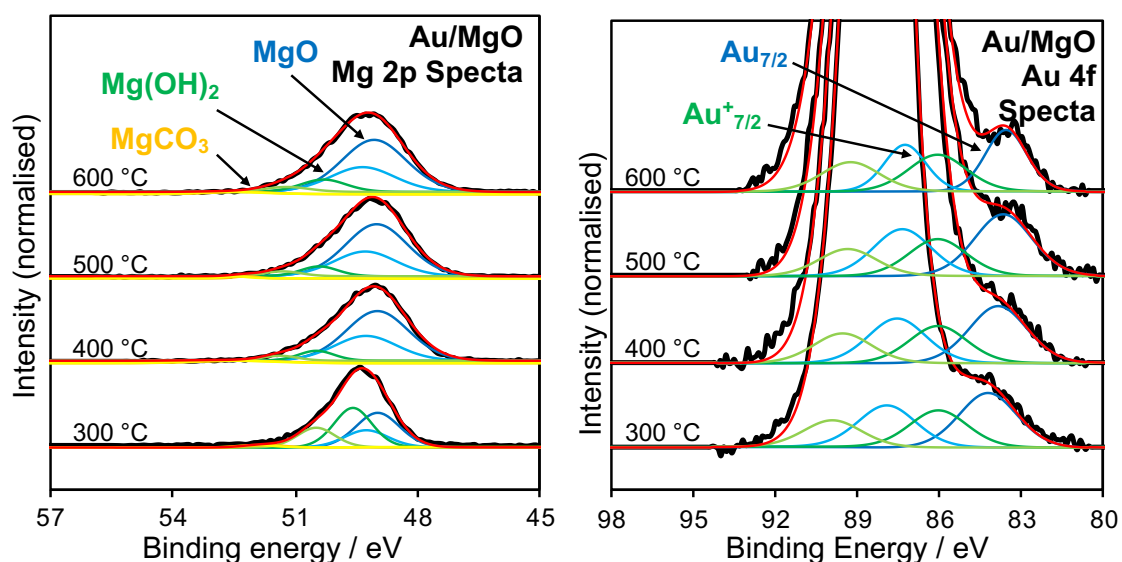


Figure 5.8. X-ray photoelectron spectra of (a) Mg 2p and (b) Au 4f for Au/MgO materials heat-treated at different temperatures.

XRD patterns in **Figure 5.3** exhibited very minor carbonate reflections which were also seen in the XPS, indicating the carbonate is a very minor species distributed throughout the material. At 300 °C, the hydroxide content was the predominant feature of the spectra, however with increased temperature decomposition occurred. What is interesting is that the hydroxide did not completely disappear as with XRD, which may be the result of atmospheric poisoning only present on the surface and not throughout the material. As XPS is a surface-sensitive technique, the hydroxide content is overrepresented relative to its bulk content.

The Au 4f spectra displayed two doublet peaks and one singlet peak, visible in **Figure 5.8**, at 84, 86 and 88 eV corresponding to Au^0 , Au^+ and Mg 2s respectively.²² Note that the Mg 2s feature is omitted to better observe the gold species. A shift to lower binding energy was observed for the metallic gold, indicative of increasing basicity, as seen in the literature¹⁹ and SBA-15 materials. The shoulder formed by the Au^0 peak was distinguishable. Unfortunately, the peak formed from the Au^+ feature and became more problematic to identify with clarity, due to the large error generated by the presence of the large Mg 2s region.

The O 1s spectra (**Figure 5.9**) showed 3 peaks at 529, 530.7 and 531.7 eV which correspond to MgO, $\text{Mg}(\text{OH})_2$ and MgCO_3 , respectively.²⁰

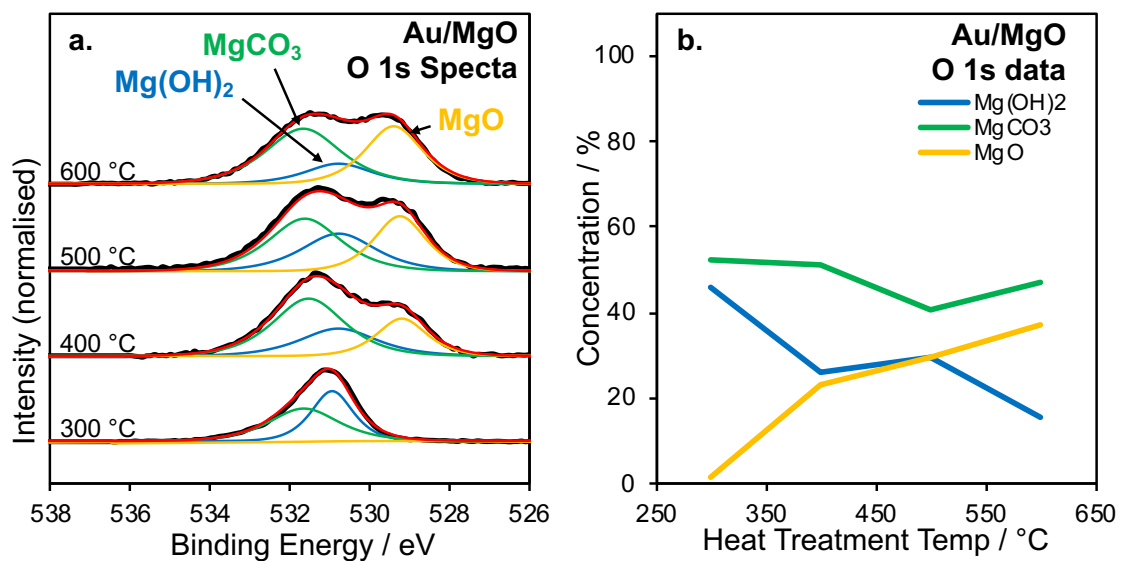


Figure 5.9. X-ray photoelectron spectrum of (a) O1s and (b) relative component concentrations for Au/MgO materials heat-treated at different temperatures.

In summary, the Au/MgO XPS confirmed the synthesised instigated formation of Mg(OH)₂ and MgCO₃, and subsequent decomposition back to MgO, which was reflected in the WAXRD (**Figure 5.4**). Both species were detected to some degree in all samples, suggesting the surface was still susceptible to atmospheric poisoning. However, the bulk remained unchanged. This was determined by comparing the relative peak area of the Mg species with their XRD patterns, thereby comparing the bulk vs surface concentration.

The Ca 2p spectra shown in **Figure 5.10** displayed 2 doublet peaks at 346.8 and 348.3 eV, corresponding to calcium carbonate/oxide, and calcium hydroxide species, respectively.²³

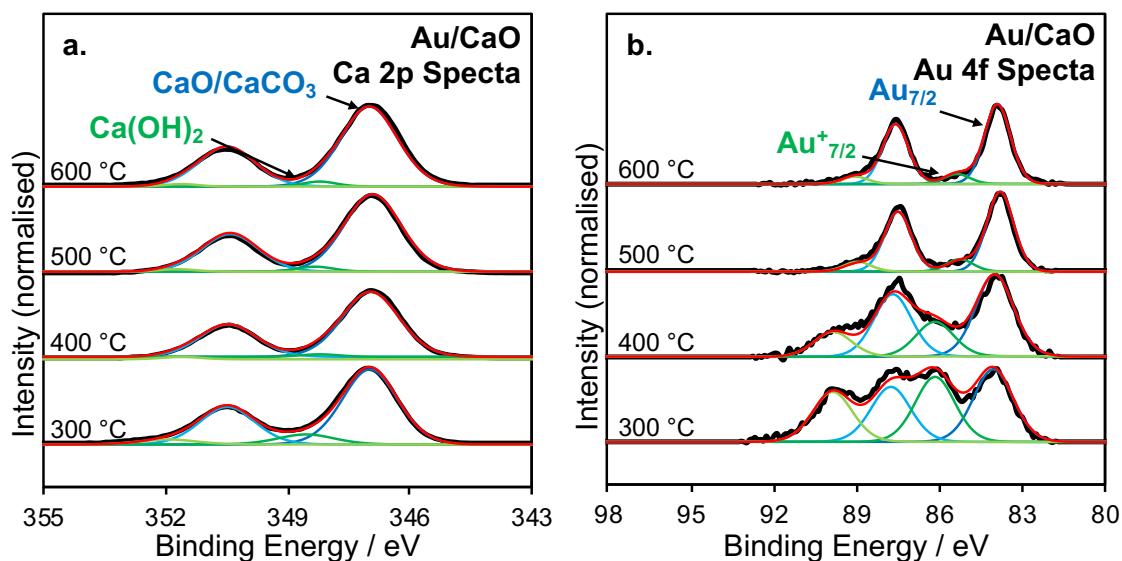


Figure 5.10. X-ray photoelectron spectra of (a) Ca 2p and (b) Au 4f for Au/CaO materials heat-treated at different temperatures.

The minor hydroxide component decreased in size as temperature increased, however, it was present even above the decomposition temperature of 580 °C. This indicated atmospheric poisoning was reforming the hydroxide species, caused by either the cooling in air or exposure to the atmosphere.

Two doublet peaks were clearly visible in the Au 4f spectra at approximately 84 and 86 eV. A shift from cationic to metallic gold was observed with increasing heat treatment temperature, a trend also observed for the hierarchical materials (**Figure 4.12b**) attributed to a shift in particle size. The relationship between particle size and $\text{Au}^0:\text{Au}^+$ ratio is illustrated in **Appendix Figure 4a.4**, however, it should be noted that both mesoporous and nano-MgO materials did not follow the trend.

The O 1s spectra displayed in **Figure 5.11** displayed 2 peaks at 530.9 and 532.2 eV, corresponding to calcium carbonate/oxide and calcium hydroxide species, respectively.²⁴ XRD determined a loss in hydroxide with temperature (**Figure 5.4**), however, this was not observed. As with the MgO materials, this may suggest the surface of the material is susceptible to the formation of hydroxide and carbonate species. When comparing the concentrations of both O 1s features, it could be argued there is a decrease in CaCO_3/CaO feature, however, this is within error.

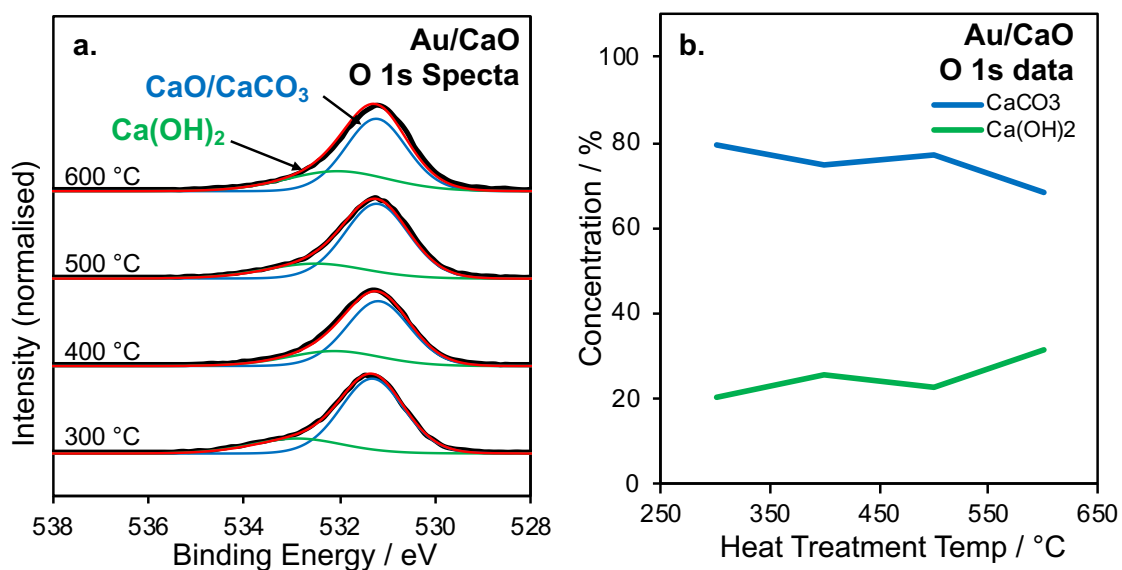


Figure 5.11. X-ray photoelectron spectrum of (a) O1s and (b) relative component concentrations for Au/CaO materials heat-treated at different temperatures.

As seen with the MgO/SBA-15 materials (**Figure 4.12**), the concentration of Au⁰ increased with temperature for SiO₂ and CaO materials (**Figure 5.12**), which is expected from materials with increasing particle size. Inversely, MgO Au⁰:Au⁺ ratio remained uniform, which could be misleading due to the poor Au peak resolution caused by the large interference of the Mg 2s component.

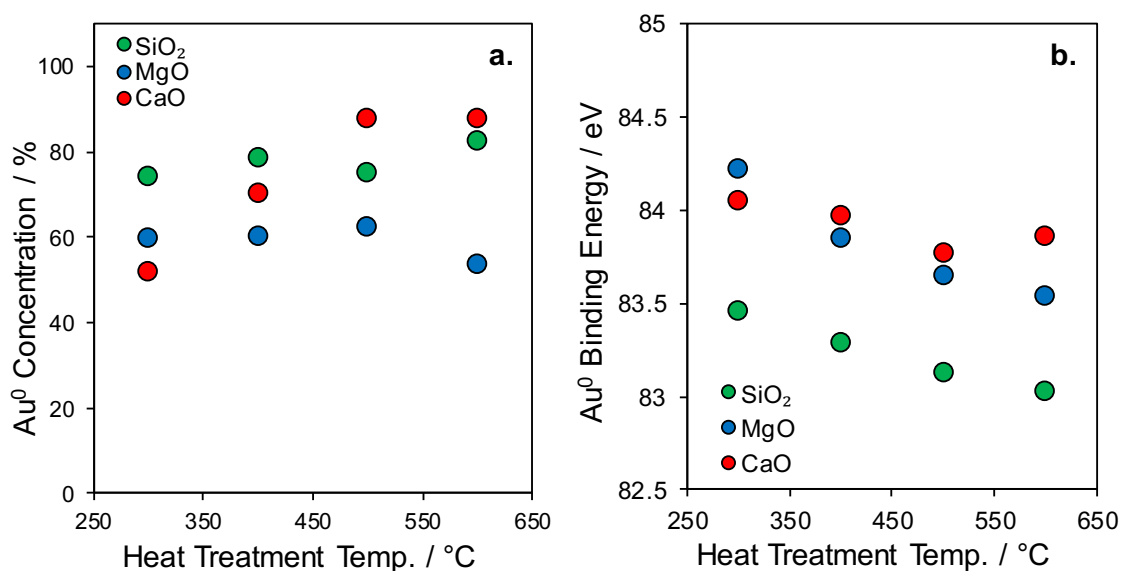


Figure 5.12. Gold (a) charge ratio and (b) binding energy as a function of temperature for bulk supported gold materials.

In summary, the Au/CaO materials showed similar characteristics as the MgO materials, exhibiting surface atmospheric poisoning and thermal decomposition back to the oxide.

However, the CaO materials did not reach the required temperature to decompose the carbonate. Gold spectra exhibited a shift in both binding energy and metallic-cationic ratio, suggesting both basicity and particle size was increasing with heat treatment temperature.

As seen in the previous chapter, the basicity of material can have an effect on the binding energy of the Au⁰ peak. This shift was observed for all bulk supported materials from 300 to 600 °C, with silica shifting from 0.5 eV, the MgO from 0.7 eV and the CaO from 0.3 eV. It was expected that alkaline earth metal oxides would exhibit increased basicity, brought on from thermal surface rearrangement, but there is no such explanation for the silica, which is slightly acidic in nature. As all materials exhibited this shift these changes may also be related to the thermal treatment.

5.2.1.4. Scanning Transmission Electron Microscopy

Transmission electron microscopy was performed in a selection of materials to determine accurate particle size and the nanostructure of the support (**Appendix Figures 4a.5-7**). This was used to mitigate the inaccuracies of the Scherrer equation.

Au/SiO₂(500) (**Appendix Figure 4a.5**) displayed small particle size uniformity with no clusters. The Scherrer equation was found to give a particle size of 7.5 nm, which was almost double the value calculated from TEM, confirming a significant portion of gold was below the limit of detection, thereby providing an overestimation of the particle size. Au/MgO(500) (**Appendix Figure 4a.6**) displayed very poor particle size uniformity and medium to large clusters throughout. Interestingly, the Scherrer particle size and TEM correlated perfectly, suggesting that for MgO materials treated to 500 °C and above, no sub 2.5 nm particles remained. Au/CaO(500) (**Appendix Figure 4a.7**) also displayed poor particle size uniformity and medium clusters throughout. As the distribution of particles was extremely large, the particle size calculated using the Scherrer equation and TEM was within error. The many reflections of CaO and its derivatives in the XRD made the particle diameter difficult to calculate using the Scherrer equation. Therefore, the other temperatures were examined using TEM.

The particle size distribution is shown in **Figure 5.13** and draws three conclusions. Firstly, the two materials with a lower surface area, Au/MgO and Au/CaO (**Figure 5.5**), exhibited very poor size distributions, whereas the silica support with the highest surface area showed a narrow distribution and reduced particle size.

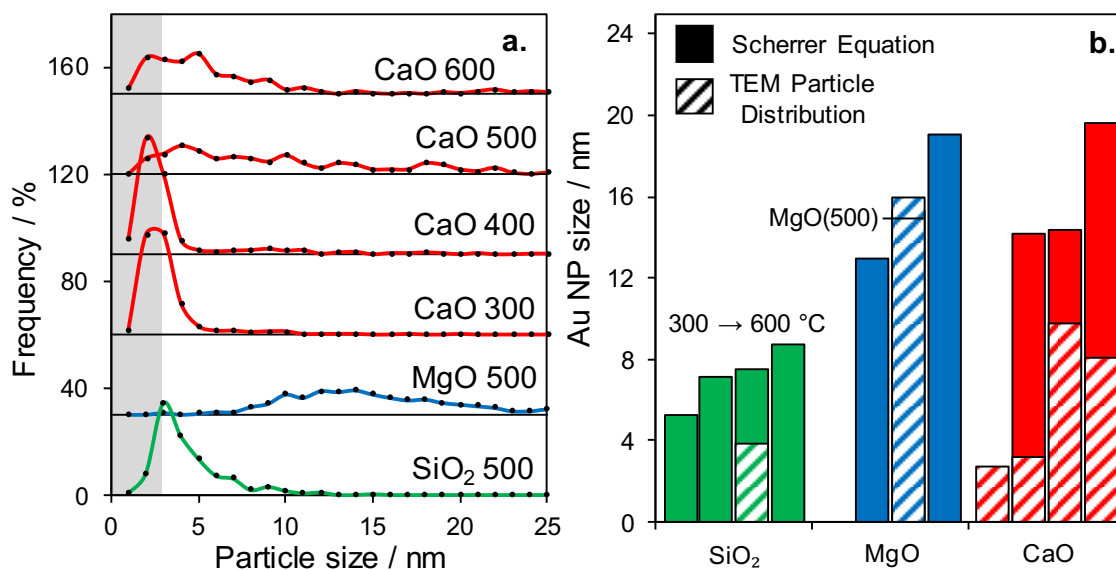


Figure 5.13. (a) Particle size distributions of Au/CaO, Au/MgO (500) and Au/SiO₂ (500) materials and (b) Au particle size determined using both TEM and XRD.

This suggests that distributing the gold over a smaller area favoured the agglomeration of particles into larger clusters upon thermal treatment. This is further evident when considering the SBA-15 materials, which had both a higher surface area and mesoporous channels to spatially separate the gold species, resulting in the smallest nanoparticles synthesised in this work. This poor distribution and large size may also be attributed to the higher gold loadings for the CaO and MgO materials.

Secondly, it has been mentioned that the particle size calculated by the Scherrer equation is inaccurate when the detection limit of the X-ray diffractometer is considered. This was first discussed with the SBA-15 materials (**Chapter 4.2.1.1**) and was also seen in this chapter.

Finally, due to time constraints, the full temperature series of MgO and SiO₂ were not analysed. As the XRD particle size cannot be always considered reliable, this means a true particle size cannot be calculated in all the materials for comparison. The narrow distribution of SiO₂ 500 material can be expected to extend to the lower treatment temperatures, with average particle size increasing with treatment temperature as seen with other materials. Au/CaO had a narrow distribution and small particle size at 300 °C, which widened and increased respectively with the treatment temperature increase. This trend would be expected to be mirrored for the MgO series due to similarities in the surface area, loading and material, however, this trend and others can only be confirmed by further microscopy.

5.2.1.5. Bulk Supported Gold Characterisation Summary

In summary, the functionalisation of bulk basic supports using the double impregnation method and subsequent heat treatments were successful. ICP-OES determined MgO and CaO materials were correctly loaded with approximately 1-1.2 wt%, whereas the SiO₂ materials exhibited poor loading of approximately 0.3-0.4 wt%. This was attributed to the reduced affinity to the acid precursor relative to the solid base supports.

XRD and XPS determined the SiO₂ materials exhibited no significant change, apart from increasing Au particle size with treatment temperature. The alkaline earth metal oxide materials were found to form their hydroxide species, and to a lesser extent carbonate species, attributed to aqueous and atmospheric poisoning. As treatment temperature increased both MgO and CaO materials decomposed back into their oxide forms, although CaCO₃ remained prevalent even at 600 °C due to a higher decomposition temperature.

Porosimetry showed the surface area of the supported materials was less than half that of the parent support, an observation also mirrored with the SBA-15 materials. This is thought to be caused by the methodology of the synthesis, which was also found to chemically alter the support. Au/MgO surface area increased with loading, thought to be caused by the thermal rearrangement of the surface from hydroxide and carbonate decomposition.

Microscopy determined that the XRD particle sizes were inaccurate, due to a large proportion of gold particles lying below the detection limit of the XRD. It also found that silica materials retained the best particle size distribution, thought to be due to the higher surface area of the support and reduced loading.

5.2.2 Selective Oxidation Screening

Catalytic screening in **Chapter 4.4** determined deactivation caused by the inhibition of gold by over oxidation products was at play for the selective oxidation of benzyl alcohol. The incorporation of an external base acted to scavenge this inhibiting species, preserving the activity for longer, and resulting in increased final conversion and a slower activity loss. The materials synthesised and characterised in this chapter were tested to assess if fully basic support (similar in chemical environment to the SBA-15 materials) with no further basic additive would result in activity retention, and if the addition of further base would bring any other benefit.

5.2.2.1. Selective Oxidation of Benzyl Alcohol

The bulk supported gold catalysts were screened for the selective oxidation of benzyl alcohol, using the conditions optimised in **Chapter 4.2**. All materials exhibited differing activity as a function of heat treatment temperature and support, shown in the conversion plots in **Figure 5.14**.

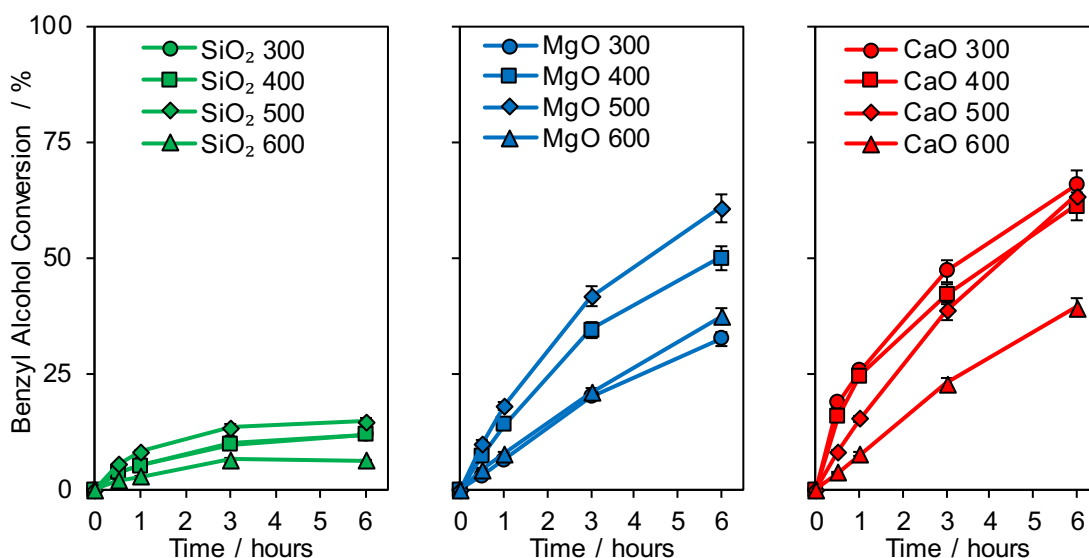


Figure 5.14. Substrate conversion profiles for the selective oxidation of benzyl alcohol using bulk supported gold materials.

Au/SiO₂ was found to be the least active material, deactivating after three hours of screening. The poor activity was associated with the poor loading (0.3 wt%), with the subsequent deactivation occurring very rapidly. The reduced activity was assumed on the basis that the silica base catalysts (Au@MgO/SBA-15) tested in chapter 4 exhibited remarkable initial activity without any basic species present.

The heating temperature that promoted the highest initial activity and the greatest final conversion for SiO₂ 500 °C. In Chapter 4.3 it was argued that this could be caused by

thermal rearrangement of the basic functionality surface.²⁵ However, the fact that this is also seen in non-basic silica supports (**Figure 5.14, left**), indicates that heat treatment also causes changes in gold functionality. This was assumed as the most feasible explanation because the thermally stable silica support showed very little variation in the XRD (**Figure 5.2**) and XPS (**Figures 5.6-7**) with temperature.

Both magnesium and calcium oxide materials showed extremely good activity (**Figure 14, middle and right**), with the Au/CaO materials performing slightly better, again thought to be due to increased loading. It is worth noting that the two materials with the lowest surface area (**Figure 5.5**) exhibited excellent activity relative to the increased surface area fumed silica. This disagrees with the common idea that high surface area materials perform as better catalytic systems, however, this does not account for both the basicity of the supports or the loading of active phase.

To determine if the addition of further basic species would hinder deactivation, the materials were screened in the presence of potassium carbonate, displayed in **Figure 5.15**.

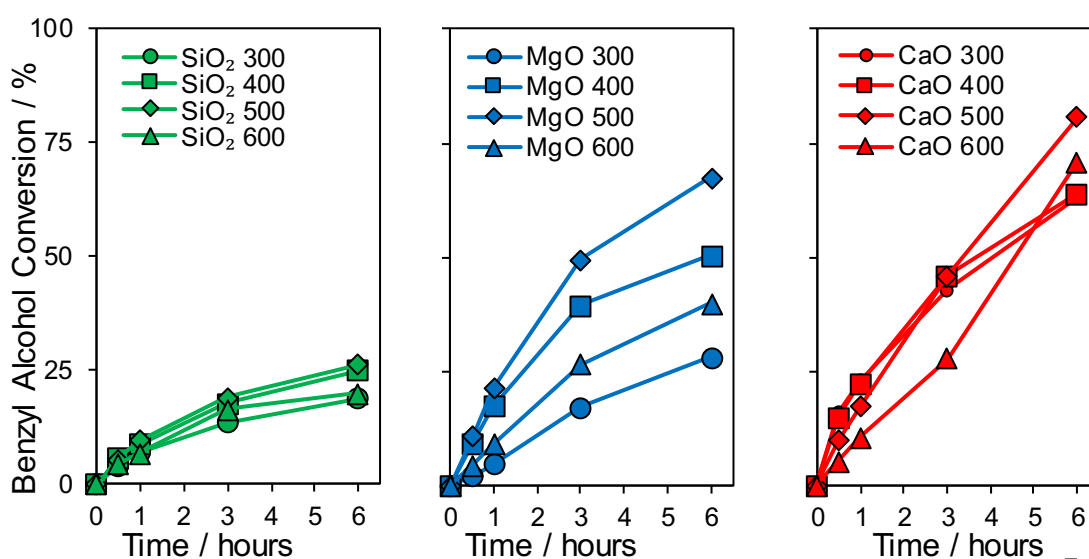


Figure 5.15. Substrate conversion profiles for the selective oxidation of benzyl alcohol using bulk supported gold materials in the presence of potassium carbonate.

A clear conclusion from the addition of the base was the preservation of activity for the Au/SiO₂ materials for longer. The lifetime of the catalyst doubled from three to six hours, credited to the inhibiting products being removed. The differing heat treatment temperatures still showed different activities, corroborating the different behaviour was linked to the gold species altered by temperature.

Both MgO and CaO materials showed very little change in activity, with their reaction profiles after six hours fairly similar regardless of the presence of base. This indicated no further effect on basicity was occurring, which confirmed the hypothesis that employing a solid base bulk support to increase the basic concentration allowed sufficient self-scavenging of the inhibiting species.

These observations are clearer when considering initial productivity (**Figure 5.16**) and final conversion (**Figure 5.17**).

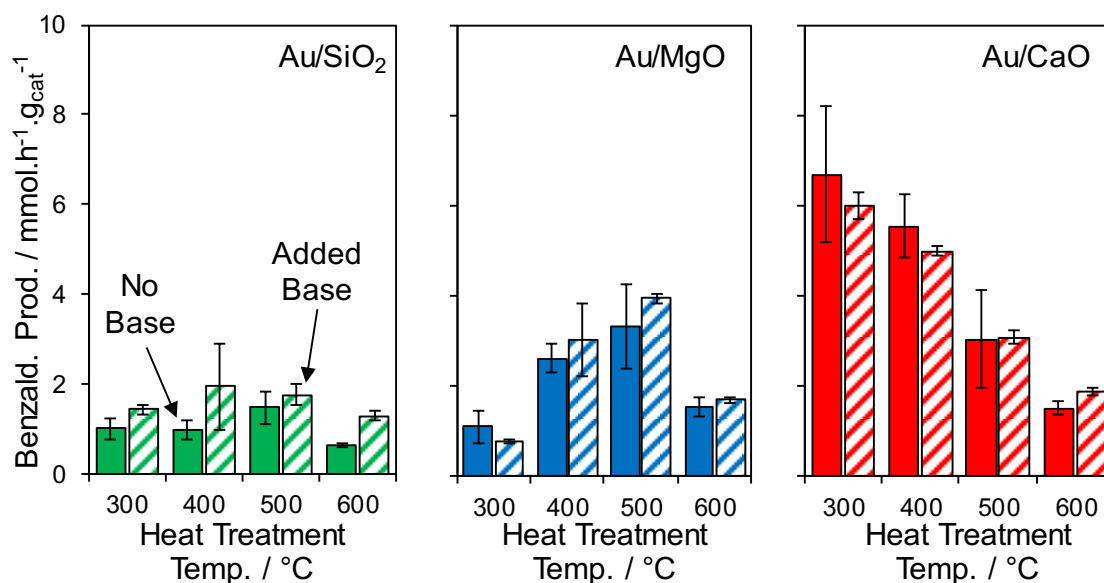


Figure 5.16. Initial benzaldehyde productivity of gold functionalised bulk supports, comparing rates with and without a potassium carbonate additive, featuring error calculated from experimental repeats.

The added base did not significantly affect the initial production of benzaldehyde, and the only differences observed were related to the support and heat treatment, that altered the characteristics and loading of the gold species.

The true benefits of the additional base were seen more clearly when examining the final conversion (**Figure 5.17**).

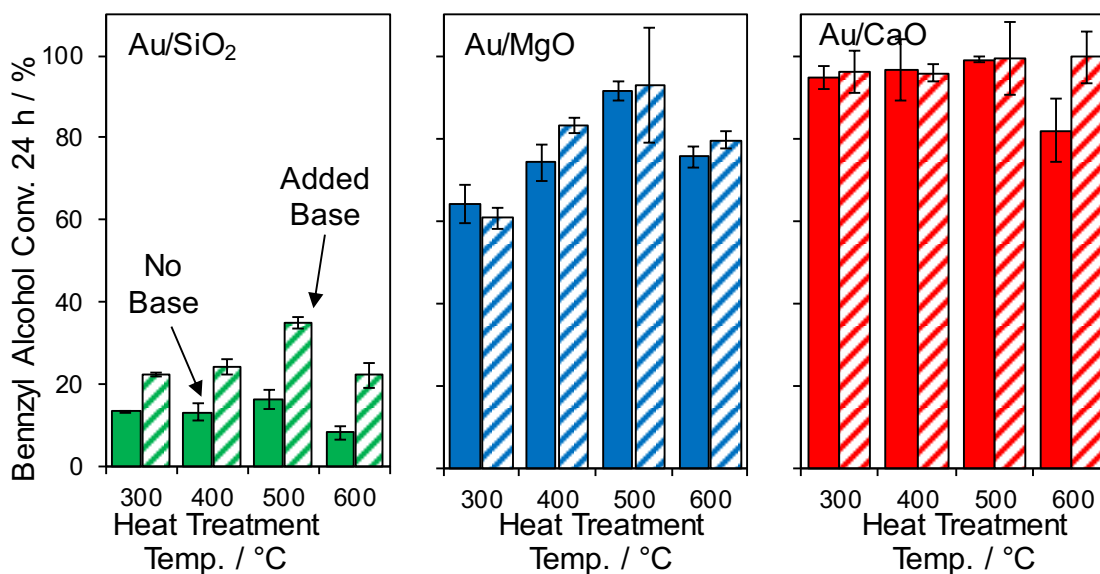


Figure 5.17. Benzyl alcohol conversion after 24 hours of gold functionalised bulk supports, comparing rates with and without a potassium carbonate additive, featuring error calculated from experimental repeats.

Silica materials showed an increase on the final conversion by twofold in the presence of base, confirming deactivation was reduced, thereby allowing the reaction to progress further. Both MgO and CaO showed little to no change in final conversion, corroborating the self-scavenging nature of these support during the reaction times monitored. Au/CaO catalysts reached near full conversion after 24 hours, which was attributed to the increased Au/CaO loading relative to Au/MgO displayed in (Figure 5.1).

Finally, a normalised rate plot is presented in Figure 5.18 to illustrate more clearly the retention of activity throughout the reaction for the alkaline supports, and the improvement in the preservation of activity presented when adding base for the SiO₂ material.

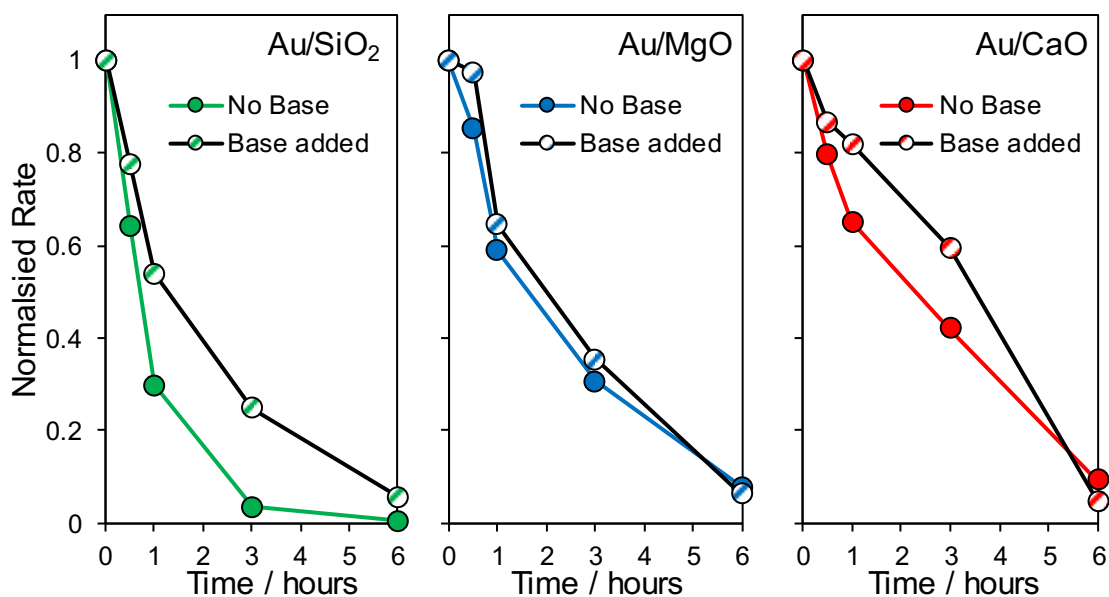


Figure 5.18. Normalised rate profile for gold functionalised bulk supports heat-treated to 500 °C, examining the influence of the presence of potassium carbonate.

5.2.2.2 Comparison of bulk materials with Au@MgO/SBA-15 Materials

The bulk supported materials treated were compared with the previous family of SBA-15 materials, for the heat-treated temperature of 400 °C, to quantify the true effect of added base (Figure 5.19).

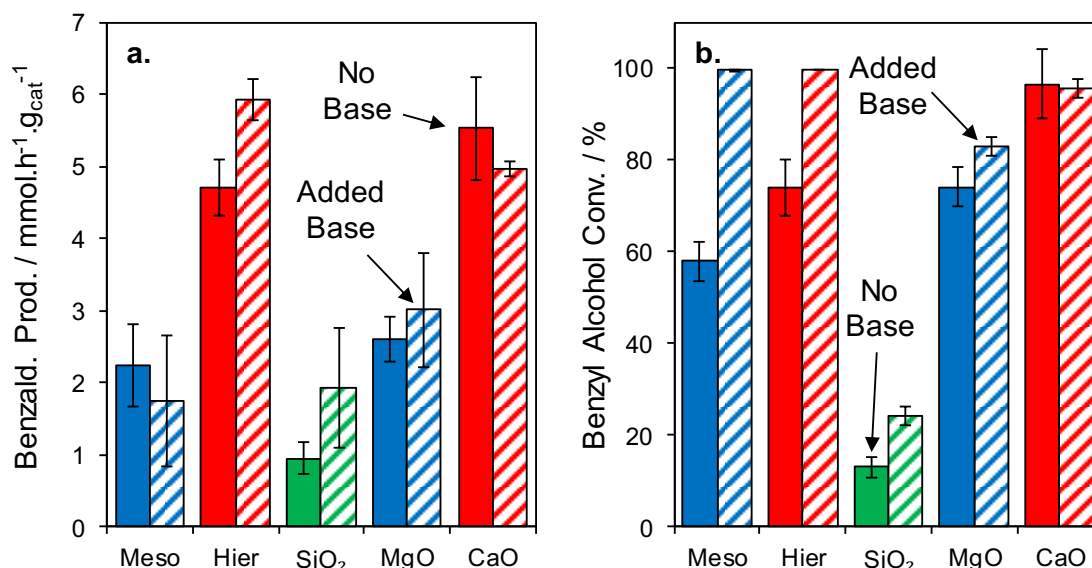


Figure 5.19. Initial productivity of (a) benzaldehyde, and (b) final conversion of benzyl alcohol for SBA-15 type and bulk supported materials treated at 400 °C, with and without base additive.

When examining the activity in Figure 5.19a, no significant change in activity is observed within error for all materials screened. As previously stated in Section 4.2.4.1, base

promotional effects have been observed in the literature^{26, 27} but are not displayed in these materials and conditions. An increase in conversion in **Figure 5.19b** is seen for the SBA-15 and SiO₂ materials, indicating a slowing of deactivation. This is not observed for the MgO and CaO materials. Both initial benzaldehyde productivity and final conversion displayed by the hierarchical SBA-15 material is comparable with both MgO and CaO materials, which is interesting as the hierarchical contains a reduced gold content.

While initial productivity is a measure of initial activity thereby a reflection of the gold species, the conversion measures the final activity which is related to the materials ability to resist deactivation. As improvement is seen for SBA-15 and SiO₂ materials, it is clear they do not have the basic concentration required to resist deactivation without an additional scavenging species. With no improvement observed, MgO and CaO materials prove to have enough intrinsic basic concentration, therefore further base addition is redundant.

It is theorised that with a greater basic concentration the SBA-15 materials would achieve a much greater activity than the bulk supported materials.

5.2.2.3. Selective Oxidation Summary

Multiple conclusions were drawn from these catalytic screenings, many applicable to the materials previously synthesised in **Chapter 4.3**. Increased loadings correlated with increased initial productivity of benzaldehyde, and was seen with all bulk catalysts. This trend was not seen in SBA-15 materials, suggesting the increased activity of the hierarchical materials was a result of structural difference; increased diffusion or more ordered porosity.

Heat treatment temperature was found to influence activity as seen in **Figure 4.5**, however, this trend was also exhibited by silica. **Chapter 4.3** speculated the temperature was causing a thermal surface rearrangement of MgO, exposing more basic facets and thereby disfavoured the deactivation. With silica also experiencing a temperature enabled growth in activity, it is more likely the activity is a result of thermal instigated adaptation of the gold species. Whether this activity change is a result of particle size, surface gold change, or other factors is unknown.

The addition of potassium carbonate was found to only mitigate deactivation in materials without sufficient basic concentration. Silica and SBA-15 materials were found to be greatly affected by the added base, however, the alkaline earth metal oxides showed little change. It was concluded that with over ten times the alkaline earth metal oxide concentration as SBA-15 materials, the bulk supported Au/MgO (and similarly Au/CaO)

contained sufficient basicity to alleviate deactivation. The additional base was therefore redundant in terms of deactivation and gave no clear benefit in terms of the increased rate.

What is curious is deactivation is still occurring as seen in the reaction profiles, regardless of basic concentration. It may be that the solid bases used are not strong enough to preferentially adsorb all inhibiting products, and therefore the use of a stronger base may prove more effective. This would be disadvantageous, as stronger base additives may prove environmentally harmful, and if liquid could demonstrate problematic to separate from the reaction mixture. One possible route to mitigate this would be grafting organic base species directly to the SBA-15 surface, as seen in literature.^{28, 29}

5.2.3 Oxidative Cross-Coupling Reaction

Section 5.2.2 illustrated the high activity for the selective oxidation of alcohols using solid base SBA-15 supports and bulk metal oxide supports. In this section, we explore their feasibility to facilitate the oxidative cross-coupling of benzyl alcohol and benzylamine to form the imine, N-Benzylidenebenzylamine (**Figure 5.20**).³⁰

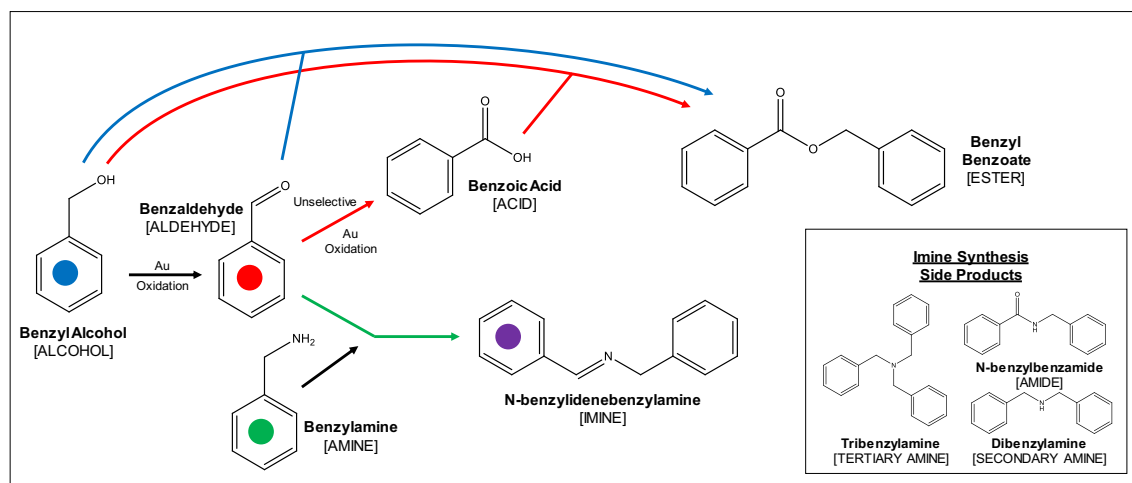


Figure 5.20. Reaction steps for the oxidative cross-coupling of benzyl alcohol and benzylamine to produce the imine, N-Benzylidenebenzylamine.

Studies with base additives have been undertaken before,^{31, 32} suggesting the presence of a basic species favours the forward reaction towards N-benzylidenebenzylamine and inhibits the reverse of the second reaction³² (hydrolysis of imine). For each support, the catalyst material that showed the highest conversion and lowest deactivation was chosen.

5.2.3.1 Oxidative Cross-Coupling of Benzyl Alcohol and Benzyl Amine

As with the previous catalytic studies in **Chapters 4.2.4** and **5.2.2**, the materials were screened with and without one mmol of potassium carbonate. This was carried out to determine if deactivation was occurring, as seen previously. The reaction profiles are pictured in **Figure 5.21**, featuring the major reactants and products. Benzyl benzoate (ester) and N-benzylbenzamine (amide) are not featured in this figure, as they were detected in trace amounts. These trace products followed similar trends to the benzaldehyde and imine production respectively. As mentioned in **Chapter 4.2.4.1**, no acid was produced in detectable quantities, therefore it is assumed the ester was produced from alcohol-aldehyde coupling rather than alcohol-acid.³³

The Au@MgO/SBA-15 materials produced in **Chapter 4.2.3** were found to be inactive without the presence of a base, however, with the addition of potassium carbonate, the hierarchical material achieved the highest imine yield recorded. The inactivity was initially thought to be from a reduced basic concentration compared to MgO and CaO materials, however, the activity displayed by the silica material proved this untrue.

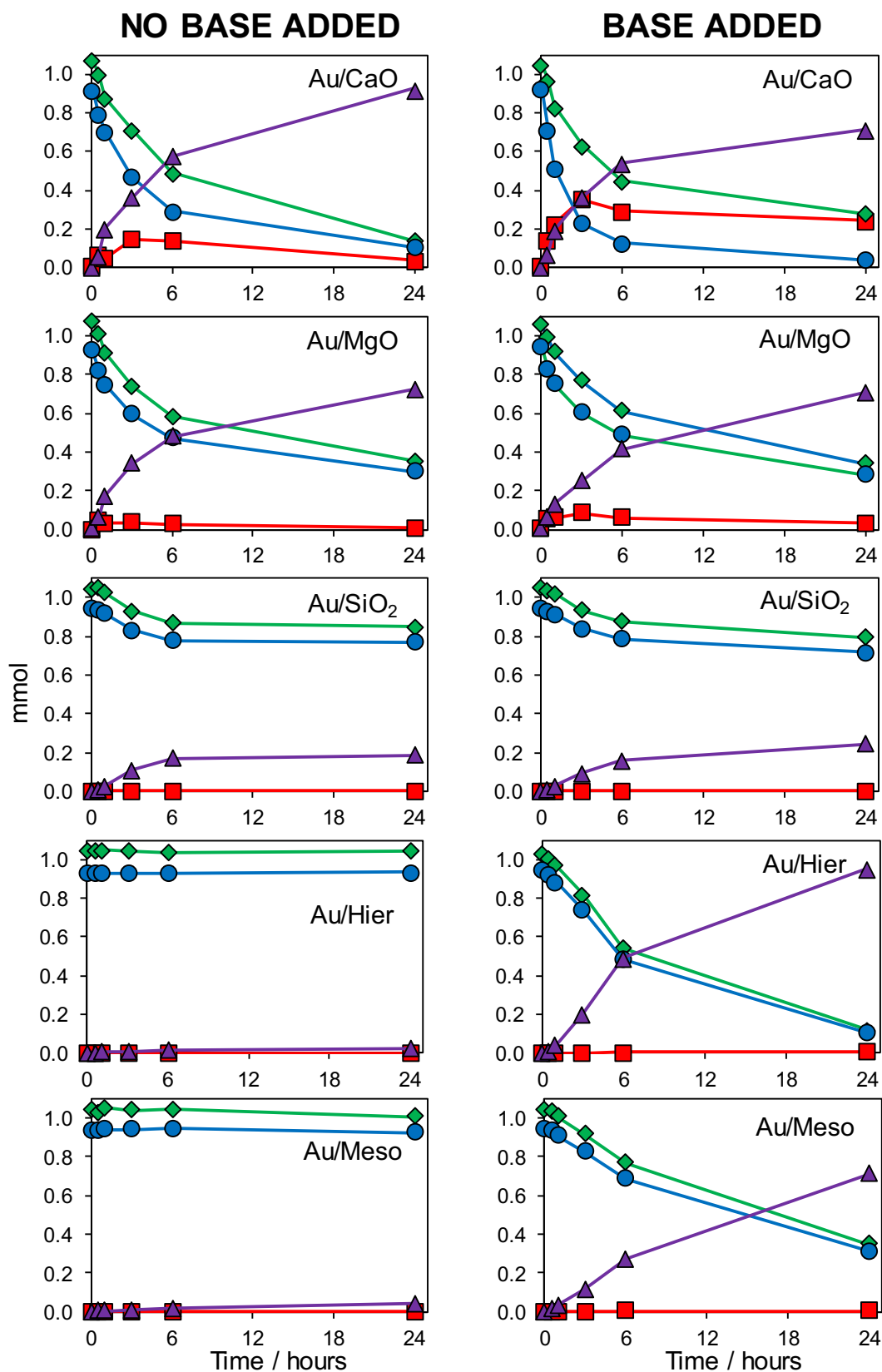


Figure 5.21. Oxidative cross-coupling reaction profiles for selected catalysts in the absence (left) and presence (right) of potassium carbonate. (●) Benzyl alcohol, (◆) benzylamine, (■) benzaldehyde, (▲) N-Benzylidenebenzylamine.

Similarly, the bulk supports were very chemically similar to the SBA-15 support, with Au/SiO₂ exhibiting similar trends in gold nanoparticle size and XPS 4f Au⁰:Au⁺ ratio. It was hypothesised that with the increased surface area, the inactivity could result from a decreased nanoparticle density. This was calculated and is displayed in **Figure 5.22**, along with the particle size distributions of the SBA-15 and gold materials. The comparable nanoparticle size and density suggest the gold sites were extremely geometrically similar, however, there was a possibility they differed electronically. It could be speculated that the SBA-15 and SiO₂/MgO/CaO active sites are not comparable.

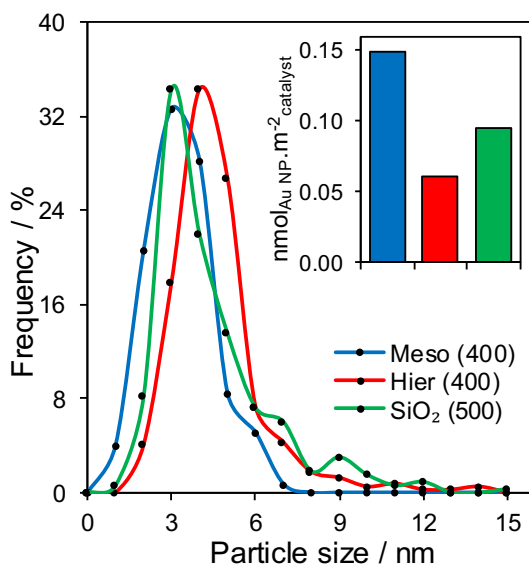


Figure 5.22. Gold nanoparticle size distribution and density for selected mesoporous, hierarchical and fumed silica supported gold.

Another difference when comparing SBA-15 with bulk material is the mesoporous structure. Steric hindrance, as seen in **Chapter 3.2.3**, may be hindering the reaction, however the coupled product would not reach the required size to experience issue with diffusion. It was also demonstrated hierarchical materials decreased diffusion limitations, however a similar improvement is not exhibited here. Also, it is unclear how the addition of base could mitigate diffusion limitations.

Another possible cause could be site inhibition or poisoning from a new species present in the reaction. The reason why this may affect only SBA-15 materials but not bulk loaded materials is not known, however, the imine profile observed in **Appendix Figure 4b.1** confirms imine is being produced at a steady (if minuscule) rate. The lack of imine rate deactivation suggests the over oxidation products are not produced in enough concentration to cause deactivation. Likewise, constant rate implies the cause of reduced activity has already stalled the catalyst before the start of the reaction, implying the new

substrate benzylamine could be preferentially adsorbed. This preferential adsorption could be a result of electronic differences between the SBA-15 and bulk sites.

To summarise, the reason for the SBA-15 materials inactivity without a base is not definitively known. We propose a number of experiments which may illuminate the culprit of the SBA-15 inactivity:

1. To determine if diffusion limitations are causing inactivity, smaller substrates will be used in comparison with the other materials. If an improvement is observed, this could indicate the mesoporous network is unsuited to this reaction. A possible solution may be pore expansion, as discussed in **Chapter 3.3**.
2. As performed in **Chapter 4.2.2 and 4.2.4**, the materials will be screened at different temperatures to calculate their activation energy. Inconsistencies between the bulk and SBA-15 materials may indicate the issue lies at the gold site or could highlight diffusion limitation as seen in **Chapter 3.2.2**.
3. The difference in activity was observed from the addition of 1 mmol of potassium carbonate. To corroborate this, the addition of different bases at differing concentrations is required. This would confirm the observation that this is base instigated, but could also elucidate the concentration required for the activity to return.
4. As previously mentioned, the imine profile of the SBA-15 materials in the absence of base discounts the effect of over oxidation products in favour of substrate inhibition. Both these theories could be confirmed by treating catalytic materials with reaction participants with subsequent filtration and washing before screening for the selective oxidation reaction. Inactivity after treating with specific compounds would elucidate the cause. It would also provide an opportunity to confirm which molecule is deactivating the gold sites for the first step. Literature uses the term 'benzoic acid and its derivatives', which may mean the acid, benzyl benzoate or another undetected species.

The order of activity for the bulk loaded materials in the absence of base followed the selective oxidation study in **Chapter 5.2.2**, which was attributed to the gold loading of the materials. This may indicate that the oxidation of benzyl alcohol was limiting the reaction. It is noted, however, that increased activity also resulted in an increased

concentration of benzaldehyde. A drop in selectivity with increased activity was observed for the selective oxidation reaction, however, it is unclear if the increased activity is contributing to the shift in products. Multiple variables have been known to shift the equilibrium between aldehyde/amine and imine, such as concentration, steric and electronic effects, temperature, and solvents. Another cause, which is more applicable here the effect of pH on the reaction.³⁰

5.2.3.2 Effect of Basicity on Imine Synthesis

Imine synthesis can often be difficult to perform as it is very sensitive to the pH of the reaction.³⁴ Too high and the hemiaminal cannot eliminate water, too low and the amine group is protonated, rendering its nucleophilicity inadequate to attack the carbonyl. The coupling substrates were chosen as model compounds for this reaction as they require no catalytic intervention, with preliminary studies (**Appendix Figure 4b.2**) finding the coupling to occur instantaneously at room temperature and pressure without agitation. This led us to believe the coupling of these two species would progress regardless of the basic content, which we were modifying to stop oxidation instigated deactivation.

This is not the case, which is evident when examining the alkaline earth metal oxide materials. In **Section 5.3.2**, we discussed how the increased basic concentration of the bulk MgO and CaO materials rendered the further addition of base redundant in further reducing deactivation. On the contrary, when combined with the subsequent cascade, the increased basic concentration acts to increase the pH, causing the protonation of the intermediate hemiaminal hydroxide to be disfavoured, as displayed in **Figure 5.23**. This prevents the further elimination of water required for the imine species.

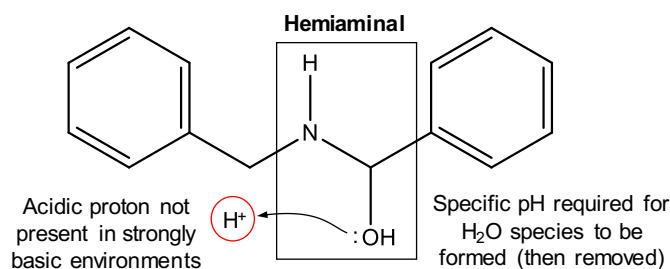


Figure 5.23. Mechanism showing the protonation of the hemiaminal intermediate.

It can be concluded that upon passing a specific pH, the water functional group formation (and subsequent elimination) becomes disfavoured, causing a build-up of benzaldehyde. As the benzaldehyde concentration is increased upon the addition of the potassium carbonate, this suggests further solid base present in the reaction further hinders the imine formation. This is highlighted in **Appendix Figure 4b.3**, which shows the difference in product yield in the absence and presence of potassium carbonate.

Cui *et al.* determined while base was required to achieve conversion via interfering in the oxidation step, increasing the basic concentration caused the selectivity and yield of the imine to decrease.³² It is noted that a Au/ZrO₂ catalyst was used, with no intrinsic basicity. They also determined the alkalinity of the bases only significantly affected the selective oxidation step. This disagrees with the fundamental organic mechanism of this reaction, however, they may not have perceived the base was instigating the drop in imine selectivity and yield as the basic concentration may have been too low. In fact, with a mildly acidic support and added base, the Au/SiO₂ material produced no aldehyde, suggesting the solid base supports provide the majority of the basicity, rather than potassium carbonate.

Benzyl alcohol conversion, displayed in **Figure 5.24** and **Table 5.1**, followed the same trend as the selective oxidation when in the absence of base. A similar conversion for both substrates was observed for Au/SiO₂ and SBA-15 materials (base added). This indicated all benzaldehyde produced was immediately consumed by the coupling step. The Au/MgO and Au/CaO materials, however, showed an increased benzyl alcohol conversion. This suggests, as previously said, the coupling step was hindered. We attributed this to the increased basicity in the reaction, disfavoured the protonation of hydroxyl species. Finally, if the benzylamine conversion is higher than benzyl alcohol, this could indicate homocoupling of the amine is taking place. This was not observed in any of the materials, and preliminary studies (**Appendix Figure 4b.4**), which found this did not occur when the benzylamine species was the only substrate present.

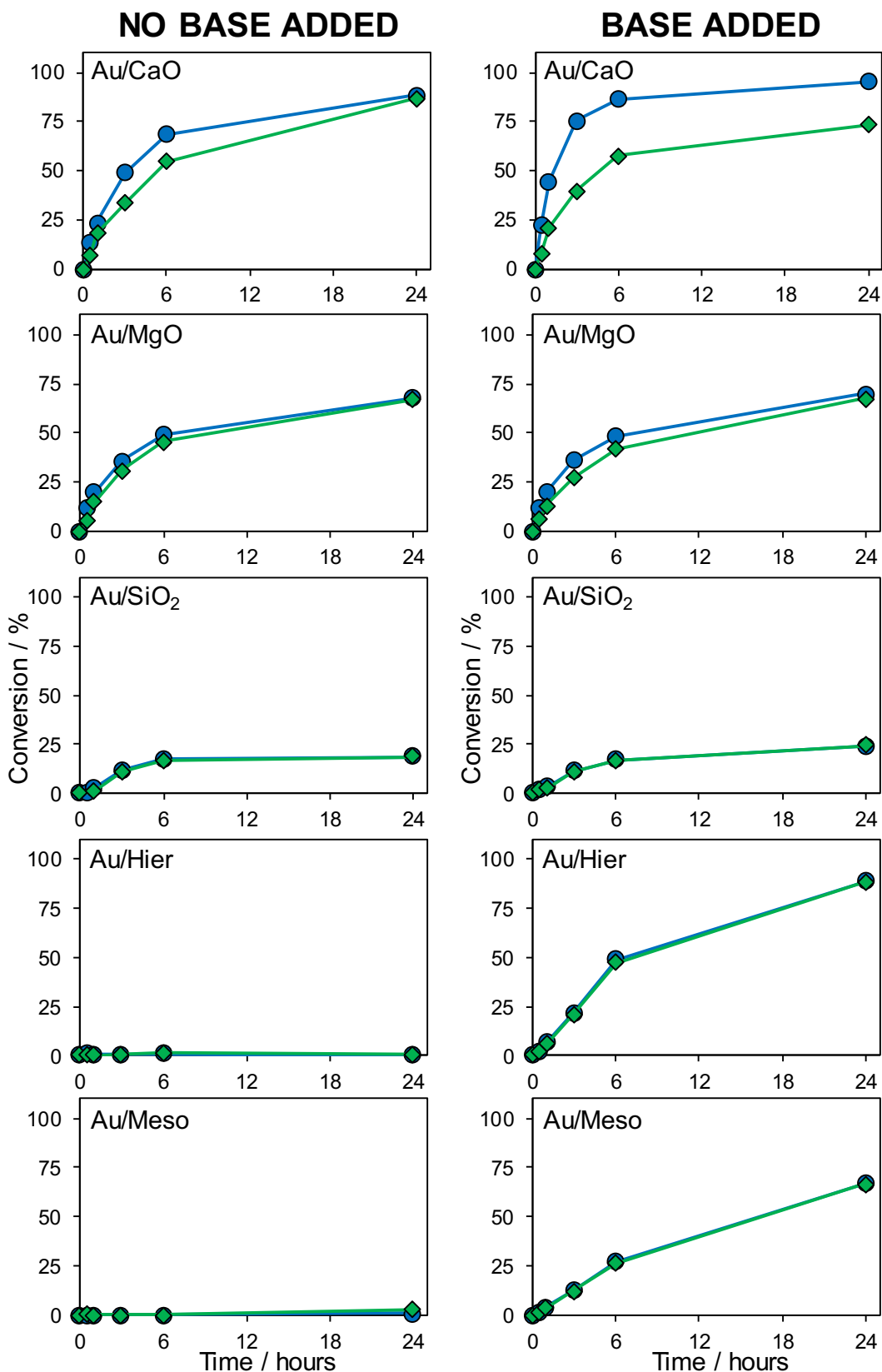


Figure 5.24. Conversion plots as a function of time for (●) benzyl alcohol and (◆) benzylamine for imine synthesis in the absence (left) and presence (right) of potassium carbonate.

5.2.3.3 Oxidative Coupling Rate Profiles

The productivity of the imine formation was examined, first as a function of time (Table 5.1), and then as a function of conversion in Figure 5.25. This enables the comparison of reaction rate among experiments at the same level of reactant concentrations.

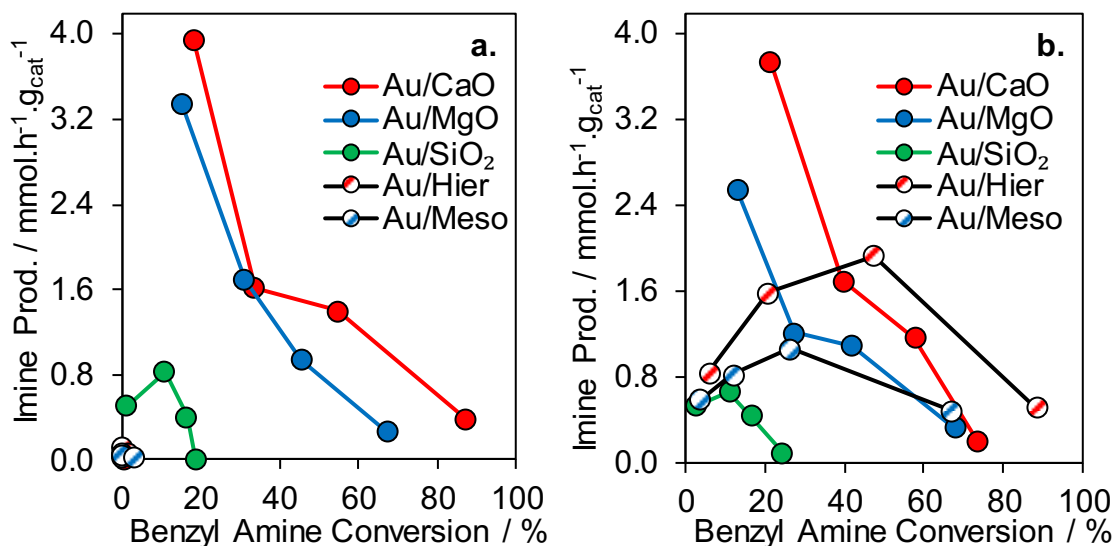


Figure 5.25. Imine productivity as a function of benzylamine conversion to highlight the deactivation of both SBA-15 and bulk supported catalysts in (a) absence and (b) presence of potassium carbonate.

Table 5.1. Data of initial rates, and conversion, yield and selectivity after 24 hours for the oxidative cross-coupling of benzyl alcohol and benzylamine for the different catalyst support tested. The bracketed values represent the screening test with the addition of K₂CO₃ (1 mmol).

	Benzyl Alcohol Conv. / %	Rate / mmol h ⁻¹ g _{cat} ⁻¹		Imine Yield / %	Imine Sel.* / %
		Benzaldehyde	Imine		
Au/Meso 400 °C	1.1 (67.0)	0.00 (0.00)	0.03 (0.59)	3.9 (68.1)	--- (99.5)
Au/Hier 400 °C	0.1 (88.5)	0.00 (0.00)	0.13 (0.84)	2.4 (92.2)	--- (99.3)
Au/SiO₂ 500 °C	18.6 (24.1)	0.00 (0.00)	0.52 (0.53)	17.9 (23.3)	100.0 (100)
Au/MgO 500 °C	68.0 (70.2)	0.64 (1.15)	3.35 (2.55)	67.2 (67.1)	98.1 (94.7)
Au/CaO 500 °C	88.4 (95.5)	0.82 (4.26)	3.95 (3.75)	85.8 (67.6)	95.1 (71.8)

* Selectivity reported is respective to the coupling products and oxidation products. For yields <5%, the resulting selectivity was inaccurate or misleading, and the value was omitted (---).

As previously observed, the SBA-15 materials showed very limited activity in the absence of base additive (**Table 5.1**). Upon addition of base, these materials exhibited an initiation period, which was also seen for the silica materials (**Figure 5.25**). The cause of the initiation period is not known and was not observed in the literature to the best of our knowledge. It could be suggested that the sites were gradually regenerated as the reaction progressed. We hypothesise in **Section 5.2.3.1** that the poison was benzylamine, as the imine yield profiles of SBA-15 materials without base (**Appendix Figure 4b.3**) showed no product inhibition.

Au/MgO and Au/CaO materials showed a steady decrease in productivity with conversion, which was observed for both with and without base. This was attributed to the steady deactivation of the Au species from over oxidation products, as seen in **Chapter 5.2.2.1**. The addition of sacrificial base was found to prolong activity in the other materials, however, this was not observed for the alkaline earth metal oxide catalysts.

5.2.3.4 Oxidative Coupling Summary

In summary, two variables were shown to have a large influence on activity for the oxidative coupling: pH and site inhibition. The effect of an increased reaction pH on the oxidative coupling of benzyl alcohol and benzylamine was found to hinder the second coupling step, which is well recorded in literature.³⁴ It was also noted that the basicity of the basic supports was enough to begin hindering the coupling step, with subsequent addition causing further disruption. Au/SiO₂ was not found to hinder the coupling, even in the presence of base, which was attributed to the acidic nature of the silica surface.

SBA-15 materials were found to be extremely inactive in the absence of base, however, showed an impressive increase when base was added. The cause of this inactivity is not known, however, we hypothesise that the presence of benzylamine was poisoning the gold sites, drastically hindering the oxidation to occur. We proposed multiple experiments which could be used to elucidate the reason for inactivity.

5.3 Conclusions and Recommendations for Further Work

In conclusion, Au/SiO₂, Au/MgO and Au/CaO materials were successfully synthesised using the double impregnation method developed by Bowker *et al.* used in the previous **Chapter 4.2.1**.^{5, 35} ICP-OES characterisation determined the materials were successfully loaded to differing degrees, which was linked to their isoelectric points. X-ray diffraction and photoelectron spectroscopy established the alkaline earth metal oxides supports were chemically altered by the impregnation, forming hydroxides and carbonate which decomposed at specific temperatures over the range of temperature treatments.

Scanning transmission electron microscopy determined MgO and CaO materials exhibited particle distributions and size larger than the SBA-15 materials, which was thought to be due to their smaller surface area. Fumed silica, however, had the largest surface area and subsequently smallest nanoparticles, comparable in size and distribution to SBA-15 materials. Thermal treatment caused decompositions in the support phases as mentioned, however also caused gold particle agglomeration and growth, as seen in the previously.

The heat-treated bulk supported gold materials were screened for the selective oxidation of benzyl alcohol using the optimised conditions from **Chapter 4.2.2**. As with the SBA-15 based materials in **Chapter 4.2.3**, materials treated at different temperatures resulted in differing activities. This was previously thought to be caused by thermal rearrangement of the MgO surface, however, the volcano plot was also exhibited by silica materials. This suggested that the changing activity with treatment temperature was also influenced by the alteration of the gold species.

Catalytic activity appeared to be directly correlated with the gold loading following the trend Au/SiO₂ << Au/MgO < Au/CaO. Deactivation was observed in all materials as previously seen in **Chapter 4.2.4**, therefore the materials were screened in the presence of 1 mmol K₂CO₃. A reduction in deactivation was observed for Au/SiO₂ materials, resulting in the lifespan of the material doubling from three to six hours. MgO and CaO materials were not affected, suggesting the addition of base was therefore redundant in terms of deactivation. It was noted deactivation was still occurring for all materials screened. To determine if this was a result of deactivation or reactant concentrations, recycling studies need to be undertaken.

Finally, the best performing catalysts were screened for the oxidative coupling of benzyl alcohol and benzylamine to produce the imine, N-benzylidenebenzylamine.

It was determined that the SBA-15 materials were inactive for this reaction without the presence of an added base. The definitive cause of this inactivity is not fully understood, however, we attributed it to a potential poisoning effect of the amine substrate. Alkaline earth metal oxide materials exhibited a significant concentration of aldehyde, which increased when screened in the presence of base. The effect of increased basicity is known to disfavour the imine formation, which was confirmed here. However, by producing the intermediate compound in significant quantities, even in the absence of added base, it was clear the MgO and CaO materials had intrinsic basicity that was ill-suited for this reaction.

If work is to be continued, the suggested experiments in **Section 5.2.1** would be performed. This would clarify the true cause of the inactivity displayed by Au@MgO/SBA-15 materials. Functionalisation of the solid base support could result in greater intrinsic basicity, resulting in further reduction of deactivation for the selective oxidation reaction. The literature points to organic species being anchored to the SBA-15 support,²⁸ however other options include other alkaline earth metal oxides, mixed oxides or dopants. Alternatively, if imine synthesis is pursued, this work could investigate the versatility of the catalytic materials by changing substrates, and thereby examining the feasibility of the catalysts in industrially relevant reactions. This may prove an interesting avenue, as bifunctionality would be required to enable the acid catalysed imine coupling of more complex substrates.

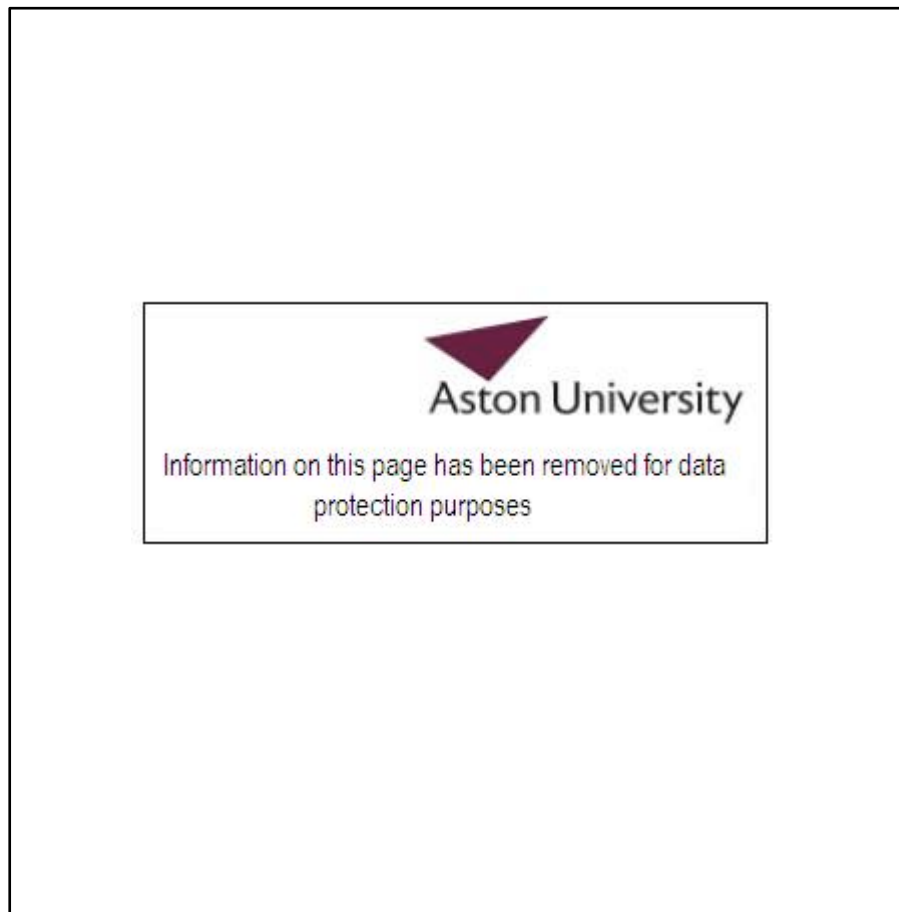
5.4 References

1. G. A. Parks, The isoelectric points of solid oxides, solid hydroxides, and aqueous hydroxo complex systems, *Chemical Reviews*, 1965, **65**, 177-198.
2. M. A. Brown, M. Arrigoni, F. Héroguel, A. Beloqui Redondo, L. Giordano, J. A. van Bokhoven and G. Pacchioni, pH dependent electronic and geometric structures at the water–silica nanoparticle interface, *The Journal of Physical Chemistry C*, 2014, **118**, 29007-29016.
3. X. Cui, W.-C. Zin, W.-J. Cho and C.-S. Ha, Nonionic triblock copolymer synthesis of SBA-15 above the isoelectric point of silica (pH=2–5), *Materials Letters*, 2005, **59**, 2257-2261.
4. S. T. Moerz and P. Huber, pH-dependent selective protein adsorption into mesoporous silica, *The Journal of Physical Chemistry C*, 2015, **119**, 27072-27079.
5. P. Perez, M. A. Soria, S. A. C. Carabineiro, F. J. Maldonado-Hodar, A. Mendes and L. M. Madeira, Application of Au/TiO₂ catalysts in the low-temperature water-gas shift reaction, *International Journal of Hydrogen Energy*, 2016, **41**, 4670-4681.
6. B. Wang, X. Xiong, H. Ren and Z. Huang, Preparation of MgO nanocrystals and catalytic mechanism on phenol ozonation, *RSC Advances*, 2017, **7**, 43464-43473.
7. A. Imtiaz, M. A. Farrukh, M. Khaleeq-ur-Rahman and R. Adnan, Micelle-assisted synthesis of Al₂O₃·CaO nanocatalyst: optical properties and their applications in photodegradation of 2,4,6-Trinitrophenol, *The Scientific World Journal*, 2013, **2013**, 641420.
8. S. Yaseri, G. Hajiaghaei, F. Mohammadi, M. Mahdikhani and R. Farokhzad, The role of synthesis parameters on the workability, setting and strength properties of binary binder based geopolymers, *Construction and Building Materials*, 2017, **157**, 534-545.
9. K. O'Connell and J. R. Regalbuto, High sensitivity silicon slit detectors for 1 nm powder XRD Size Detection Limit, *Catalysis Letters*, 2015, **145**, 777-783.
10. K. Sneha, A. Esterle, N. Sharma and S. Sahi, Yucca-derived synthesis of gold nanomaterial and their catalytic potential, *Nanoscale Research Letters*, 2014, **9**, 627.
11. J. Malinowski, G. Dercz, K. Prusik, L. Pajak, R. Pielaszek and W. Pudlo, Structure studies on nanocrystalline powder of MgO xerogel prepared by sol-gel method, *Materials Science-Poland*, 2009, **27**, 201-207.
12. M. G. KIM, U. DAHMEN and A. W. SEARCY, Structural transformations in the decomposition of Mg(OH)₂ and MgCO₃, *Journal of the American Ceramic Society*, 1987, **70**, 146-154.
13. D. Beruto, L. Barco, A. W. Searcy and G. Spinolo, Characterization of the porous CaO particles formed by decomposition of CaCO₃ and Ca(OH)₂ in vacuum, *Journal of the American Ceramic Society*, 1980, **63**, 439-443.
14. A. Irabien, J. R. Viguri, F. Cortabitarte and I. Ortiz, Thermal dehydration of calcium hydroxide. 2. Surface area evolution, *Industrial & Engineering Chemistry Research*, 1990, **29**, 1606-1611.

15. I. Galan, F. P. Glasser and C. Andrade, Calcium carbonate decomposition, *Journal of Thermal Analysis and Calorimetry*, 2013, **111**, 1197-1202.
16. N. Masoud, T. Partsch, K. P. de Jong and P. E. de Jongh, Thermal stability of oxide-supported gold nanoparticles, *Gold Bulletin*, 2019, **52**, 105-114.
17. J. B. Lowe and R. T. Baker, Deformation of ordered mesoporous silica structures on exposure to high temperatures, *Journal of Nanomaterials*, 2014, **2014**, 13.
18. O. Ntwaeaborwa, G. Mhlongo, S. Pitale, M. Dhlamini, R. Kroon and H. Swart, Cathodoluminescence properties of SiO₂: Ce₃⁺, Tb₃⁺, SiO₂: Ce₃⁺, Pr₃⁺ and SiO₂: PbS, *Cathodoluminescence*, Naoki Yamamoto, IntechOpen, 2012.
19. Y. Song, J. K. Mobley, A. H. Motagamwala, M. Isaacs, J. A. Dumesic, J. Ralph, A. F. Lee, K. Wilson and M. Crocker, Gold-catalyzed conversion of lignin to low molecular weight aromatics, *Chemical Science*, 2018, **9**, 8127-8133.
20. H. Lu, S. Ding and D. W. Zhang, Investigation of thermal stability of atomic-layer-deposited MgO thin films on Si(100) using X-Ray photoelectron spectroscopy, *Electrochemical and Solid-State Letters*, 2010, **13**, G25-G28.
21. A. Sasahara, T. Murakami and M. Tomitori, Hydration of MgO(100) surface promoted at [011] Steps, *The Journal of Physical Chemistry C*, 2015, **119**, 8250-8257.
22. X. Cao, J. Zhou, H. Wang, S. Li, W. Wang and G. Qin, Abnormal thermal stability of sub-10 nm Au nanoparticles and their high catalytic activity, *Journal of Materials Chemistry A*, 2019.
23. A. S. Marriott, A. J. Hunt, E. Bergström, K. Wilson, V. L. Budarin, J. Thomas-Oates, J. H. Clark and R. Brydson, Investigating the structure of biomass-derived non-graphitizing mesoporous carbons by electron energy loss spectroscopy in the transmission electron microscope and X-ray photoelectron spectroscopy, *Carbon*, 2014, **67**, 514-524.
24. H. Craft, R. Collazo, M. Losego, Z. Sitar and J. Maria, Surface water reactivity of polycrystalline MgO and CaO films investigated using X-ray photoelectron spectroscopy, *Journal of Vacuum Science & Technology A*, 2008, **26**, 1507-1510.
25. J. M. Montero, P. Gai, K. Wilson and A. F. Lee, Structure-sensitive biodiesel synthesis over MgO nanocrystals, *Green Chemistry*, 2009, **11**, 265-268.
26. S. K. Klitgaard, A. T. DeLa Riva, S. Helveg, R. M. Werchmeister and C. H. Christensen, Aerobic oxidation of alcohols over gold catalysts: role of acid and base, *Catalysis Letters*, 2008, **126**, 213-217.
27. E. Skupien, J. R. Berger, P. V. Santos, J. Gascon, M. Makkee, T. M. Kreutzer, J. P. Kooyman, A. J. Moulijn and F. Kapteijn, Inhibition of a gold-based catalyst in benzyl alcohol oxidation: understanding and remediation, *Catalysts*, 2014, **4**.
28. T. Wang, X. Yuan, S. Li, L. Zeng and J. Gong, CeO₂-modified Au@SBA-15 nanocatalysts for liquid-phase selective oxidation of benzyl alcohol, *Nanoscale*, 2015, **7**, 7593-7602.
29. A. Beloqui Redondo, M. Ranocchiari and J. A. van Bokhoven, Synthesis of sub-nanometer gold particles on modified silica, *Dalton Transactions*, 2016, **45**, 2983-2988.
30. R. D. Patil and S. Adimurthy, Catalytic methods for imine synthesis, *Asian Journal of Organic Chemistry*, 2013, **2**, 726-744.

31. W. Cui, B. Zhaorigetu, M. Jia, W. Ao and H. Zhu, Synthesis of imines from amines in aliphatic alcohols on Pd/ZrO₂ catalyst under ambient conditions, *RSC Advances*, 2014, **4**, 2601-2604.
32. W. Cui, H. Zhu, M. Jia, W. Ao, Y. Zhang and B. Zhaorigetu, One-pot synthesis of imines from benzyl alcohol and amines on Au/ZrO₂ catalyst, *Reaction Kinetics, Mechanisms and Catalysis*, 2013, **109**, 551-562.
33. J. C. F. Rodríguez-Reyes, C. M. Friend and R. J. Madix, Origin of the selectivity in the gold-mediated oxidation of benzyl alcohol, *Surface Science*, 2012, **606**, 1129-1134.
34. J. Clayden, N. Greeves and S. Warren, *Organic Chemistry*, OUP Oxford, 2012.
35. M. Bowker, A. Nuhu and J. Soares, High activity supported gold catalysts by incipient wetness impregnation, *Catalysis Today*, 2007, **122**, 245-247.

Appendix



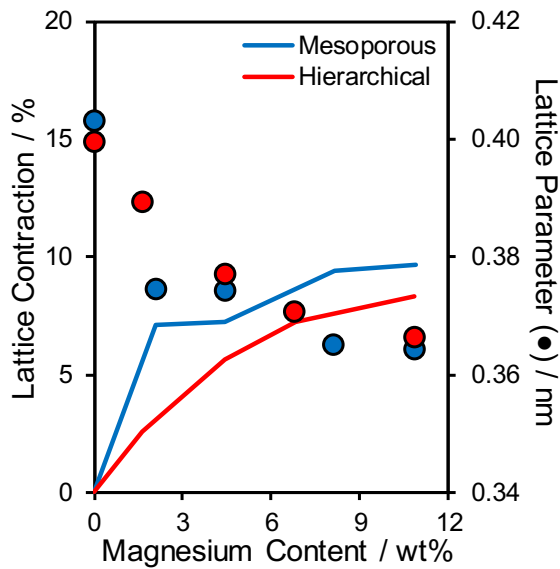
A wild PhD student in her natural habitat

Appendix 1 for Chapter 1

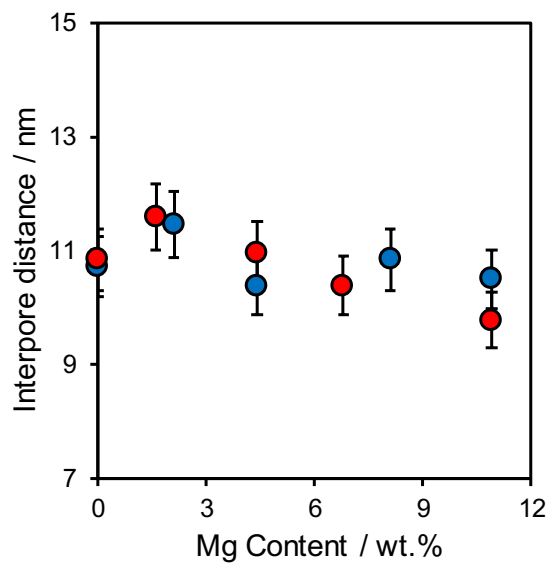
The twelve principles of green chemistry as defined by IUPAC.

1. **Prevention** - Preventing waste is better than treating or cleaning up waste after it is created.
2. **Atom Economy** - Synthetic methods should try to maximize the incorporation of all materials used in the process into the final product. This means that less waste will be generated as a result.
3. **Less hazardous chemical syntheses** - Synthetic methods should avoid using or generating substances toxic to humans and/or the environment.
4. **Designing safer chemicals** - Chemical products should be designed to achieve their desired function while being as non-toxic as possible.
5. **Safer solvents and auxiliaries** - Auxiliary substances should be avoided wherever possible, and as non-hazardous as possible when they must be used.
6. **Design for energy efficiency** - Energy requirements should be minimized, and processes should be conducted at ambient temperature and pressure whenever possible.
7. **Use of renewable feedstocks** - Whenever it is practical to do so, renewable feedstocks or raw materials are preferable to non-renewable ones.
8. **Reduce derivatives** - Unnecessary generation of derivatives—such as the use of protecting groups—should be minimized or avoided if possible; such steps require additional reagents and may generate additional waste.
9. **Catalysis** - Catalytic reagents that can be used in small quantities to repeat a reaction are superior to stoichiometric reagents (ones that are consumed in a reaction).
10. **Design for degradation** - Chemical products should be designed so that they do not pollute the environment; when their function is complete, they should break down into non-harmful products.
11. **Real-time analysis for pollution prevention** - Analytical methodologies need to be further developed to permit real-time, in-process monitoring and control before hazardous substances form.
12. **Inherently safer chemistry for accident prevention** - Whenever possible, the substances in a process, and the forms of those substances, should be chosen to minimize risks such as explosions, fires, and accidental releases.

Appendix 2 for Chapter 3



Appendix Figure 2.1. Silica lattice contraction as a function of magnesium loading for mesoporous and hierarchical MgO/SBA-15 materials.

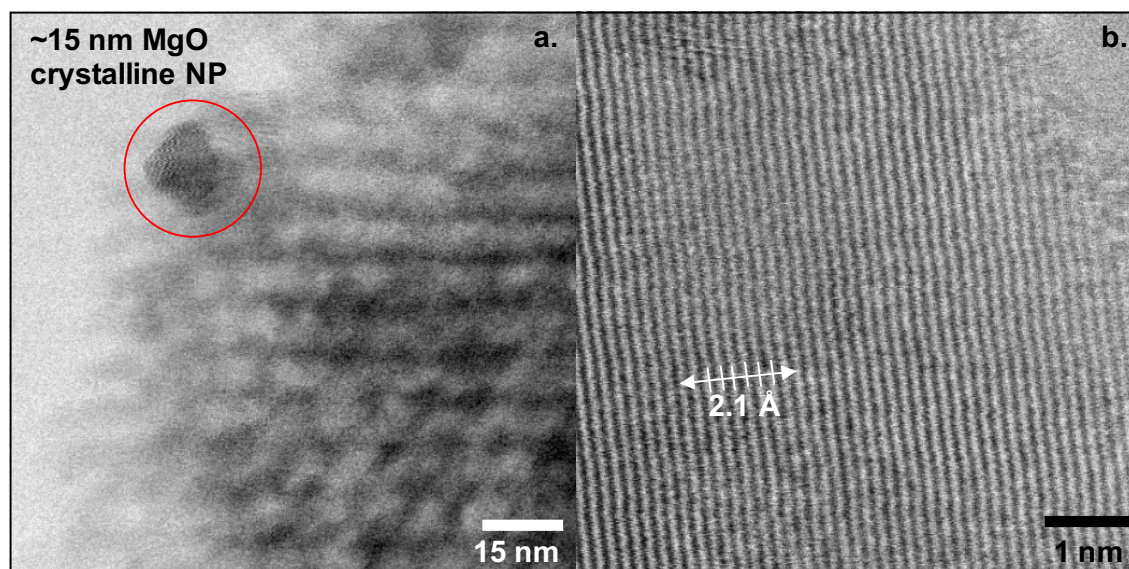


Appendix Figure 2.2. Interpore distances of mesoporous and hierarchical materials, calculated using low-angle X-ray diffraction reflections.

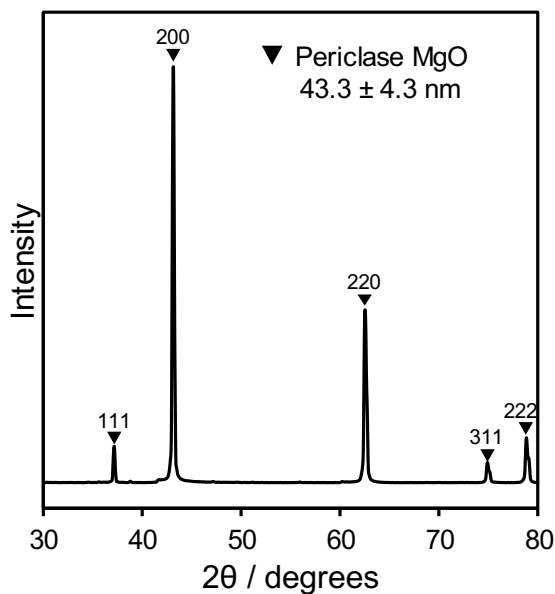
Appendix Table 2.1 The surface area determined using BET and t-plot microporosity analysis from micro and mesopores with pore sizes calculated with DFT (slit pore, NLDFT equilibrium mode) calculations respectively.

	Mg Content (wt%) ^a	Surface area (m ² .g ⁻¹) ^b		Pore size (nm) ^{b,c}		Mg Content (wt%) ^a	Surface area (m ² .g ⁻¹) ^b		Pore size (nm) ^{b,c}
		Total	Micro				Total	Micro	
Mesoporous	0.0	370 ± 37	72 ± 7	5.2	Hierarchical	0.0	265 ± 27	0	5.0
	2.1	502 ± 50	142 ± 14	5.2		1.6	232 ± 23	0	5.0
	4.4	525 ± 53	126 ± 13	4.5		4.4	322 ± 32	14 ± 1	4.9
	8.1	604 ± 60	130 ± 13	4.0		6.8	327 ± 33	0	4.2
	10.9	650 ± 65	143 ± 14	3.9		10.9	294 ± 29	0	3.8

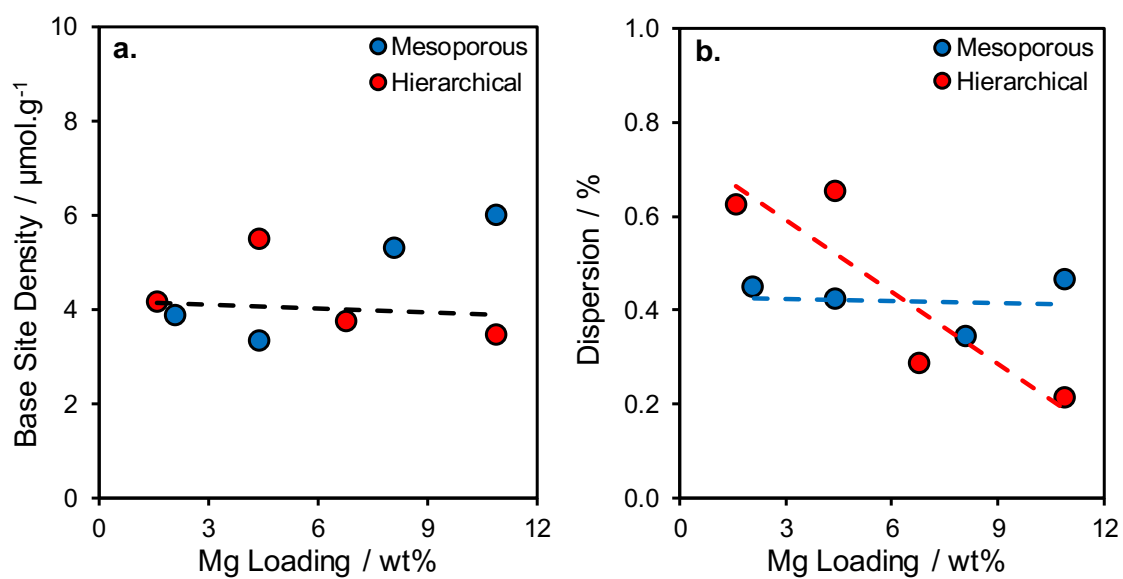
^a Determined by ICP-OES, ^b Determined by N₂ porosimetry. ^c Pore size distributions are displayed in **Figure 3.9**.



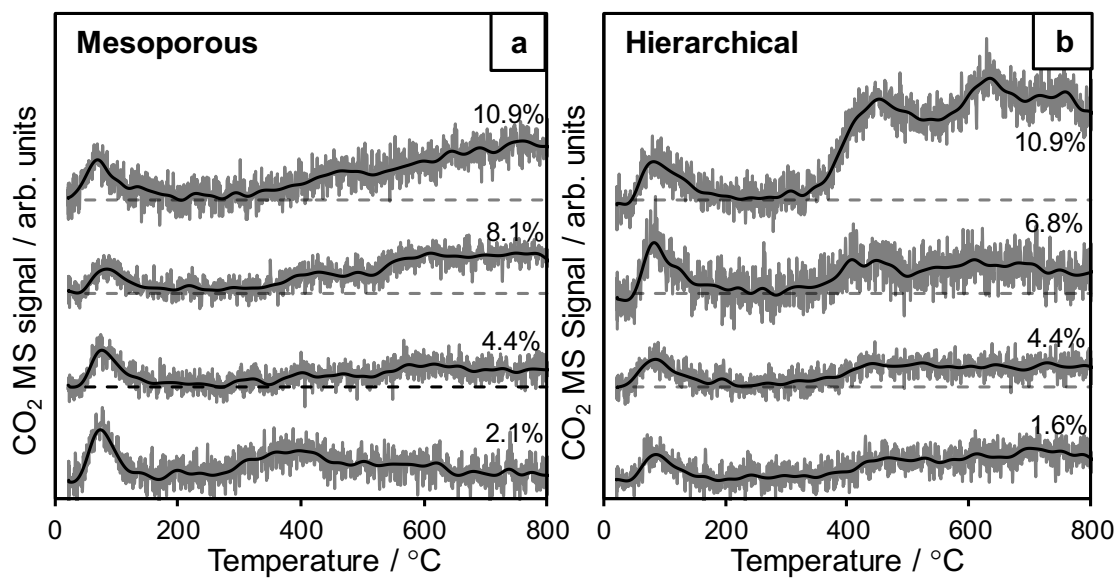
Appendix Figure 2.3. Transmission electron micrographs of 10.9 wt% mesoporous MgO/SBA-15, displaying (a) surface nanoparticle and (b) lattice structure.



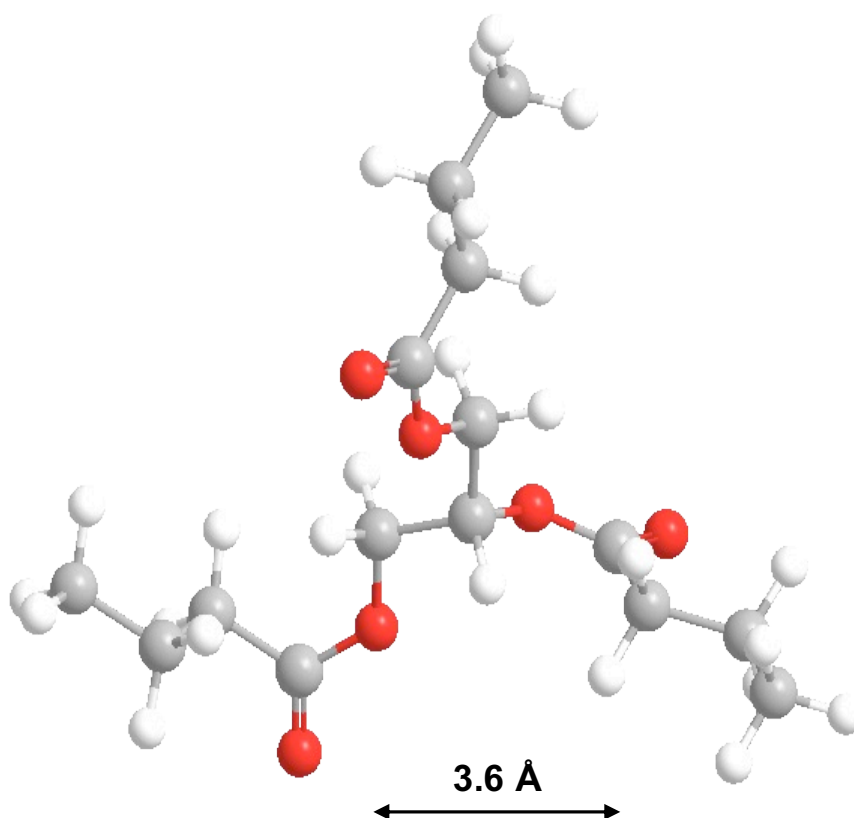
Appendix Figure 2.4. Wide-angle X-ray diffraction pattern of MgO sample used as an XPS and catalyst benchmark.



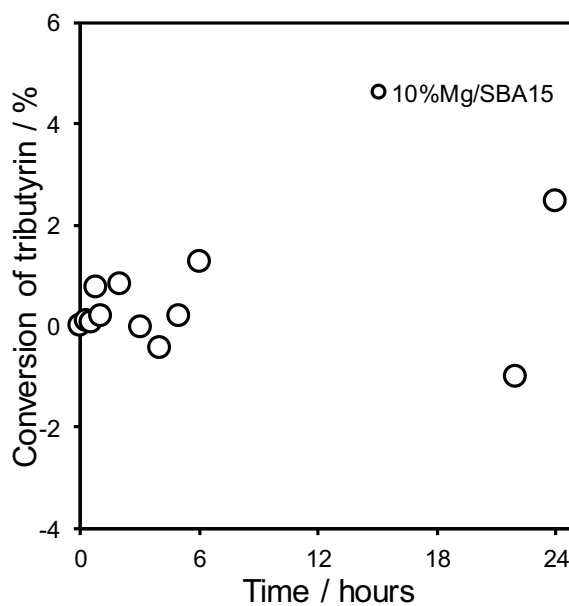
Appendix Figure 2.5. (a) Base site density and (b) magnesium dispersion as a function of magnesium loading, for both mesoporous (blue) and hierarchical (red) materials.



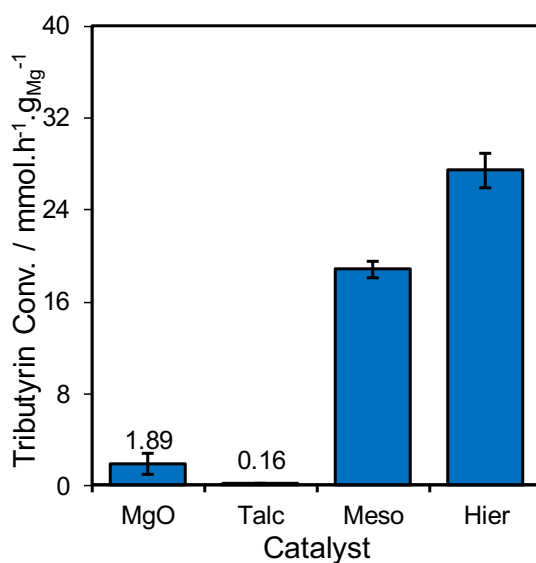
Appendix Figure 2.6. Temperature programmed desorption of CO₂ from (a) mesoporous and (b) hierarchical materials as a function of CO₂ mass spectrometry signal over temperature.¹⁻⁴



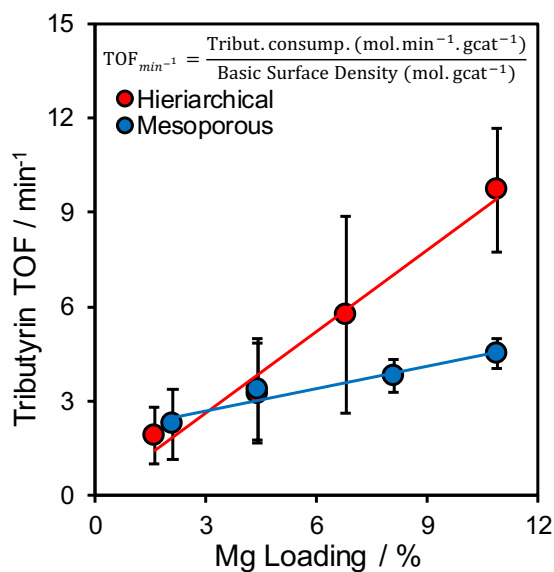
Appendix Figure 2.7. Model of tributyrin calculated using Chemdraw.



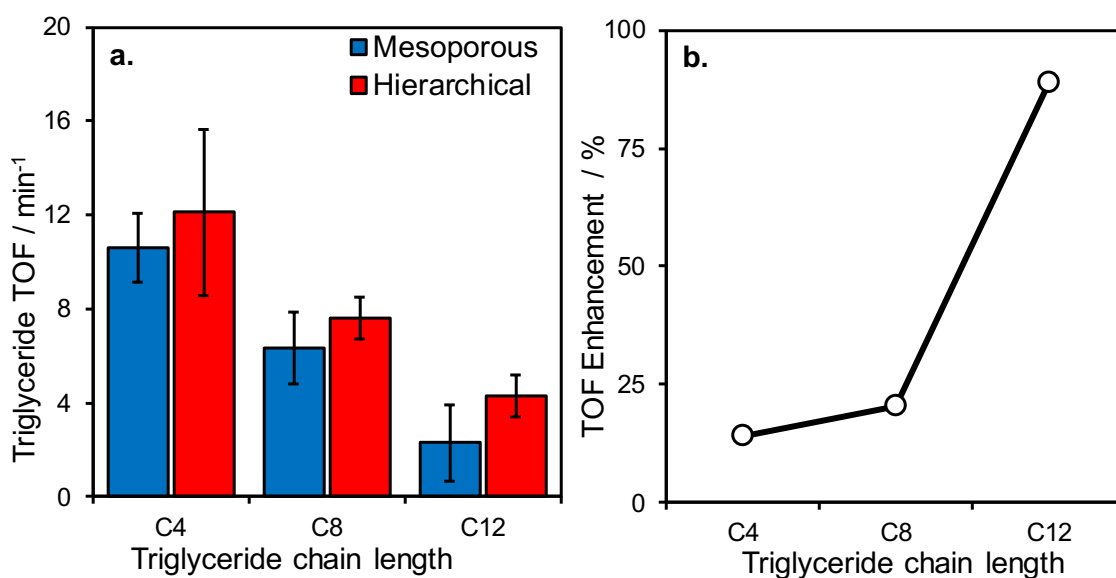
Appendix Figure 2.8. Tributyrin conversion profile using a 10 wt% nominally loaded MgO/SBA-15 synthesised using a one-pot cooperative self-assembly method.



Appendix Figure 2.1. Tributyrin conversion initial rate normalised to magnesium content of each material. Benchmark transesterification reaction using bulk MgO (calcined Mg precursor using same conditions), talc (hydrated magnesium silicate), mesoporous, and hierarchical magnesium oxide functionalised SBA-15.



Appendix Figure 2.2. Tributyrin turnover frequency normalised using the bases site density, error calculated from the sum of catalytic screening and base site density percentage error.



Appendix Figure 2.3. (a) Triglyceride conversion turn over frequency and (b) rate enhancement brought on from using a macropore network as a function of chain length for mesoporous and hierarchical 4.4 wt% MgO/SBA-15.

Appendix 3 for Chapter 4

Appendix 3a: Chemometrics and DoE Appendix

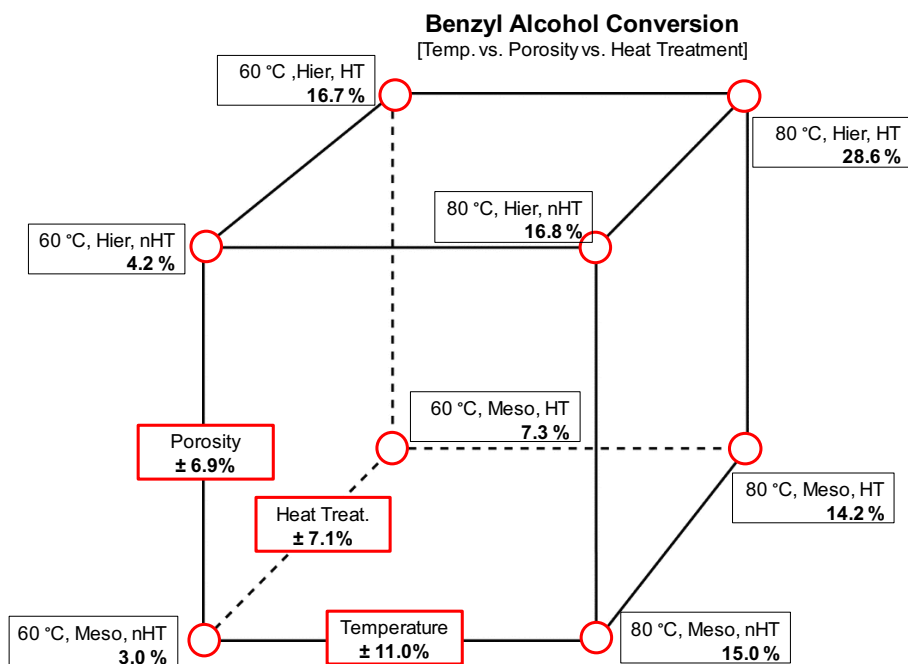
How is this achieved? Below is an example of the chemometric process.

1. The levels of each factor are given a value -1 or +1.
E.g. Reaction Temperature: 60 C₋₁/ 80 C₊₁
2. The response for each reaction is multiplied by the factor (or combination of factors) being examined.
E.g. Conv. of 60% at 60 C₋₁ = 60 x -1 = -60
3. The sum of all the factor response repeats is divided half the number of values, to give an overall average response.
E.g. Conv at 60 C: -60 + 80 + -42 + 62 = 40/2 = 20 %
4. If the overall response has a value larger than twice that of the error associated with the response, then it strongly influences the reaction.
E.g. Conversion error (5%, therefore 10%), 20 > 10, therefore temperature has a significant influence on conversion. On average, the temperature rise will increase conversion by 20 %.

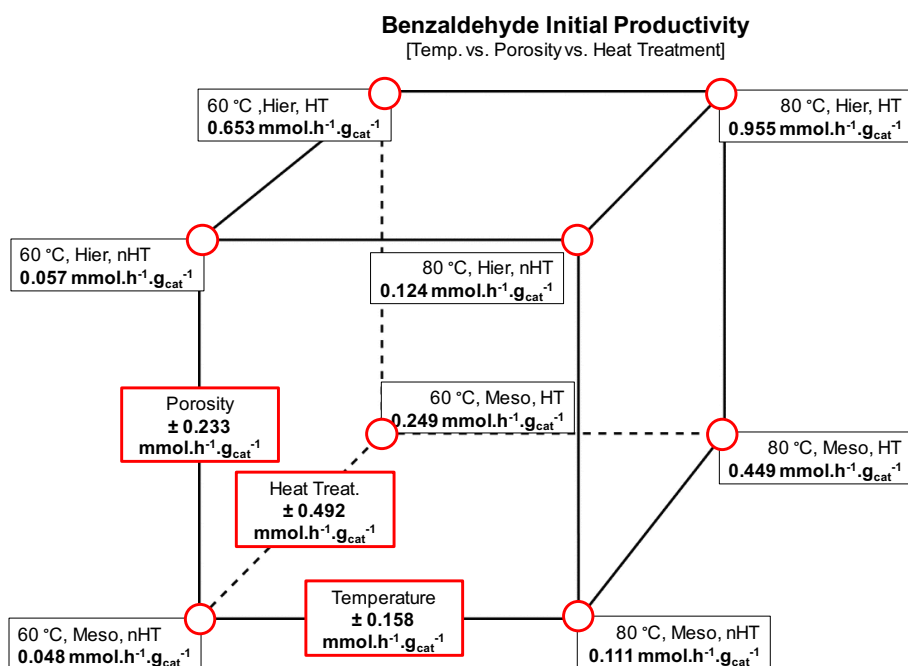
Appendix Table 3a.1. Chemometric data showing how the 5 factors interacted with the 3 responses; conversion, activity, and selectivity. Data in green implies a significant interaction and data in amber signifying an interaction below error. Data in black signifies a non-significant response.

	Benzyl Alcohol Conversion / %	Benzaldehyde Initial Prod. / mmol.h ⁻¹ .g _{cat} ⁻¹	Selectivity to Benzyl Benzoate / %
Error	5.32	0.21	0.092
2 x Error	10.64	0.42	0.184
1	11.04	0.158	-0.553
2	3.45	0.015	0.150
3	-3.64	0.027	1.483
4	6.85	0.233	0.507
5	7.12	0.492	-0.264
1 x 2	5.05	0.012	-0.004
1 x 3	0.12	0.149	-1.055
1 x 4	1.20	0.026	0.107
1 x 5	-1.62	0.093	0.380
2 x 3	-2.42	0.006	0.088
2 x 4	1.39	-0.011	0.202
2 x 5	-1.40	0.009	-0.223
3 x 4	-0.55	-0.009	-0.379
3 x 5	-1.65	0.003	-0.625
4 x 5	5.02	0.222	0.504
1 x 2 x 3	-4.32	0.009	0.165
1 x 2 x 4	0.56	0.047	-0.030
1 x 2 x 5	-1.59	0.038	0.208
1 x 3 x 4	1.26	0.091	0.434
1 x 3 x 5	0.49	0.125	0.744
1 x 4 x 5	1.26	0.025	-0.326
2 x 3 x 4	-1.64	0.054	-0.184
2 x 3 x 5	1.39	0.042	0.190
2 x 4 x 5	-0.53	-0.003	0.063
3 x 4 x 5	-0.62	-0.026	0.392
1 x 2 x 3 x 4	-1.13	0.001	0.392
1 x 2 x 3 x 5	0.83	0.003	-0.212
1 x 2 x 4 x 5	-0.33	0.055	-0.043
1 x 3 x 4 x 5	-0.24	0.070	-0.289
2 x 3 x 4 x 5	0.62	0.045	0.214
1 x 2 x 3 x 4 x 5	0.49	-0.013	-0.150

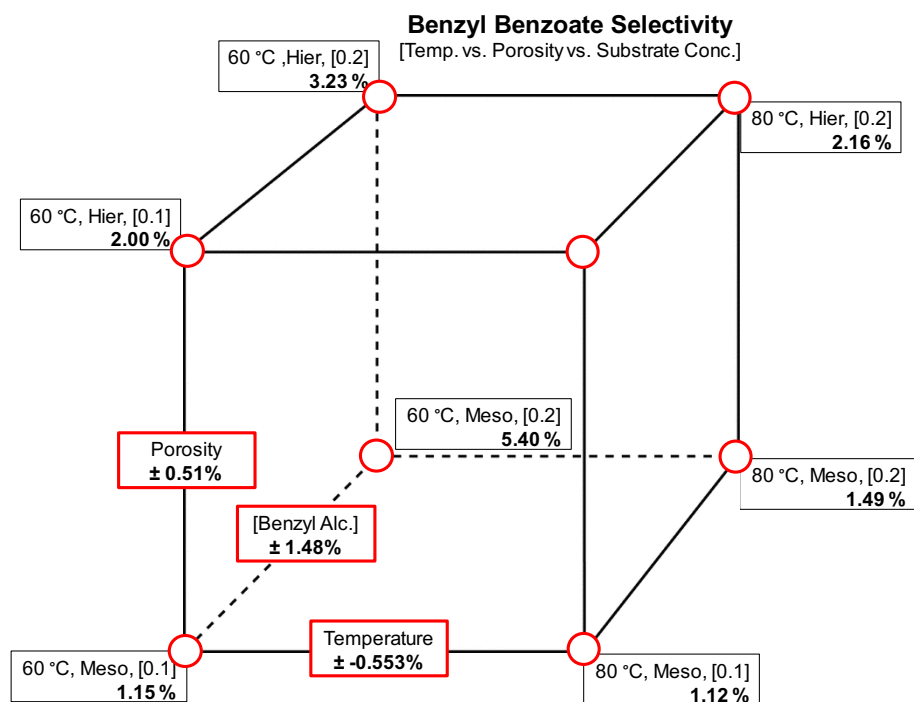
	Factors	Description	+1	-1
1	Temp. / °C	Reaction Temperature	80	60
2	RPM	Stirring Speed	800	600
3	[Benzyl Alc.] / mol.dm ⁻³	Substrate Concentration	0.2	0.1
4	Porosity	Pore network	Hierarchical	Mesoporous
5	Heat Treat.	Heat Treatment	550 °C, 2 hr, 10 °C.min ⁻¹	No Heat Treatment



Appendix Figure 3a.1. Cube schematic for the influence of reaction temperature, porosity and heat treatment on benzyl alcohol conversion.

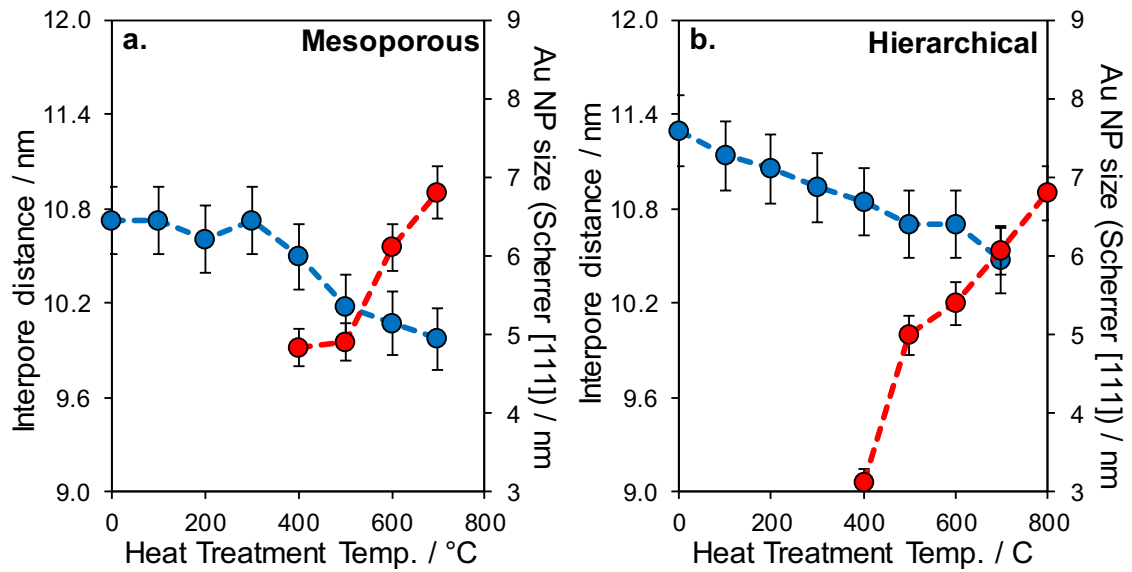


Appendix Figure 3a.2. Cube schematic for the influence of reaction temperature, porosity and heat treatment on benzaldehyde productivity.

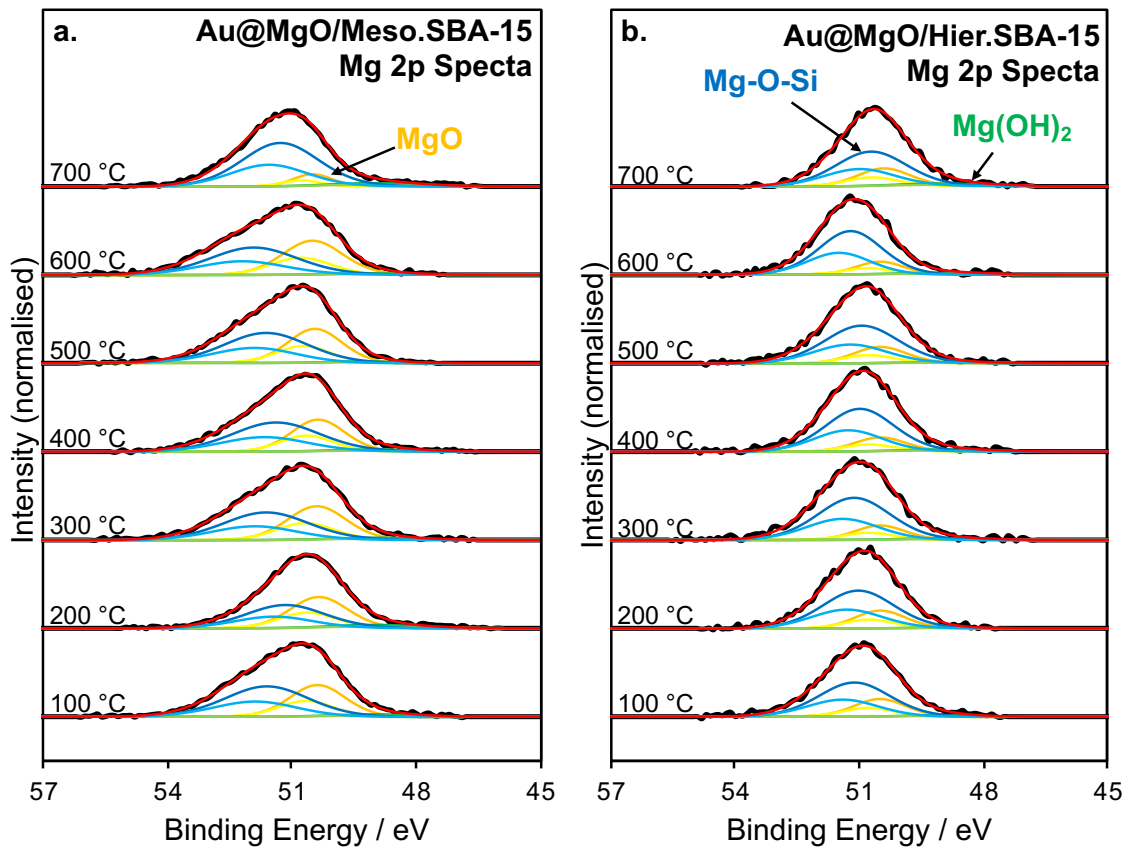


Appendix Figure 3a.3. Cube schematic for the influence of reaction temperature, porosity and substrate concentration on benzyl benzoate selectivity.

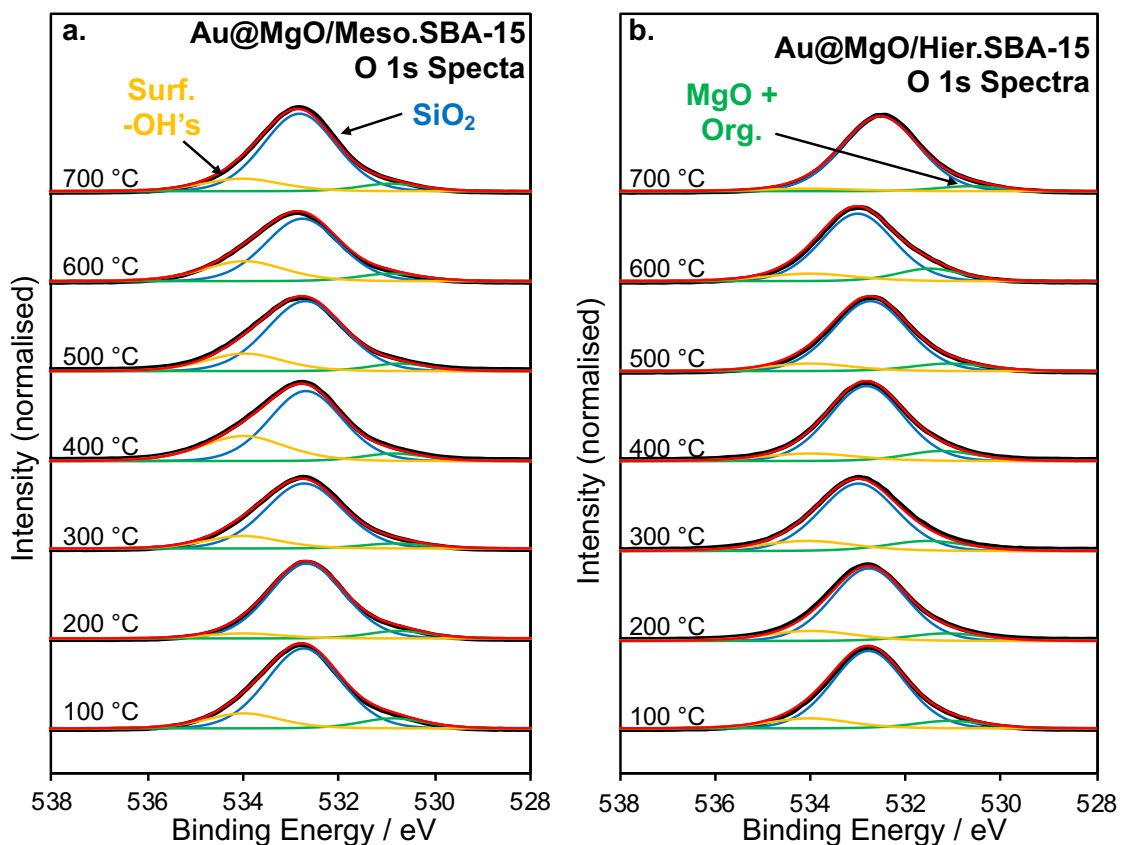
Appendix 3b: Heat Treatment Study Appendix



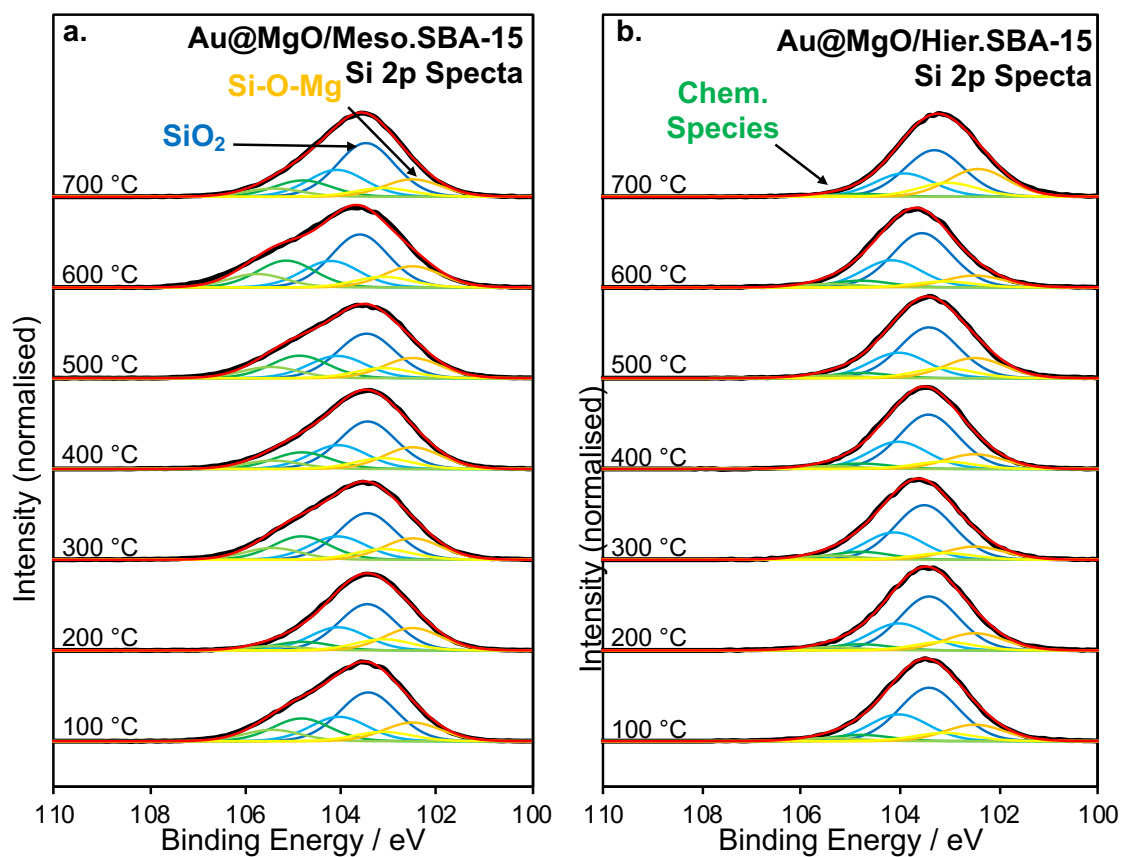
Appendix Figure 3b.1. Interpore distance and gold particle size determined using LAXRD and WAXRD Scherrer equation respectively for (a) mesoporous and (b) hierarchical materials.



Appendix Figure 3b.2. Mg 2p X-ray photoelectron spectra of (a) mesoporous and (b) hierarchical materials respectively.



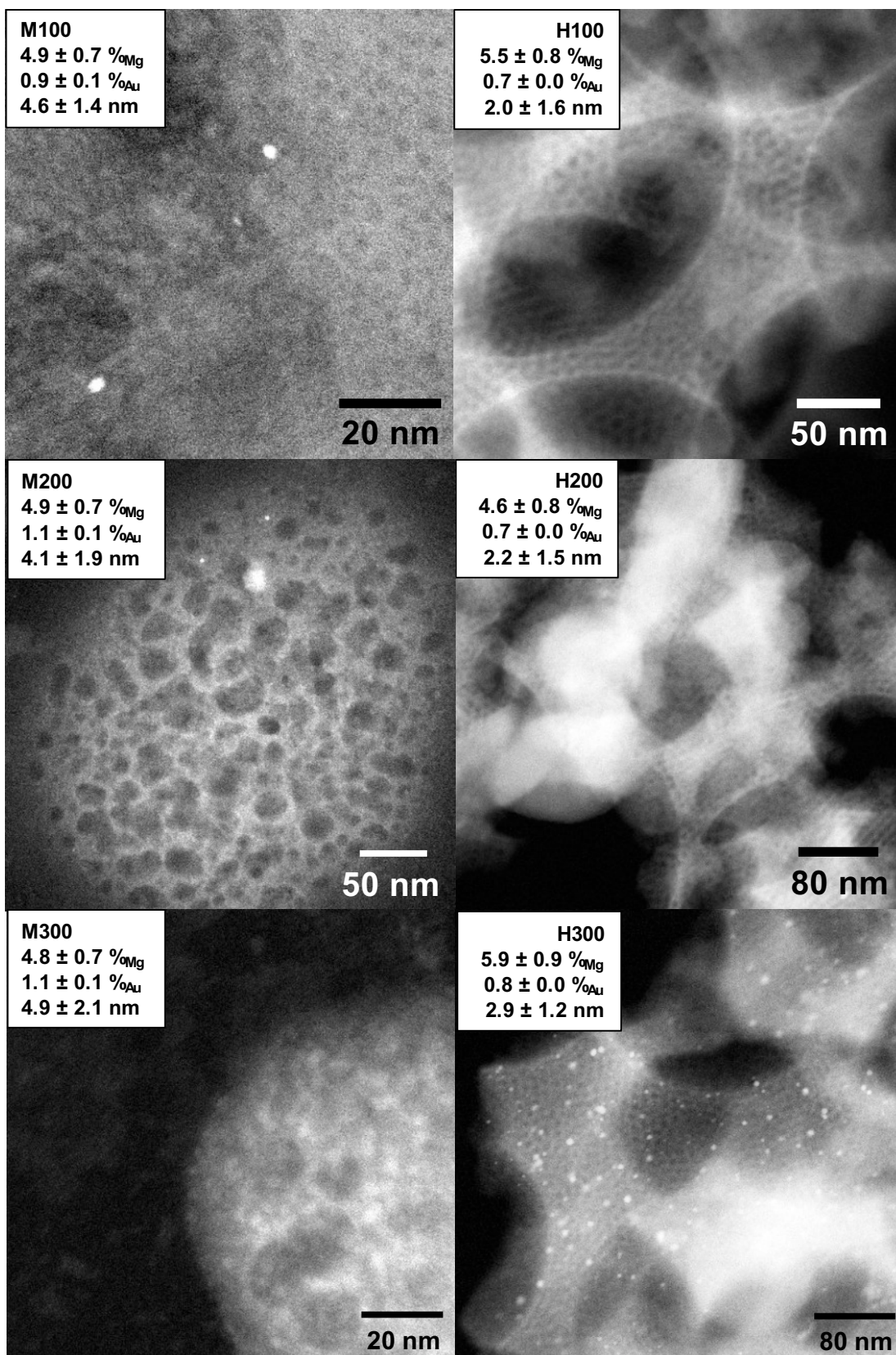
Appendix Figure 3b.3. O 1s X-ray photoelectron spectra of (a) mesoporous and (b) hierarchical materials respectively.



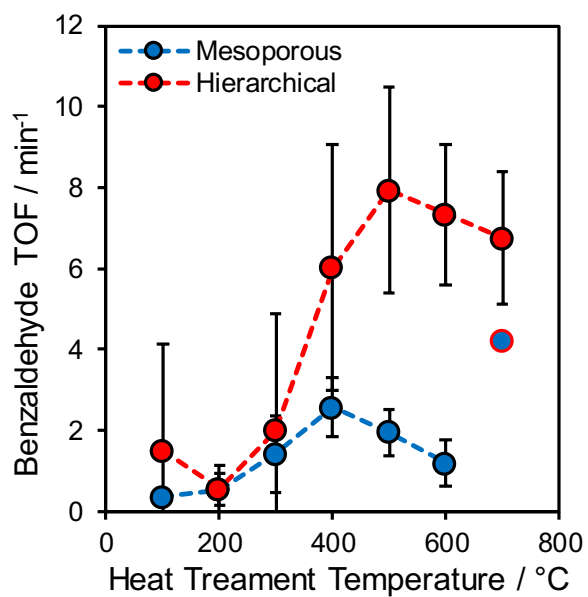
Appendix Figure 3b.4. Si 2p X-ray photoelectron spectra of (a) mesoporous and (b) hierarchical materials respectively.



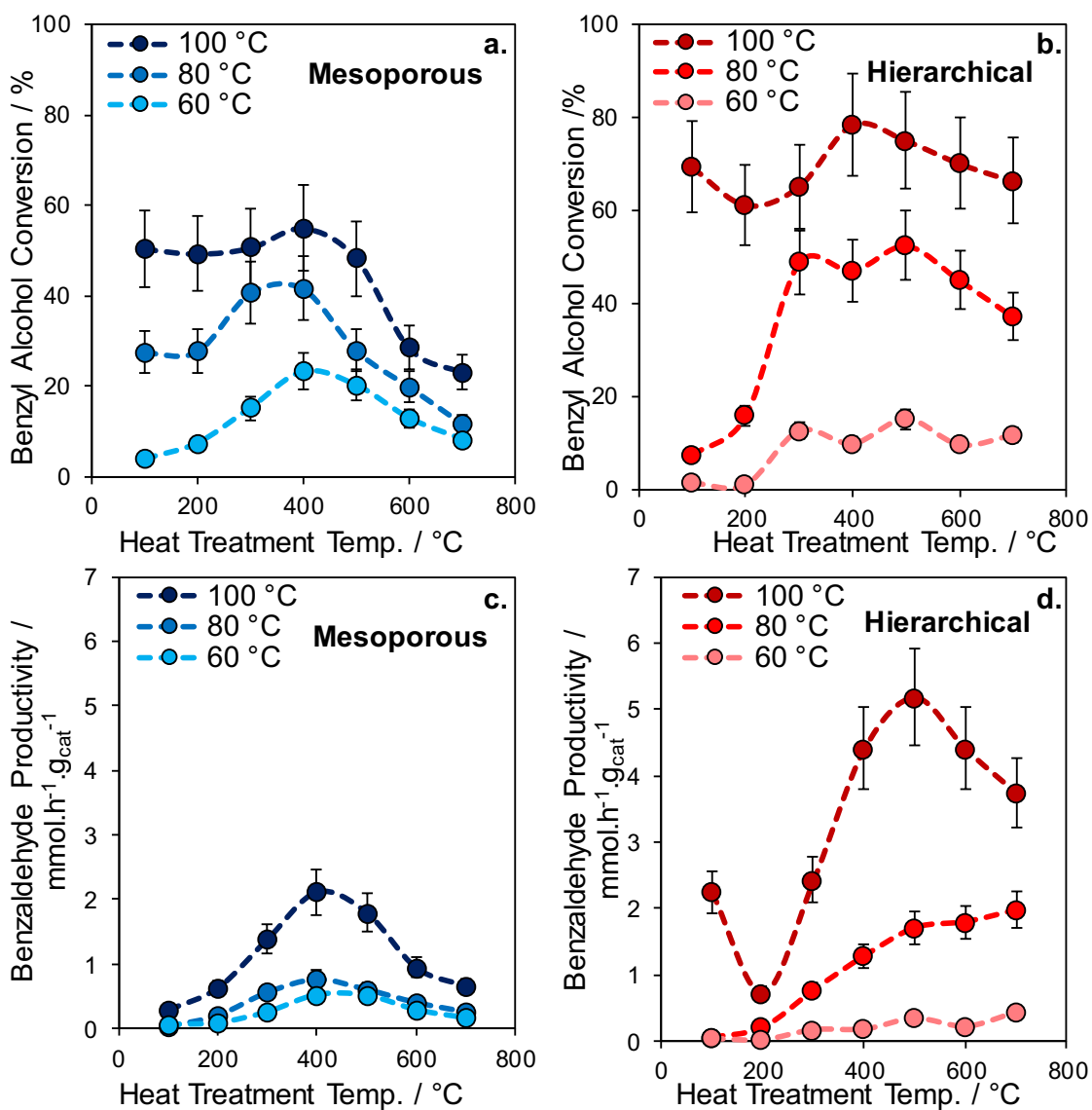
Appendix Figure 3b.5. Colour change in mesoporous Au@MgO/SBA-15 materials heated from 100-800 °C.



Appendix Figure 3b.6. Transmission electron microscopy micrographs of mesoporous (left) and hierarchical (right) Au@MgO/SBA-15 materials, heat-treated at 100, 200 and 300 °C.



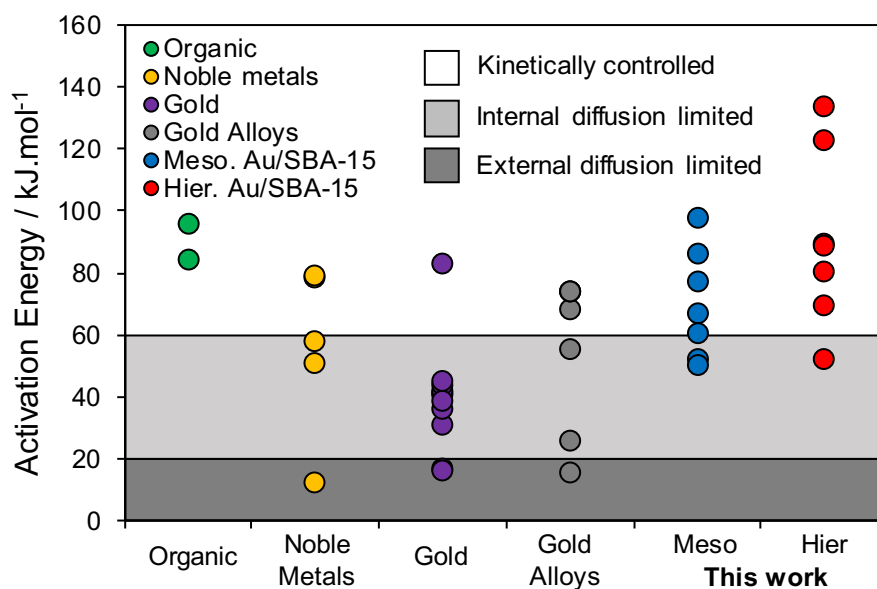
Appendix Figure 3b.7. Turn over frequencies taken from the initial productivity of benzaldehyde and normalised to the approximated site densities, taken from particle sizes counted from TEM and calculated using the Scherrer equation from WAXRD.



Appendix Figure 3b.8. The (a,b) final conversion of the substrate and (c,d) initial rate of productivity of the selective product benzaldehyde for (a,c) mesoporous and (b,d) hierarchical heat-treated materials for the selective oxidation of benzyl alcohol.

Appendix Table 3b.1. Literature review of kinetic studies undertaken on materials used for the selective oxidation of benzyl alcohol.

	Material	E _a / kJ.mol ⁻¹	Solvent	Benzyl Alcohol / mol.dm ⁻³	Oxidant	DOI
1	ammonium molybdate	84	Solventless	-	H ₂ O ₂	https://doi.org/10.1016/j.cej.2004.07.014
	tungstic acid	96				
2	Ru/Al ₂ O ₃	78.2	toluene	1.0	O ₂ flow	https://doi.org/10.1016/j.apcata.2005.04.042
3	Pt/ZrO ₂	79	n-heptane	0.2	O ₂ flow	https://doi.org/10.1002/ceat.200700072
4	Au/meso. SiO ₂ NPs	82.7	toluene	3.2	O ₂	https://doi.org/10.1016/j.apcatb.2013.04.029
	Pd-Au/meso. SiO ₂ NPs	25.9				
	Pd/meso. SiO ₂ NPs	50.7				
5	0.4%Au/MgO	30.5	Trifluorotoluene	1	none	https://doi.org/10.1016/j.jcat.2010.11.013
	0.8%Au/MgO	36				
	1.5%Au/MgO	40.2				
	3%Au/MgO	41				
	5%Au/MgO	41.8				
	10%Au/MgO	43.5				
6	1Au5Pd/APS-S16	16.7	Solventless	-	O ₂ flow	https://doi.org/10.1016/j.apcata.2010.03.026
	Au/APS-S16	16.1				
	Pd/APS-S16	12.3				
	1Au3Pd/APS-S16	15.5				
7	Pd/Activated carbon	57.9	P-xylene	1	O ₂ flow	https://doi.org/10.1002/cctc.201600368
8	Au	45	Water	0.05	O ₂ flow	https://doi.org/10.1016/j.jcat.2013.02.011
	Au _{0.99} Ag _{0.01}	55				
	Au _{0.98} Ag _{0.02}	68				
	Au _{0.95} Ag _{0.05}	74				
	Au _{0.90} Ag _{0.10}	74				
	Au _{0.85} Ag _{0.15}	74				
9	Au/Titanium silicate	38.2	water	1.67	H ₂ O ₂	https://doi.org/10.1016/j.molcata.2012.09.026

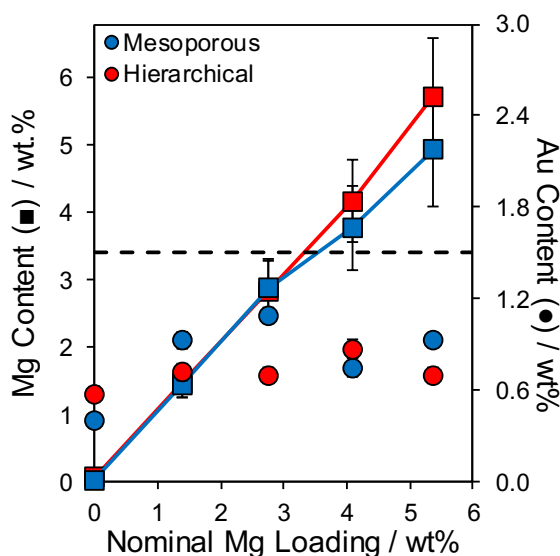


Appendix Figure 3b.9. Comparison between the materials produced in this study and other materials in the literature, as a function of activation energy.

Appendix 3c: Magnesium Loading Study

In **Chapter 3.2.2**, it was determined that increasing the loading of MgO correlated linearly with an increase in activity for the transesterification of tributyrin. This was attributed to an increased basic concentration, as the number of none uniformly dispersed MgO nanoparticles increased.

Therefore, it was decided to investigate the effect of increasing the basic concentration on the catalytic selective oxidation of benzyl alcohol, where it has been demonstrated that basic additives or species can favour the selective step, and scavenge the inhibiting products. It was offered that a weak base such as MgO would cause a minimal change in activity, however, it would mitigate the deactivation of the material as seen. This was thought to be occurring in **Chapter 4.2.3**, however this required confirmation. Both mesoporous and hierarchical MgO/SBA-15 were loaded with varying Mg (0-5 wt%) and Au (~1.5 wt%), and before undergoing the 'optimum' heat treatment from the previous section. ICP-OES analysis was performed (**Appendix Figure 3c.1**), showing a linear trend respective to the magnesium content. As seen in **Chapter 3.2.2**, hierarchical materials were synthesized with higher Mg content than mesoporous. Gold impregnation was partially successful, with approximately half the nominal loading (black line) being achieved.

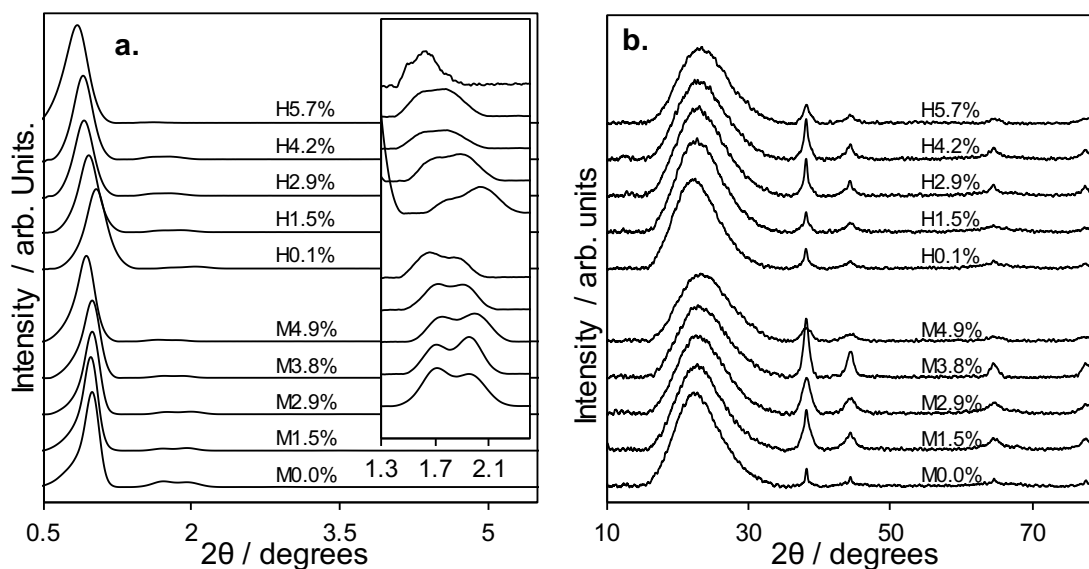


Appendix Figure 3c.1. ICP-OES Au and Mg loading data for mesoporous and hierarchical Au@MgO/SBA-15 materials.

Mesoporous materials had a varied gold loading with no clear trend, whereas hierarchical materials had a relatively constant loading, similar to the materials in **Section 4.2.3.1**. A probable cause of the reduced Au loading in both materials is the washing step, where

the gold can be pulled out of the material. As mentioned in **Chapter 4**, the isoelectric point dictates the gold should preferentially bind to the MgO species. As the Mg loading decreased, a reduced gold loading was thought to occur, however, this was not the case. It is suggested that using an incipient wetness impregnation caused the gold to be trapped within the material, therefore other methods such as LPRD could result in the predicted decrease in Au Loading.

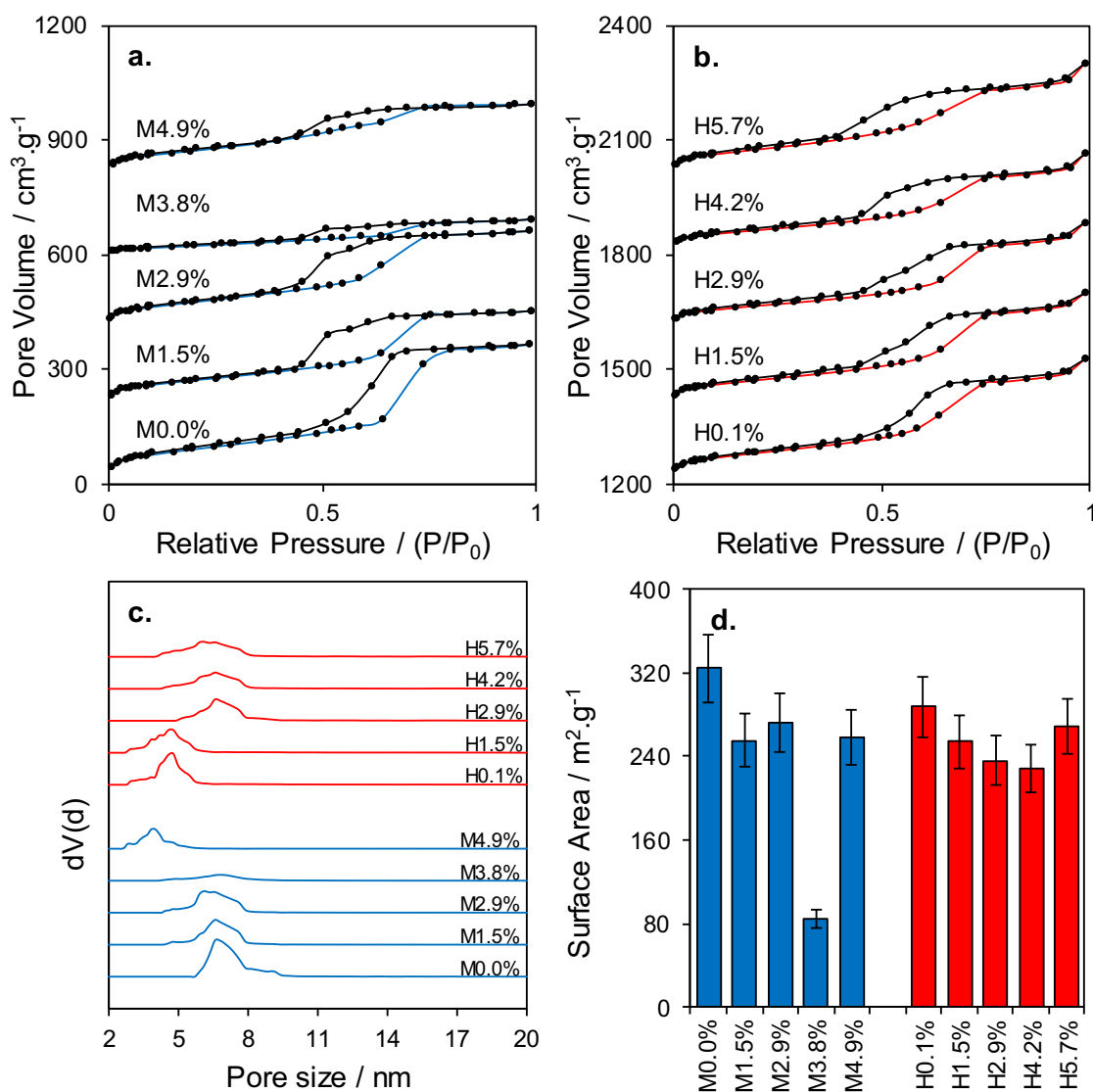
All materials showed the 11 and 20 low-angle reflections indicative of SBA-15, displayed in **Appendix Figure 3c.2a**. The definition of the 11 and 20 peaks differed between porosities and is explained in **Section 3.2.2.2**. Inter pore distance is reported constant for all materials, at 10.5 ± 0.5 nm, corroborating observations in **Chapter 3.2.2.2** and **4.2.3.1**.



Appendix Figure 3c.2. (a) The low-angle and (b) wide-angle X-ray diffraction patterns for mesoporous and hierarchical Au@MgO/SBA-15 materials.

WAXRD showed an amorphous silica peak at $20-25^\circ$, a slight shift to higher degrees was observed, as seen and explained in **Chapter 3.2.2.1**. Gold reflections increased in intensity up to M3.8 and H4.2 respectively. The highest loaded materials, from the previous subchapter, showed a reduced reflection. This could reflect the lack of reproducibility between batches.

A characteristic for SBA-15 type materials type IV nitrogen porosimetry isotherm was displayed for all materials in **Appendix Figures 3c.3a** and **3c.3b**, suggesting a successful synthesis. The hysteresis of both materials shifted from a type H1 to an H2 as loading increased, as observed in **Chapter 3.2.2.2**.



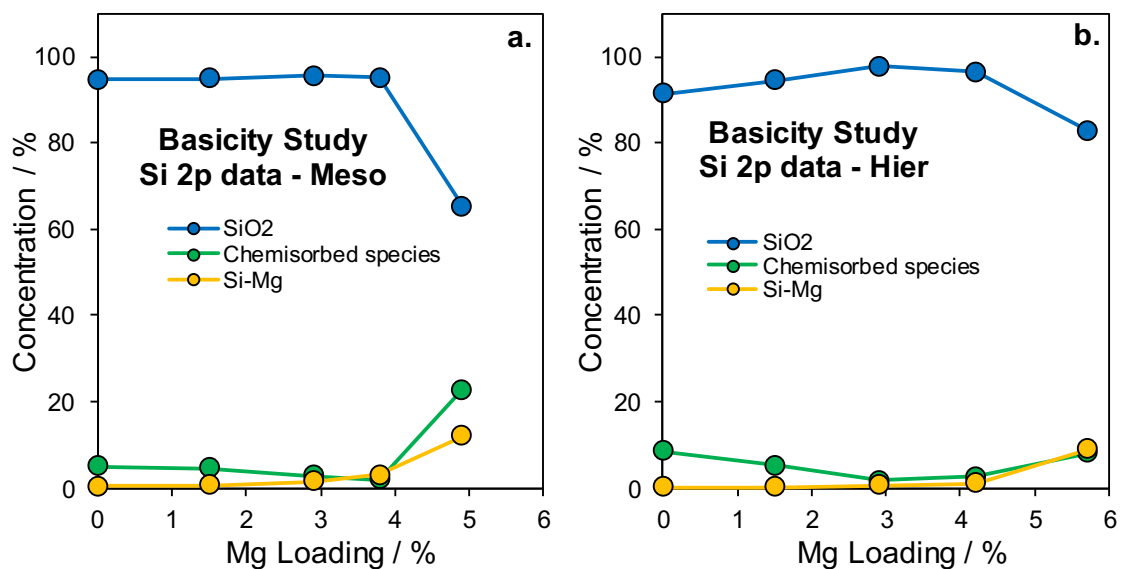
Appendix Figure 3c.3. Nitrogen Porosimetry isotherms for (a) mesoporous and (b) hierarchical Au@MgO/SBA-15 materials, with subsequent (c) pore size distributions and (d) surface areas.

The surface area was similar within error for all materials with the exception of M3.8, suggesting the synthesis was not successful for this sample (**Appendix Figure 3c.3d**). Due to the thermal and chemical stability of SBA-15, it is unlikely the synthesis error occurred during the gold impregnation, therefore it most likely occurred during the synthesis of the parent support. Pore size distributions were not consistent with previous work, with a mean pore size of 4-5 or 6-7 nm, with no trend visible (**Appendix Figure 3c.3c**). The previously mentioned M3.8 material displayed a pore size distribution of a lower intensity than other materials, suggesting a less uniform pore network.

X-ray photoelectron spectroscopy was undertaken for this study, investigating the same regions as **Section 4.2.3.1**; Si 2p, O 1s, Mg 2p, and Au 4f. All spectra found a significant

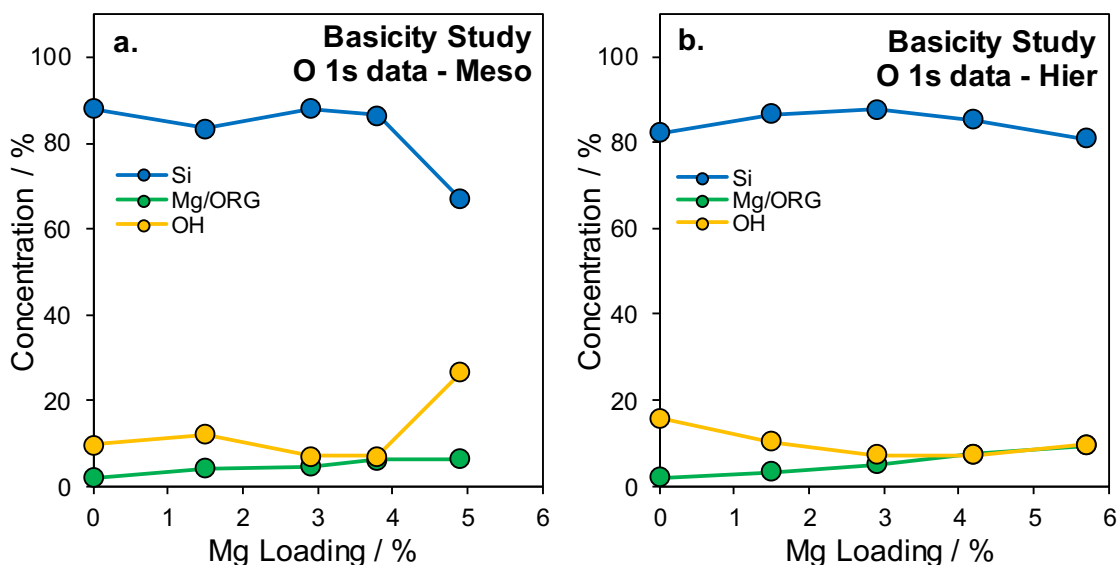
difference between the materials produced for this study and the materials from the previous study (M4.9 and H5.7). This is thought to be due to the irreproducible nature of the synthesis causing these differences.

As seen with **Section 4.2.3.1**, there are three Si 2p components at 101.9, 103.2 and 105.2 eV which correspond to Si-O-Mg and organic contaminants, SiO₂ and chemisorbed species bound to the silica surface respectively. The two minor components followed an inverse trend with each other as MgO loading increased, shown in **Appendix Figure 3c.4**. As previously seen in **Chapter 3.2.2.4**, the Si-O-Mg component gradually increased with loading, however, this also caused the chemisorbed species to decrease, suggesting silica surface was converted from being populated by surface hydroxyl and other organics to being populated by MgO.



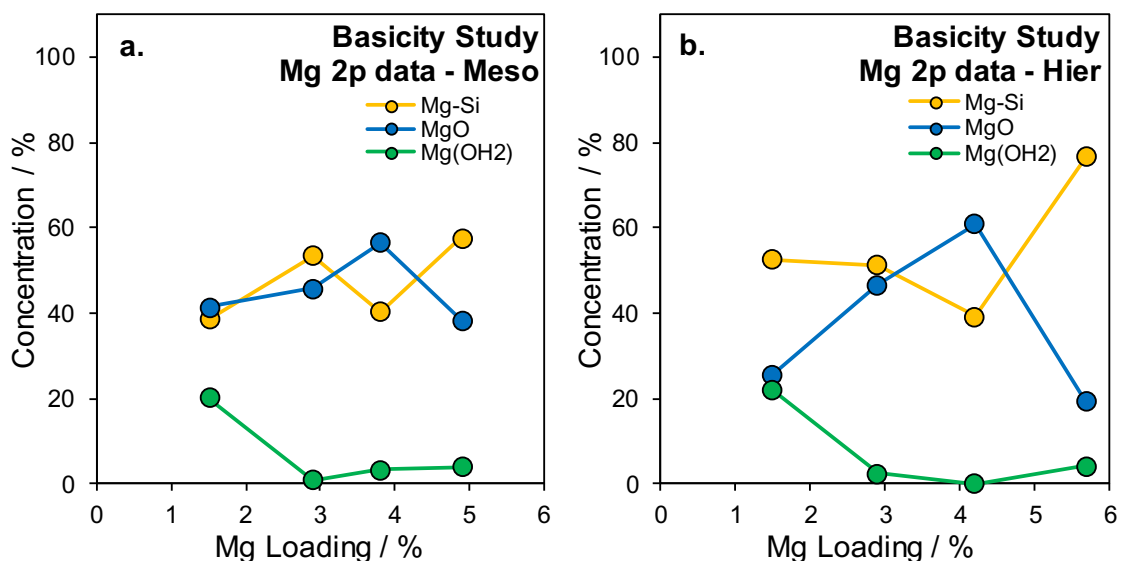
Appendix Figure 3c.4. Relative component concentrations for (a) mesoporous and (b) hierarchical Au@0-6%MgO/SBA-15 in the Si 2p region.

The O 1s spectra shown in **Appendix Figure 3c.5** displayed 3 peaks at 530.4, 532.5 and 534.4 eV which correspond to MgO and organic contaminants, SiO₂ and hydroxyl species bound to the silica surface, respectively. As previously seen, the MgO/Organic component increased in intensity as Mg loading increased. This is accompanied by the decrease in surface hydroxyl species, suggesting the MgO functionality replaced the other surface species, as seen with the Si 2p region (**Appendix Figure 3c.4**). Both materials followed this trend, with the only outlier being the highest loaded mesoporous material, further suggesting inconsistencies with the batch synthesis methodology.



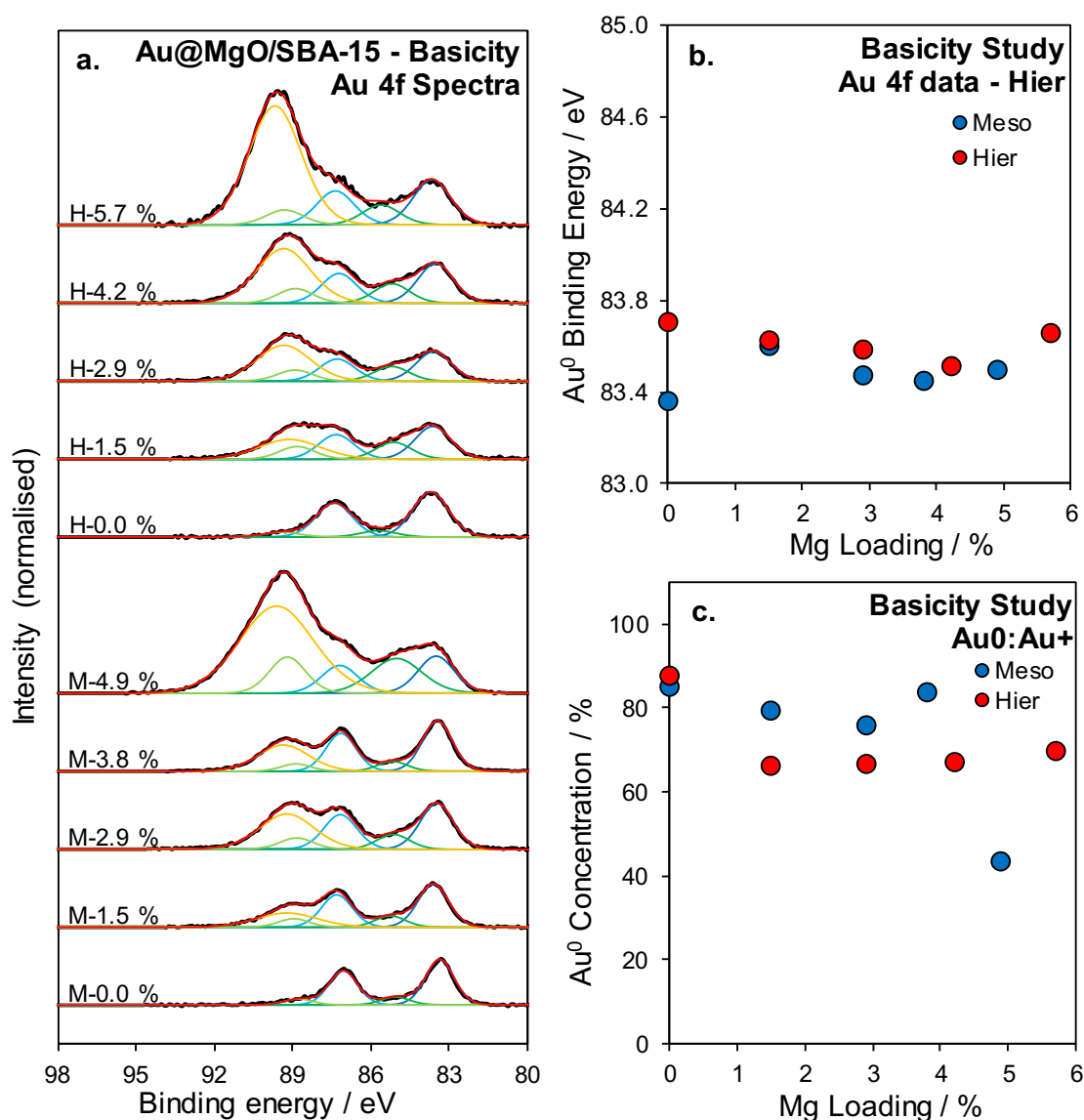
Appendix Figure 3c.5. Relative component concentrations for (a) mesoporous and (b) hierarchical Au@0-6%MgO/SBA-15 in the O 1s region.

The Mg 2p spectra shown in **Appendix Figure 3c.6** displayed 3 doublet peaks at 49.1, 50.1 and 51.0 eV which correspond to Mg(OH)₂, MgO and Mg-O-Si respectively. These features were similar to the Mg 2p spectra of the parent supports (**Chapter 3.2.2.5**), however, the Mg-O-Si component shifted to higher BE. The intensity of the spectra increased with loading, however, the ratio between the three components remained comparatively consistent throughout all materials. The only exception was the highest loaded hierarchical material, which as previously discussed was most likely caused by the irreproducibility of the synthesis.



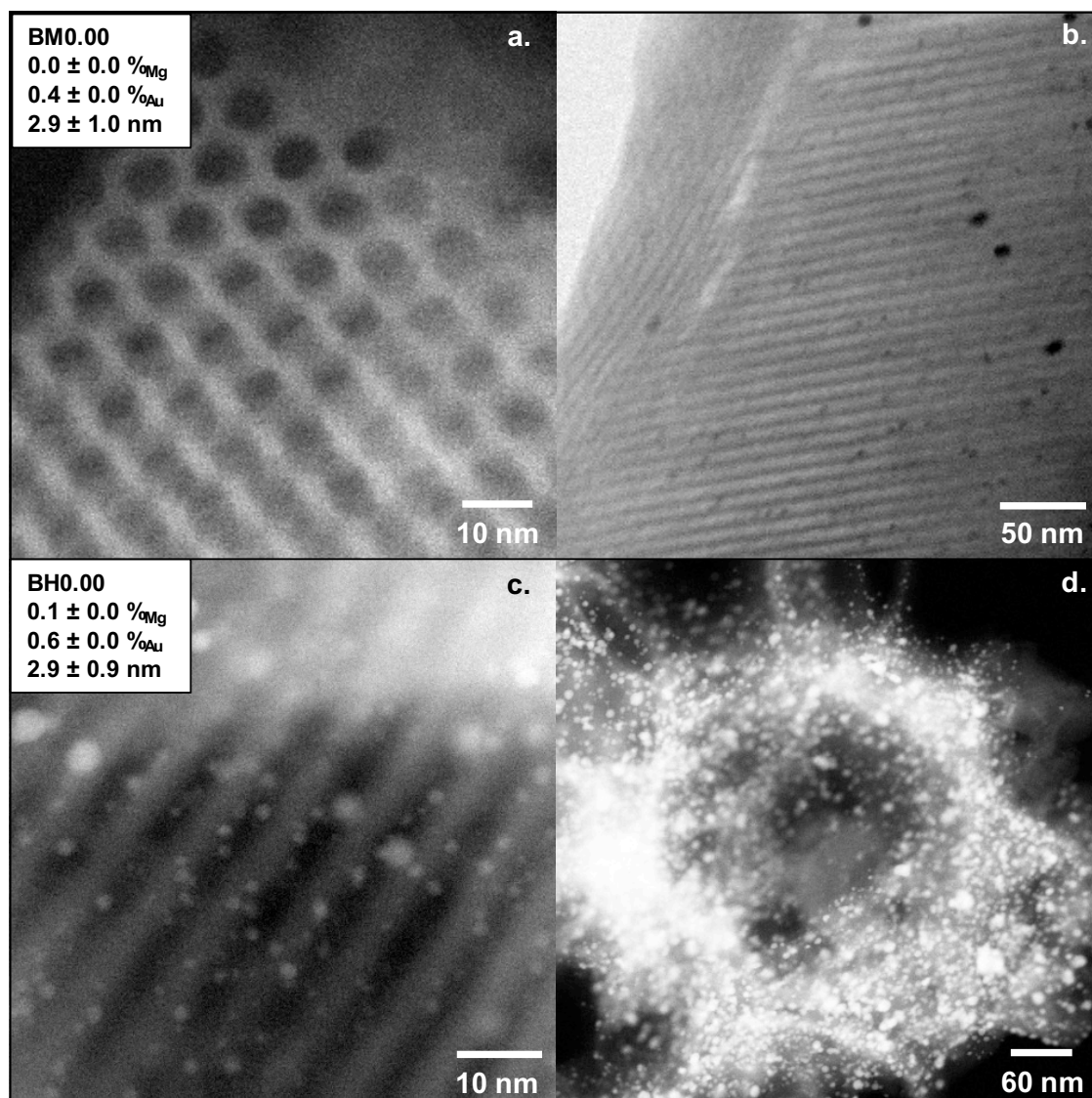
Appendix Figure 3c.6. Relative Mg 2p component concentrations for (a) mesoporous and (b) hierarchical Au@0-6%MgO/SBA-15 in the Mg 2p region.

As seen in **Section 4.2.3.1**, **Appendix Figure 3c.7** displays 3 peaks, two doublet peaks at approximately 84 and 86 eV, which correspond to metallic (Au^0) and cationic gold (Au^+), and the single Mg peak at 90 eV. The $\text{Au}_{7/2}$ feature did not shift to lower binding energy, which would be indicative of increasing basicity.⁵ This indicated that the MgO was not getting more basic, suggesting the only increase was the frequency of basic sites. The Mg 2s component increased in size with Mg loading, which was expected. The Au^0 to Au^+ ratio remained approximately constant regardless of loading, except for the highest loaded mesoporous material, which displayed an increased Au^+ feature. Again, this was attributed to inconsistencies in the synthesis.

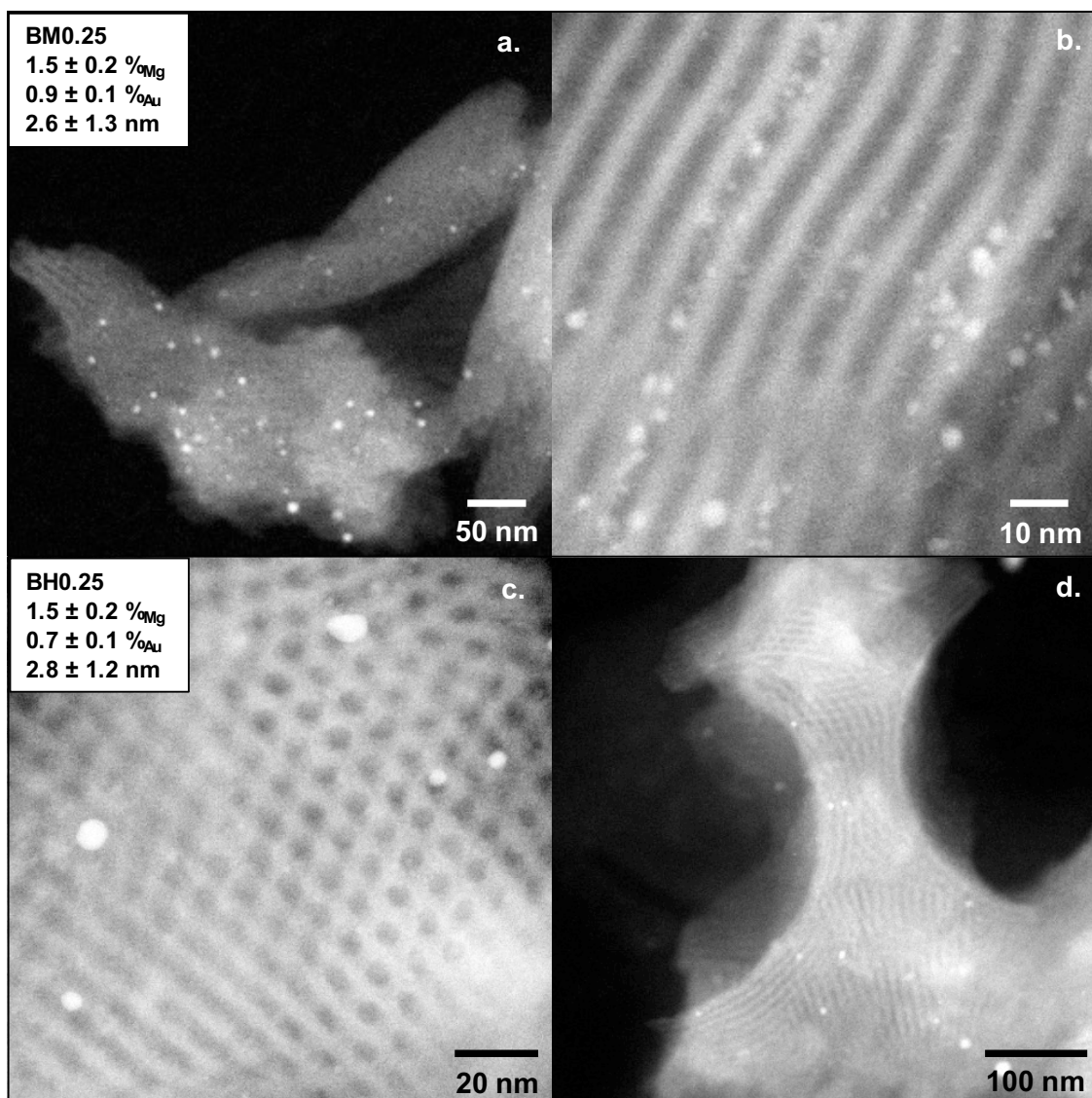


Appendix Figure 3c.7. X-ray photoelectron Au 4f spectra of (a) Au@0-6%MgO/SBA-15 materials and the Au^0 (b) binding energy and (c) relative Au^0 concentration relative to magnesium loading.

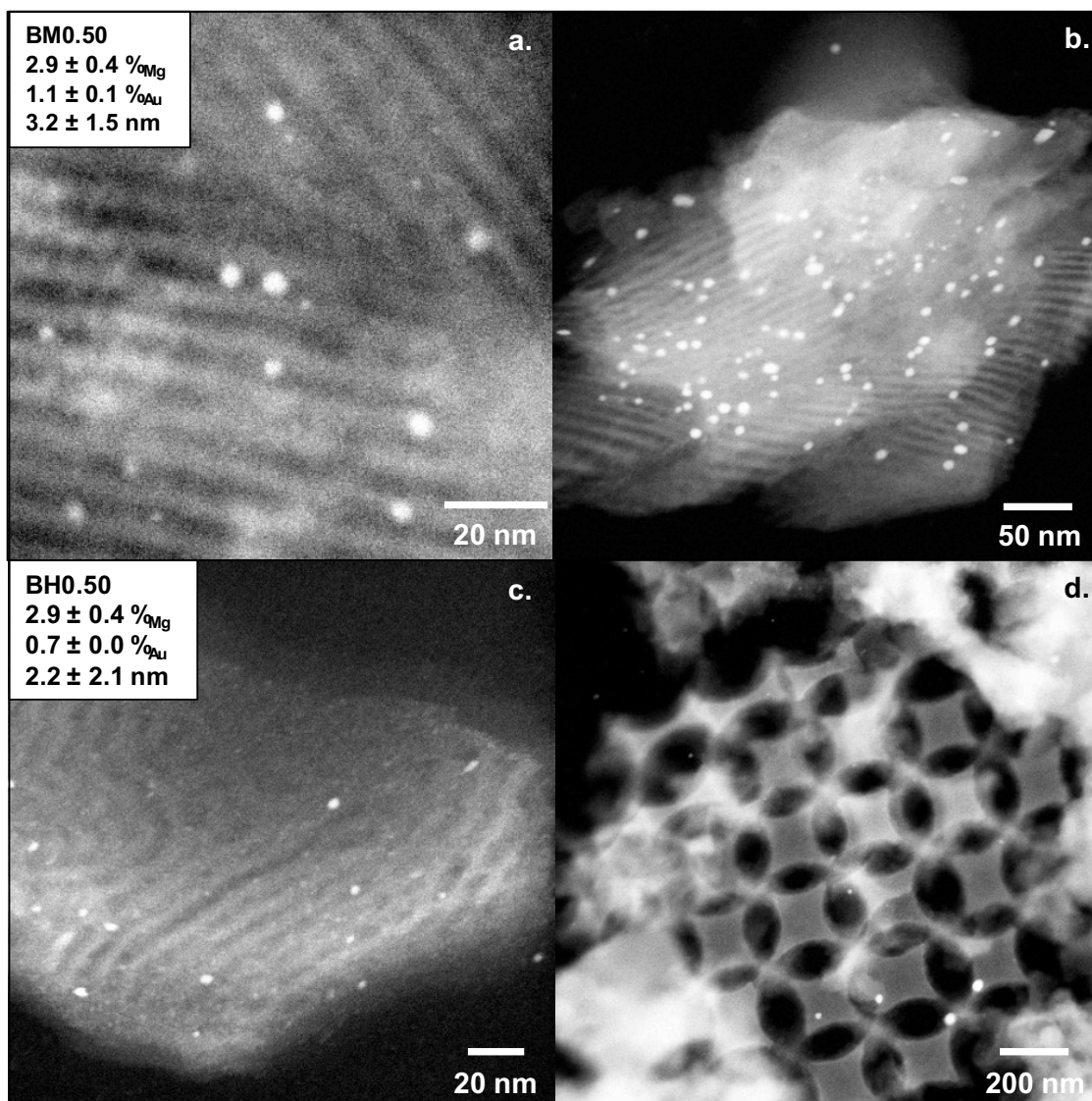
The TEM analysis showed both small nanoparticles (1-3 nm), retained within the mesopore network, and larger particles (> 10 nm) on the surface. The clearly defined mesoporous and meso-macropore network was maintained throughout loadings and impregnation, meaning the synthesis was a partial success. TEM is displayed in **Appendix Figure 3c.8-11**.



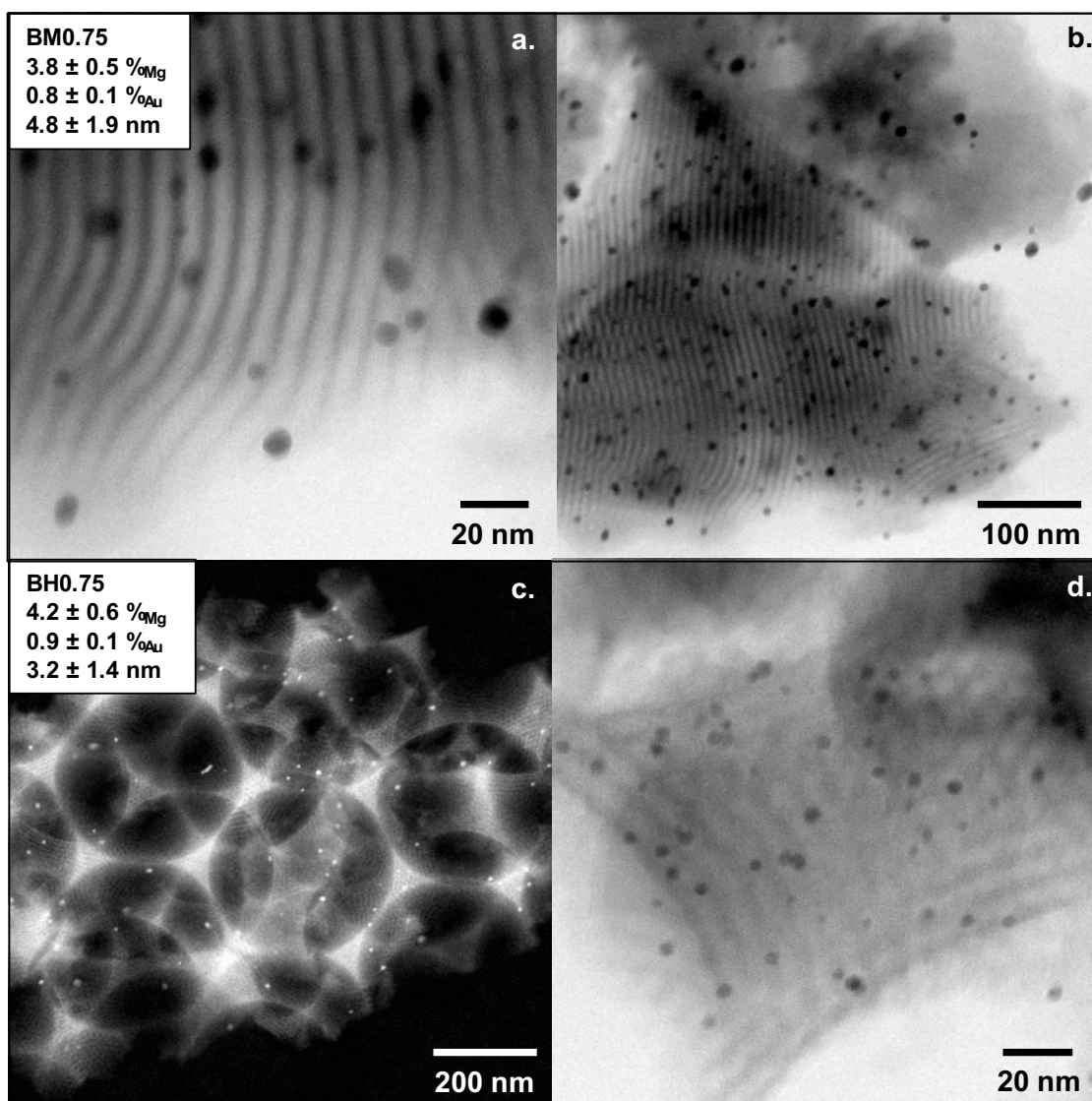
Appendix Figure 3c.8. Transmission electron micrographs of (a,b) mesoporous and (c,d) hierarchical Au@MgO/SBA-15.



Appendix Figure 3c.9. Transmission electron microscopy micrographs of (a,b) mesoporous and (c,d) hierarchical Au@0.25MgO/SBA-15 materials.



Appendix Figure 3c.10. Transmission electron microscopy micrographs of (a,b) mesoporous and (c,d) hierarchical Au@0.5MgO/SBA-15 materials.

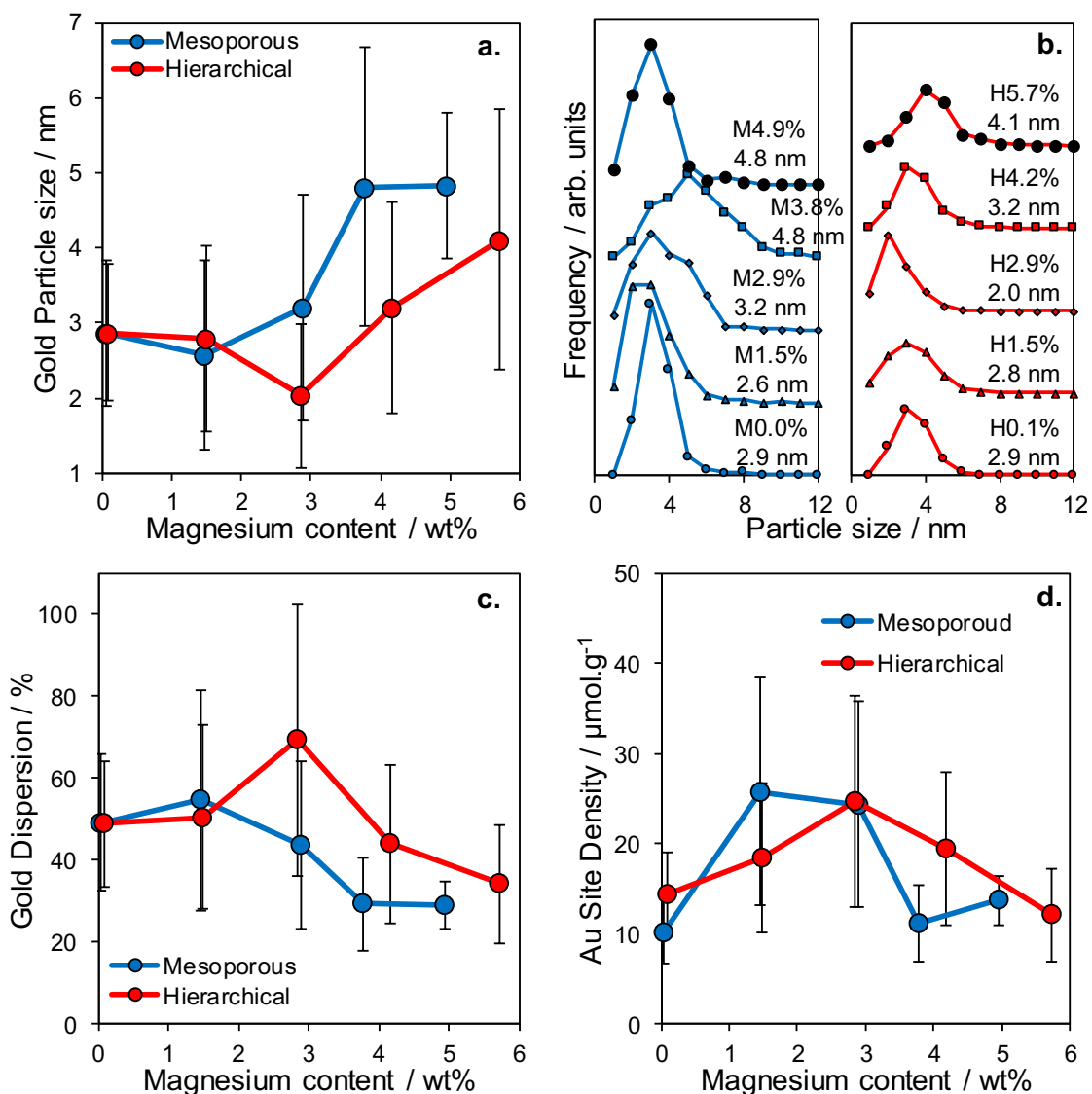


Appendix Figure 3c.11. Transmission electron microscopy micrographs of (a,b) mesoporous and (c,d) hierarchical Au@0.75MgO/SBA-15 materials.

A broadening of the particle size distribution, featured in **Appendix Figure 3c.12b**, exhibits a wider distribution of nanoparticles. In **Figure 3.9**, pore size was found to decrease with loading, attributed to the MgO functionality forming small particles. It could be hypothesised that gold impregnation within the mesopores was favoured for all SBA-15 type materials. As MgO NPs began to constrict the mesopore channels, wider distributions and larger Au NPs outside the mesopores were observed.

As observed during the heat treatment study, the significant error associated with determining the particle size using TEM was reflected in the subsequent data derived from it. The data in **Appendix Figure 3c.12** show trends such as increasing particle size, constant site density and decreasing dispersion with increased Mg loading. However, these trends were within error, proving it impossible to convincingly draw conclusions.

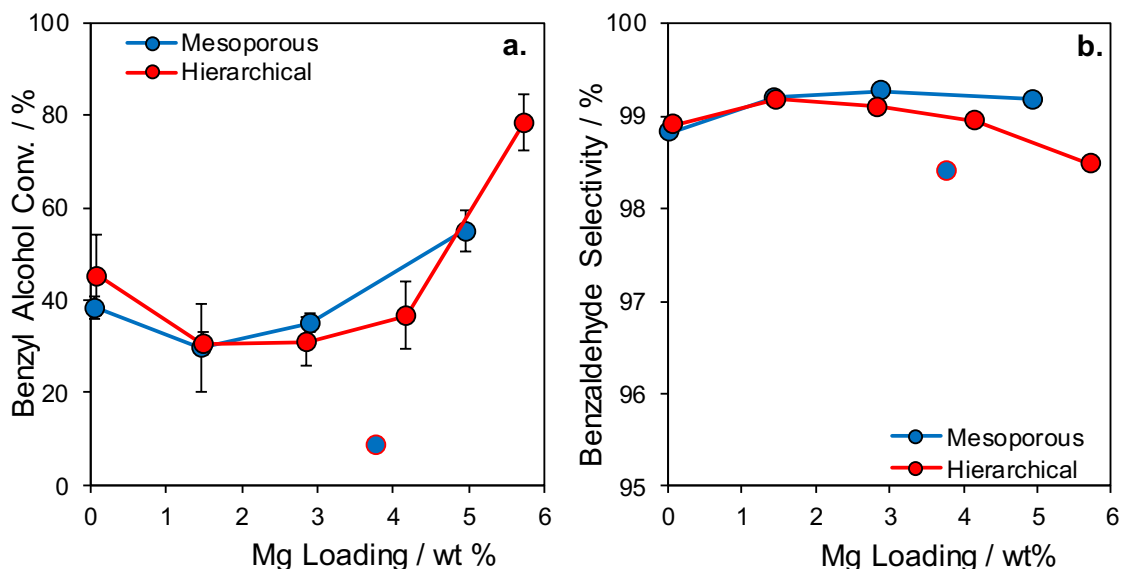
When considering the particle size distributions however, it was clear that most materials exhibited similar distributions, with the major exception of BM0.75, which had been shown to be a defective material using nitrogen porosimetry. Both materials exhibited a slight shift to larger particles with loading, while retaining a significant proportion within the size limit of the mesopore network.



Appendix Figure 3c.12. Data sets determined from TEM calculations of particle size, with; average particle size (top middle), particle size distributions for mesoporous and hierarchical (top right), gold dispersion (bottom left) and gold site density (bottom right) all as a function of magnesium loading.

Mesoporous and hierarchical materials with varied Mg loading were screened using the selective oxidation of benzyl alcohol, and the conditions optimised in **Chapter 4.2.2**. All materials exhibited good selectivity to the aldehyde product (**Appendix Figure 3c.13b**), achieving decent conversion after 24 hours (**Appendix Figure 3c.13a**). Literature has

determined increased basicity results in increased selectivity to the aldehyde,⁶⁻⁸ however an increasing concentration of MgO functionality does not bring this about.

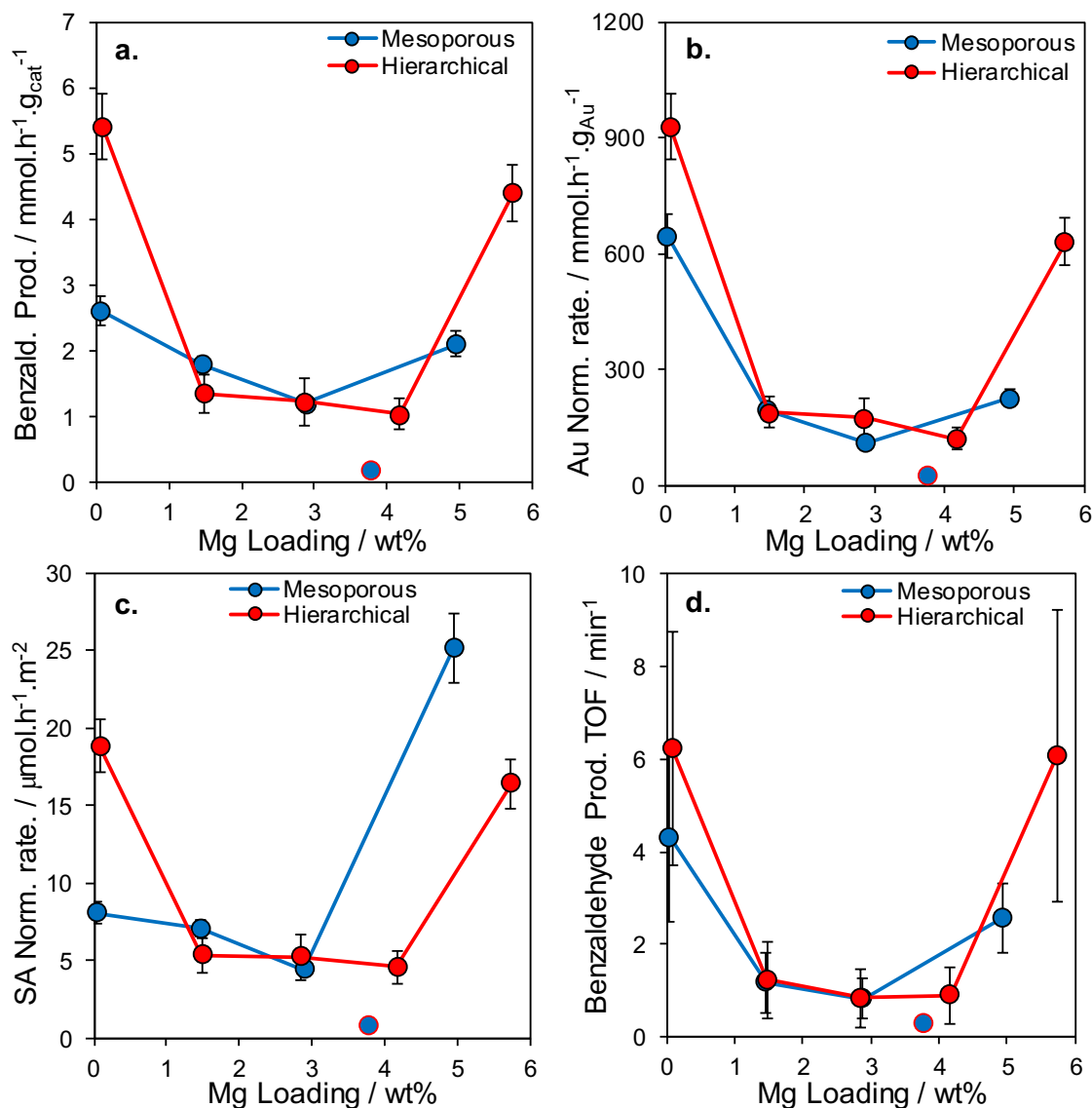


Appendix Figure 3c.13. Screening data for the selective oxidation of benzyl alcohol, using mesoporous and hierarchical gold functionalised SBA-15 materials containing varying loadings of magnesium oxide. (a) Final substrate conversion after 24 hours (bottom left) and (b) selectivity to the aldehyde product.

When examining the rate of benzaldehyde productivity in **Appendix Figure 3c.14a** it gave unexpected results, with the initial productivity of benzaldehyde following a 'U' plot. Au@MgO/SBA-15 materials with no MgO presence exhibited the highest activity, decreasing following the impregnation of MgO and returning to a high activity for 5-6 wt% Mg. Au@MgO/SBA-15 materials displayed the highest initial activity but relatively low conversion, which suggested that without a base functionality the material rapidly deactivated. To elucidate the cause of the trend, the calculated rate was normalised to surface area (**Appendix Figure 3c.14b**), gold loading (**Appendix Figure 3c.14c**) and approximated site density (**Appendix Figure 3c.14d**). This was ultimately unsuccessful, as the trend was still observed when normalised to catalyst mass, differing concentrations of gold, active sites and physical properties.

What is clear is by changing the MgO content within the material, other material properties were also altered, making the investigation of a single factor impossible. It is observed in the literature that Au@MgO/SBA-15 is an excellent material for these reactions,⁹⁻¹¹ which was confirmed by the reaction data in this study, in spite of their rapid deactivation. The subsequent drop and rise in activity with Mg loading suggested that a small MgO content hindered the reaction, until the balance changed and it caused the

activity to increase. The data also suggested that a further increase in loading may facilitate a further rise in activity.

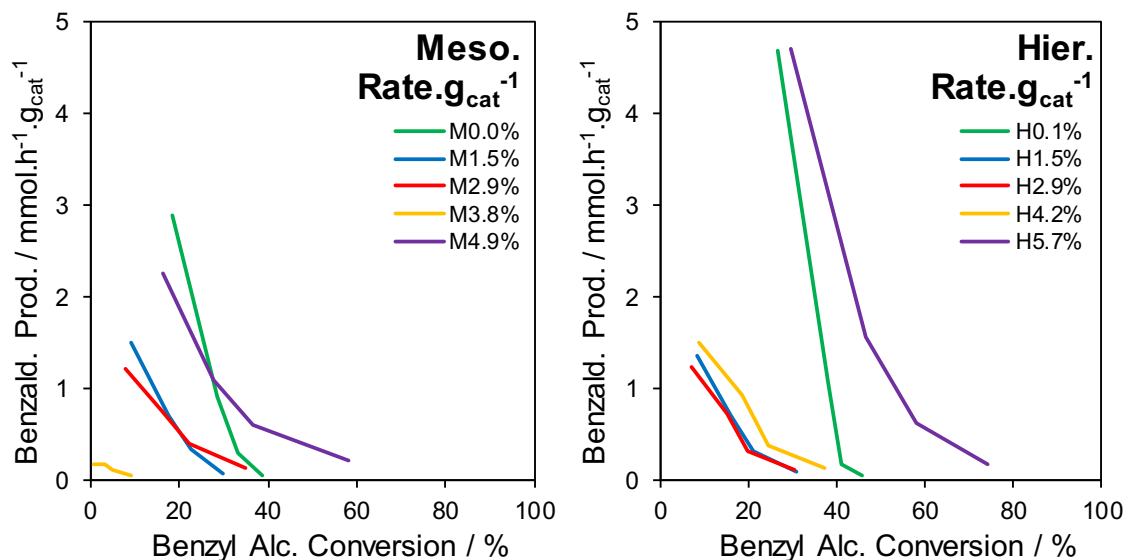


Appendix Figure 3c.14. Raw (a) aldehyde productivity for mesoporous and hierarchical materials with varied Mg loading. Rate normalised to (b) gold loading (top right), (c) surface area and (d) approximated site density to give the turn over frequency (TOF). The outlying sample (M3.8) is outlined in red, due to the failed synthesis.

Productivity was shown to vary in **Section 4.2.3.2**, therefore it was decided to show rate as a function of conversion, to omit the effect of changing concentration.

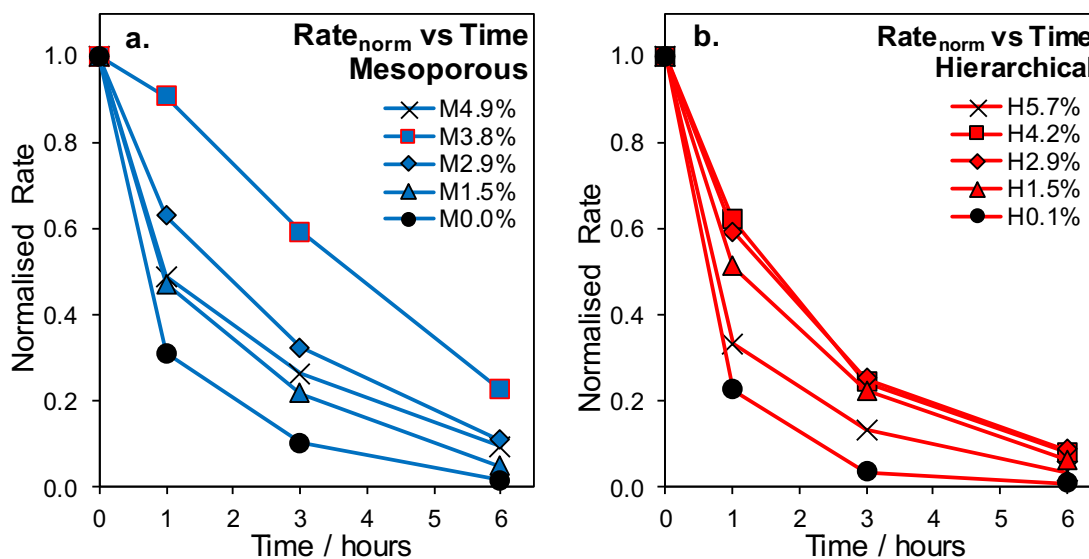
Figure 4.17 showed 400-700 °C heat-treated materials displayed a similar shaped profile, evident when the normalised rate was examined. The rate vs. conversion profiles in **Appendix Figure 3c.15** gave different slopes, implying deactivation was occurring at

differing rates. The current study, by contrast, showed differing plot shapes, with the materials with no MgO presence seemingly deactivating at a faster rate.



Appendix Figure 3c.15. The productivity of benzaldehyde product as a function of benzyl alcohol conversion for (a) mesoporous and (b) hierarchical.

The difference in rates of deactivation can be seen clearly when the activities of all materials are normalised, shown in **Appendix Figure 3c.16**. Discounting the outlier material, (determined as such due to the poor physical characteristics determined using nitrogen porosimetry (**Appendix Figure 3c.3**)), both mesoporous and hierarchical exhibited a curve, also seen by materials in **Section 4.2.3.2**. The difference between loadings was the sharpness of the curve, with Au@MgO/SBA-15 being the material deactivating most rapidly. Interestingly, the highest loaded MgO/SBA-15 supports followed closely behind with respect to activity loss. A conclusion from this was the reduced ability of Au@MgO/SBA-15 supported gold to stop the deactivation, resulting in the poor conversion seen previously. What it was also clear was the minor improvement in retention of activity by the highest loaded MgO/SBA-15 materials, resulting in the best reaction conversion.



Appendix Figure 3c.16. Normalised rate profiles for (a) mesoporous and (b) hierarchical as a function of time. Data points outlined in red are given as outliers.

In summary, this study was partially successful to show the increased rate of deactivation of Au@MgO/SBA-15. Unfortunately, this study did not determine the definitive cause of the high initial activity of the Au@MgO/SBA-15 materials, and subsequent 'U' trend in the activity. This study also revealed the irreproducibility with the method, which was particularly evident with the sample M-3.8, which displayed diminished surface area and activity relative to the other materials. Also when comparing the M&H-0-4 to the M&H5 materials, there was a noted difference in WAXRD peaks intensity, XPS spectra features, and TEM.

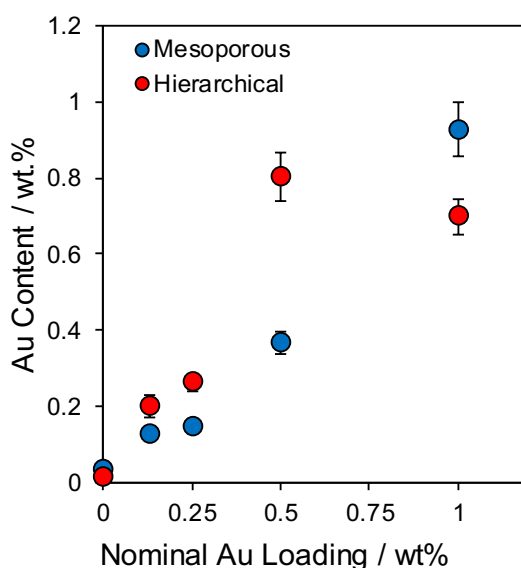
The aim was to change the MgO loading, without altering the gold species. TEM determined that this was not possible, with average particle size and distribution changing with Mg loading. XPS of the Au 4f region determined that the Au⁰ component did not shift, suggesting the basicity of the materials was not altered.

What can be concluded, however, is that the basic species was required to reduce the rate of deactivation, therefore it was decided to study the effect of Au loading. It was hypothesized that decreasing Au concentration would result in smaller, monodisperse nanoparticles, allowing for the particle size to be investigated in the absence of changing temperature and therefore changing basicity.

Appendix 3d: Gold Loading Study

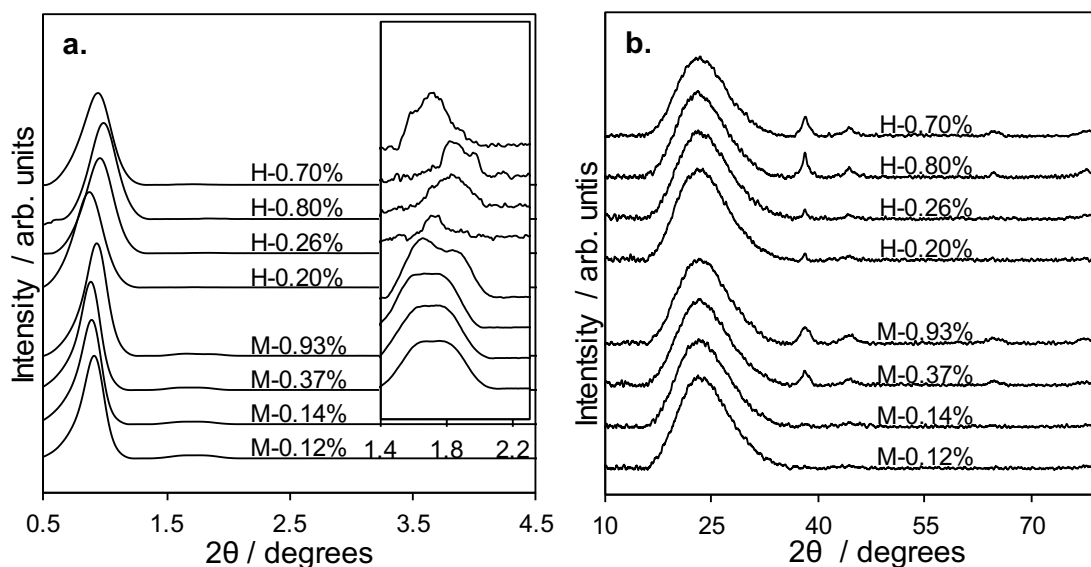
In the literature, it has been determined that increasing gold content causes an increase in particle size distribution spread, and therefore average particle size.¹² It was determined that another method should be used to study particle size, without changing the support properties as seen in **Section 4.2.3.1**. As with the MgO loading study (**Appendix 3c**), it was unlikely changing one variable would not affect other material properties, however, it is useful in determining if loading will affect the activity in a linear fashion.

ICP-OES analysis was run on the mesoporous and hierarchical materials with varied gold loadings displayed in **Appendix Figure 3d.1**, giving a linear trend suggesting the synthesis was successful. All materials exhibited gold loadings slightly lower than the nominal, apart from the hierarchical nominally 0.5% loading material. This was attributed to an experimental error in the gold impregnation.



Appendix Figure 3d.1. ICP-OES gold loadings for mesoporous and hierarchical Au@MgO/SBA-15 materials.

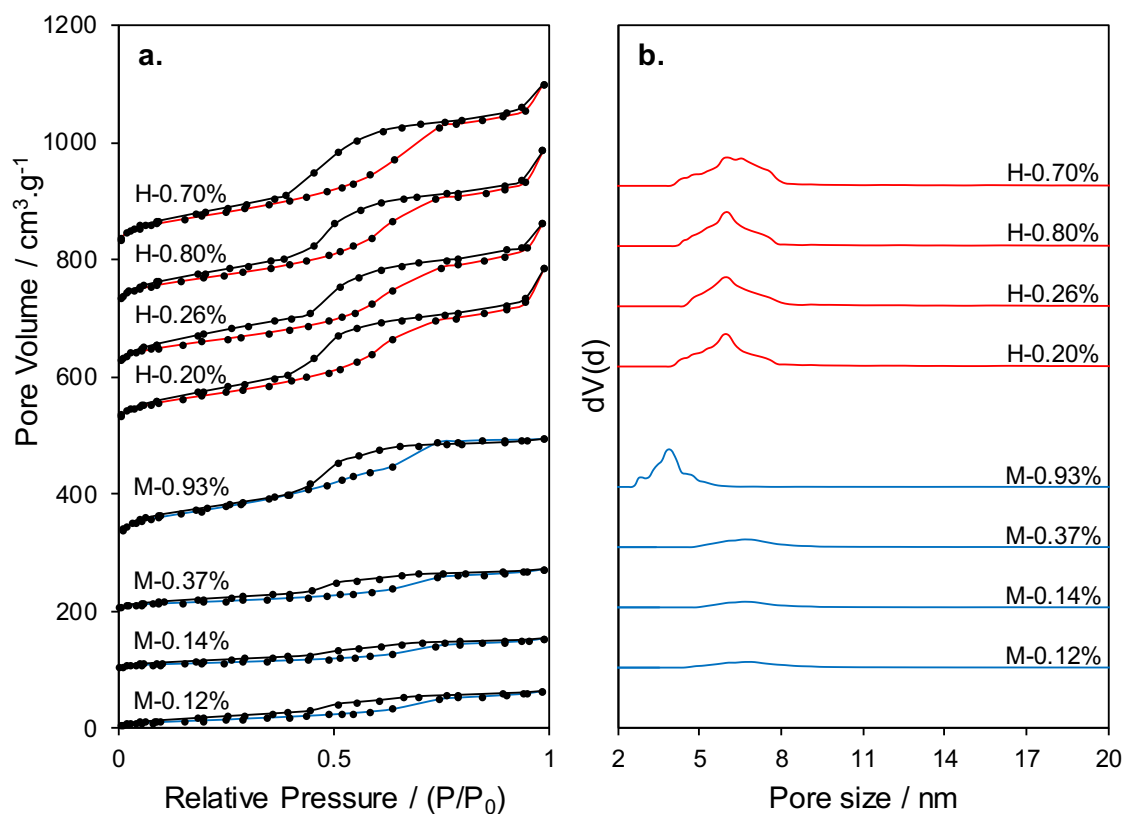
In **Appendix Figure 3d.2a**, low-angle X-ray diffractometry demonstrated long-range ordered mesoporosity had been achieved for both mesoporous and hierarchical materials. The 11 and 20 reflections were more defined for the mesoporous material which is discussed in **Chapter 3.2.2.2**. Mesoporous materials gave no real change in the inter pore distance as seen previously, and the hierarchical material reflections were not well defined enough to offer values.



Appendix Figure 3d.2. The (a) low-angle and (b) wide-angle X-ray diffraction patterns of mesoporous and hierarchical Au@MgO/SBA-15 materials, with varied gold loadings notated by their weight percent.

Wide-angle X-ray diffractometry displayed two features; an amorphous silica hump from the SBA-15 pore framework, and minor Au reflections which increased in intensity with gold loading. No MgO reflections were observed, however, this corroborated the data from the previous chapter. As discussed previously, due to the poor signal to noise ratio and a large proportion of gold species below the limit of detection, the particle size could not be accurately determined from this dataset using the Scherrer equation.

Nitrogen porosimetry displayed in **Appendix Figure 3d.3a** revealed that the mesoporous materials derived from the parent support exhibited a different isotherm to the material from **Section 4.2.3.1**. While the presence of a type IV isotherm indicated a successful synthesis of an ordered mesoporous material, there were discrepancies in the support synthesis. Pore size distribution was also poorly defined for these materials (**Appendix Figure 3d.3b**) and also displayed a larger pore size, possibly due to pore destruction. In addition, they exhibited a surface area approximately five times smaller than expected, displayed in **Appendix table 3d.1**. This indicated an error in the MgO/SBA-15 support synthesis, as seen previously in the Mg loading study (**Appendix 3c**). No micropore contribution was observed, indicating the TLCT synthesis was drastically reducing the micropore area.



Appendix Figure 3d.3. Nitrogen porosimetry (a) isotherms and (b) pore size distributions for Au@MgO/SBA-15 materials with varied gold loadings.

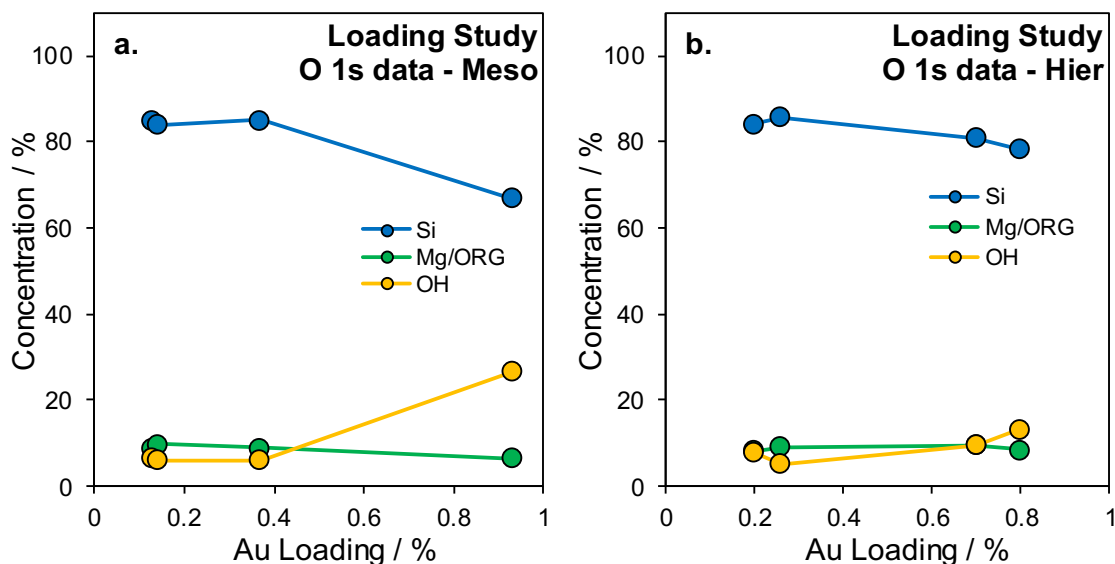
Appendix Table 3d.1. Surface area and microporous area determined by BET and T-plot functions for nitrogen porosimetry data for mesoporous and hierarchical Au@MgO/SBA-15 materials with varied gold loading.

Nominal Au Loading / %	Surface Area / m ² .g ⁻¹		Micropore Area / m ² .g ⁻¹	
	Meso	Hier	Meso	Hier
0.13	46.9	244.1	0.0	0.0
0.25	38.6	216.7	0.0	0.0
0.50	55.2	246.8	0.0	0.0
1.00	258.2	268.8	0.0	0.0

The O 1s spectra displayed 3 peaks at 530.4, 532.5 and 534.4 eV which correspond to MgO and organic contaminants, SiO₂ and hydroxyl species bound to the silica surface, respectively.

Both mesoporous and hierarchical material exhibited no real change in feature binding energy or relative intensity displayed in **Appendix Figure 3d.4**, with the exception of the

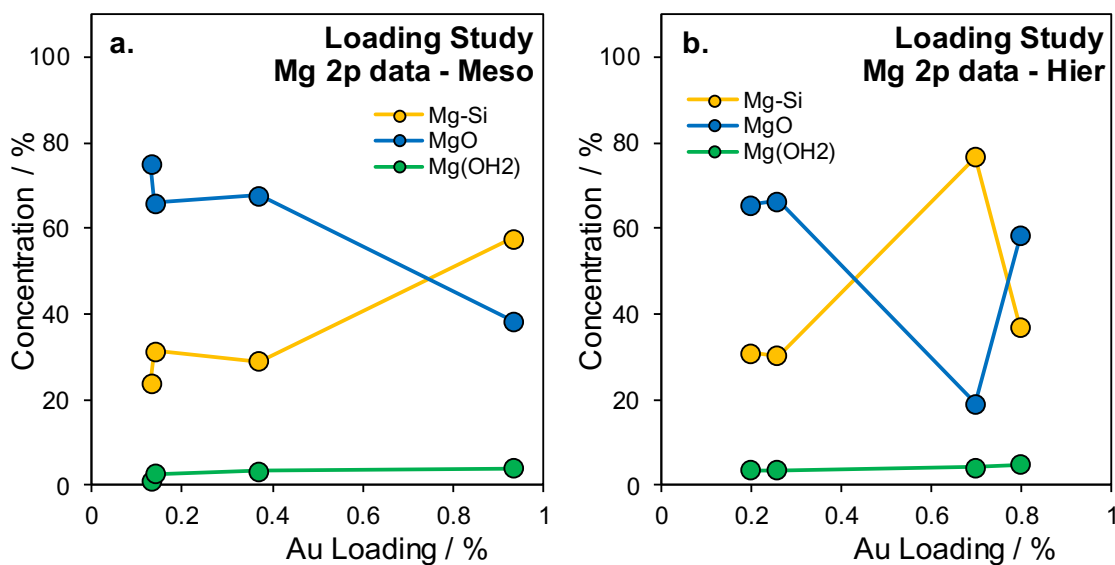
highest loaded mesoporous material. The majority of materials followed this trend as the only variable separating them was Au loading, therefore the oxides remained constant. The larger hydroxide component displayed by the M-0.93% was possibly caused by an increased surface area, differing from the other mesoporous samples due to an error in the synthesis.



Appendix Figure 3d.4. O 1s relative component concentration as a function of Au Loading for (a) mesoporous and (b) hierarchical materials with varied gold loadings.

The Mg 2p spectra displayed 3 doublet peaks at 49.1, 50.1 and 51.0 eV which correspond to $\text{Mg}(\text{OH})_2$, MgO and Mg-O-Si, respectively, with their relative component concentrations displayed in **Appendix Figure 3d.5**.

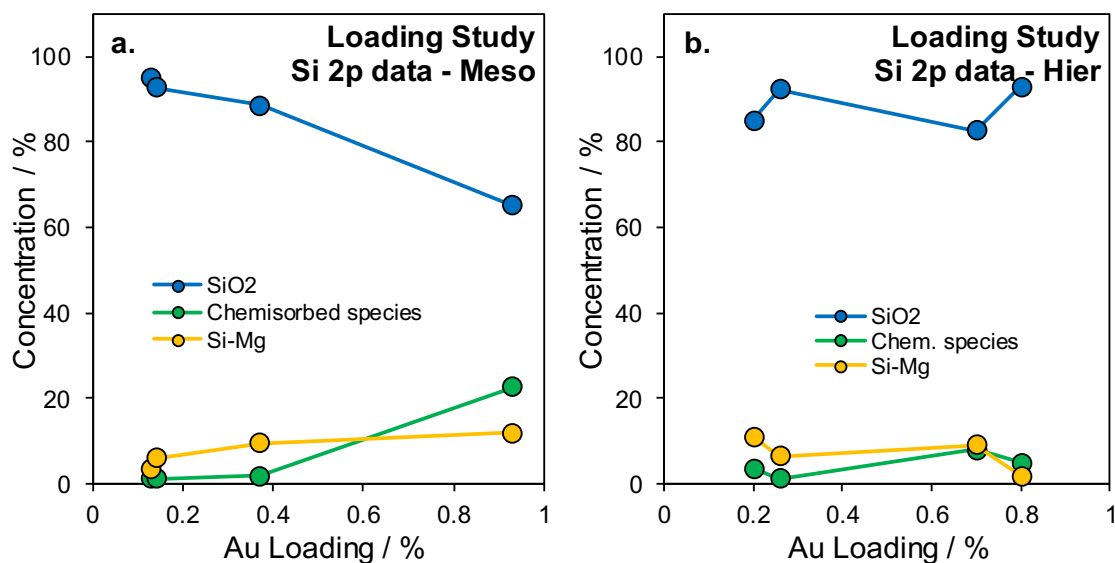
A shift was observed for the H.70% and M.93% materials to higher binding energy in the Mg 2p spectra, which was attributed to a shift to the MgO feature. However, it is worth noting that these samples were created in a previous batch. A potential explanation is the irreproducibility of the synthesis, which has been seen multiple times when evaluating the magnesium and gold variable loading studies.



Appendix Figure 3d.5. Mg 2p relative component concentration as a function of Au Loading for (a) mesoporous and (b) hierarchical materials with varied gold loadings.

As seen with the heat treatment study, basicity study and parent support Si 2p spectra in the previous chapter, there are three components at 101.9, 103.2 and 105.2 eV which correspond to Si-O-Mg and organic contaminants, SiO₂ and chemisorbed species bound to the silica surface respectively.

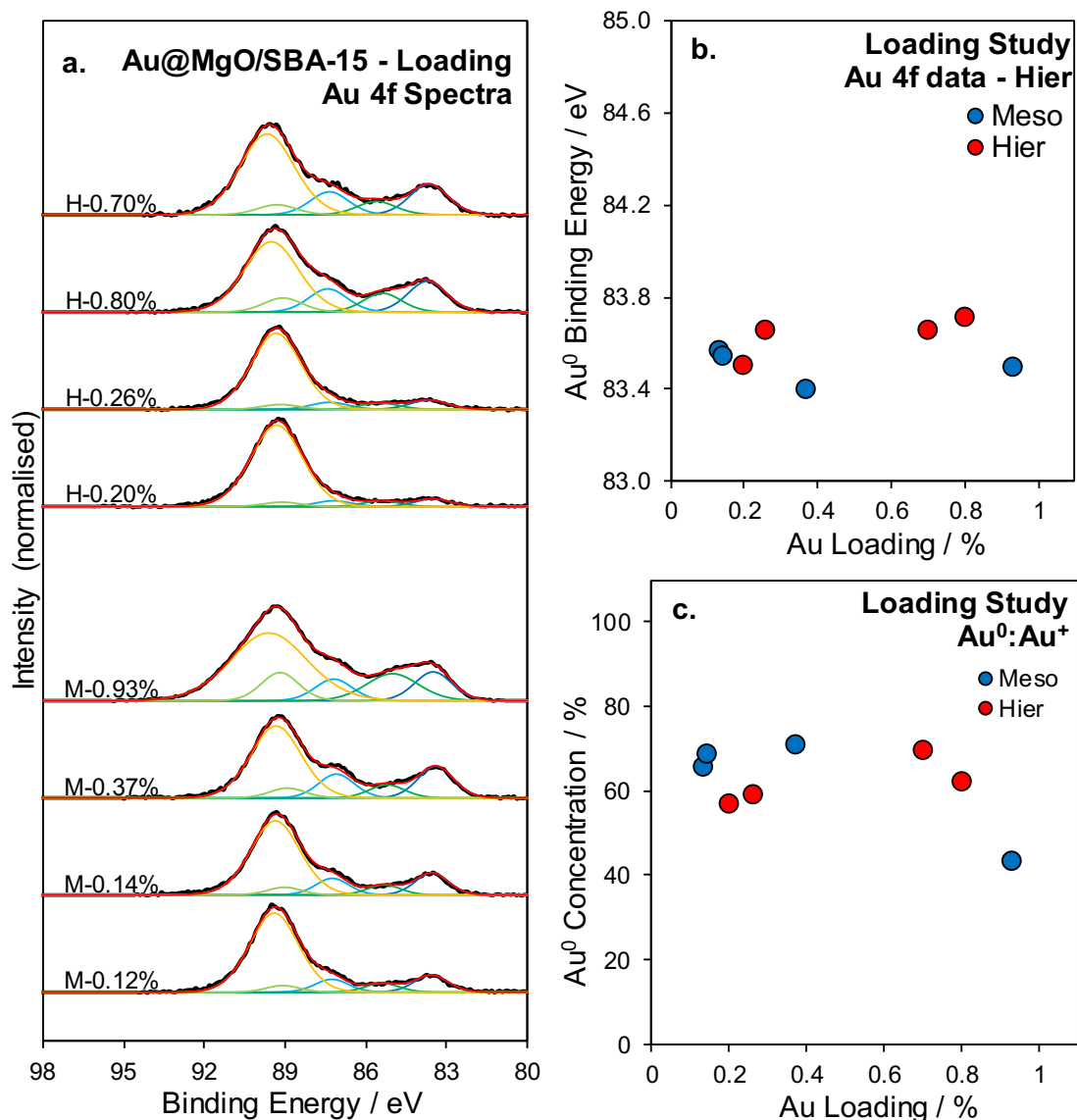
There was no real change in the Si-O-Mg feature displayed in **Appendix Figure 3d.6** suggesting the MgO coating remained constant throughout both sets of materials. The highest loaded mesoporous materials contained a significant proportion of chemisorbed species, potentially suggesting the sample was exposed to excess atmospheric poisoning. This makes sense as the material was synthesised in a previous batch to the other samples.



Appendix Figure 3d.6. Si 2p relative component concentration as a function of Au Loading for (a) mesoporous and (b) hierarchical materials with varied gold loadings.

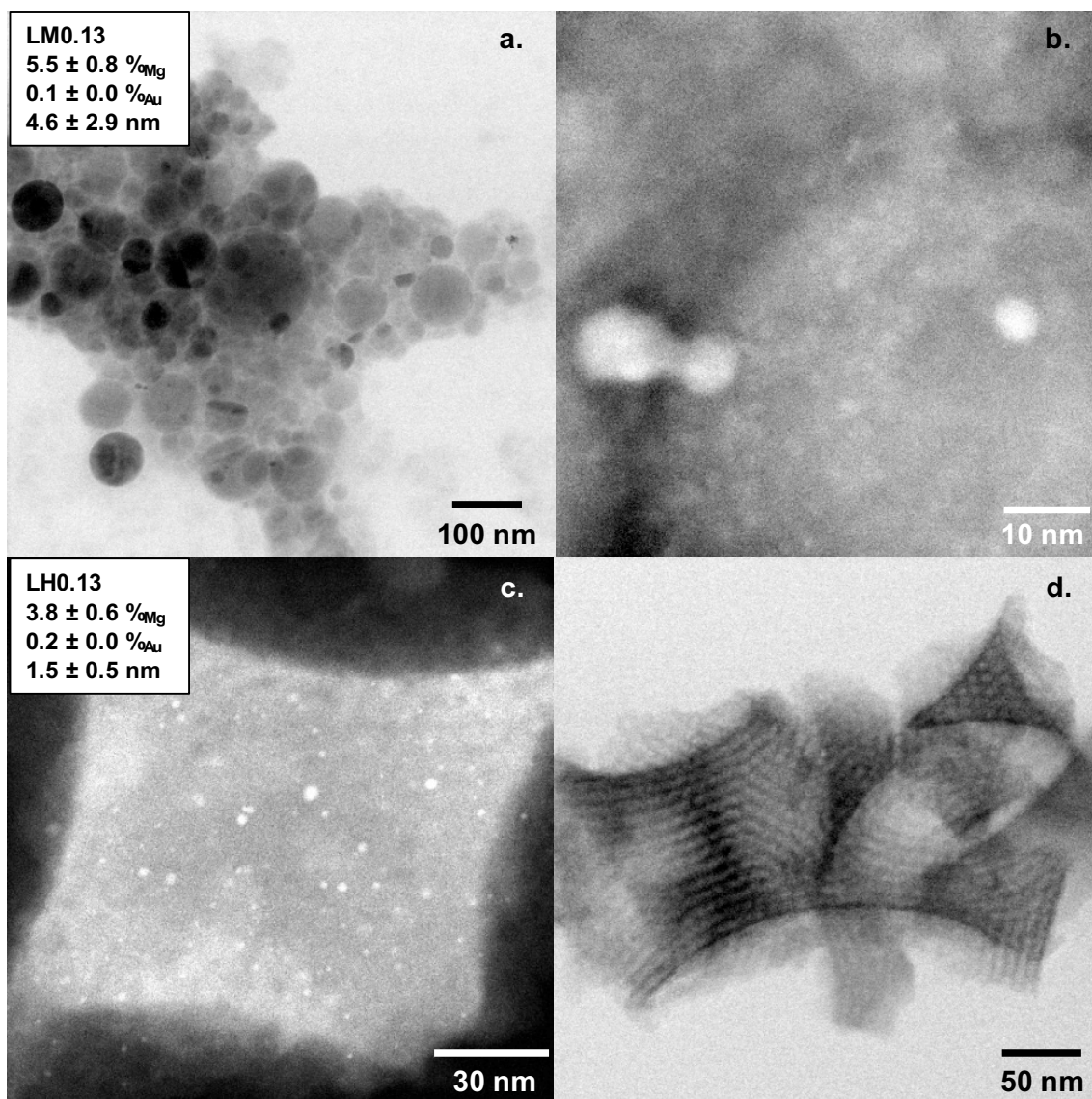
As seen in the heat treatment study Au 4f spectra, **Appendix Figure 3d.7** displayed 3 peaks displayed, two doublet peaks at approximately 84 and 86 eV which correspond to metallic (Au^0) and cationic gold (Au^+) and the single MgO peak at 90 eV.

Relative to the Mg 2s feature, the Au metallic and cationic features increased with loading. The $\text{Au}^{0/2}$ binding energy remained constant at approximately 83.6 eV, suggesting the basicity of the material remained unchanged, as expected. The ratio between metallic and cationic gold also remained relatively constant, with the exception of the highest loaded mesoporous material. This suggests the makeup of sites was remaining constant regardless of the gold loading.

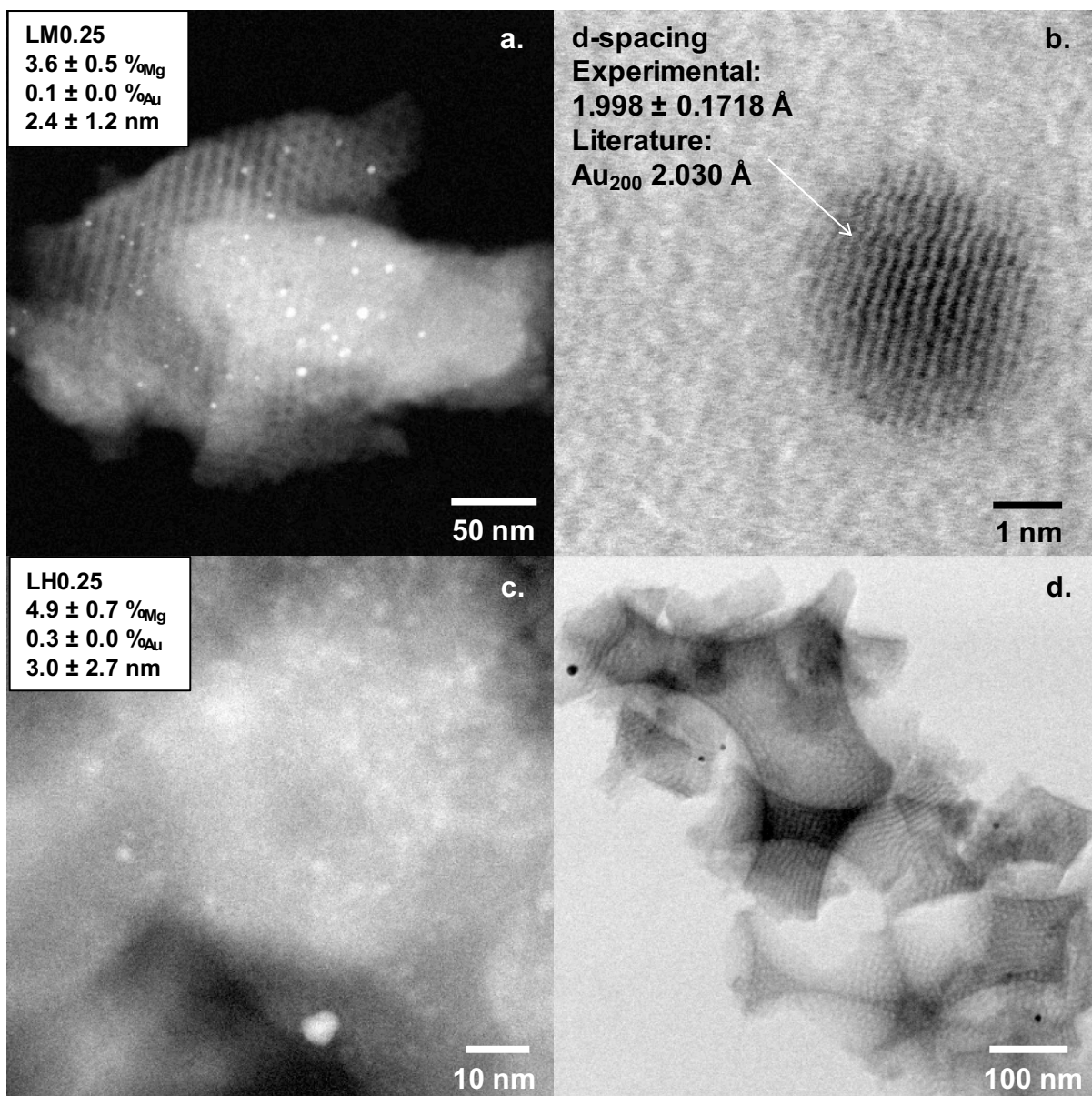


Appendix Figure 3d.7. Au 4f X-ray photoelectron (a) spectra and (b) Au⁰ binding energy and (c) Au⁰:Au⁺ ratio for mesoporous and hierarchical materials with varied gold loadings.

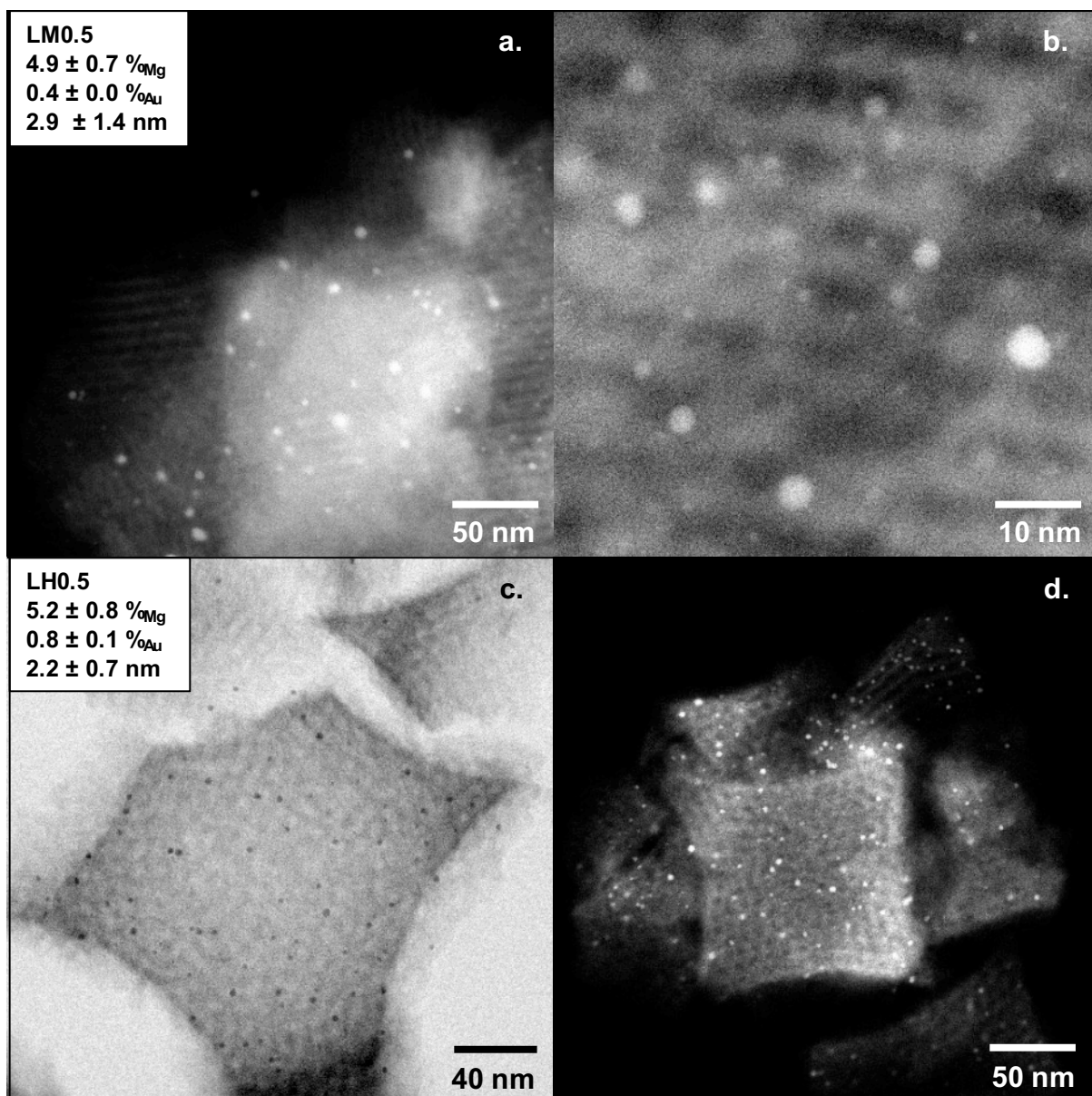
TEM analysis, displayed in **Appendix Figures 3d.8-10**, confirmed the successful synthesis of SBA-15, corroborating XRD, and N₂ porosimetry measurements. The difference in physical characteristics observed in the mesoporous materials, especially prevalent in the nitrogen porosimetry data, was also observed in the TEM. Microscopy of the low surface area materials confirmed they had an abnormal structure, especially seen in **Appendix Figure 3d.8a**.



Appendix Figure 3d.8. TEM micrographs for (a,b) mesoporous and (c,d) hierarchical Au@MgO/SBA-15 materials with 0.13% nominal gold loadings.



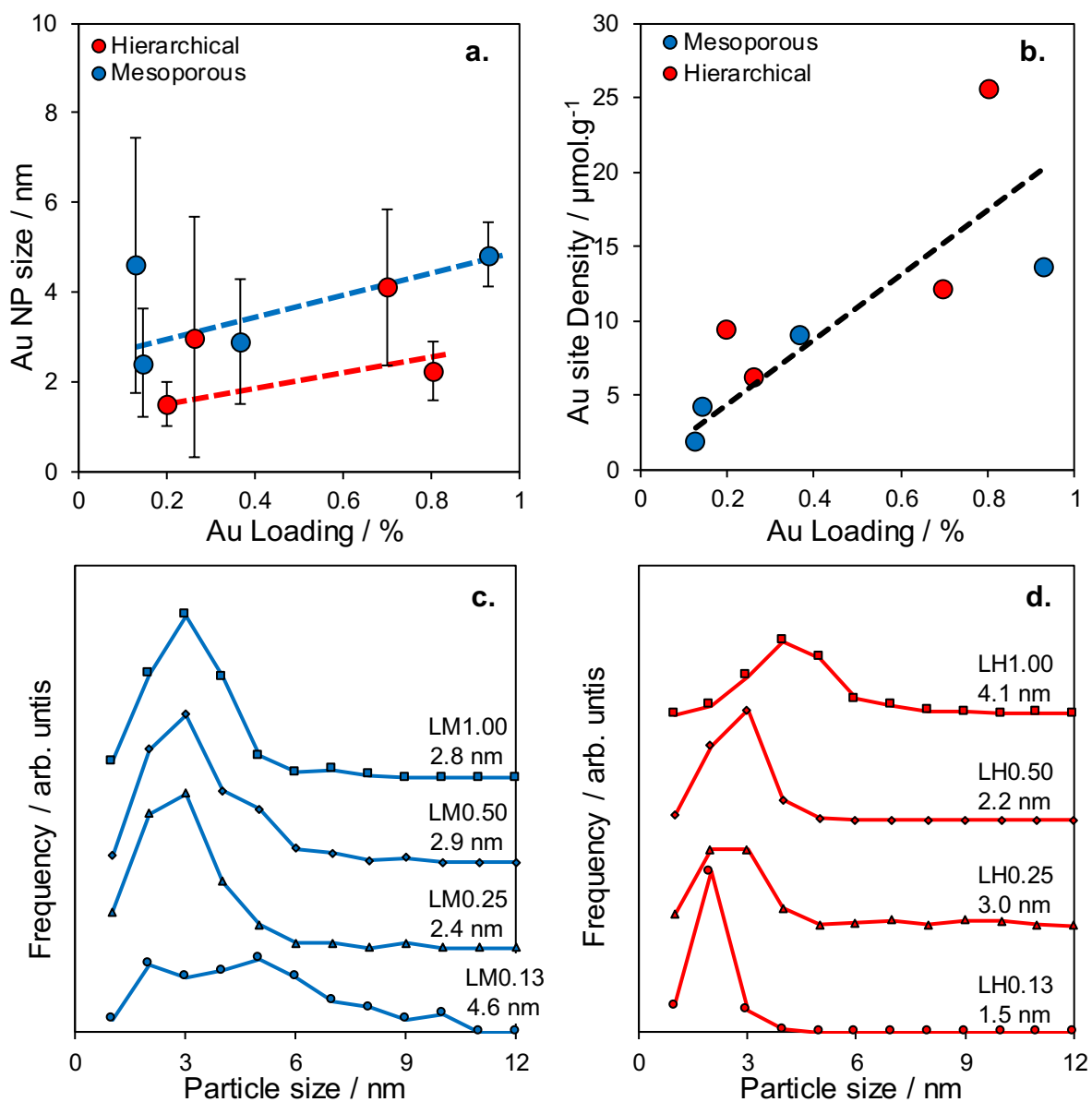
Appendix Figure 3d.9. TEM micrographs for (a,b) mesoporous and (c,d) hierarchical Au@MgO/SBA-15 materials with 0.25% nominal gold loadings.



Appendix Figure 3d.10. TEM micrographs for (a,b) mesoporous and (c,d) hierarchical Au@MgO/SBA-15 materials with 0.5% nominal gold loadings.

While TEM did show they contain ordered long mesoporous channels, it also showed large silica particles, instead of the larger support particles typically seen. Apart from the LM.13 material, particle size distribution remained relatively narrow (**Appendix Figure 3d.11**), suggesting the impregnation method was reproducible. This further suggests the error observed in the synthesis was in the first synthesis step of the parent material. There appeared to be no real trend regarding NP size and loading for mesoporous materials, however, hierarchical materials did exhibit a small increase in particle size distribution (**Appendix Figure 3d.11d**), when considering nominal loading, however with respect to actual gold loading, there was no visible trend.

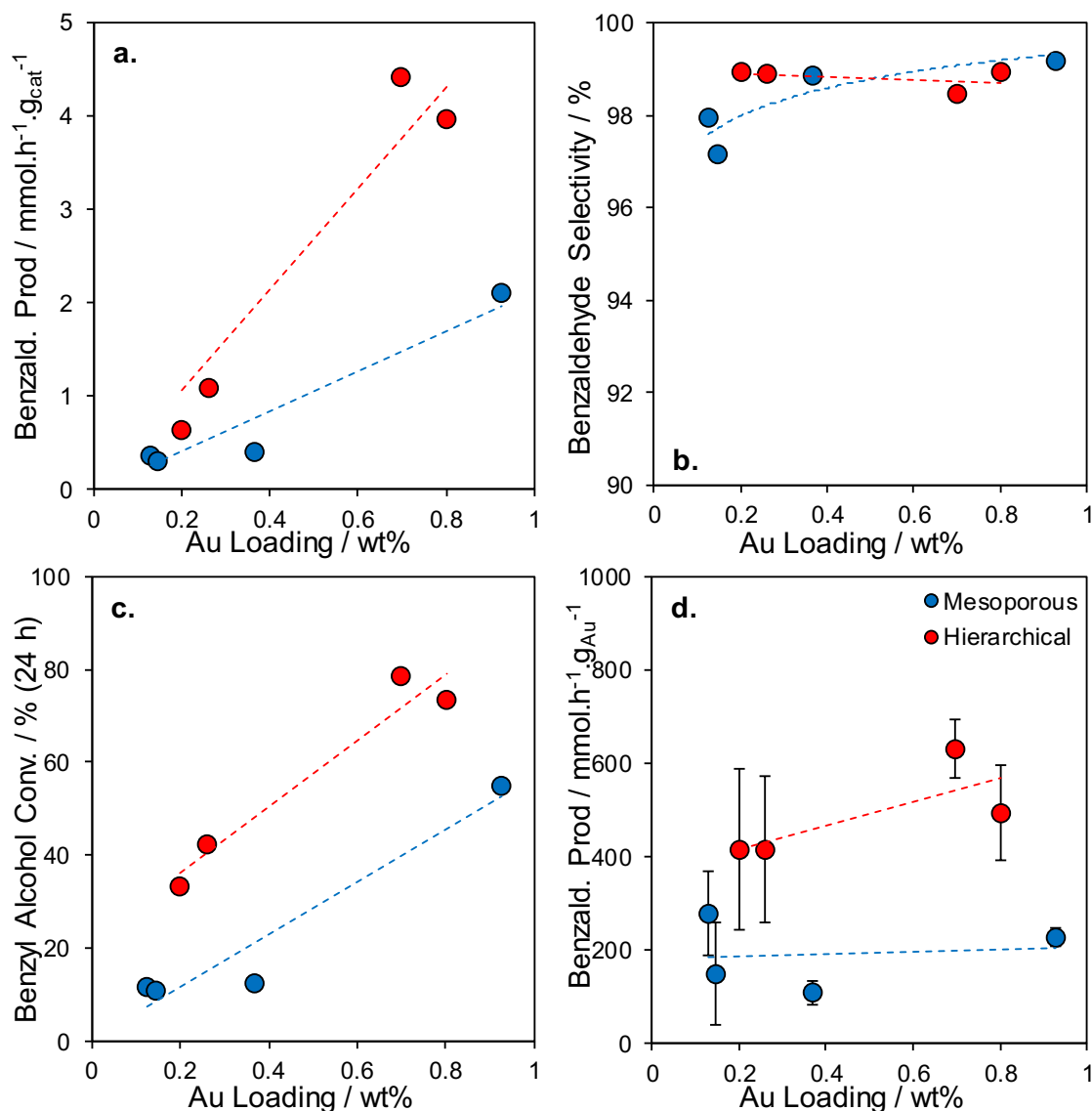
A trend was observed however when considering the approximated site density vs. Au loading. This suggests that when using the particle size and loading to calculate an approximate density, the apparently randomized particle size is normalised. This could indicate that Au loading had no observable effect on particle size, resulting in a linear positive correlation between the number of sites and the amount of gold.



Appendix Figure 3d.11. (a) Average particle size, (b) site density and particle size distributions for (c) mesoporous and (b) hierarchical materials with varied gold loadings.

Screening of materials using the selective oxidation of benzyl alcohol, shown in **Appendix Figure 3d.12**, resulted in a linear trend for both materials for both substrate final conversion and product formation rate respective of gold loading. Selectivity determined after 24 hours for all materials is above 97 %, with the remaining detected

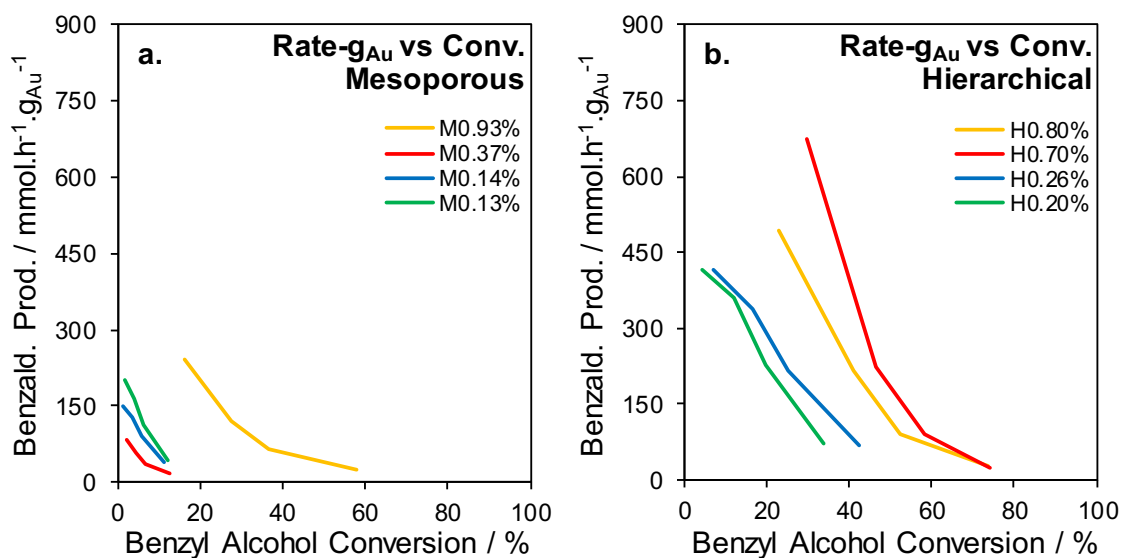
product being the coupling ester product. The rate was further normalised to gold mass within the reaction, resulting in a plateau trend within error.



Appendix Figure 3d.12. Screening data for the selective oxidation of benzyl alcohol, using mesoporous and hierarchical gold functionalised SBA-15 materials containing varying loadings of gold oxide. Selective product (a) productivity and (b) selectivity, final substrate conversion after (c) 24 hours and (d) Au mass normalised benzaldehyde rate.

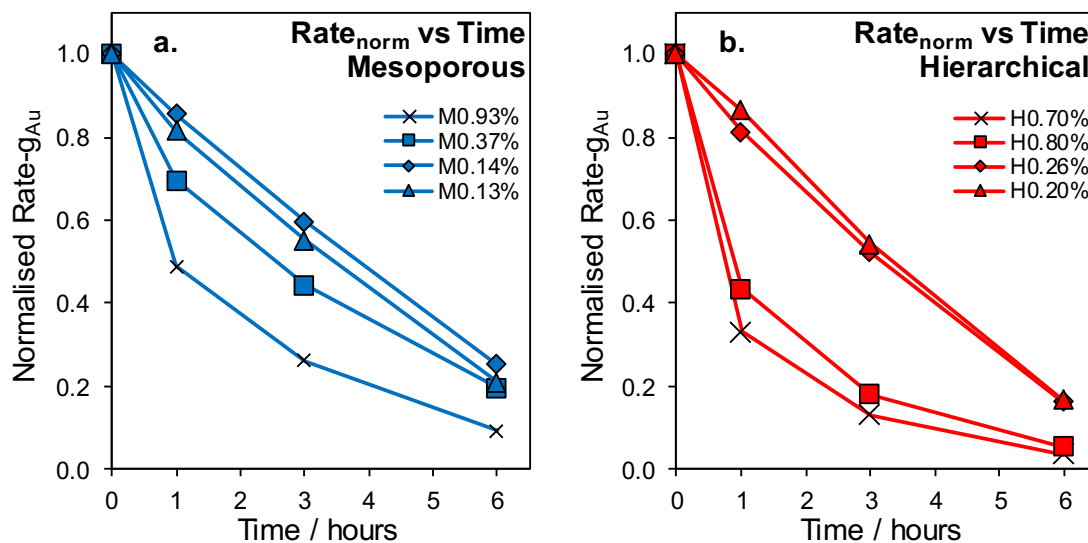
When examining the rate as a function of substrate conversion in **Appendix Figure 3d.13**, it is clear that the higher loaded materials performed better for both materials. To better compare the materials, the rate was normalised to gold mass in the reaction. Deactivation was observed at the same approximate rate for all materials, suggesting the MgO content may play a large role in this, as seen in the basicity study.

The deactivation slope became more similar between all materials, especially seen in the hierarchical materials. The mesoporous materials still exhibited a difference in plot shape and rate, however, this can be attributed to the difference in support formation. As the grouping of data has become smaller, this could suggest gold loading plays a significant role in determining activity, rather than particle size.



Appendix Figure 3d.13. Gold content normalised rate versus substrate conversion for (a) mesoporous and (b) hierarchical Au@MgO/SBA-15 materials with varied gold content.

To better compare the rates of deactivation, the gold mass normalised rates were further normalised, resulting in the true normalised rate observed in **Appendix Figure 3d.14**. Flat deactivation plots were seen at lower loadings, along with the curved plots seen in previous studies (**Section 4.2.3.2 and Appendix 3c**). This may suggest that the rate loss was linear below a specific initial activity.



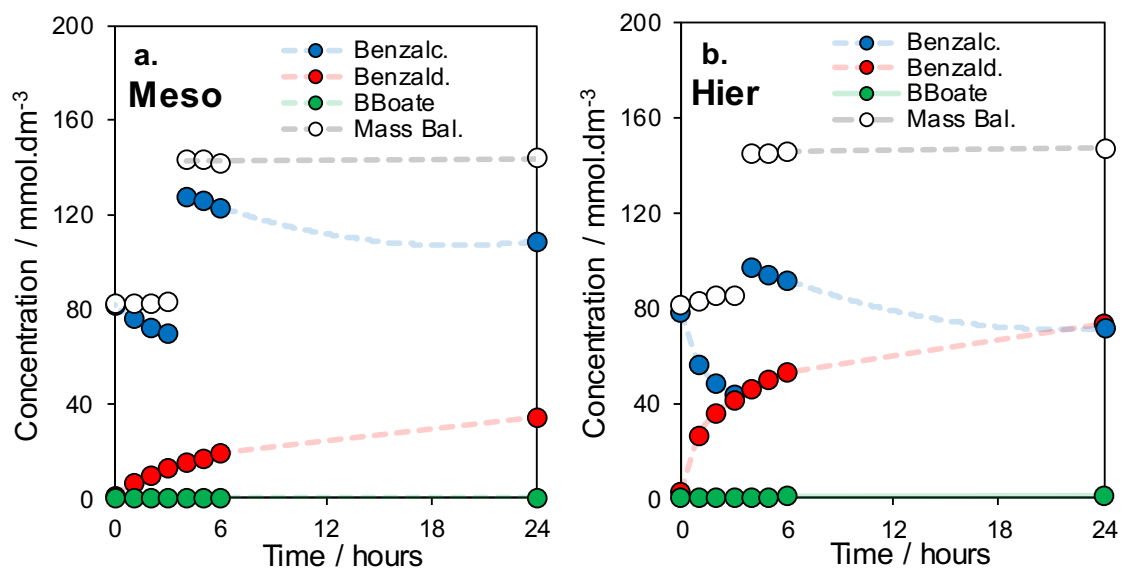
Appendix Figure 3d.14. Gold content normalised Au-rate versus time for (a) mesoporous and (b) hierarchical Au@MgO/SBA-15 materials with varied gold content.

This study was undertaken to alter nanoparticle size without changing the parent support. Unfortunately, this was not possible with the methodology used, resulting in no observable trend between particle sizes and loading. Characterisation data confirmed successful synthesis for most materials however, as with the **Appendix 3c** study, identified materials with defective physical properties. All defective samples resulted from the same parent support, which suggests the irreproducible synthesis step is the production of the MgO/SBA-15.

Catalytic screening exhibited linear trends when comparing final conversion and initial product formation rate against loading, however when normalised to gold content the initial rate plateaued. The normalised rate profiles of the initially faster materials suggested a very rapid initial production of an inhibiting product, causing rapid deactivation. As a greater proportion of sites were deactivated, the activity decreased producing less of the inhibiting product. This slowdown was evident with all normalised rate profiles observed thus far, with the MgO functionality decreasing this deactivation but not stopping it entirely.

The screening data paired with the non-correlated particle size concluded that varying the Au loading had no effect on the particle size, but simply produced more of the monodisperse 2-4 nm Au NPs, resulting in a linear correlation between activity and loading. This disagrees with the literature, however, the synthesis technique in these studies has consistently produced particles with a broader distribution than seen here.

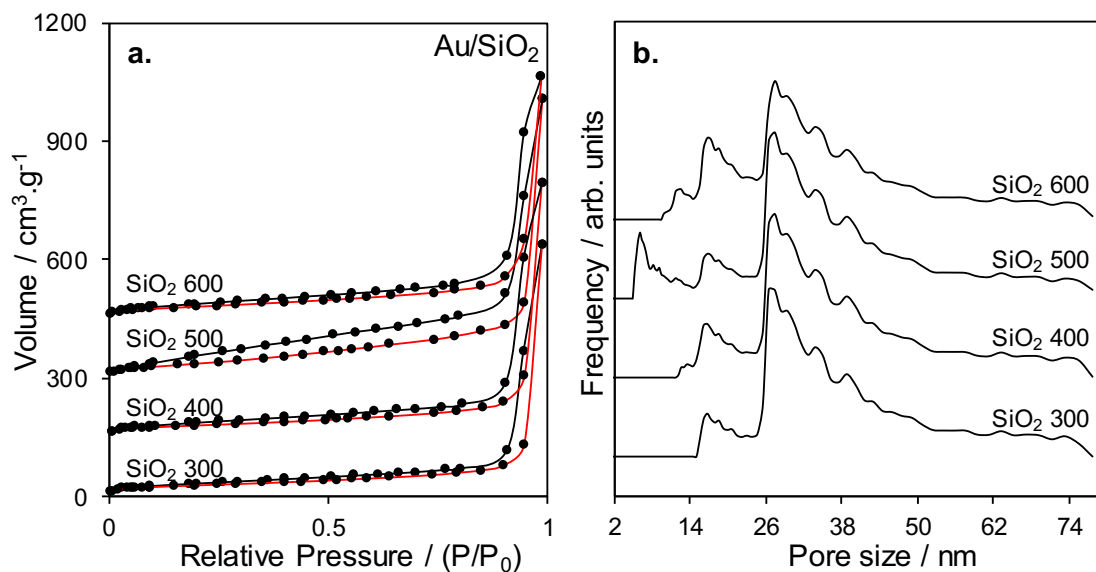
Appendix 3e: Deactivation Study Appendix



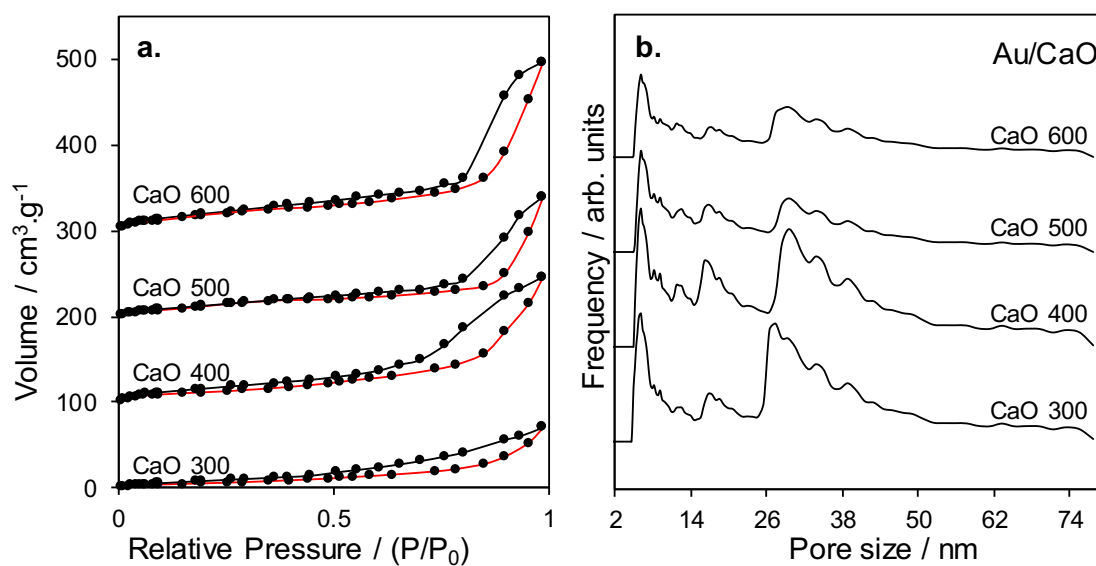
Appendix Figure 3e.1. Reaction profiles for (a) mesoporous and (b) hierarchical when 1 mmol of the substrate is added partway through the reaction.

Appendix 4 for Chapter 5

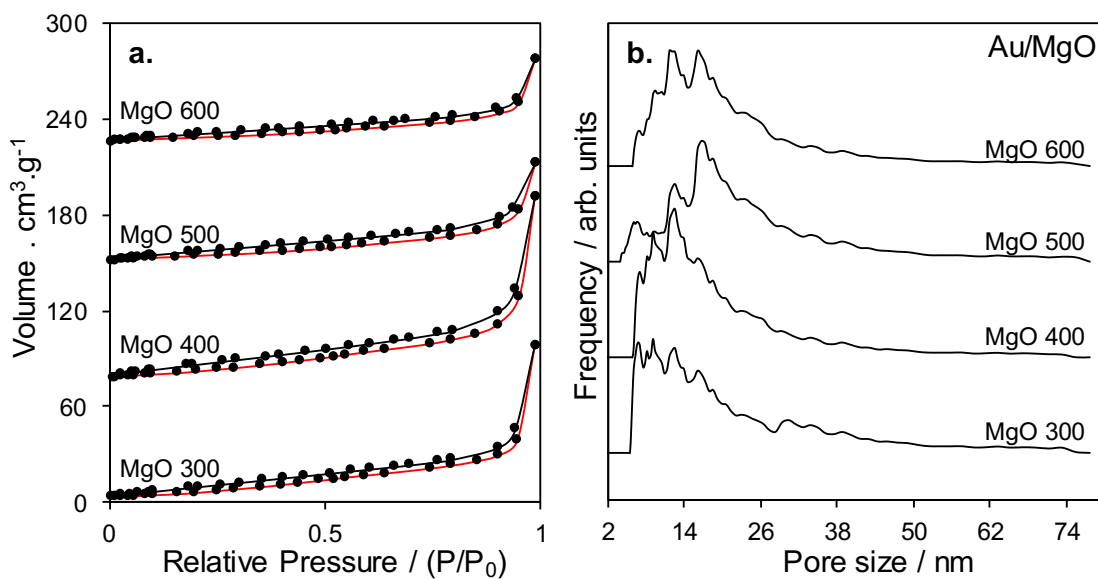
Appendix 4a: Characterisation



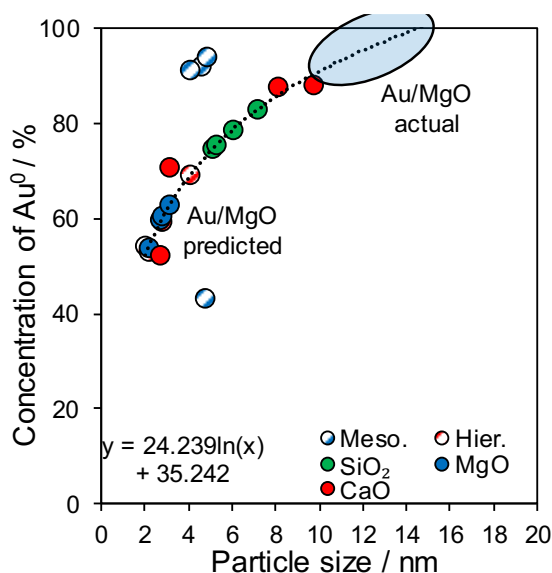
Appendix Figure 4a.1. (a) Nitrogen porosimetry isotherms and (b) pore size distributions for Au/SiO₂ heat-treated to different temperatures.



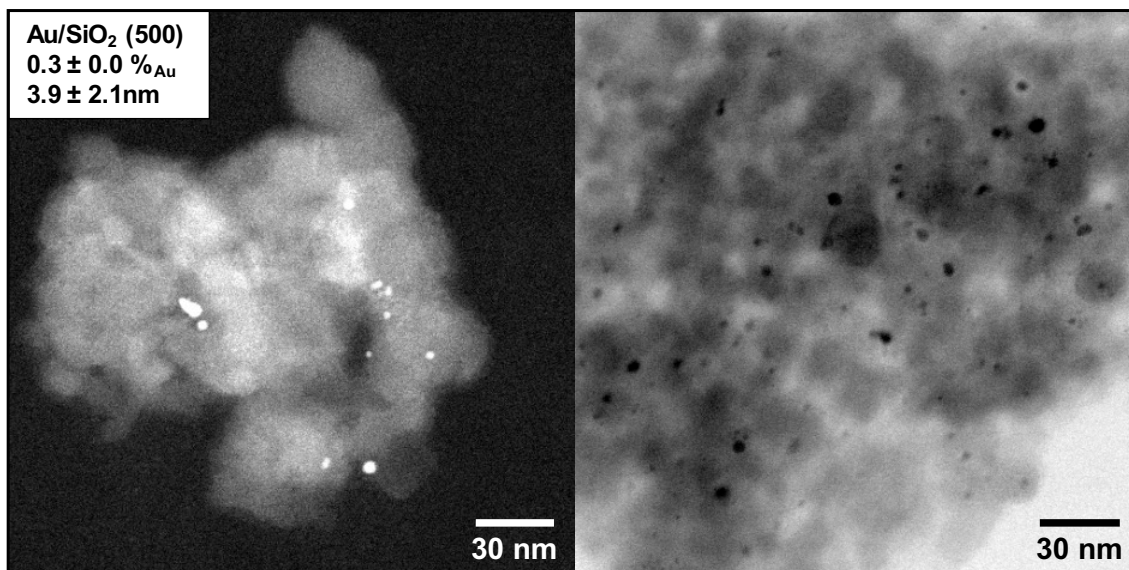
Appendix Figure 4a.2. (a) Nitrogen porosimetry isotherms and (b) pore size distributions for Au/MgO heat-treated to different temperatures.



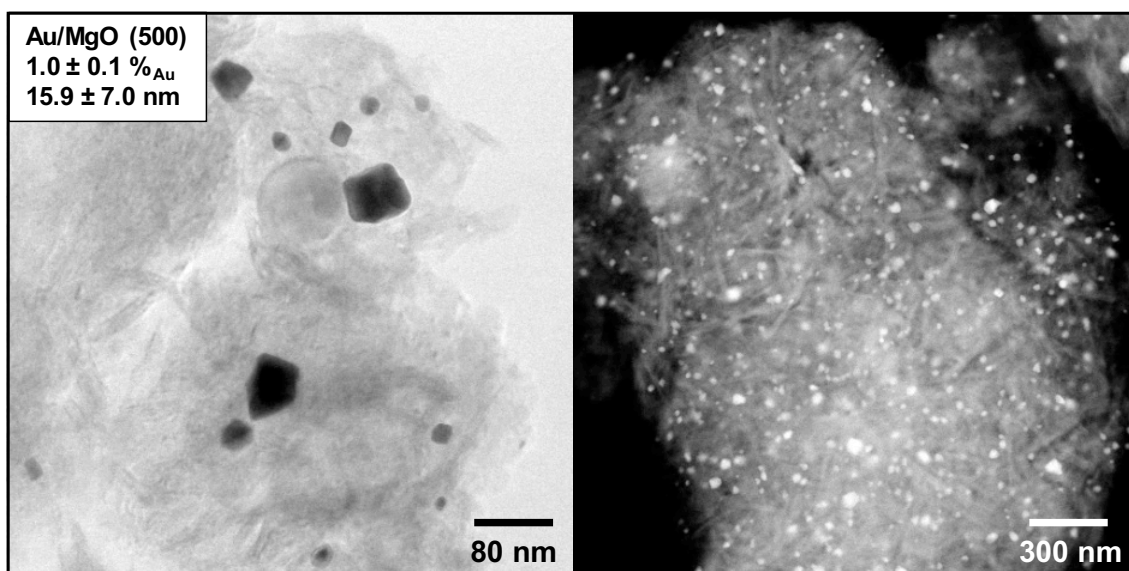
Appendix Figure 4a.3. (a) Nitrogen porosimetry isotherms and (b) pore size distributions for Au/CaO heat-treated to different temperatures.



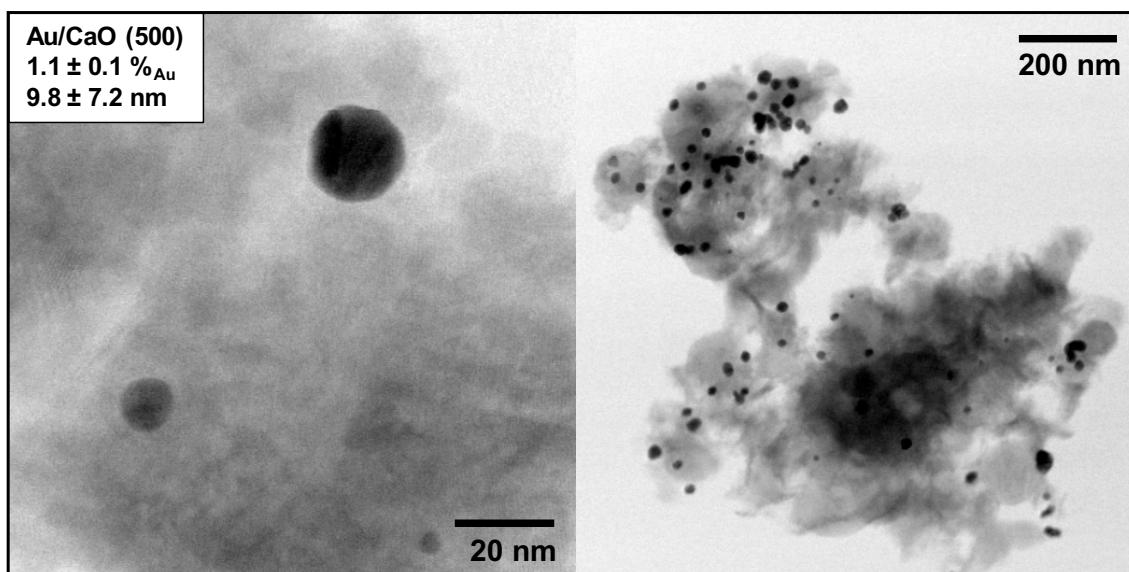
Appendix Figure 4a.4. Extrapolation of particle size using gold metallic to gold cationic species ratio calculated using XPS.



Appendix Figure 4a.5. Transmission electron micrographs of Au/SiO₂ heat-treated at 500 °C.

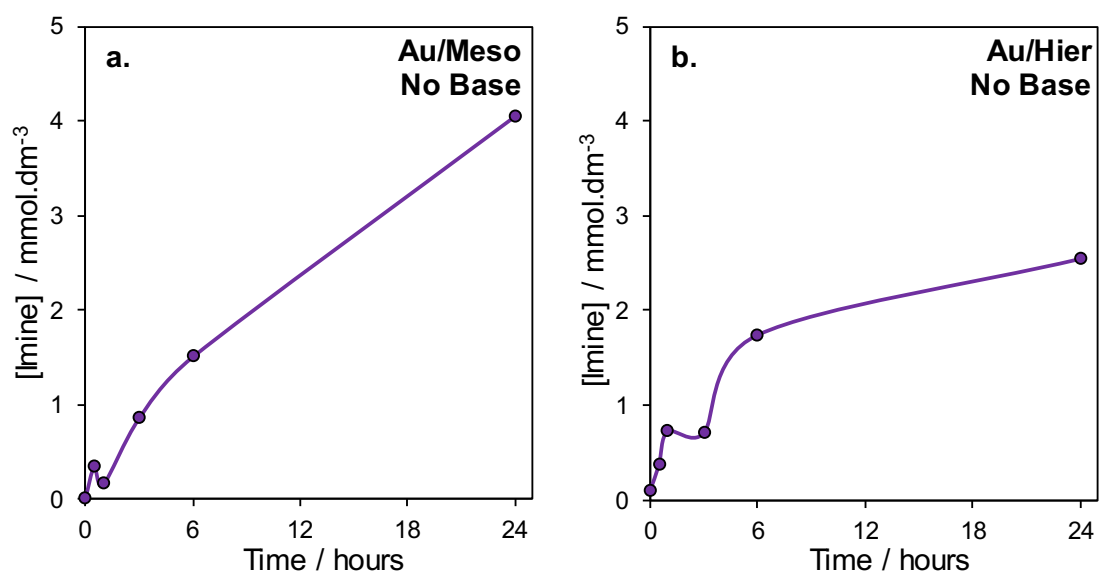


Appendix Figure 4a.6. Transmission electron micrographs of Au/MgO heat-treated to 500 °C.

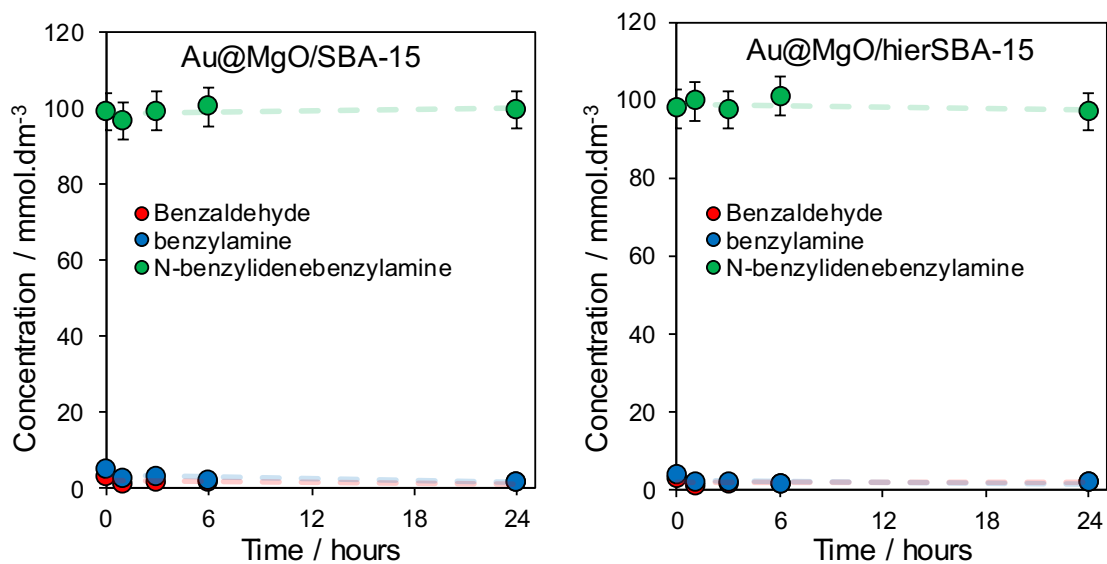


Appendix Figure 4a.7. Transmission electron micrographs of Au/CaO heat-treated to 500 °C.

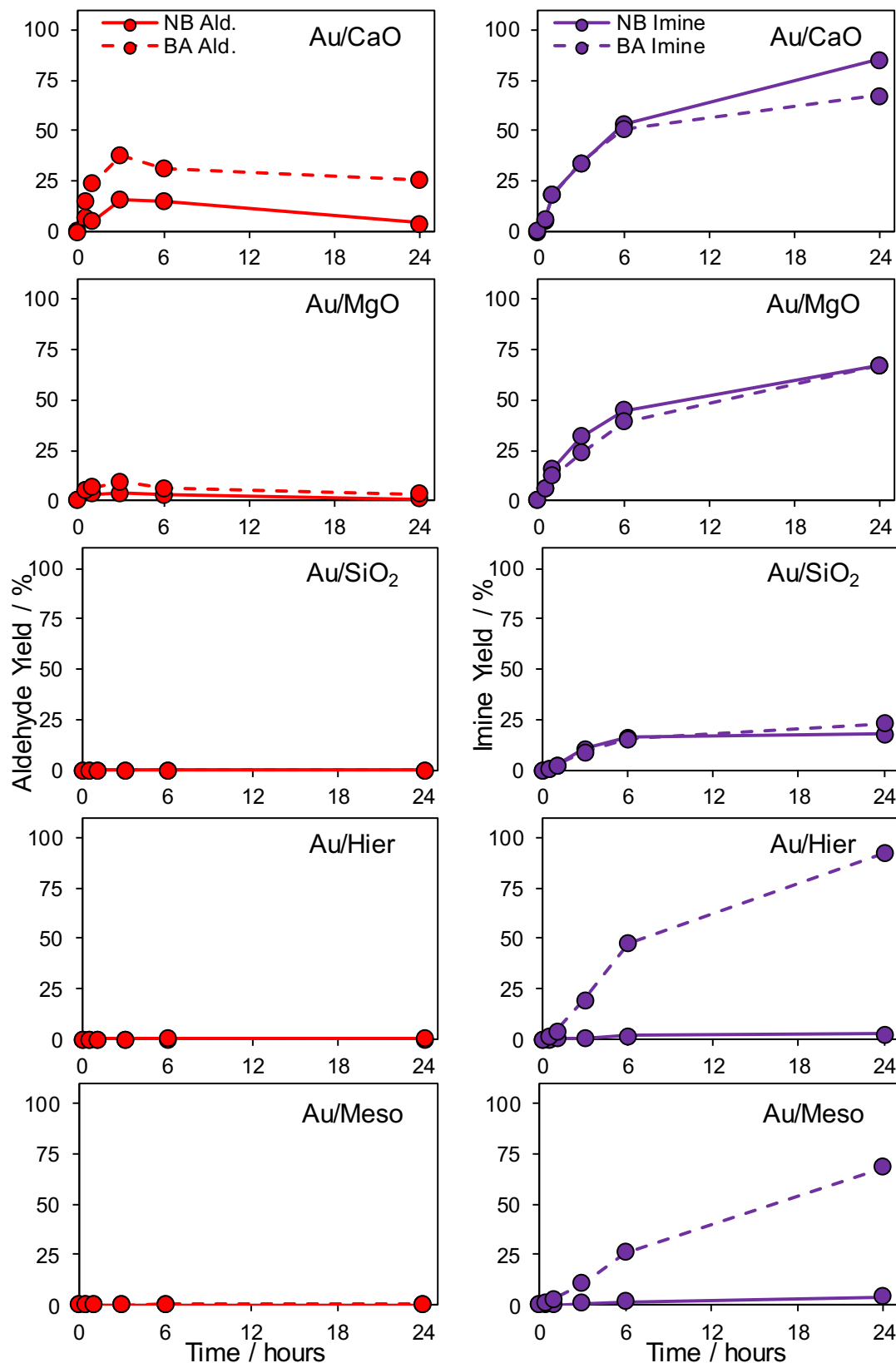
Appendix 4b: Oxidative Coupling



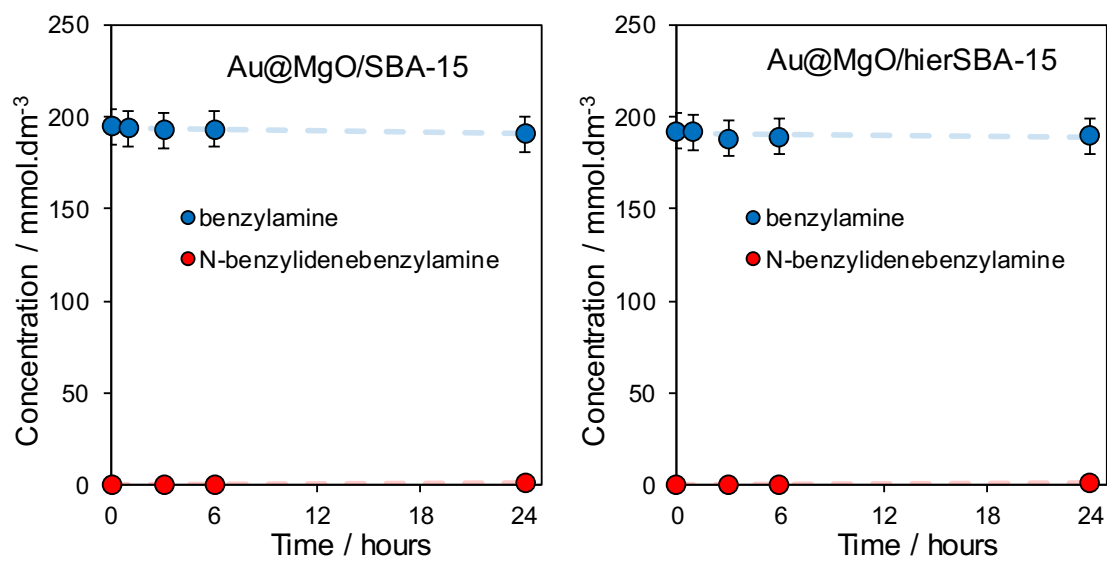
Appendix Figure 4b.1. Imine concentration as a function of time for (a) mesoporous and (b) hierarchical catalysts without the added base.



Appendix Figure 4b.2. The preliminary reaction between benzaldehyde and benzylamine.



Appendix Figure 4b.3. Benzaldehyde (left) and N-benzylidenebenzylamine (right) yield as a function of time for selected catalyst in the absence (NB – no base) and presence (BA – base added) of potassium carbonate.



Appendix Figure 4b.4. Preliminary homocoupling reaction of benzylamine.

Appendix References

1. L. She, J. Li, Y. Wan, X. Yao, B. Tu and D. Zhao, Synthesis of ordered mesoporous MgO/carbon composites by a one-pot assembly of amphiphilic triblock copolymers, *Journal of Materials Chemistry*, 2011, **21**, 795-800.
2. T. Selvamani, A. Sinhamahapatra, D. Bhattacharjya and I. Mukhopadhyay, Rectangular MgO microsheets with strong catalytic activity, *Materials Chemistry and Physics*, 2011, **129**, 853-861.
3. J. I. Di Cosimo, V. K. Díez, C. Ferretti and C. R. Apesteguía, Catalysis, The Royal Society of Chemistry, 2014, **26**, 1-28.
4. X. Fu, N. Zhao, J. Li, F. Xiao, W. Wei and Y. Sun, Carbon dioxide capture by MgO-modified MCM-41 Materials, *Adsorption Science & Technology*, 2009, **27**, 593-601.
5. Y. Song, J. K. Mobley, A. H. Motagamwala, M. Isaacs, J. A. Dumesic, J. Ralph, A. F. Lee, K. Wilson and M. Crocker, Gold-catalyzed conversion of lignin to low molecular weight aromatics, *Chemical Science*, 2018, **9**, 8127-8133.
6. E. Skupien, J. R. Berger, P. V. Santos, J. Gascon, M. Makkee, T. M. Kreutzer, J. P. Kooyman, A. J. Moulijn and F. Kapteijn, Inhibition of a gold-based catalyst in benzyl alcohol oxidation: understanding and remediation, *Catalysts*, 2014, **4**.
7. S. K. Klitgaard, A. T. DeLa Riva, S. Helveg, R. M. Werchmeister and C. H. Christensen, Aerobic oxidation of alcohols over gold catalysts: role of acid and base, *Catalysis Letters*, 2008, **126**, 213-217.
8. C. P. Ferraz, M. A. S. Garcia, É. Teixeira-Neto and L. M. Rossi, Oxidation of benzyl alcohol catalyzed by gold nanoparticles under alkaline conditions: weak vs. strong bases, *RSC Advances*, 2016, **6**, 25279-25285.
9. A. Kumar, V. P. Kumar, A. Srikanth, V. Vishwanathan and K. V. R. Chary, Vapor phase oxidation of benzyl alcohol over nano Au/SBA-15 catalysts: effect of preparation methods, *Catalysis Letters*, 2016, **146**, 35-46.
10. A. Kumar, B. Sreedhar and K. V. R. Chary, Highly dispersed gold nanoparticles supported on SBA-15 for vapor phase aerobic oxidation of benzyl alcohol, *Journal of Nanoscience and Nanotechnology*, 2015, **15**, 1714-1724.
11. Y. Liu, H. Tsunoyama, T. Akita and T. Tsukuda, Size effect of silica-supported gold clusters in the microwave-assisted oxidation of benzyl alcohol with H₂O₂, *Chemistry Letters*, 2010, **39**, 159-161.
12. M. Murdoch, G. Waterhouse, M. Nadeem, J. Metson, M. Keane, R. Howe, J. Llorca and H. Idriss, The effect of gold loading and particle size on photocatalytic hydrogen production from ethanol over Au/TiO₂ nanoparticles, *Nature Chemistry*, 2011, **3**, 489-492.